Development and Applications of Quantum Chemistry to Open Shell Systems

Paul Murphy

Submitted for the degree of Doctor of Philosophy

Heriot-Watt University

Institute of Chemical Sciences

School of Engineering and Physical Sciences

May 20, 2017

Abstract

This thesis investigates the applicability of a range of computational techniques across a range of open shell chemical systems from the geometrically simple but electronically complex to the geometrically complex but electronically simple. Initially an investigation into a range of geometrically simple but electronically complicated systems is presented. The Monte Carlo Configuration Interaction method (MCCI) is applied to challenging transition metals dimers such as ScNi in order to establish the ground state potential energy surface, from equilibrium bond lengths through to dissociation using highly compact wavefunctions compared to Full Configuration Interaction (FCI). It shall be demonstrated that the ScNi dimer represents the current limit of this technique. Software development of MCCI is then undertaken in order to perform calculations of spin-orbit coupling interactions. Results on B, C, O, F, Si, S, F, Cl, OH, NO, CN and C_2 species are shown to be comparable with other techniques using the one-electron Breit-Pauli Hamiltonian. The application of quantum chemistry to geometrically complex but electronically simple systems is then considered. Density Functional Theory (DFT) is used to investigate the mechanism and energetic barriers leading to ring inversion of the biscalix[4]arene supra-molecule. A minimum barrier height of 19.31 kcalmol^{-1} to inversion is elucidated along with details of the complete mechanistic pathway to inversion. The focus then moves to polymetallic clusters of calix[4]arene. A DFT study is made of the preferential binding of calix[4]arene towards first row transition metals of various oxidation and spin states. Results indicate that Cu^{3+} (singlet) species will preferentially bind to the lower rim over other metals in the study. The final DFT-related work presented is a study of the preferential binding at the upper rim of polymetallic calix[4]arene clusters towards a range of important small gas molecules. It was found that gases such as NH_3 and SO_2 bind most strongly to the upper rim with the inclusion of a transition metal at the lower rim providing strengthening of the host-guest binding.

Acknowledgements

In any endeavour, there are always individuals who assist you on your journey and it is fitting to pay tribute to their efforts. In that regard I would like to express my thanks to my supervisor Professor Martin J. Paterson for his guidance, insight and vision in helping me define the work I have undertaken over the last three years and for making himself available to me on the occasions where I have required assistance.
I would also like to express my thanks to Dr Scott J. Dalgarno for his guidance on the calixarene work undertaken as part of this thesis. In particular I would like to thank him for allowing me access to his laboratory and supplies for a range of synthetic work I completed over several years.
I would like to extend my thanks to Dr Jeremy Coe for the many hours of advice and fruitful discussions on Quantum Chemistry in general and MCCI and Spin-Orbit Coupling in particular.
Finally I would like to thank my family for their support during the many hours of work I have devoted to this PhD: Jayne, Craig, Katie, Amy and Daisy the Beagle. Without them it would not have been possible for me to succeed.

List of Publications

1. J.P. Coe, P. Murphy, M.J. Paterson, "Applying Monte Carlo Configuration Interaction to Transition Metal Dimers: Exploring the Balance between Static and Dynamic Correlation", *Chem. Phys. Lett.*, **2014**, 604, 46-52.

2. P. Murphy, S.J. Dalgarno, M.J. Paterson, "Elucidating the Ring Inversion Mechanism(s) for Biscalixarenes", *J. Phys. Chem. A*, **2014**, 118, 7986-8001.

3. P. Murphy, R.G. McKinlay, S.J. Dalgarno, M.J. Paterson, "Toward Understanding of the Lower Rim Binding Preferences of Calix[4]arene", *J. Phys. Chem. A*, **2015**, 119, 5804-5815.

4. P. Murphy, S.J. Dalgarno, M.J. Paterson, "Transition Metal Complexes of Calix[4]arene: Theoretical Investigations into Small Guest Binding within the Host Cavity", *J. Phys. Chem. A*, **2016**, 120, 824-839.

5. M. Coletta, R. McLellan, P. Murphy, B.T. Leube, S. Sanz, R. Clowes, K.J. Gagnon, S.J. Teat, A.I. Cooper, M.J. Paterson, E.K. Brechin, S.J. Dalgarno, "Bis-Calix[4]arenes: From Ligand Design to the Directed Assembly of a Metal-Organic Trigonal Antiprism", *Chem. Eur. J.*, **2016**, 22, 8791-8795.

6. P. Murphy, S.J. Dalgarno, M.J. Paterson, "Systematic Methylation of the Tetraphenolic Pocket of Calixarenes: Effect on Small Guest Binding within the Host Cavity", *manuscript under preparation.*

7. P. Murphy, J.P. Coe, M.J. Paterson, "Ab-initio Calculation of Spin-Orbit Coupling in Small Molecules using the Monte Carlo Configuration Interaction Technique: Method Development and Proof of Concept", *manuscript under preparation.*

Contents

Nomenclature

$\hat{\Theta}$	General Operator
$\mathcal{H}$	Hamiltonian Operator
$\vec{f}$	Vector
$\vec{r}$	Spatial Vector
$\vec{l}$	Angular Momentum
$\vec{p}$	Linear Momentum
$\vec{s}$	Spin Vector
$\vec{j}$	Total Angular Momentum Vector
$\vec{m}$	Dipole Moment Vector
$f(x)$	Function
ϕ	Atomic Orbital Wavefunction
ψ	Molecular Spatial Orbital Wavefunction
χ	Molecular Spin-Orbital Wavefunction
Ψ	Slater Determinant or CSF Wavefunction
Φ	Multiconfigurational or Multireference Wavefunction
$\boldsymbol{F}$	General Matrix
F or F_{mn}	General Scalar Quantity or Matrix Element
h	Planck's Constant
$\hbar$	$h/2\pi$
$\hat{\nabla}$	Kinetic Energy Operator
$\hat{V}$	General Potential Energy Operator
$\hat{h}$	One-Electron Operator
$\hat{J}$	Two-Electron Coulombic Operator
$\hat{K}$	Two-Electron Exchange Operator
$\mathrm{S}_{\mu\nu}$	Overlap Matrix Element
Z_c	Nuclear Charge for Atom c

X	Non-Unitary Transformation Matrix
U	Unitary Transformation Matrix
C	Coefficient Matrix
$F_{\mu\nu}$	Fock Matrix Elements
$H_{\mu\nu}^{CORE}$	One Electron Matrix Elements
$G\mu\nu$	Two Electron Matrix Elements
ρ	Electron Density
$E[\rho]$	Energy Functional in ρ
$J[\rho]$	Correlation Functional in ρ
$K[\rho]$	Exchange Functional in ρ
$T[\rho]$	Kinetic Energy Functional in ρ
λ	Perturbation Strength Indicator
$\hat{s}$	Operator for Single Electron Spin
$\hat{s}_Z$	Operator for Single Electron Spin Projected on Z Axis
$\hat{S}$	Operator for Many Electron Spin
$\hat{S}_Z$	Operator for Many Electron Spin Projected on Z Axis

$$\hat{\alpha} = \begin{pmatrix} 0 & \hat{\sigma}_{x,y,z} \\ \hat{\sigma}_{x,y,z} & 0 \end{pmatrix}$$

$$\hat{\sigma}_x = \begin{pmatrix} 0 & 1 \\ 1 & 0 \end{pmatrix}$$

$$\hat{\sigma}_y = \begin{pmatrix} 0 & -i \\ i & 0 \end{pmatrix}$$

$$\hat{\sigma}_z = \begin{pmatrix} 1 & 0 \\ 0 & -1 \end{pmatrix}$$

$$\hat{\beta} = \begin{pmatrix} I & 0 \\ 0 & -I \end{pmatrix}$$

$\mathcal{H}^{so}$	Breit-Pauli Spin-Orbit Coupling Hamiltonian
Γ_m	Symmetry of Object m

Abbreviations

BSSE	Basis Set Superposition Error
C4	Calix[4]arene
CASSCF	Complete Active Space Self-Consistent Field
CASPT2	CASSCF with additional PT2 perturbative corrections
CGTO	Contracted Gaussiam Type Orbital
CI	Configuration Interaction
CIS	Configuration Interaction Singles
CISD	Configuration Interaction Singles and Doubles
CISDT	Configuration Interaction Singles, Doubles and Triples
CISD(T)	CISD with Triples estimated
CISDT(Q)	CISDT with Quadruples estimated
CPCM	Conductor-like Polarisable Continuum Model
CSF	Configuration State Function
DFT	Density Functional Theory
ECP	Effective Core Potential
EOM-CCSDT	Equations Of Motion - with CCSDT
FCI	Full Configuration Interaction
FCIQMC	FCI with Quantum Monte Carlo
GGA	Generalised Gradient Approximation
GTO	Gaussian Type Orbital
HF	Hartree-Fock Theory
HSAB	Hard-Soft Acid-Base Theory
LDA	Local Density Approximation
LDF	Local Density Functional

LCAO-LDF	Linear Combination of Atomic Orbitals - LDF
LSDA	Local Spin Density Approximation
MCCI	Monte Carlo Configuration Interaction
MCSCF	Multi-Configurational Self-Consistent Field
MO	Molecular Orbital
MP2	Moller-Plesset 2nd Order Perturbation Theory
MRCI	Multi-Reference Configuration Interaction
NBO	Natural Bond Order
NMR	Nuclear Magnetic Resonance
NO	Natural Orbital
PCM	Polarisable Continuum Model
PT2	Second Order Perturbation Theory
RHF	Restricted Hartree-Fock Theory
ROHF	Restricted Open Shell Hartree-Fock
SCF	Self-Consistent Field
SD	Slater Determinant
SDD	Stuttgart-Dresden Effective Core Potential
SMD	Solvation Model based on Density
SOC	Spin-Orbit Coupling
STO	Slater Type Orbital
TBC4	*p*-Tertbutyl Calix[4]arene
TDDFT	Time-Dependent DFT
TFD	Thomas-Fermi-Dirac Model
UHF	Unrestricted Hartree-Fock Theory
UMP2	Unrestricted MP2
VDW	van der Waal
XRD	Single Crystal X-Ray Diffraction

Chapter 1

Introduction

1.1 Time-Independent Schrödinger Equation

In order to solve problems involving the energies, reactivity or properties of chemical systems at the molecular level, one must subject the system to a quantum mechanical treatment. Here, the mechanics involved deviates significantly from that described by Newton, requiring instead the Schrödinger wave equation [1], with correspondence between the two mechanical descriptions occurring as the energy levels of the system coalesce to a continuum as $h \to 0$. Although the Schrödinger equation was initially derived in time-independent form, with the time-dependent form subsequently discovered at a later date, it is convenient to present the theory in the reverse order. Therefore we start from the time-dependent form and derive the time-independent version from consideration of this [2]. The time-dependent form of the Schrödinger equation, in atomic units, is shown in equation 1.1, where $\vec{r}$ is a position vector.

$$\mathcal{H}\Psi(\vec{r},t) = i\hbar\frac{d}{dt}\Psi(\vec{r},t) \tag{1.1}$$

The solution, $\Psi(\vec{r},t)$, to this differential equation can be constructed, via separation of distance and time variables, as the product of two functions $\psi(\vec{r})$ and $\phi(t)$ as shown in equation 1.2.

$$\Psi(\vec{r},t) = \psi(\vec{r})\phi(t) \tag{1.2}$$

Substituting equation 1.2 into equation 1.1 and dividing throughout by $\psi(\vec{r})\phi(t)$ leads to equation 1.3.

$$\frac{\mathcal{H}\psi(\vec{r})\phi(t)}{\psi(\vec{r})\phi(t)} = \frac{i\hbar}{\psi(\vec{r})\phi(t)}\frac{d}{dt}\psi(\vec{r})\phi(t) \tag{1.3}$$

On the left hand side of this equation, the Hamiltonian operator, $\mathcal{H}$, only contains spatial dependence allowing commutation with $\phi(t)$. On the right hand side of the equation, $\psi(\vec{r})$ can commute with the partial differential operator leading to equation 1.4.

$$\frac{\phi(t)\mathcal{H}\psi(\vec{r})}{\psi(\vec{r})\phi(t)} = \frac{i\hbar\psi(\vec{r})}{\psi(\vec{r})\phi(t)}\frac{d}{dt}\phi(t) \tag{1.4}$$

Cancelling out on both sides leads to equation 1.5.

$$\frac{\mathcal{H}\psi(\vec{r})}{\psi(\vec{r})} = \frac{i\hbar}{\phi(t)}\frac{d}{dt}\phi(t) \tag{1.5}$$

Because both sides of the above equation now contain only one variable, the only way they can be equivalent to each other is if they are both equal to the same constant. This constant is called E and the resultant spatial equation is shown in equation 1.6 with the time-dependent part shown in equation 1.7.

$$\mathcal{H}\psi(\vec{r}) = E\psi(\vec{r}) \tag{1.6}$$

$$\frac{i\hbar}{\phi(t)}\frac{d}{dt}\phi(t) = E \tag{1.7}$$

The time-dependent equation 1.7 is a first order differential equation with solutions shown in equation 1.8.

$$\phi(t) = e^{-iEt/\hbar} \tag{1.8}$$

The wavefunction $\Psi(\vec{r}, t)$ can therefore be described as shown in equation 1.9.

$$\Psi(\vec{r}, t) = \psi(\vec{r})e^{-iEt/\hbar} \tag{1.9}$$

From here it is a simple matter to show that both the expectation value for any time-independent operator ($\hat{\Theta}$) and the probability density function of the wavefunction are both independent of time and can be expressed as shown in equations 1.10 and 1.11.

$$\left\langle \hat{\Theta} \right\rangle = \langle \psi(\vec{r}) | \hat{\Theta} | \psi(\vec{r}) \rangle \tag{1.10}$$

$$|\Psi(\vec{r}, t)|^2 = \psi^*(\vec{r})\psi(\vec{r}) \tag{1.11}$$

Hence the use of the time-independent Schrödinger equation for systems with non-varying potential energy is justified and the eigenvectors subsequently form stationary states of the system.

1.2 Born-Oppenheimer Approximation

The Schrödinger equation is thus seen to be an eigenvalue equation consisting of a Hamiltonian operator, $\mathcal{H}$, the eigenvector ψ, which is the wavefunction, and an eigenvalue constant E. In this case, the constant E is the energy of the system extracted from the wavefunction based on a Hamiltonian operator which contains kinetic and potential energy terms pertinent to the system under consideration. In order to solve the Schrödinger Equation for chemical systems, one must first construct a suitable Hamiltonian operator $\mathcal{H}$, by consideration of the energetic interactions experienced by the constituent parts of the chemical system. Containing a series of positively charged nuclei and negatively charged electrons, determination of the interactions within a chemical system is straightforward: each nucleus and electron will have kinetic energy, nuclei will experience repulsion from all other nuclei, electrons will experience attraction to each nucleus and electrons will repel one another. Five terms are therefore required in the Hamiltonian operator to fully capture the energetics of the chemical system (neglecting relativistic effects). In atomic units, therefore, the non-relativistic Hamiltonian is described mathematically as in equation 1.12, where M is the number of nuclei, m_a is the mass of nucleus a, N is the number of electrons, R_{ia} is the distance between electron i and nucleus a, R_{ab} is

the distance between nuclei a and b and r_{ij} is the distance between electrons i and j.

$$\mathcal{H} = -\sum_{a=1}^{M} \frac{1}{2m_a}\hat{\nabla}_a^2 - \frac{1}{2}\sum_{i=1}^{N}\hat{\nabla}_i^2 - \sum_{a=1}^{M}\sum_{i=1}^{N}\frac{Z_a}{r_{ia}} + \sum_{i=1}^{N}\sum_{j=1}^{N}\frac{1}{r_{ij}} + \sum_{a=1}^{M}\sum_{b=1}^{M}\frac{Z_a Z_b}{R_{ab}} \quad (1.12)$$

This complicated equation can initially be simplified by recognising that the mass of a proton is approximately 1800 times heavier than that of an electron. On average, the nuclei and electrons within a molecule tend to share the same kinetic energy as the molecule moves around. Being much lighter however, the electrons are able to move much faster than the nuclei. A reasonable approximation can then be made to model the chemical system as a series of stationary nuclei around which the electrons move. The first term in equation 1.12, the kinetic energy of the nuclei, is then considered zero. For similar reasons, the fifth term, describing the nuclear-nuclear repulsion is considered a constant and thus commutes with the Hamiltonian. This term can therefore be removed from the Hamiltonian and treated as a constant energy term at the end, leaving only terms which describe the electronic energy of the system within the Hamiltonian as shown in equation 1.13. This series of approximations is called the Born-Oppenheimer Approximation [3] and the chemical system can be thought of as a nuclear framework on which the electrons instantaneously follow the nuclei as the nuclei move. This essentially results in the concept of a potential energy surface on which the nuclei freely move.

$$\mathcal{H}_{elec} = -\frac{1}{2}\sum_{i=1}^{N}\hat{\nabla}_i^2 + \sum_{a=1}^{M}\sum_{i=1}^{N}\frac{Z_a}{r_{ia}} + \sum_{i=1}^{N}\sum_{j=1}^{N}\frac{1}{r_{ij}} \quad (1.13)$$

Because this work is concerned only with the electronic Hamiltonian equation, for clarity, the subscript on $\mathcal{H}_{elec}$ is dropped and from this point forward, it is assumed that $\mathcal{H}$ represents the Born-Oppenheimer electronic Hamiltonian.

1.3 Basis Set Expansion

Before discussing the Hartree-Fock approximation, it is an appropriate time to pause briefly to discuss the concept of basis sets and the variational principle.

Having described simplifications to the Hamiltonian operator through the Born-Oppenheimer Approximation, the focus now turns to approximation of the unknown wavefunction ψ from equation 1.6. A function in Hilbert space can be described by an infinite linear combination of known basis functions, ϕ_μ, which span that space as described by equation 1.14, where $c_{\mu i}$ are the coefficients of ϕ_μ for a particular unknown wavefunction ψ_i.

$$\psi_i = \sum_{\mu=1}^{\infty} c_{\mu i}\phi_\mu \tag{1.14}$$

In terms of practical solutions to the Schrödinger equation, an infinite solution is not suitable. Nevertheless, we can approximate ψ_i using a finite length, truncated series of basis functions pertinent to the problem at hand, mindful of the fact that any truncation will inevitably result in errors describing the exact wavefunction as the finite basis set will not be able to span the correct space. The implementation of truncation therefore takes us to equation 1.15, where K is the basis set truncation length.

$$\psi_i = \sum_{\mu=1}^{K} c_{\mu i}\phi_\mu \tag{1.15}$$

From here, the selection of basis functions must be made and this will be covered later. Substituting the basis set approximation of equation 1.15 into equation 1.6 leaves us with the equation 1.16.

$$\mathcal{H}\sum_{\mu=1}^{K} c_{\mu i}\phi_\mu = E_i \sum_{\mu=1}^{K} c_{\mu i}\phi_\mu \tag{1.16}$$

In order to determine the energy of such a system, it is necessary to calculate the expectation value for the Hamiltonian (energy) operator in the basis of ϕ_μ. This is done by multiplying both sides of equation 1.16 by $c^*_{\nu i}\phi^*_\nu$ and integrating over all spatial co-ordinates. This leads to equation 1.17.

$$\sum_{\mu,\nu=1}^{K} c^*_{\nu i}c_{\mu i}\int d\vec{r}_1 d\vec{r}_2\ \phi^*_\nu(\vec{r}_1)\mathcal{H}\phi_\mu(\vec{r}_2) = \sum_{\mu,\nu=1}^{K} E_i c^*_{\nu i}c_{\mu i}\int d\vec{r}_1 d\vec{r}_2\ \phi^*_\nu(\vec{r}_1)\phi_\mu(\vec{r}_2) \tag{1.17}$$

We can simplify this equation to use Dirac notation as shown in equation 1.18

$$\sum_{\mu,\nu=1}^{K} c_{\nu i}^{*} c_{\mu i} \langle \phi_\nu | \mathcal{H} | \phi_\mu \rangle = \sum_{\mu,\nu=1}^{K} E_i c_{\nu i}^{*} c_{\mu i} \langle \phi_\nu | \phi_\mu \rangle \tag{1.18}$$

which is in the form of equation 1.19

$$\boldsymbol{HC = ESC} \tag{1.19}$$

This equation is the general case for non-orthogonal functions. As we shall see later, simplification is achieved with orthonormal wavefunctions. We have thus converted the time-independent Schrödinger equation, 1.6, into a system of linear equations which can be solved using standard computational techniques as will be shown.

1.4 Variational Principle

Because we are using a finite basis set expansion to describe the wavefunction, not only will errors be introduced into our calculations, we also cannot know the exact result we are seeking. The variational principle [4] allows us to reach some conclusions however. The process is relatively simple. In order to solve the time-independent Schrödinger equation, 1.6, we re-write it as equation 1.20 recognising that we have more than one wavefunction ψ_i.

$$\mathcal{H}\psi_i = E_i \psi_i \tag{1.20}$$

We then multiply both sides of the equation by ψ_j^* and integrate over all space and spin coordinates. In Dirac notation, we thus have equation 1.21.

$$\langle \psi_j | \mathcal{H} | \psi_i \rangle = E \langle \psi_j | \psi_i \rangle \tag{1.21}$$

Now dividing both sides by $\langle \psi_j | \psi_i \rangle$ allows us to obtain an expression for the energy as shown in equation 1.22.

$$E = \frac{\langle \psi_j | \mathcal{H} | \psi_i \rangle}{\langle \psi_j | \psi_i \rangle} \tag{1.22}$$

If the wavefunctions form an orthonormal set, the denominator will be equal to 1, simplifying the calculations and we are left with equation 1.23.

$$E = \langle \psi_j | \mathcal{H} | \psi_i \rangle \tag{1.23}$$

The variational principle can be stated as in equation 1.24 for such orthonormal wavefunctions.

$$\langle \psi_j | \mathcal{H} | \psi_i \rangle \geq \epsilon_o \tag{1.24}$$

where ϵ_o is the exact ground state energy of the system. In other words we optimise the wavefunction to produce the minimum energy, at which point we have the best wavefunction possible to describe the ground state for the basis set used. In order to optimise our wavefunction and thus obtain the ground state energy, we note that the wavefunctions ψ_i and ψ_j can be expressed in terms of the truncated basis set as described earlier in equation 1.15. Substituting the truncated basis set into equation 1.24 we obtain equation 1.25.

$$\sum_{\mu,\nu=1}^{K} c_{\nu i}^{*} c_{\mu j} \langle \phi_\nu | \mathcal{H} | \phi_\mu \rangle \geq \epsilon_o \tag{1.25}$$

Because the basis set functions ϕ are usually fixed, the only available degrees of freedom are in the choice of the basis set coefficients $c_{\mu j}$ and $c_{\nu i}$ and the coefficients are optimised to produce the minimum energy. The technique used is that of the Lagrange method of undetermined multipliers, with the constraint that the wavefunctions used are orthonormalised such that the sum of the squares of the coefficients is 1. Incorporating this constraint into equation 1.24 and minimising the energy with respect to the coefficients leads us to the ground state energy of the system.

1.5 Hartree-Fock Theory

We have, so far, described the simplification of the wavefunction by using a truncated basis set and we have also described that it is possible to optimise the resultant

wavefunction to produce a minimum energy for the ground state of the system. Unfortunately the Hamiltonian, despite simplifications brought about by the Born-Oppenheimer approximation and the neglect of relativistic effects, is still unsolvable. The problem can be seen in the Born-Oppenheimer electronic Hamiltonian shown in equation 1.26.

$$\mathcal{H} = -\frac{1}{2}\sum_{i=1}^{N}\hat{\nabla}_i^2 + \sum_{a=1}^{M}\sum_{i=1}^{N}\frac{Z_a}{r_{ia}} + \sum_{i=1}^{N}\sum_{j=1}^{N}\frac{1}{r_{ij}} \tag{1.26}$$

It is the final electron-electron repulsion term which causes the problem. When we have more than one electron present, it is not possible to calculate the interaction between any pair of electrons without knowing their individual interactions with all of the other electrons and nuclei: essentially the paired electron interactions are coupled. The result is a highly non-linear problem which cannot be solved analytically. Before proceeding, further simplifications are required. The first successful approach to this was the Hartree-Fock approximation, also called the Mean Field Approximation [5]. In the Mean Field Approximation, the system is treated as a series of non-interacting electrons, each described by its own wavefunction. This approximation allows, by separation of variables, the total electronic wavefunction to be described by a simple product of functions, each representing a single electron, called the Hartree Product as shown in equation 1.27 for a two electron wavefunction, dependent on both spatial and spin co-ordinates, $(\vec{x}_1, \vec{x}_2...)$ where $\chi(\vec{x}_i) = \psi(\vec{r}_i)\rho(\vec{\omega})$.

$$\Psi^{HP} = \chi_i(\vec{x}_1)\chi_j(\vec{x}_2) \tag{1.27}$$

The Hartree Product however does not reflect the necessary property that electrons are indistinguishable and therefore does not satisfy the Pauli Principle, which requires that the wavefunction must be antisymmetrised with respect to exchange of any two fermionic electrons. In order to satisfy the Pauli Principle, the wavefunction must take the following form shown in equation 1.28 for a simple two electron wavefunction where a normalisation factor of $\frac{1}{\sqrt{2}}$ is included.

$$\Psi(\vec{x}_1, \vec{x}_2) = \frac{1}{\sqrt{2}}(\chi_i(\vec{x}_1)\chi_j(\vec{x}_2) - \chi_j(\vec{x}_1)\chi_i(\vec{x}_2)) \tag{1.28}$$

This form of the antisymmetrised wavefunction can be expressed in a more compact fashion using a Slater Determinant as shown in equation 1.29.

$$\Psi(\vec{x}_1, \vec{x}_2) = \frac{1}{\sqrt{2}} \begin{vmatrix} \chi_i(\vec{x}_1) & \chi_j(\vec{x}_1) \\ \chi_i(\vec{x}_2) & \chi_j(\vec{x}_2) \end{vmatrix} \tag{1.29}$$

Of course, almost all real systems contain more than two electrons and thus the more general N-particle solution to equation 1.28 is shown in equation 1.30 (with $\vec{x}$ prefixes dropped) with the equivalent normalised Slater Determinant shown in equation 1.31. $\hat{P}_n$ is the permutation operator which generates the n-th permutation of the electrons and q_n is the number of orbital transpositions required to achieve that permutation from the original wavefunction.

$$\Psi(\vec{x}_1, \vec{x}_2, ..., \vec{x}_N) = \frac{1}{\sqrt{N!}} \sum_{n=1}^{N!} (-1)^{q_n} \hat{P}_n \chi_i(1)\chi_j(2)....\chi_k(N) \tag{1.30}$$

$$\Psi(\vec{x}_1, \vec{x}_2, ..., \vec{x}_N) = \frac{1}{\sqrt{N!}} \begin{vmatrix} \chi_i(1) & \chi_j(1) & .... & \chi_k(1) \\ \chi_i(2) & \chi_j(2) & .... & \chi_k(2) \\ .... & .... & .... & .... \\ \chi_i(N) & \chi_j(N) & .... & \chi_k(N) \end{vmatrix} \tag{1.31}$$

This single determinant approximation of the wavefunction is the core of the Hartree-Fock approximation and once this form of the wavefunction is inserted into the Schrödinger equation, an expression for the energy constructed with it and that energy subsequently minimised with respect to the orbital coefficients, via the Variational Principle described earlier, we are left with the Hartree-Fock equation shown in equation 1.32, where $\hat{h}$ is the one-electron operator shown in equation 1.33 and electrons 1 and 2 are used by convention. The next two terms are operators which are best described when shown acting on an orbital $\chi_a(1)$. $\hat{J}_b(1)\chi_a(1)$ is the two-electron Coulomb operator defined in equation 1.34 and $\hat{K}_b(1)\chi_a(1)$ is called the two-electron Exchange operator shown in 1.35, a and b are the orbital indices and electron indices are shortened from $\vec{x}_1$ to simply 1 etc.

$$\left[\hat{h}(1) + \sum_{b \neq a} \hat{J}_b(1) - \sum_{b \neq a} \hat{K}_b(1)\right] \chi_a(1) = \epsilon_a \chi_a(1) \tag{1.32}$$

$$\hat{h}(1) = -\frac{1}{2}\hat{\nabla}_1^2 - \sum_A \frac{Z_A}{r_{1A}} \tag{1.33}$$

$$\hat{J}_b(1)\chi_a(1) = \left[\int d\vec{x}_2\ \chi_b^*(2)\frac{1}{r_{12}}\chi_b(2)\right]\chi_a(1) \tag{1.34}$$

$$\hat{K}_b(1)\chi_a(1) = \left[\int d\vec{x}_2\ \chi_b^*(2)\frac{1}{r_{12}}\chi_a(2)\right]\chi_b(1) \tag{1.35}$$

The quantity contained within square brackets in equation 1.32 is called the Fock operator, $\hat{f}(1)$. It can be seen that although the exchange part of the equation has no classical equivalent, the Coulombic operator shows that the electron in orbital χ_a essentially experiences the total average potential of the remaining electrons in the system. This is in contrast to the exact Schrödinger equation whereby the electron in orbital χ_a would experience the individual potential of each of the remaining electrons through the $\frac{1}{r_{ij}}$ term as shown in equation 1.26 and is a direct consequence of approximating the total electronic wavefunction by a single Slater Determinant. As such, the Hartree-Fock approximation is considered a single reference method with several consequences which will now be explored.

The use of an average field potential for the two-electron terms means that electron correlation is not properly taken account of, resulting in electrons being allowed to unreasonably encroach on each other within Hartree-Fock calculations. Although there is some correlation, via the Pauli principle, between electrons of the same spin which prevents those electrons sharing the same spatial orbitals (bearing in mind however that this correlation is still underestimated due to the Mean Field Approximation), there is no such restraint on electrons of opposing spin. Despite the fact that electrons of opposing spin still should repel each other, both can co-exist in the same spatial orbital in the Hartree-Fock approximation. Electrons are allowed to be packed closer together than expected and therefore Hartree-Fock calculations result in higher absolute energies as a result of the electrons not having the flexibility to move further apart under the repulsive forces of the individual electron potentials. Because of the closer packing of electrons, atoms are allowed to become closer than they should with consequent reduction in bond length predictions. Despite the problems described above however, Hartree-Fock calculations recover around 99% of the total energy of a molecule, with the remaining 1% lost due to the poor treatment of

electron correlation. Absolute energies of chemical species are of limited importance in Chemistry applications however. Instead, the relative energy differences between species are crucial in determining the reactivity, thermodynamics and properties of chemical systems. These relative energy differences can be comparable with the correlation energy error and thus it is crucial that correlation errors are addressed sufficiently to make these *ab initio* calculations of practical use. Techniques for doing this will be considered later. For now however, the discussion of Hartree-Fock theory continues with a look at the practicalities of solving the highly non-linear eigenvalue equation using iterative techniques.

1.6 Roothaan-Hall Equations

The first stage in dealing with the Hartree-Fock equations, shown in equation 1.32, is to integrate out the spin component. Once this has been completed, using the closed shell restricted Hartree-Fock case as an example, we are left with the purely spatial version shown in equation 1.36.

$$\hat{f}(1)\psi_i(1) = \epsilon_i\psi_i(1) \tag{1.36}$$

At this stage, the entire differential equation problem can be transformed into an algebraic problem, the Roothaan-Hall equations [6][7], and thus in an ideal form for solution by computer methods, using linear algebra techniques. The approach taken by Roothaan was to expand the unknown molecular orbitals in a finite linear expansion of known basis functions as shown in equation 1.37.

$$\psi_i = \sum_{\nu=1}^{K} c_{\nu i}\phi_\nu \tag{1.37}$$

The task now is to identify the optimal coefficients, $c_{\nu i}$. This is done by pre-multiplying both sides of equation 1.37 by ϕ_μ^* and integrating over all space as shown in equation 1.38.

$$\sum_\nu c_{\nu i}\left[\int d\vec{r}_1\phi_\mu^*(1)\hat{f}(1)\phi_\nu(1)\right] = \epsilon_i\sum_\nu c_{\nu i}\left[\int d\vec{r}_1\phi_\mu^*(1)\phi_\nu(1)\right] \tag{1.38}$$

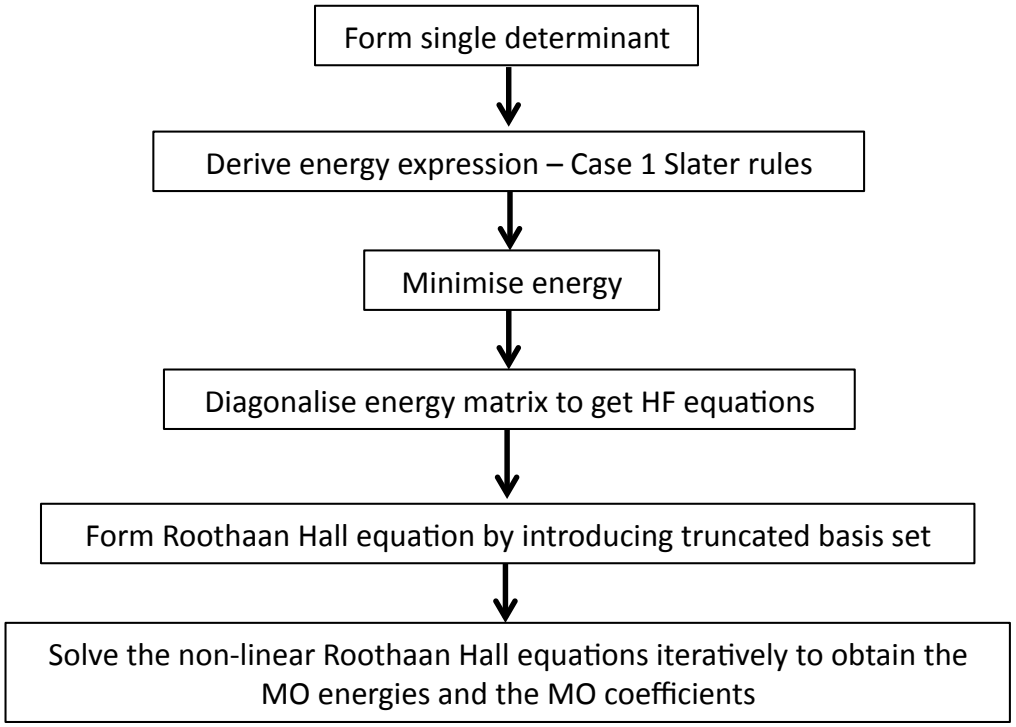

Figure 1.1: Procedure for solving Hartree-Fock equation via basis set expansion

This equation takes the form of the algebraic Roothaan-Hall equations shown in 1.39.

$$\boldsymbol{FC} = \boldsymbol{SC}\epsilon \tag{1.39}$$

The integro-differential Hartree-Fock equations have now been replaced by the algebraic Roothaan-Hall equations and can now be solved using iterative matrix techniques. Notice however from equation 1.38 that although we are attempting to find the wavefunction as a solution to the equations, the wavefunction also appears in the operator. In other words we cannot solve the Roothaan-Hall equations to find the wavefunction unless we already know the wavefunction. This is an example of a highly non-linear equation which must be solved iteratively using the Self Consistent Field (SCF) Process as will be described in the next section. In summary then, the Hartree-Fock process can be summarised in figure 1.1.

1.7 Self-Consistent Field (SCF) Procedure

The Self-Consistent Field (SCF) procedure [8] is an iterative solution to the highly non-linear Hartree-Fock equations and, for illustrative purposes, a general solution is provided here for the Restricted Closed Shell Hartree-Fock case using the Roothaan-Hall equations derived in the previous section. Initially a nuclear geometry is established, representing the system in question. This stage will include specification of the desired basis set and will also establish necessary parameters such as the various atomic numbers, Z, the number of electrons in the system, N, and the co-ordinates of the constituent atoms, which subsequently provide the inter-nuclear distances, R. From this initial geometry specification, all of the information is available to calculate the integrals required for the SCF calculations, namely the overlap integrals $S_{\mu\nu}$, the core Hamiltonian one-electron integrals, $H_{\mu\nu}^{CORE}$ and the two-electron integrals, $(\mu\nu|\lambda\sigma)$, which are contained within the $\boldsymbol{F}$ term of the Roothaan-Hall equations. These integrals are defined in equations 1.40, 1.41 and 1.42 respectively.

$$H_{\mu\nu}^{CORE} = \int d\vec{r}_1 \, \phi_\mu^*(1) \Big(-\frac{1}{2}\hat{\nabla}_1^2 - \sum_c \frac{Z_c}{|r_1 - R_c|} \Big) \phi_\nu(1) \tag{1.40}$$

$$S_{\mu\nu} = \int d\vec{r}_1 \, \phi_\mu^*(1)\phi_\nu(1) \tag{1.41}$$

$$(\mu\nu|\lambda\sigma) = \int d\vec{r}_1 d\vec{r}_2 \, \phi_\mu^*(1)\phi_\nu(1)\frac{1}{r_{12}}\phi_\lambda^*(2)\phi_\sigma(2) \tag{1.42}$$

The $S_{\mu\nu}$ matrix elements cause a problem here in terms of solving the Roothaan-Hall equations because although the orbitals are normalised, they are not in general orthogonal. This results in a more complicated set of equations which are difficult to solve. This situation is resolved by finding a non-unitary transformation matrix, $\boldsymbol{X}$, which transforms the orbitals to an orthonormal set as shown in equation 1.43.

$$\phi_\mu^{'} = \sum_\nu X_{\mu\nu}\phi_\nu \tag{1.43}$$

This $\boldsymbol{X}$ matrix can be derived from the diagonalisation of $\boldsymbol{S}$ by a unitary matrix, $\boldsymbol{U}$, using any one of a number of techniques available for the purpose, such as the Lanczos, Davidson or Davidson-Liu algorithms [9][10][11]. These techniques

establish the unitary matrix, $\boldsymbol{U}$ which acts on $\boldsymbol{S}$ to produce a diagonalised matrix, $\boldsymbol{s}$, a transformation possible as a result of the Hermitian character of $\boldsymbol{S}$. This is shown in equation 1.44. $\boldsymbol{X}$ can be derived directly from $\boldsymbol{s}$ using one of a variety of approaches such as Symmetric Orthogonalisation or Canonical Orthogonalisation, equations 1.45 or 1.46 respectively. A guess is then made of the required density matrix for the system. This density matrix is described in equation 1.47. Of course, at this stage, the co-efficients $c_{\lambda a}$ and $c^*_{\sigma a}$ are unknown (the SCF procedure is attempting to optimise them). It is not unusual for the zero density matrix to be used as the initial guess. A $\boldsymbol{G}$ matrix is then able to be constructed using this density matrix and the two-electron integrals as shown in 1.48. The Fock matrix is then simply the addition of the $H^{CORE}_{\mu\nu}$ and $\mathrm{G}_{\mu\nu}$ matrices as show in equation 1.49. The Fock matrix is then transformed using the $\boldsymbol{X}$ matrix to take advantage of the, now orthogonally transformed, orbitals as shown in equation 1.50.

$$\boldsymbol{s} = \boldsymbol{U}^\dagger \boldsymbol{S} \boldsymbol{U} \tag{1.44}$$

$$\boldsymbol{X}_{symmetric} = \boldsymbol{U}\boldsymbol{s}^{-1/2}\boldsymbol{U}^\dagger \tag{1.45}$$

$$\boldsymbol{X}_{canonical} = \boldsymbol{U}\boldsymbol{s}^{-1/2} \tag{1.46}$$

$$P_{\lambda\sigma} = 2\sum_{a}^{\frac{N}{2}} c_{\lambda a} c^*_{\sigma a} \tag{1.47}$$

$$G_{\mu\nu} = \sum_{\lambda\sigma} P_{\lambda\sigma}[(\mu\nu|\sigma\lambda) - \frac{1}{2}(\mu\lambda|\sigma\nu)] \tag{1.48}$$

$$F_{\mu\nu} = H^{CORE}_{\mu\nu} + G_{\mu\nu} \tag{1.49}$$

$$\boldsymbol{F}' = \boldsymbol{X}^\dagger \boldsymbol{F} \boldsymbol{X} \tag{1.50}$$

The Roothaan-Hall equations can now be solved by diagonalising $\boldsymbol{F}'$ to give the orbital energies and the corresponding orbital wavefunction coefficients $\boldsymbol{C}'$ which

can then be transformed using $\boldsymbol{X}$ to recover the $\boldsymbol{C}$ matrix of MO coefficients as shown in equation 1.51.

$$\boldsymbol{C} = \boldsymbol{X}\boldsymbol{C}' \tag{1.51}$$

From the $\boldsymbol{C}$ matrix, a new density matrix can be created as in equation 1.47. This new density matrix is compared to the previous (old) density matrix, perhaps via a least squares calculation, in order to determine whether differences between them fall within the convergence criteria set out at the start of the calculation. If convergence has not yet been achieved, the process of the Fock matrix formation, transformation of the Fock matrix, diagonalisation of the transformed Fock matrix and the density matrix formation is repeated until convergence is reached. If on the other hand the result is considered converged, then the SCF procedure has completed and we have our set of orbitals with their corresponding energies, from which the electronic energy of the system can be determined as described by equation 1.52.

$$E_{elec} = \frac{1}{2}\sum_{\mu}\sum_{\nu} P_{\nu\mu}(H_{\mu\nu}^{CORE} + F_{\mu\nu}) \tag{1.52}$$

The total energy of the system can then be found using equation 1.53, where we add the nuclear-nuclear repulsion term which was omitted from the electronic Hamiltonian as a result of the Born-Oppenheimer approximation.

$$E_{total} = E_{elec} + \sum_{A=1}^{M}\sum_{B>A}^{M}\left(\frac{Z_A Z_B}{R_{AB}}\right) \tag{1.53}$$

Once the SCF calculation is complete, the orbitals can then be used for calculating the expectation values of other properties of interest, such as dipole moments, or for geometry optimisation of the system. The SCF process can be summarised in figure 1.2. Note that in this process, the integrals can be stored on disk and recovered when necessary or can be calculated "on the fly" using direct methods in situations where disk storage is limited or performance suffers from slow disk access.

The Hartree-Fock solution therefore is the best possible solution to the Schrödinger equation using a single Slater Determinant, representing the antisymmetrised wavefunction. In order to improve upon this, electron correlation must be taken into

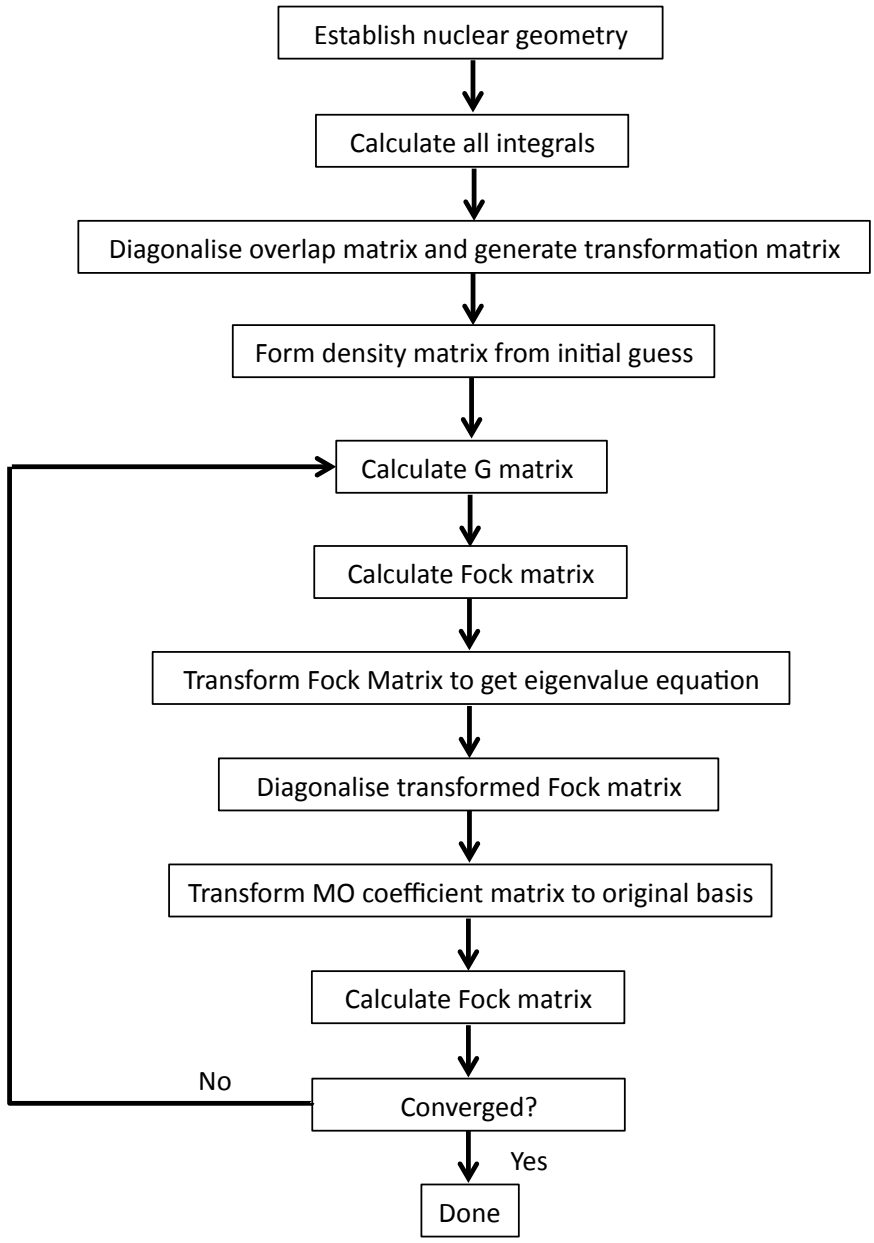

Figure 1.2: Overview of the Self-Consistent Field (SCF) method for solving non-linear Hartree-Fock equations.

account and this is now discussed.

1.8 Electron Correlation

As a result of the Pauli principle, each electron creates a hole around it known as the Fermi Hole, in which there is a zero probability of finding another electron with the same spin. In other words, electrons of the same spin have some correlation, termed Fermi or Exchange Correlation and the Hartree-Fock approximation allows some of this correlation energy to be recovered, albeit subject to the constraints of the Mean Field Approximation described earlier. Another electron of opposite spin however can inhabit this space: that is, electrons of differing spin have no correlation and this type of correlation energy is completely neglected in the Hartree-Fock approximation. In the effort to recover electron correlation, post Hartree-Fock techniques are employed. Electron correlation can be categorised as either Static Correlation or Dynamic Correlation and both of these will now be discussed in turn [12] [13] [14].

1.8.1 Static Correlation

Static Correlation is most easily understood by consideration of molecular systems at geometries where many low lying electronic configurations approach near degeneracy. The situation is illustrated using the H_2 molecule shown in figure 1.3. At equilibrium, the σ_g and σ_u^* molecular orbitals are very well spaced energetically and thus the HOMO-LUMO gap is large. Under these circumstances a single reference wavefunction, $\Psi_o = \left|\sigma_g^2\right\rangle$, proves to be a very good approximation of the ground state of the system. As the bond length increases towards dissociation however, the two molecular orbitals become closer in energy shrinking the HOMO-LUMO gap towards zero. This results in the lowest excited electronic configurations and the ground electronic configuration approaching degeneracy. In addition to the potential for significant convergence problems at these geometries, use of a single reference wavefunction will not allow sufficient flexibility in the wavefunction to best capture the description of the real chemical system under investigation. This lack of flexibility in the wavefunction results in artificially high energy for the ground

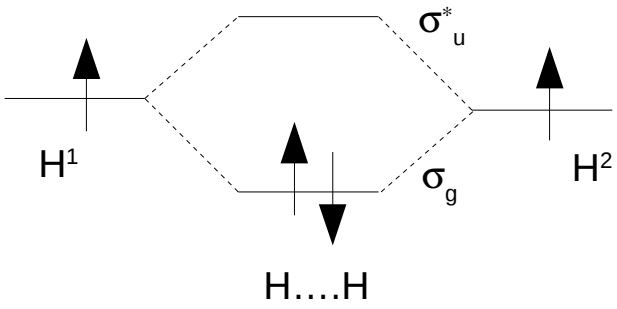

Figure 1.3: Recovery of static correlation when applied to the H_2 molecule.

state. Ultimately, at this point it becomes less meaningful to talk about a single ground state electron configuration and, instead, a superposition of the degenerate configurations becomes more appropriate. The artificial increase in energy, due to using a single reference method to describe what is essentially a multi-reference system, is termed static correlation and it can be recovered using a variety of post Hartree-Fock techniques such as Configuration Interaction (some examples of which include CIS, CISD, MCSCF, CASSCF and MCCI). Allowing all possible electronic configurations to be included in the wavefunction results in what is called the Full Configuration Interaction solution. The FCI solution for the H_2 molecule contains only single and double excitations from the HF reference wavefunction, but single excitations can be eliminated from symmetry considerations. The required wavefunction near dissociation is therefore $\Phi_o = c_0 \left|\sigma_g^2\right\rangle + c_1 \left|\sigma_u^2\right\rangle$, where c_0 and c_1 are appropriate coefficients.

Static correlation is a weak, long range effect, the recovery of which manifests itself in a wavefunction containing a relatively small number of electronic configurations with large coefficients in the wavefunction expansion. CI and FCI will be described in detail in a later section.

1.8.2 Dynamic Correlation

Dynamic Correlation is perhaps more intuitively simple to understand as it relates to the energetic contribution caused by the immediate response of an electron to the approach of another electron. It is a short range effect involving many strong interactions. As explained above, this dynamic correlation is poorly described by

Hartree-Fock for electrons of the same spin which approach each other, due to the use of the Mean Field Approximation. A worse problem however is that there is no allowance within the Hartree-Fock approximation for electron correlation between electrons of opposing spins. The net result of both of these problems is that electrons can become artificially close to each other causing bond lengths which are too short and electronic energies which are too high due to the increased Coulombic interactions between these electrons. This type of correlation can be most easily corrected for by using advanced techniques such as Multi-Reference Configuration Interaction (MRCI), Perturbation Theory (such as MP2) or even by using Density Functional Theory (DFT). It should be noted, however, that DFT is still considered a single reference theory and therefore it will generally be poorer at recovery of dynamic correlation than the other techniques listed above. The use of MRCI has been shown to recover much of the dynamic correlation energy and this manifests itself in the large number of electron configurations with small coefficients in the wavefunction expansion and will be discussed in a later section.

1.9 Perturbation Theory

One way to recover electron correlation is to use Perturbation Theory and a general discussion of this is now undertaken. In order to obtain solutions to unknown problems it can be possible to use the result of a known system and apply a small perturbation using a power series in order to converge on an approximate solution to the unknown system, providing the perturbation is very small: in other words, the unknown system differs only slightly from the known system for which a solution has been obtained. For the Schrödinger equation shown in equation 1.54 this can be described by splitting the Hamiltonian for the new system into two: one part for the known solved system, $\mathcal{H}_o$, and the other representing the perturbation, $\mathcal{H}'$, required to move from the solved problem to the new unsolved problem as shown in equation 1.55. The value of λ dictates the strength of the perturbation, but for the purposes of this discussion the precise value is not important.

$$\mathcal{H}\Psi = E\Psi \tag{1.54}$$

$$\mathcal{H} = \mathcal{H}_o + \lambda\mathcal{H}^{'} \tag{1.55}$$

This perturbation of the Hamiltonian will have a knock-on effect on the resulting energy and wavefunction, which can be described as shown in equations 1.56 and 1.57

$$E = E_o + \lambda E^{'} \tag{1.56}$$

$$\Psi = \Psi_o + \lambda\Psi^{'} \tag{1.57}$$

Substituting equations 1.55, 1.57 and 1.56 into equation 1.54 and expanding leads to equations 1.58 and 1.59

$$(\mathcal{H}_o + \lambda\mathcal{H}^{'})(\Psi_o + \lambda\Psi^{'}) = (E_o + \lambda E^{'})(\Psi_o + \lambda\Psi^{'}) \tag{1.58}$$

$$\mathcal{H}_o\Psi_o + \lambda\mathcal{H}^{'}\Psi_o + \lambda\mathcal{H}_o\Psi^{'} + \lambda^2\Psi^{'}\mathcal{H}^{'} = E_o\Psi_o + \lambda E_o\Psi^{'} + \lambda E^{'}\Psi_o + \lambda^2 E^{'}\Psi^{'} \tag{1.59}$$

Comparing terms with equivalent powers of lambda results in equations 1.60, 1.61 and 1.62.

$$\mathcal{H}_o\Psi_o = E_o\Psi_o \tag{1.60}$$

$$\mathcal{H}^{'}\Psi_o + \mathcal{H}_o\Psi^{'} = E_o\Psi^{'} + E^{'}\Psi_o \tag{1.61}$$

$$\mathcal{H}^{'}\Psi^{'} = E^{'}\Psi^{'} \tag{1.62}$$

Equation 1.60 is just the solution to the unperturbed known problem. Equation 1.61 is the first order corrected equation and equation 1.62 is the second order corrected equation. For the purposes of this work only the first order correction is of interest. To find the first order correction to the energy, it is necessary to multiply both sides

of equation 1.61 by Ψ_o^* and integrate over all space. In Dirac notation, equation 1.63 results.

$$\langle \Psi_o | \mathcal{H}^{'} | \Psi_o \rangle + \left\langle \Psi_o \middle| \mathcal{H}_o \middle| \Psi^{'} \right\rangle = \left\langle \Psi_o \middle| E_o \middle| \Psi^{'} \right\rangle + \langle \Psi_o | E^{'} | \Psi_o \rangle \tag{1.63}$$

From here it is a simple matter to show that the first order correction to the energy is as shown in equation 1.64. In other words, the first order correction to the energy for the unknown system is the expectation value of the perturbation operator acting on the ground state wavefunction of the unperturbed known system.

$$E^{'} = \langle \Psi_o | \mathcal{H}^{'} | \Psi_o \rangle \tag{1.64}$$

Having found the first order correction for energy, the last remaining unknown quantity is the corresponding first order correction to the wavefunction. To proceed, it is recognised that within the limit of the basis set, the ground state wavefunction of the solved known solution is a complete set. This means that the perturbed wavefunction for the unknown solution can be expressed as a linear combination of the ground state orbitals as shown in equation 1.65.

$$\Psi^{'} = \sum_i c_i \Psi_i \tag{1.65}$$

Substituting this expansion into equation 1.61, pre-multiplying both sides of the resultant equation by Ψ_j^* where j is any configuration other than the ground state, integrating over all space and re-arranging leads to equation 1.66.

$$\sum_i c_i \langle \Psi_j | \mathcal{H}_o | \Psi_i \rangle - \sum_i c_i \langle \Psi_j | E_o | \Psi_i \rangle = \langle \Psi_j | E^{'} | \Psi_o \rangle - \langle \Psi_j | \mathcal{H}^{'} | \Psi_o \rangle \tag{1.66}$$

Due to the orthonormality of the wavefunctions, the summations collapse to a single non-zero term when $i = j$. Additionally, the first term on the right hand side is zero. Taking this into account leads to equations 1.67 and 1.68 and ultimately to equation 1.69.

$$c_j \langle \Psi_j | \mathcal{H}_o | \Psi_j \rangle - c_j E_o = - \langle \Psi_j | \mathcal{H}^{'} | \Psi_o \rangle \tag{1.67}$$

$$c_j E_j - c_j E_o = -\langle \Psi_j | \mathcal{H}^{'} | \Psi_o \rangle \tag{1.68}$$

$$c_j = \frac{\langle \Psi_j | \mathcal{H}^{'} | \Psi_o \rangle}{E_o - E_j} \tag{1.69}$$

At this stage, the first order corrections to the energy of the system and the wavefunction as a result of the perturbation have been obtained. Higher order corrections are obtained in a similar way.

1.10 Configuration Interaction

Another way to fully capture the electron correlation energy from a Hartree-Fock calculation is to extend the wavefunction using a basis of the Hartree-Fock reference and all possible excited electron configurations from this reference. Mathematically this is represented as in equation 1.70, where Ψ_o represents the ground state Hartree-Fock electron configuration, $|S\rangle, |D\rangle, |T\rangle$ and $|Q\rangle$ represent all of the excited electron configurations obtained by single, double, triple and quadruple excitation from the Hartree-Fock reference wavefunction and the C_i values are the respective coefficients in the Configuration Interaction wavefunction.

$$\Phi_o = C_o |\Psi_o\rangle + C_S |S\rangle + C_D |D\rangle + C_T |T\rangle + C_Q |Q\rangle + ... \tag{1.70}$$

Including all possible configurations within the CI wavefunction is called the Full Configuration Interaction (FCI) [15] [16]. The number of configurations can be calculated as shown in equation 1.71 for Slater Determinants, where N, n_α and n_β are the number of spatial orbitals, the numbers of alpha and beta spin electrons respectively in the system and M is the resulting number of Slater determinants.

$$M = \binom{N}{n_\alpha}\binom{N}{n_\beta} \tag{1.71}$$

For illustrative purposes, figure 1.4 shows the configurations included in the FCI solution for the H_2 molecule using a minimal basis set.

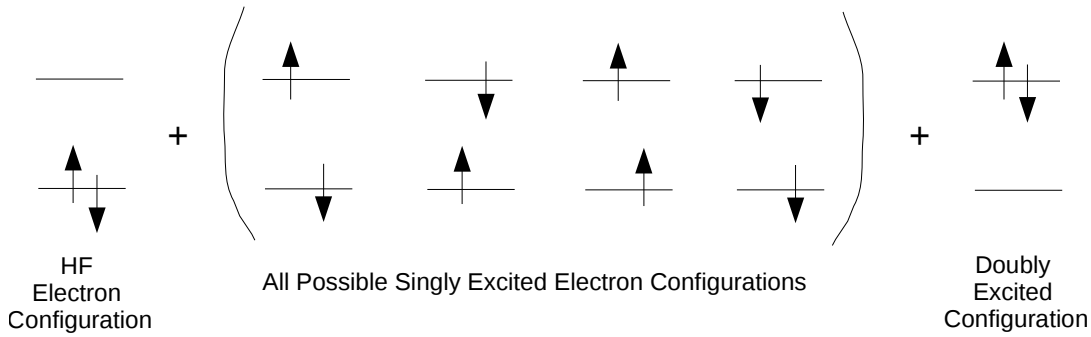

Figure 1.4: The FCI solution for the H_2 molecule (minimal basis set). Note that as a consequence of Brillouin's Theorem, the singly excited electron configurations will not mix directly with the Hartree-Fock reference and in this case can be removed from the FCI solution on symmetry grounds.

Even for small systems, an FCI solution leads to enormous wavefunctions, and for almost all systems this becomes computationally intractable. For example, the FCI solution for H_2O using the 6-31g basis set requires 1,656,369 Slater Determinants. In order to reduce the number of configurations required, a CI wavefunction containing only single and double excitations (CISD) from the Hartree-Fock reference can be used as these are usually the most important electron configurations in describing the system, although in the case of the H_2 molecule above this makes no difference as only single and double excitations are available. At this stage it should be noted that Brillouin's Theorem states that the singly excited configurations cannot mix directly with the Hartree-Fock wavefunction and therefore matrix elements which involve singly excited configurations and the Hartree-Fock wavefunction will be zero. In the case of H_2 this causes a significant reduction in the number of configurations required. In general however, singly excited configurations do mix directly with doubly excited configurations and thus mix indirectly with the Hartree-Fock reference and therefore can be very important in describing the chemical system.

For large systems, CISD can generate too many configurations to be of practical use and other more advanced techniques are described later. For systems which can use CI techniques, triple excitations can be estimated and added to the CISD wavefunction - CISD(T). Alternatively, triple excitations can be calculated directly with quadruple excitations estimated - CISDT(Q). This will depend on the system in question and the accuracy required. Truncated CI methods such as CISD do

however suffer from problems with size extensivity and size consistency [17] and these problems will be discussed now. From a computational point of view, the energy of two molecules A and B separated by an infinite distance in the same calculation should be equivalent to the total energy of each of them calculated in isolation.

$$E_{AB}(R_{AB} \rightarrow \infty) = E_A + E_B \tag{1.72}$$

For truncated CI calculations, this equation does not hold. In particular, the left hand side of equation 1.72, $E_{AB}(R_{AB} \rightarrow \infty)$, is artificially high in energy; an error called *size consistency*. The size consistency problem occurs in truncated CI techniques such as CISD because of the neglect of quadruple excitations in the calculation of the infinitely separated AB dimer on the left hand side of equation 1.72. The calculations of the isolated A and B molecules include quadruple excitations indirectly because on the right hand side of the equation, double excitations can be performed in both calculations at the same time: this is essentially a quadruple excitation in all but name. By definition, the left hand side of the equation includes both A and B in the same calculation and therefore only double excitations across the entire infinitely-separated dimer is allowed. Consider a system of N H_2 molecules. We should, for example, be able to model N infinitely separated, and therefore non-interacting, H_2 molecules as N times the energy of one molecule. Because we can see that size consistency problems occur even for $N = 2$ in the $A - B$ dimer above, we can be certain that CISD calculations will have increasing problems as N increases. More generally, truncated CI techniques do not produce energies which increase in proportion with the number of particles in the system, a problem known as *size extensivity*. In other words, the problem is not limited only to non-interacting molecules: it is also pertinent to atoms. To demonstrate the scaling problem, it can be shown that for N non-interacting H_2 molecules, a CISD calculation produces a correlation energy as shown in equation 1.73 where Δ is an energy term related to the difference in energy between the two molecular orbitals in the minimal basis H_2 molecule and K_{12} is the exchange energy. This can be compared to the exact correlation energy shown in equation 1.74.

$$^{N}E_{corr}(CISD) = \Delta - \sqrt{\Delta^2 + NK_{12}^2} \tag{1.73}$$

$$^{N}E_{corr}(Exact) = N(\Delta - \sqrt{\Delta^2 + K_{12}^2}) \tag{1.74}$$

Clearly the CISD correlation energy does not scale correctly with N. Worse still, as N approaches large values, such as may be found in a macroscopic system, the CISD correlation energy approaches the value shown in equation 1.75

$$^{N}E_{corr}(CISD) \ -\sqrt{N}K_{12} \tag{1.75}$$

To see the problem here, divide both sides by N to illustrate the correlation energy recovered per molecule and allow N to approach ∞, to approximate very large systems, as shown in equation 1.76. As can be seen the amount of correlation energy recovered tends towards zero at macroscopic levels rendering CISD useless for modelling large systems.

$$\lim_{N\to\infty}(^{N}E_{corr}(CISD)) = -\frac{K_{12}}{\sqrt{N}} = 0 \tag{1.76}$$

Examples of the performance of CI can be found in the literature. Rosenberg *et al.* [18] used the technique to measure the ground state geometry of the water molecule. The H-O-H angle was found to be 104.93° using CISD and 104.58° using CISD with the Davidson correction shown in equation 1.77. Note that ΔE_Q is the correction for quadruple excitations and a_o^2 is the coefficient of the HF wavefunction. This compared very well with the experimental value of 104.52°. By comparison the SCF result was 106.08°. A similar result was found for the equilibrium O-H bond length. Results were found to be 0.9398 Å (SCF), 0.9527 Å (CISD) and 0.9573 Å (CISDQ) compared to 0.9572 Å from experiment. Here the problem of over-binding by SCF is clearly seen, with capture of correlation effects by CI correcting the problem.

$$\Delta E_Q = (1 - a_o^2)(E_{CISD} - E_{HF}) \tag{1.77}$$

1.11 Multi-Configuration Self-Consistent Field

Although CISD can be used to capture electron correlation, there are other techniques which aim to optimise this process. Multi-Configuration Self-Consistent Field (MCSCF) is one such technique [19] [20]. This is achieved through the construction of a multiconfigurational wavefunction consisting of a linear combination of a number of Slater Determinants (SDs) or Configuration State Functions (CSFs), each representing a different electron configuration obtained by excitation directly from the Hartree-Fock reference. Slater Determinants have been described earlier and CSFs will be discussed later. As with Configuration Interaction, the variational principle applies to this MCSCF wavefunction, with the lowest energy initially being determined from minimisation of the energy with respect to the coefficients of each SD or CSF. With MCSCF however, unlike CI, after each iteration of the SD/CSF coefficient minimisation procedure the molecular orbitals (MOs) themselves are also re-optimised. The cycle of minimising the SD/CSF coefficients is repeated using these new MOs. Only when the energy is minimised with respect to both SD/CSF coefficients and MO coefficients is the procedure complete, revealing the final optimised multiconfigurational wavefunction. Unfortunately, for other than very small systems, the number of configurations included can rapidly become unwieldy even if only Single and Double excitations from the HF reference wavefunction are included. A range of techniques can be implemented to ease the computational effort required by recognising that not all configurations will be important in describing the system. Early attempts at solving this problem focussed on selecting the important configurations through mathematical means. Obviously this is not ideal and other methods were sought to convert this largely mathematical problem to one which allowed an element of chemical intuition in determining the key electronic configurations. Complete Active Space Self-Consistent Field (CASSCF) [21] is the most commonly used implementation of this technique and, in general, works by splitting the Hartree-Fock orbitals into three separate spaces. Firstly an active space is determined using chemical intuition. This space consists of the orbitals (occupied and virtual) and electrons considered most important in describing the system and the activity or property under investigation (such as bond breaking). A full configuration interaction (FCI) is performed within these orbitals with the addition of re-optimisation of the MOs themselves. The use of FCI in the active space allows

this space to be considered complete within the limit of the basis set (hence the name Complete Active Space). The resulting MOs are transformed into Natural Orbitals (NOs), which are those orbitals which diagonalise the density matrix, the eigenvalues of which are interpreted as the orbital occupancies. It is important to recognise that these orbitals will now have partial electron occupancy with occupancies between 0 and 2. Occupancies close to either 0 or 2 are indicative of a poor choice of active space and this allows a degree of diagnosis of the MOs chosen. The second space is the inactive space which consists of MOs which are doubly occupied in all configurations. Depending on the implementation of CASSCF used, it may be possible to exclude these MOs from the MO re-optimisation process. The final space is the external space consisting of all MOs which have zero electron occupancy in all configurations. The inactive and external spaces are thus included in the wavefunction in order to correctly optimise the MOs. An example CASSCF space is shown in figure 1.5 for a seven electron system with an active space of three electrons in four orbitals.

CASSCF can make use of direct methods of integral evaluation, where the integrals are re-calculated when needed rather than stored individually. This technique reduces the amount of disk storage required at the expense of greater computational effort but which allows CASSCF to be used in solving very long MCSCF expansions. Whilst the CI coefficients are minimised variationally, MO optimisations are performed using orbital rotations where the objective is to optimise the MO coefficients to minimise the overall MCSCF energy rather than to minimise the energy of the individual constituent SDs or CSFs. The energy of the system is invariant to many MO rotations, for example rotations between two MOs which are always doubly occupied, and significant computational savings are made by not performing these MO rotations. This approach is also believed to lead to faster convergence.

One final note regarding MCSCF calculations should be made here. Root-flipping occurs when a state n is desired where n is not the ground state and is very close in energy, but slightly higher than another state $n-1$. In order to find the energy of state n, the MOs are optimised for this state. This results in the energy of state $n-1$ being artificially higher than optimal due to the variational principle. If the two states are initially close enough in energy, the calculation can then give the incorrect impression that state n is lower in energy than state $n-1$. Subsequently, state $n-1$

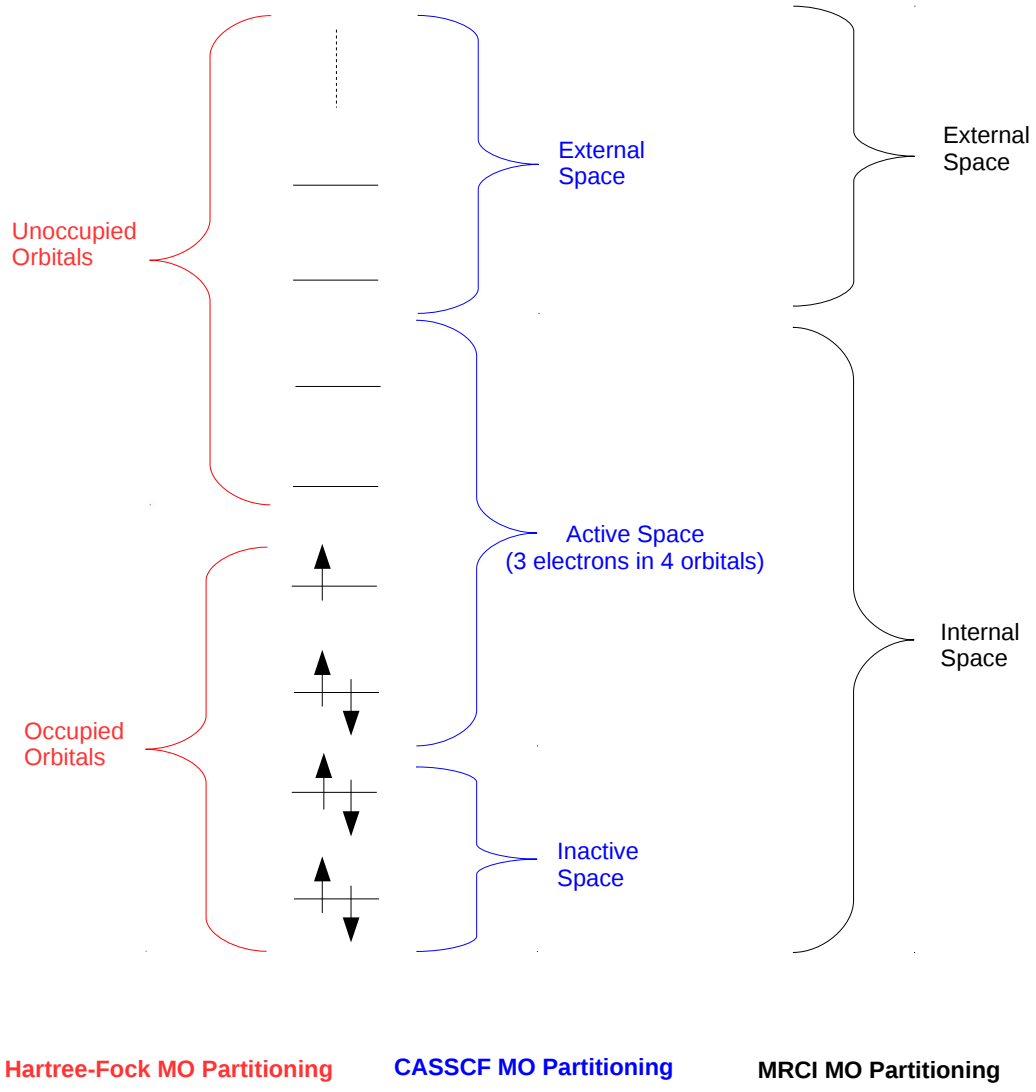

Figure 1.5: Molecular orbital partitioning for a 7 electron system showing comparison of Hartree-Fock, CASSCF and MRCI methods.

is now optimised as the second root and its energy is lowered variationally whereas state n is raised in energy and another flip in the ordering of these two states can occur. Therefore every step in the convergence process involves a flip of these two energy levels and convergence is never reached. This is called root-flipping. State averaging solves this problem by using a compromise set of orbitals which is designed to best describe both states n and $n-1$ and can be extended to more than 2 excited states [22].

In summary, therefore, Hartree-Fock gives the optimal orbitals for a single Slater Determinant solution. CI allows these orbitals to be used to expand the wavefunction in a linear combination of electron configurations in order to capture electron correlation. MCSCF techniques then give the optimal orbitals for this CI expansion through ensuring orbitals are re-optimised.

Example CASSCF calculations by Roos [21], of the $X^1\Sigma_g^+$ ground state of N_2 using an active space consisting of the orbitals: $2\sigma_u, 3\sigma_g, 1\pi_u, 1\pi g$ and $3\sigma_u$, predict the equilibrium bond length, $R_e = 1.108$ Å. This compares very favourably with the experimental value of 1.098 Å and is a significant improvement over Hartree-Fock estimates of 1.069 Å. Dissociation energies of 8.759 eV compared less well to experiment (9.905 eV) but vibrational frequency prediction of 2332.6 cm^{-1} was in excellent agreement with 2358.6 cm^{-1} from experiment.

1.12 Multi-Reference Configuration Interaction

In adopting techniques to capture electron correlation, consideration must be given to the nature of the zeroth order wavefunction. In the case of CI calculations, that zeroth order wavefunction is usually the Hartree-Fock solution, which in most cases is a relatively poor choice - particularly for systems exhibiting multi-reference behaviour in the ground state. For such systems, a CI solution which incorporates all possible excited configurations from the Hartree-Fock reference will necessarily require too many configurations to be of practical use. For this reason, CI techniques are normally limited to single and double excitations from the Hartree-Fock reference as described earlier. For the recovery of dynamic correlation, considerably more electronic configurations must be included in the wavefunction description.

This can be best achieved by including singly and doubly excited configurations from an MCSCF reference wavefunction in a technique called Multi-Reference Configuration Interaction (MRCI) [23] [24] [25]. The MCSCF wavefunction provides an appropriate zeroth order wavefunction for MRCI, particularly in the case of the study of excited states or bond formation where a single restricted closed shell reference provides a very poor description. The MCSCF wavefunction itself suffers from having to rely on the judicious choice of either active space or important configurations and applying a CI treatment to this zeroth order wavefunction via MRCI can compensate for any errors introduced as a result of poor choices made at the MCSCF level. Blind application of single and double excitations using MRCI however can lead to very large configuration spaces, restricting the size of system which can be studied. Efficiencies can be found however. For instance, MRCI can result in unwanted redundancy. This can be clearly seen when considering the fact that a particular electron configuration can be reached by singly or doubly exciting more than one reference configuration. To illustrate MRCI further, the Molpro [26] implementation of MRCI is now discussed.

MRCI, as developed in Molpro, applies a technique of generation of excited electron configurations from the entire MCSCF wavefunction rather than to each individual configuration of the reference wavefunction individually. By this process, called Fully Internal Contracted MRCI, large savings in terms of the MRCI wavefunction length can be made. Equivalent configurations derived from different references can be contracted in much the same way as done with Atomic Orbitals within basis sets. For this implementation of MRCI, the criterion for inclusion in the contraction is that the proposed new configuration makes first order perturbative corrections to the zeroth order wavefunction to allow dominant configurations to be included in a balanced way. This contracted MRCI solution shows results which are as good as uncontracted MRCI solutions but at a fraction of the cost computationally both in terms of convergence time and wavefunction length. The MRCI wavefunction consists of several parts as described in equation 1.78.

$$\Psi = \sum_k a_k \psi_k^r + \sum_s \sum_a c_s^a \psi_s^a + \sum_p \sum_{ab} c_p^{ab} \psi_p^{ab} + \sum_I c_I \psi_I \tag{1.78}$$

The first term, involving ψ_k^r describes the reference MCSCF wavefunction where the

a_k are the coefficients optimised during the MCSCF calculation. These configurations span what is termed the reference subspace. The second term describes both the configurations where a single excitation has been made into the external subspace (i.e. into orbitals not occupied in any of the MCSCF reference configurations) and also those configurations which have been doubly excited but only one electron is excited into the external space (the other being excited into the internal space - i.e. an orbital occupied in one of the MCSCF reference configurations). These doubly excited configurations are referred to as semi-external doubly excited configurations and the set of configurations covered by both of these single and double excitations span what is termed the semi-external subspace. The third term consists of configurations which have been doubly excited and both electrons have been placed into the external space. These configurations span what is termed the fully external subspace. The final term is the set of configurations involving only internal orbitals which are excited to other internal orbitals (those occupied in at least one reference configuration). The configurations span what is termed the internal space. The reference configurations from the MCSCF calculations also span the internal subspace. Figure 1.5 summarises how MOs are partitioned by MRCI for an example system with seven electrons. The configuration coefficients of each term are re-optimised during the MRCI calculation but the MO coefficients remain as computed during the MCSCF calculation with the exception of systems at near degeneracy where it is necessary to relax (re-optimise) the MO coefficients in order to correctly describe the system. Figure 1.6 shows each of these terms diagrammatically.

The same principle of full internal contraction (FIC) of configurations finds application in methods such as perturbative treatments of CASSCF wavefunctions (CASPT2 [27] and NEVPT2 [28]). There are however other MRCI methods of contraction available. External contraction [25] involves the separate contraction of singly external excitations and doubly external excitations with contraction coefficients determined by first order Perturbation Theory. PC-MRCI [29] and PC-CASPT2 [30] both use the method of partially internal contraction (PC). This method of contraction leaves some classes of excitation uncontracted. Single excitations to the external subspace and single excitations in the internal subspace are both left uncontracted and this allows the construction of higher order density matrices to be avoided. The method of strong contraction (SC) [29] also finds application

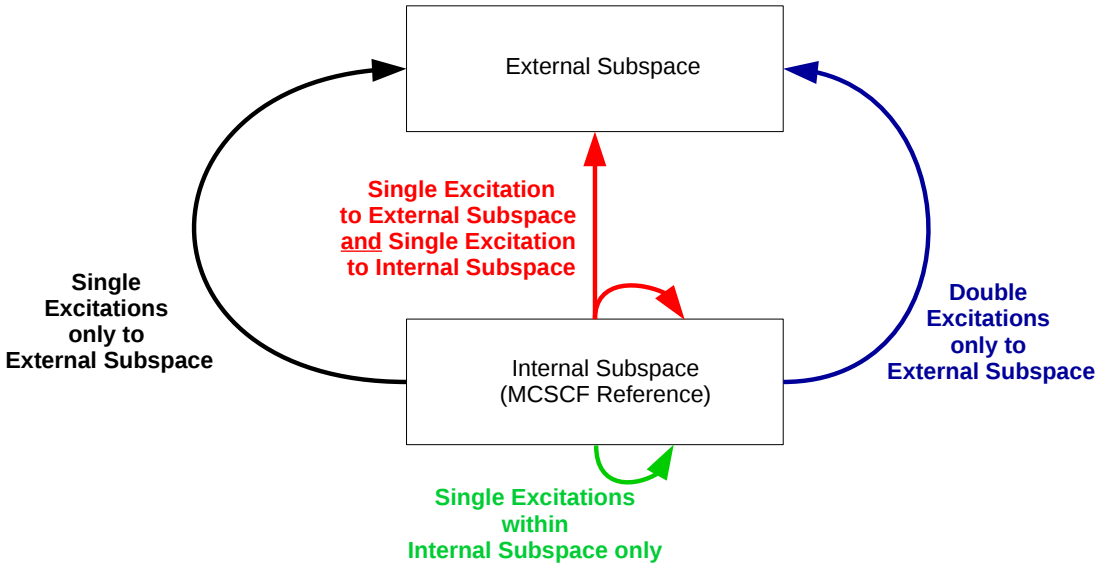

Figure 1.6: Allowed MRCI excitations. Black and red excitations are those of term 2, blue excitations are for term 3 and green excitations are for term 4 of equation 1.78. The MO partitioning by MRCI is described in figure 1.5.

and results in significantly more compact wavefunctions than those used in other contractions but this will not be discussed further here. The energy results of MRCI calculations using FIC, SC and PC contractions on a variety of small molecules such as N_2, O_2, CO OH, CH and CN, were compared to uncontracted MRCI results [31]. The SC scheme was found to be least accurate with energy results showing 5-6% error compared to to the uncontracted results. FIC and PC results were shown to be more accurate with errors of just 2%. A similar result was seen when other properties such as excitation energies and geometries were considered.

Werner *et al.* [23], used the internally contracted MRCI technique on the $X^2\Pi$ ground state of the OH radical. The equilibrium bond length was calculated as 0.971 Å, in excellent agreement with the experimental value of 0.970 Å. This internally contracted MRCI scheme showed improvement on MCSCF which predicted 0.973 Å. Dipole moment predictions of 1.672 D were also shown to be improved over SCF (1.765 D), MCSCF (1.676 D) and CI (1.693 D), with experimental values of 1.668 D. Vibrational frequency analysis showed ω_e predictions of 3737.4 cm^{-1} in excellent agreement once again with experimental values of 3737.8 cm^{-1}. The vibrational predictions in particular were significantly better for internally contracted

MRCI than all other techniques reported. Similar improvements were seen for the treatment of the $A^2\Sigma^+$ first excited state for this radical.

1.13 Monte Carlo Configuration Interaction

As described earlier, in order to fully capture all of the electron correlation energy associated with a molecular system and achieve an exact result, within the limitations of the basis set and the Born-Oppenheimer approximation, a FCI calculation is required. CISD was shown to be a suitable alternative for some larger systems but such truncated CI techniques were seen to suffer from problems of size extensivity and size consistency problems as well as problems related to the size of the wavefunction. The Monte Carlo Configuration Interaction technique (MCCI) [32][33][34][35] is a configuration interaction technique designed to ease the problems associated with the large wavefunctions present in CISD calculations. MCCI attempts to include only those single and double excitations which are the most important in describing the system, thus eliminating relatively unimportant configurations and in doing so creates a highly compact wavefunction, in comparison to CISD, which can recover a large amount of static correlation energy with a wavefunction spanning only a fraction of the configuration space. It is also specifically designed to overcome the problems of chemical intuition required in specification of the active space of techniques such as CASSCF and other MCSCF techniques which require knowledge of important configurations in advance. As such, it is a black box technique which requires the user to vary a single parameter, c_{min}, which sets the cut-off level for the size of coefficient a configuration must possess in the growing MCCI wavefunction, below which that configuration is discarded. MCCI uses a single Restricted Open Shell Hartree-Fock (ROHF) wavefunction (where paired electrons share the same spatial orbital), or Unrestricted Hartree-Fock wavefunction (where all alpha and beta electrons are allowed to occupy different spatial orbitals) [36], with one and two electron integrals made available by a variety of other quantum chemical programs such as Columbus [37] and Molpro [26], as a starting point and augments this reference by generating new electron configurations by performing random walks in Hilbert space in a process called *branching*. Branching involves the generation of new configurations which have been created from random single

and double excitations initially from the HF reference, retaining the spin and spatial symmetry of the reference. In this way, a CI vector is gradually built up from the HF reference and these newly constructed configurations which represents the system under consideration. For subsequent branching iterations, single and double excitations can be constructed from any configuration within the growing CI vector. Once the branching stage is complete, Hamiltonian and Overlap matrices are constructed during a process called *generation*, using one and two-electron MO integrals from the external quantum chemistry packages listed above, in the basis of the growing CI vector. These matrices are diagonalised, using either the Davidson [10] or Davidson-Lui [11] diagonalisation algorithms, to reveal the value of the coefficients of each configuration. All configurations with a coefficient of less than the value of c_{min} are then discarded in a process called *pruning*. Because MCCI is a parallel procedure, all processes involved in calculating the CI space now exchange their respective configuration lists which have been found during this iteration. All processes receive the new configurations found by all other processes and augment their own configuration list with these new configurations, removing any duplicates found. Convergence is then tested in terms of both change in energy and change in CI vector length. Only when both are converged is full convergence achieved. As a truncated CI technique, MCCI suffers from problems of size extensivity and size consistency. These problems can be overcome by reducing the c_{min} value to a point where the FCI solution is approached although the size of the system will determine how practical this approach is. Nevertheless, MCCI is capable of capturing much of the static correlation energy with a highly compact wavefunction a fraction of the size of those generated by other CI techniques. This highly compact wavefunction can then be used as the zeroth order wavefunction for further recovery of dynamic correlation and MCCI contains support for a second order perturbation theory method, PT2, for this purpose [38]. Figure 1.7 summarises the MCCI process.

An interesting insight is gained by reorganising the MCCI matrix elements, $c_A \langle \Psi_A | \mathcal{H} | \Psi_B \rangle c_B$, in terms of decreasing coefficient. Figure 1.8 [33] shows this performed for the HF molecule using double-zeta basis set and a c_{min} value of 10^{-4}. In this diagram, the matrix elements are colour-coded according to the value of the contribution of the element to the energy. Yellow elements appear on the diagonal,

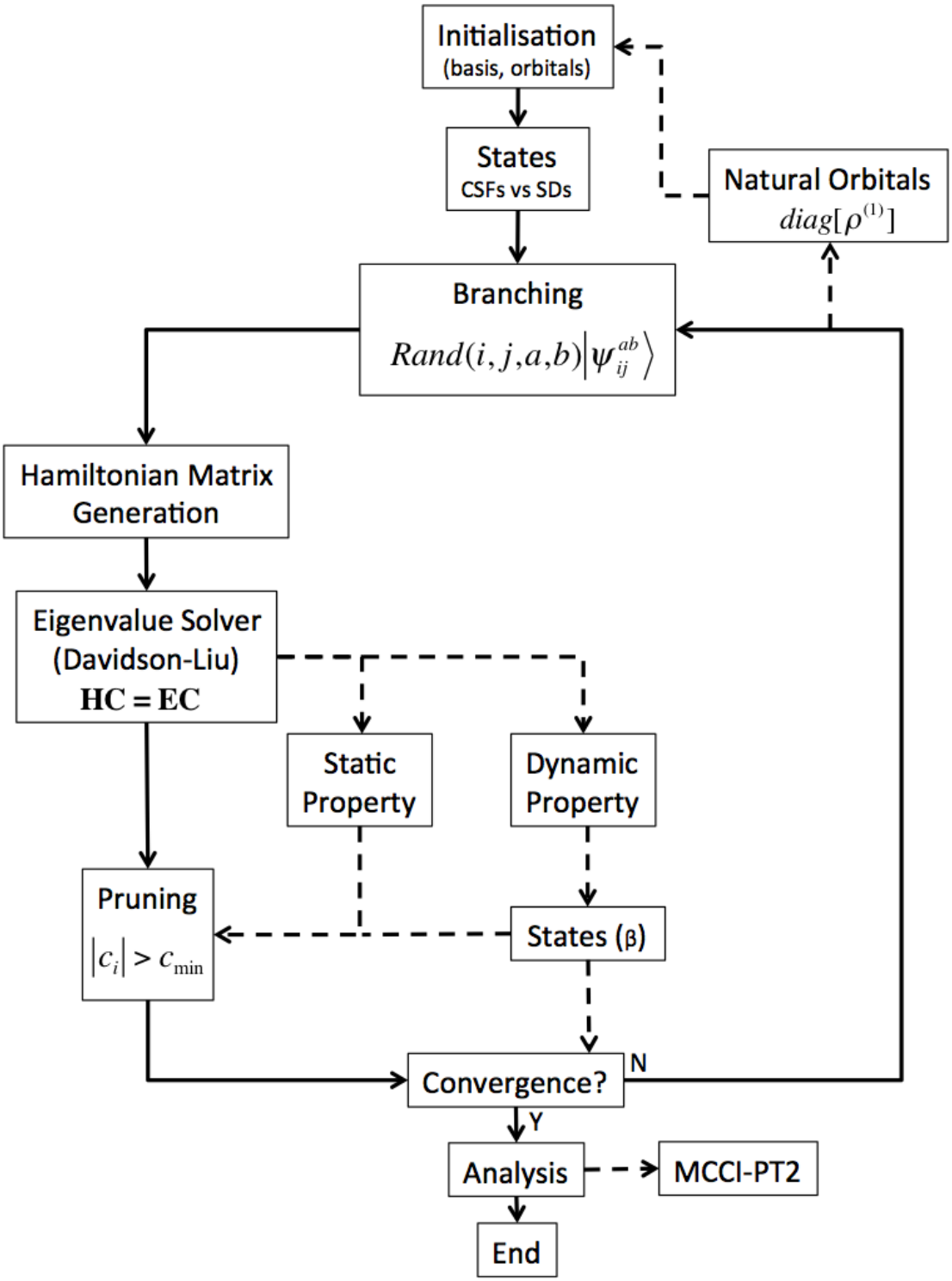

Figure 1.7: Block diagram showing the key components of the Monte Carlo Configuration Interaction (MCCI) method. Diagram reproduced by kind permission of M.J. Paterson from previous unpublished work

reddish regions represent the strongest non-diagonal terms and blue regions represent weak non-diagonal interactions. It is clear that smaller coefficients will favour interaction with larger coefficient terms and will not favour interaction with other weaker terms.

Figure 1.9 shows the performance of MCCI against a range of other computational methods [35] for the ground state energy of the Ne atom. As can be seen, MCCI is able to outperform CISDTQ with less than 10% of the electron configurations and approaches near FCI performance with just 1.5% of the FCI space. It can also be seen that despite using stochastic methods, MCCI is capable of predicting the ground state energy with remarkable levels of consistency over a large number of runs with reproducibility errors of just 5.8 x 10^{-8} au. Other systems have shown similar results [38].

1.14 Basis Sets

A basis set is a collection of n linearly independent vectors which spans an n dimensional space [39]. As a result of this, the basis set can describe any vector within that space. Because vectors are a general class of object, they can be of any type. For example, in three dimensional space we could use the basis set of $\vec{x}_1, \vec{x}_2, \vec{x}_3$ to describe any spatial vector in the form $r = c_1\vec{x}_1 + c_2\vec{x}_2 + c_3\vec{x}_3$ where $\vec{r}$ is any spatial vector in 3 dimensional space and c_1, c_2 and c_3 are the co-ordinates or coefficients of the basis set. More compactly we can write this as $\vec{r} = \sum_{i=1}^{3} c_i\vec{x}_i$. If we are able to specify all 3 components of r then the basis set is said to be a complete description of $\vec{r}$ or simply *complete* for short. We are however not limited to spatial vectors: vectors can be functions. Here however, an infinite number of basis vectors must be used and we write $f = \sum_{i=1}^{\infty} c_i\phi_i$, the basis vectors in this case being functions themselves. One reason for expressing any vector as a linear combination of basis vectors in this way could be for reasons of convenience. It could be, for example, that a problem may require the addition of two vectors. It is a simple exercise to perform this type of operation when the vectors in question are described in terms of the basis set shown above. Alternatively, and pertinent to this work, it may be that the true nature of the function vector f is not known. In that case, the only hope we have is to describe the function using the basis set. Of course, use of a

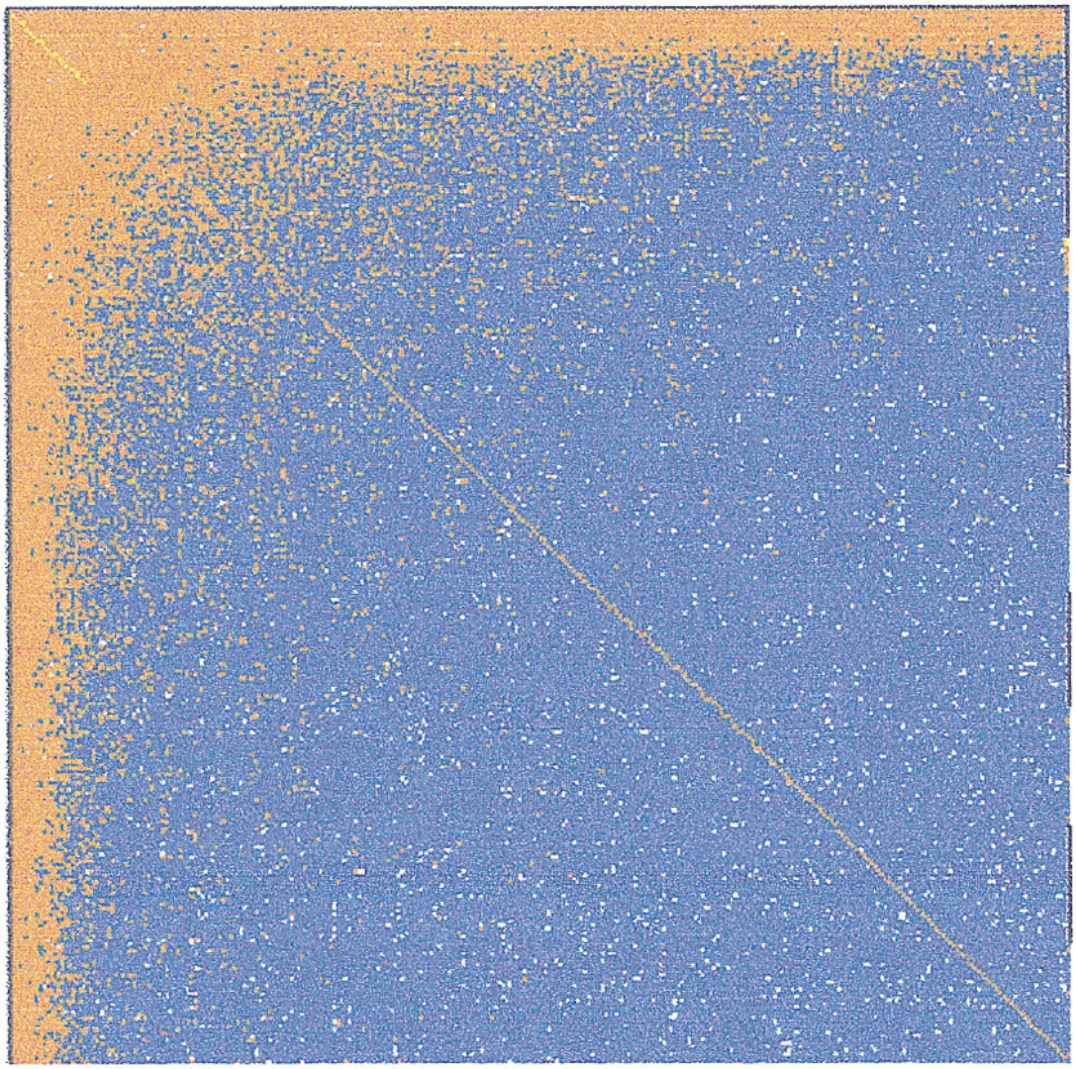

Figure 1.8: The MCCI matrix elements for the HF molecule, weighted by coefficients, organised by decreasing value. Yellow/red squares show strong interactions with blue square representing weak interactions. Here it can be seen that the matrix is highly sparse with only a relatively small number of interactions having importance. Figure reproduced from reference [33] with kind permission of publisher.

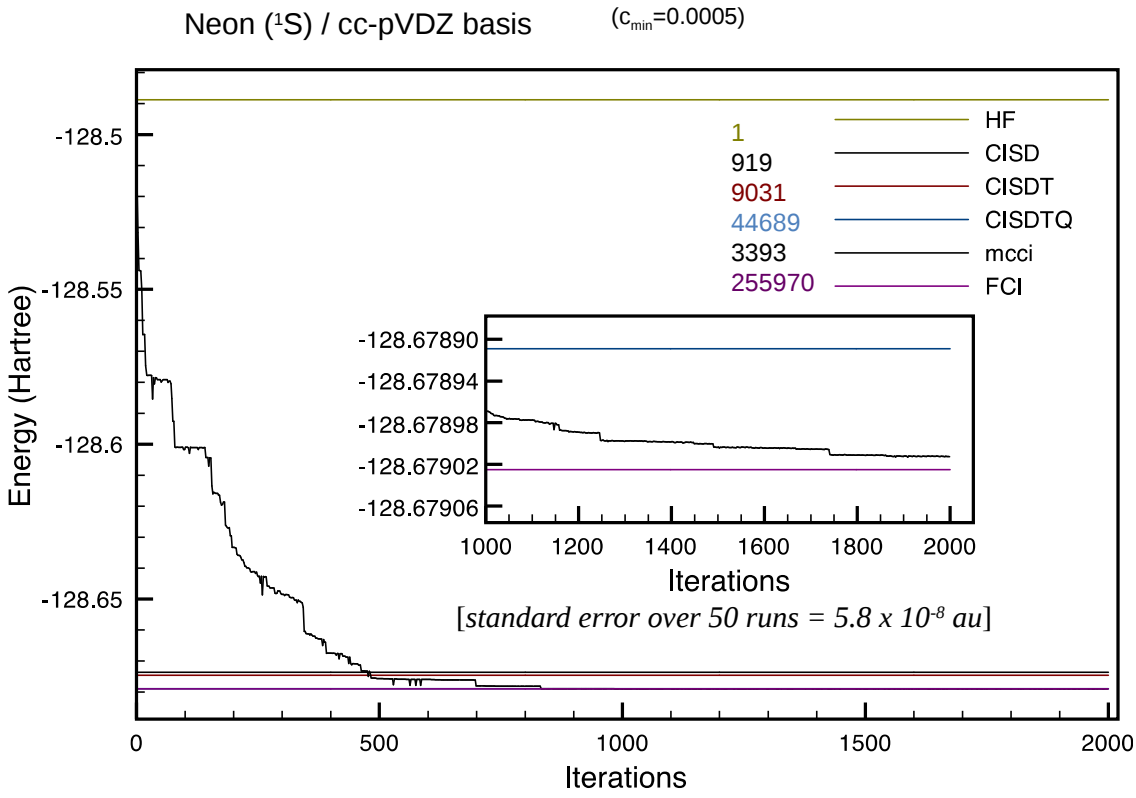

Figure 1.9: Comparison between the energy convergence of the Ne atom in the ground state using MCCI, HF, CISD, CISDT, CISTDQ and FCI [35]

complete basis set is hopeless as this requires an infinite number of functions. It is possible however, to make approximations to the function using a truncated basis set, $f = \sum_{i=1}^{K} c_i \phi_i$. Obviously this will result in errors in describing the function f, but if sufficient care is exercised in the choice of basis function used, reasonably accurate results can be obtained. Two common types of basis function which find general application in quantum chemistry are the Slater Type Orbital (STO) and the Gaussian type orbital (GTO). The aim in quantum chemistry is to use basis functions to describe a set of molecular orbitals. These orbitals indicate where the electrons are most likely to be found in any system and they are constructed from linear combinations of atomic orbitals. Atomic orbitals in turn are constructed directly from a linear combination of either STO or GTO [40] basis sets. In a real chemical system, the electrons move around as they feel the attraction and repulsion from the nuclei and other electrons respectively. The aim is to model this mathematically as realistically as possible and thus the more molecular orbitals there are, the more positional flexibility the electrons have and the more accurate the model of the real system is. The format of an STO and a GTO are shown in equations 1.79 and 1.80 and their physical form appears in figures 1.10 and 1.11. Here, we define the angular momentum of the orbital as $L = a + b + c$. An s-type orbital would therefore have $a = b = c = 0$ whilst a p-type orbital has a choice of either $a = 1, b = c = 0$, $b = 1, a = c = 0$ or $c = 1, a = b = 0$ as expected for p_x, p_y and p_z respectively. ζ controls the width of the function and N is a normalisation constant.

$$\phi^{STO} = N x^a y^b z^c e^{-\zeta r} \tag{1.79}$$

$$\phi^{GTO} = N x^a y^b z^c e^{-\zeta r^2} \tag{1.80}$$

An STO displays the correct behaviour for describing an electron in a hydrogenic atom, with a maximum amplitude close to the nucleus before dropping away to zero as the distance from the nucleus increases. Unfortunately this type of function can be difficult to work with in terms of using linear combinations of them to approximate a molecular system. Instead GTOs are preferred. As can be seen however, the use of GTOs to approximate STOs introduces some problems: they are too flat near the nucleus and the fall-off at both medium and long range is too rapid. The

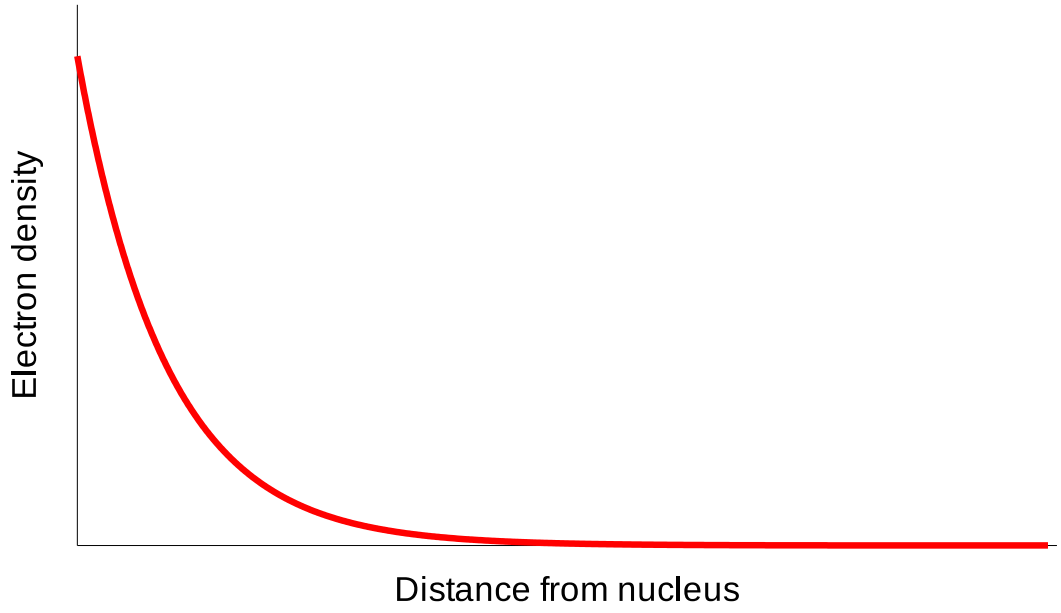

Figure 1.10: Functional form of a typical STO function. The values of a, b and c are all zero, $\zeta = 1$ and N = 1

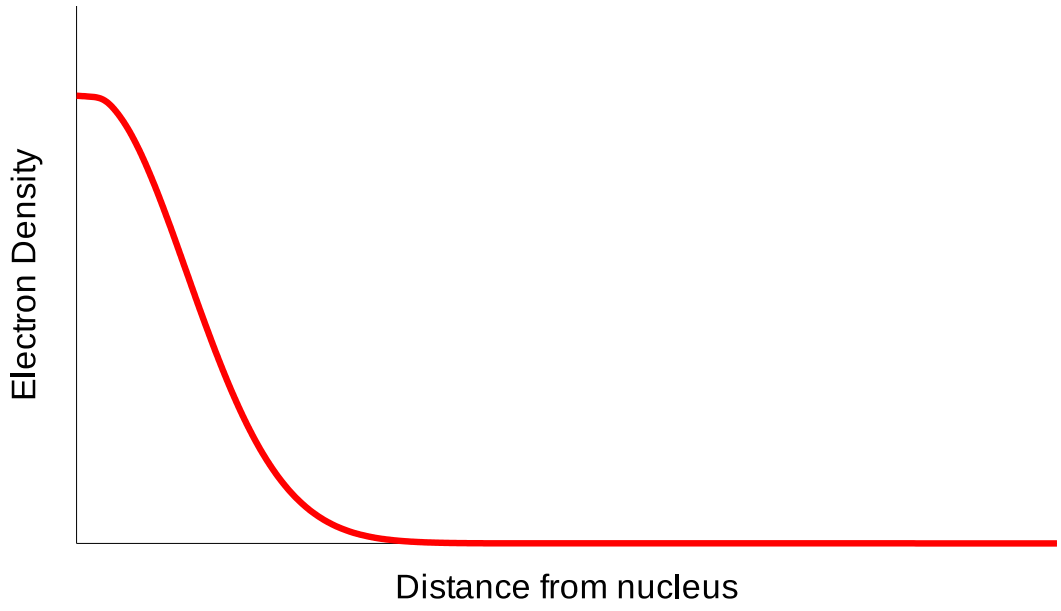

Figure 1.11: Functional form of a typical GTO function. The values of a, b and c are all zero, $\zeta = 1$ and N = 1

major advantage of their use however stems from the property that multiplying two GTOs results in a third GTO which is placed between the first two. This is particularly useful when manipulating two-electron integrals, which are integrals involving four atomic centres. Using GTOs, this problem is reduced to a pair of two atomic centred GTOs. STOs can be approximated by a linear combination of several GTOs. The result is a *contracted* GTO (CGTO). An example is shown in equation 1.81 where each term in the summation is called a *primitive* GTO. The basis set STO-nG is a simple example of the use of such a CGTO. Here n primitive GTOs are linearly combined to produce an approximation to one STO. Once we have all of the desired approximated STO functions, our set of atomic orbitals is complete. It is however inefficient and undesirable to have to re-calculate the c_i and the ζ coefficients of equation 1.81 in every calculation. Each atomic orbital will therefore have a different but optimised and fixed pair of c_i and ζ values which will subsequently not change during molecular orbital optimisation.

$$\phi^{CGTO} = N \sum_{i=1}^{K} c_i x^a y^b z^c e^{-\zeta r^2} \tag{1.81}$$

For core molecular orbitals, the position of the electrons is relatively fixed and therefore such contractions are very valuable in reducing the computational complexity of the system. Valence orbitals, however, require a greater degree of flexibility and it is common to find that a split valence approach is used.

Basis sets are arranged in categories. A minimal basis set is the smallest possible basis set for a system and provides one STO, GTO or CGTO function per occupied orbital in the atom. For H_2, for example, a minimal basis set will provide two molecular orbitals, the well known σ_g and σ_u^* orbitals. Another example would be the C_2 molecule using STO-3G basis set which uses 3 primitive GTOs per atomic orbital and 10 CGTOs for the subsequent molecular orbitals.The next step up in quality would be a double zeta (DZ) basis set whereby 2 basis functions (CGTOs or GTOs) are used per atomic orbital. For the B atom, this would result in 10 basis functions instead of 5 basis functions for the minimal basis set. Following on from this we have triple zeta and quadruple zeta etc. which, for the B atom, would require 15 and 20 basis functions. The value of ζ can be altered in a basis function to produce a wider or narrower amplitude spectrum depending on what shape of

orbital is required for the system. The use of multiple zeta basis sets therefore allows an increasing degree of flexibility in terms of where electrons can sit radially. As the size of the atom increases, not all electrons are going to be influenced by the chemical environment. It can be argued that only valence electrons need the flexibility offered by multiple zeta functions. In this case split valence basis sets are useful where the core atomic orbitals are modelled by a single CGTO and valence orbitals treated with multiple zeta functions. A double zeta split valence basis on the B atom would then require 1 basis function for the core $1s$ orbital and 8 basis functions for the valence orbitals - 9 basis functions in total. For triple zeta split valence on the B atom we require 13 basis functions and so on.

Beyond simply increasing the size of the basis set, it is possible to introduce flexibility in the shape of the basis set by introducing polarisation functions. An example would be to consider the hydrogen atom. The electron density in the free atom is isotropic and therefore spherical. A $1s$ orbital is therefore the correct shape to describe the system. In a chemical bond however, it is known that the electron density of the hydrogen atom shifts into the space between the bound atoms. In this instance, the $1s$ orbital is a poor descriptor of the electron density around the hydrogen atom. In order to introduce anisotropy into the hydrogen atom to prepare it for bonding, the $1s$ orbital must be mixed with a higher angular momentum orbital, in this case a p orbital. It is a general rule that to polarise an orbital with angular momentum l, it is necessary to mix in functions of angular momentum $l+1$. Therefore to polarise a p orbital, an orbital of angular momentum d must be introduced etc. This mixing of orbitals of higher angular momentum is called *polarisation*.

At this point it is worth pointing out that angular momentum functions can be in pure form or in cartesian form. At the $l = 2$ level, i.e. d-type orbitals, there are differences between these forms which require mentioning. There are 5 pure angular momentum functions at this level: d_{xy}, d_{yz}, d_{xz}, $d_{x^2-y^2}$ and d_{z^2}. They are, however, not eigenfunctions of the angular momentum operator and it is common to see cartesian d functions used instead - of which there are 6: d_{x^2}, d_{y^2}, d_{z^2}, d_{xy}, d_{yz} and d_{xz}. This is equivalent to using the 5 pure angular momentum functions with the addition of an extra linear combination of $d_{x^2} + d_{y^2} + d_{z^2}$ resulting in an 6th s type orbital. Using cartesian basis functions therefore requires one more basis function than using pure angular momentum and typically results in lower energies

as the extra basis function provides more flexibility. For angular momentum values greater than d, there is a widening gap between the number of pure and cartesian functions. For example, there are 7 pure f momentum functions whilst cartesian functions use 10 basis functions: a difference of 3 basis functions whilst for g angular momentum, 14 cartesian basis functions are required compared to 9 pure angular momentum functions: a difference of 5.

The final category of general basis function we consider here are diffuse functions. Diffuse functions have very small ζ values to allow capture of electron density far from the nucleus. This is very useful for anionic systems and systems for which Rydberg states are important.

A discussion is now presented of the key basis sets used in the course of this work covering Pople and Dunning basis sets as well as effective core potentials.

1.14.1 Pople-style Basis Sets

The first set of basis sets considered in this work is the series of Pople basis sets. Our investigations cover the minimal basis set STO-3G [41][42], the split valence double zeta basis set 6-31G [43][44][45][46], and finally the split valence triple zeta basis set 6-311G [47][48].

STO-3G is a minimal basis set, originally designed for the first two rows of the periodic table, which attempts to approximate an STO using a linear combination of three primitive GTOs as shown in equations 1.82, 1.83, 1.84 and 1.85 for $1s$, $2s$, $2p$ and $3d$ orbitals respectively, with the Gaussian functions themselves described earlier in equation 1.80. Initially a fit to STOs with $\zeta = 1$ is obtained, followed by a scaling as shown in equation 1.86 depending on the atom.

$$\phi_{1s}(\zeta = 1, r) = \sum_{k}^{3} d_{1s,k} g_{1s}(\alpha_{1k}, r) \tag{1.82}$$

$$\phi_{2s}(\zeta = 1, r) = \sum_{k}^{3} d_{2s,k} g_{1s}(\alpha_{2k}, r) \tag{1.83}$$

$$\phi_{2p}(\zeta = 1, r) = \sum_{k}^{3} d_{2p,k} g_{2p}(\alpha_{2k}, r) \tag{1.84}$$

$$\phi_{3d}(\zeta = 1, r) = \sum_{k}^{3} d_{3d,k} g_{3d}(\alpha_{3k}, r) \tag{1.85}$$

$$\phi^{'}(\zeta, r) = \zeta^{3/2} \phi(1, \zeta r) \tag{1.86}$$

For computational ease, the expansion is built using $1s$, $2p$ and $3d$ Gaussian functions only with the ns, np and nd expansions sharing the same α value (although the $d_{n,k}$ values are specific to the atomic orbital). The values of α and $d_{n,k}$ are optimised by fitting to STO calculated results using a least squares method from UHF atomic calculations. It is generally considered that the STO-3G basis set is too small for meaningful calculations. There are also problems near the nucleus as a result of the inability of three GTOs to effectively reproduce the desired cusp of the STO function. The basis set performs reasonably well for geometries but is poor for relative energies, force constants, dipole moments and other properties as a result of the sensitivity of electron distribution to the value of ζ used. For very large systems however, this basis set may be the only choice.

Following on from the minimal basis set, we consider the split valence basis sets. The names for these basis sets follows a standard format: *k-lnm++G***. Here the value of k determines the number of primitive GTOs used for each core orbital and l, n and m represent the number of GTO primitives used for the inner valence, mid valence and outer valence regions. The '++' symbols represent the use of a diffuse function for both non-H atoms (first +) and H atoms (second +). The G signifies that Gaussian functions are being used and the '**' symbols represent the inclusion of polarisation functions for non-H atoms (first *) and H atoms (second *). The basis set 6-31G therefore uses six GTO primitives for each core orbital, three primitives for each inner valence region and one primitive for the mid (technically called the outer in this double zeta case) valence region. 6-31G uses the same mathematical form for the basis primitives shown in equations 1.87 and 1.88.

$$\phi_{kl} = \sum_{i=1}^{n_k} d_{kl,i} g_l(\alpha_{k,i}, r) \tag{1.87}$$

$$\phi_{kd}(r) = \sum_{i=1}^{n_k+1} d_{kd,i} g_l(\alpha_{kd,i}, r) \tag{1.88}$$

The primitives are contracted as follows. The 6 core primitive GTOs form a single CGTO basis function for each atomic orbital. The 3 inner valence primitives form a single CGTO and the outer valence is left uncontracted. Thus 1 CGTO and a uncontracted GTO form the basis for each valence atomic orbital. Therefore for the carbon atom, as an example, 22 primitives are used (6 for 1s, 4 for 2s and 12 for 2p) and after contraction 9 basis functions are used. Values of α and d, for the first two rows of the periodic table, are chosen to minimise ground state atomic energies using UHF calculations for this basis set. For rows three and above, atomic ROHF calculations are used. The exceptions to this are Na and Mg. For Na, the ground state is optimised without any $3p$ functions at all. This is followed by introduction of $3p$ orbitals and optimisation of the excited ^2P state, with no $3s$ contribution, holding all other coefficients and exponents fixed. For Mg, the approach is taken to minimise the ^3P excited state with a single electron in each of the $3s$ and one of the $3p$ orbitals. In this way, a good description of the necessary p functions is achieved. Rescaling of values of ζ were chosen to minimise the molecular energy within standard molecule sets with no rescaling of core orbitals. One disadvantage of this average rescaling is that inaccuracies are inevitable. Within each standard molecule set however, the range of ζ values was found to be fairly small. Significant improvements are seen over STO-3G results. Atomisation energies are seen to be less than experiment and both absolute binding energies and dipole moments are poorly characterised. Relative binding energies and geometries however perform reasonably well against experiment. Absolute energies are also considerably improved over STO-3G results.

The addition of polarisation functions of higher angular momentum to the 6-31G basis set to create 6-31G* and 6-31G** allows a shift in the electron density away from the nucleus, resulting in better descriptions of chemical bonding for systems exhibiting features such as hyper-valency. Geometries are better matched to experiment and vibrational frequencies are considerably improved.

As with STO-3G, s and p orbitals share the same exponent, α, values. With the Pople basis sets, care must be taken to prevent valence shells mathematically collapsing into the core region during optimisation as this would improve the core description at the expense of the more important valence area. To prevent this, the basis functions are optimised in shells. The core is optimised first holding the valence area constant. Once the core optimisation is complete, this region is then

held fixed whilst the valence regions are optimised. Six uncontracted Cartesian d-type polarisation functions are added to all 2nd row elements and K and Ca from the third row. Their exponents are optimised by averaging values used to minimise the energies of a variety of common molecular environments for each atom. Three p-type polarisation functions are added to H. Transition metals receive 10 uncontracted Cartesian f-type functions which are optimised from average values needed for the minimisation of the energies of a number of metal fluoride and metal carbonyl compounds. Coefficients and exponents for the transition metals are obtained by minimising ROHF high spin, high angular momentum ground states for the atoms. $4p$ orbitals are included for all third row elements and treated as valence orbitals, subject to the double zeta treatment. Where it is possible to use them, the 6-31G* and 6-31G** basis sets are considered the minimum required basis sets for use with correlated methods.

The most significant disadvantage of the Pople basis sets described so far is that they are based on atomic calculations with coefficients and exponents optimised using single determinant methods (UHF/ROHF). We now consider the 6-311G** Pople basis set which aims to capture electron correlation effects. 6-311G** calculations attempt to overcome the double zeta limitations in the following way: coefficients and exponents are optimised to minimise atomic ground states at the UMP2 level of theory which incorporates some electron correlation effects; a triple zeta approach on the valence region is employed, giving more flexibility at more diffuse parts of the valence region; pure uncontracted angular momentum functions are used for d-type polarisation functions, reducing the number of integrals and a single uncontracted p-type polarisation function is used for H atoms. The UMP2 calculation is performed in several steps. Firstly a UHF calculation is performed followed by optimisation of exponents and coefficients via minimisation of a UMP2 calculation where a frozen core approach is taken to prevent valence functions optimising the core region at the expense of the valence region. During the UMP2 stage, the core coefficients and exponents are held fixed from the UHF stage. Polarisation for the H atom is done by selecting an exponent which is the average of exponents needed to minimise the energy of a variety of diatomic hydrides. In the frozen core approximation, Group 1 and 2 elements have the same problem as seen with the 6-31G basis sets and a similar approach is used to resolve the difficulties. 6-311G** is found to produce good

agreement with experimental geometries and excellent agreement with experimental atomisation energies.

1.14.2 Correlation Consistent Basis Sets

The Dunning family of basis sets[49][50][51][52] are labelled as (aug)-cc-pVXZ, where the (aug) prefix indicates the use of diffuse functions, cc means *correlation consistent*, p means that polarisation functions are added by default and X = D,T,Q,5 to indicate double zeta, triple zeta etc. The aim of these basis sets is to recover dynamical correlation from the valence region whilst treating the core orbitals as frozen. In this context, *correlation consistent* means that angular momentum functions are progressively added in sets, all members of each set contributing roughly the same to the electron correlation capture. For example, once a 2nd d function is added, this is equivalent to adding a single f function and therefore both are added together. In this example the increase in the basis set would be from $1d$ to $2d1f$. A third d function is equivalent to a 2nd f function and a g function and therefore the next step is to increase the basis set from $2d1f$ to $3d2f1g$ etc. The *sp* functions are supplemented every time more higher angular momentum polarisation functions are added. The VXZ basis set process is therefore described as follows. Firstly, to include functions with higher angular momentum. Secondly, to introduce these higher angular momentum functions in groups which have similar effects on recovering the correlation energy. *sp* functions are optimised from HF atomic calculations with higher angular momentum functions subsequently optimised from CISD calculations. This results in a compact basis set which compares favourably with other much larger basis sets. The O atom is used as the benchmark system for the entire first row because it contains many of the features found in the other atoms from B to Ne (a singlet in the 2s orbital and one 2p orbital, and a triplet in the remaining 2p orbitals). Progressively higher angular momenta were added and the quantities of each of these higher angular momenta were also increased in a systematic manner until energy convergence was achieved. Subsequent to benchmarking on the O atom, comparative checks were made on OH and O_2 to ensure that atomic calculations were still valid in a molecular environment: this proving to be the case. The same basis set as designed for the O atom was then used for atoms B to Ne and shown to give comparable results in both atomic and molecular

environments simply by including electron correlation effects from the CISD calculations. The contractions for 1st row elements are as follows: [3s2p1d](cc-pVDZ), [4s3p2d1f](cc-pVTZ), [5s4p3d2f1g](cc-pVQZ), [6s5p4d3f2g1h](cc-pV5Z). As an example, the O atom using the cc-pVDZ basis set will use 3 functions for the 2s orbital and 2 functions for each of the 2p orbitals plus a single set of 5 pure d functions for a total of 14 basis functions. For elements of the second (and subsequent) row, an extra sp set has been included.

1.14.3 Effective Core Potentials

The number of basis functions required for larger atoms rapidly becomes unwieldy. For atoms such as Sn, the vast majority of the 50 electrons within the atom are core and will not be unduly affected by the chemical environment even where bond breaking takes place. Therefore, for normal basis set calculations on an atom this size, an inordinate amount of time would be spent on electrons which are not important to the problem under study. For this reason, the Effective Core Potential (ECP) or pseudo-potential was invented [2][19]. The ECP handles the core as a separate entity from the valence electrons. The core is treated as an averaged potential (which can include relativistic effects) and is approximated as a series of functions such as parameterised Gaussians or polynomials which will be dependent on distance between the electrons and the nucleus. From normal all-electron atomic calculations (such as HF), the valence orbitals then require modification to remove the nodal structure which penetrates the core region. This is demonstrated in figure 1.12. Following this, the parameters are fitted to produce a set of modified valence orbitals which match those produced by the all electron calculation. Of course, this fitting procedure will be dependent on the nature of the basis set and therefore an ECP will include a pseudo-potential and a basis set and the two must be paired in order to give a good approximation of the system. As an example of the scale of reduction in basis functions, using a 3-21G basis set for Sn, 33 CGTOs are required whilst using the common SDD basis set, just 8 CGTOs are required. We now move on to discuss the ECPs used within this work.

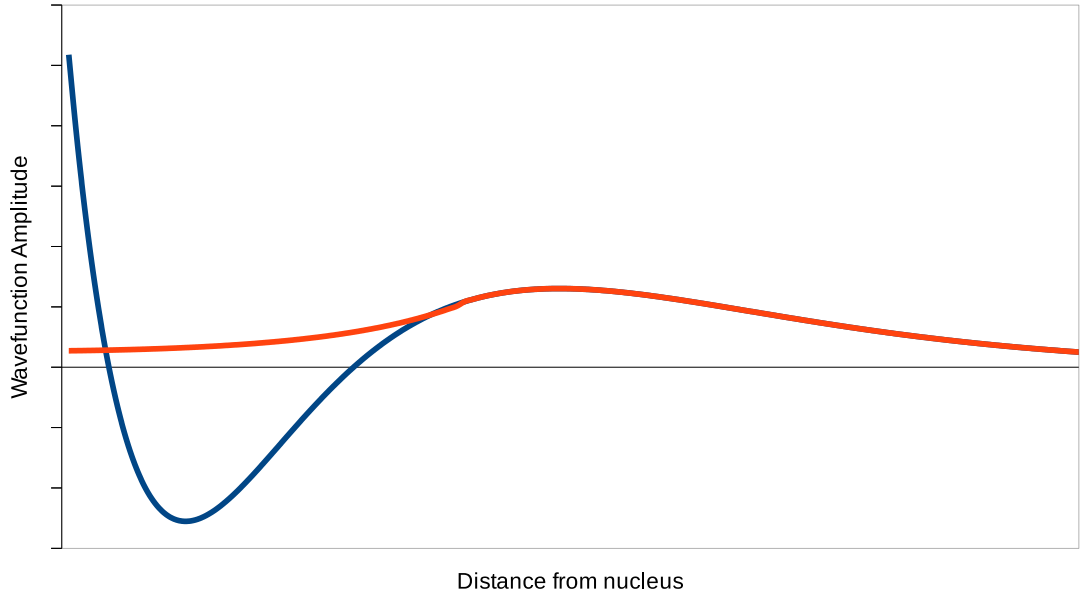

Figure 1.12: A qualitative picture showing the modification of a 2s orbital (blue) to remove the nodal structure within the core region during the development of a general ECP. Here the orange line shows the modified 2s orbital. Notice that the core part of the 2s orbital is now free of nodes

1.14.4 Stuttgart-Dresden Effective Core Potential(SDD)

SDD [53] has been used to describe 1st row transition metals within this work. For these metals, the $3s$ and $3p$ orbitals have a similar size to the $3d$ valence orbitals. It therefore makes sense to include these as valence orbitals because changes in the $3d$ orbitals will likely affect both of them. Additionally, the $4s$ and $4p$ orbitals are also included as valence orbitals. SDD therefore specifies a Neon-like, $X^{(Z-10)+}$ core for 1st row transition metals where X = Sc $\rightarrow$ Zn, i.e. 10 electrons are treated as core. The remaining $Z - 10$ electrons are treated as valence. The valence Hamiltonian can therefore be described as in equation 1.89 where i is the range of valence electrons. The central term, $\hat{V}(\vec{r}_i)$ is the pseudopotential, representing the core, which is experienced by the valence electrons. The form of this pseudo potential will not be discussed further other than to say that it contains parameters which are optimised by fitting to HF valence energies across the various electronic states of the one-electron $X^{(Z-11)+}$ cations using Gaussian basis functions with an attempt made to correct for relativistic effects. The basis set for the valence region of SDD is an optimised (8s7p6d1f)/[6s5p3d1f]-GTO basis set with exponents and coefficients

optimised from the minimisation of the lowest s^1d^{n+1} configuration states for Sc $\rightarrow$ Cu. For Zn, the ^1S ground state, s^2d^{10} is minimised instead. Because of the near degeneracy of $4s$ and $4p$ orbitals, 2 diffuse functions of p-type are added. These are optimised by minimising the lowest ^3P state of Zn, $s^1p^1d^{10}$, and the p^1d^{n+1} configuration of Sc $\rightarrow$ Cu. One further diffuse s and one diffuse d function are both added without optimisation.

$$\mathcal{H} = -\frac{1}{2}\sum_i \hat{\nabla}_i^2 + \sum_i \hat{V}(\vec{r}_i) + \sum_{i<j} \frac{1}{r_{ij}} \tag{1.89}$$

Errors in the energies of low lying electronic states of the atoms Sc through Zn were found to be less than 2.5 kcalmol^{-1} [53]. The effect on Zr_4O_2(methacrylate)$_{12}$ clusters of using SDD was investigated by Kreutzer *et al.* [54] and compared to the performance obtained using the Def2TZVP basis set. These transition metal oxo clusters are important nano-particle mimics and provide an easily synthesised building block for hybrid materials. It was found that there was little difference in using SDD compared to Def2TZVP (approx. 0.3 to 0.8 kcal mol^{-1}) when considering ligand binding energies. A similar result was observed when considering bond lengths within the cluster with SDD showing typical bond length MAE of 0.01 to 0.06Å. Finally, vibrational mode results were found to be closer to experiment when using SDD than when using Def2TZVP with results typically within 20 to 80 cm^{-1} of experiment depending on the DFT functional used.

1.14.5 BSSE

The use of truncated basis sets in practice causes a problem known as Basis Set Superposition Error (BSSE). Because basis sets are nuclear centred and truncated, an error can be introduced when comparing between two different isomers of the same compound or when comparing the interaction energies of van der Waal bonded systems. To understand the problem, a weakly bound dimer of two molecules A and B is considered. When A and B are bound together, the electron density of the atoms of molecule A are described by the basis functions centred on the atoms of molecule A but are also partly described by those centred on the atoms of molecule B. This is as a direct result of the use of truncated basis sets and it is an artefact of the calculation which results in artificially lowered energies for the dimer. When

molecules A and B are infinitely separated (modelled in separate calculations), this artificial lowering of energy is no longer available to either molecule. Therefore when calculating the binding energy of the dimer, we are confronted by the problem of over-binding of the dimer. For strongly bound compounds this is not a significant problem but for weakly bound complexes this can be a serious problem and must be accounted for. Although increasing the basis set improves matters, this can rapidly become computationally intractable for large systems. In this work, BSSE corrections are approximated by a technique called Counterpoise Correction [55]. Three calculations are initially made. Firstly, molecules A and B are geometry optimised in separate calculations with their respective basis sets a and b. Then the dimer AB is geometry optimised containing the basis functions from both individual molecules - ab. The difference between the energy of the dimer and the total energy of the individual separate molecules is the binding energy as shown in equation 1.90.

$$E_{bind} = E(AB)_{ab} - E(A)_a - E(B)_b \tag{1.90}$$

Of course this gives a binding energy which contains an error as a result of BSSE and it is necessary to approximate what this BSSE contribution might be. In order to do this it should be noted that the geometry of the A and B molecules in the dimer is not the same as in the free molecules. To proceed, a single point calculation is performed on molecule A alone at the geometry it holds in the dimer. A second single point calculation is then performed on molecule A at the geometry it holds in the dimer but this time including the basis functions (ghost orbitals) centred throughout space at the locations where atoms from molecule B would be expected to be found (but without molecule B actually being present in the calculation). This gives us two single point energies for molecule A at the geometry of the dimer: one with BSSE and one without. The difference between them is the Counterpoise error for molecule A. This is repeated for molecule B. To find the true binding energy of the dimer, we simply subtract the total Counterpoise error for A and B from the binding energy reported in equation 1.90.

1.15 Density Functional Theory

The problem of solving the Schrödinger equation involves a wavefunction consisting of 4N co-ordinates where N is the number of electrons in the system (3 spatial and one spin co-ordinate per electron). As seen earlier, this creates severe computational problems, in particular with regard to the number of two-electron integrals. An alternative attempt to solve the Schrödinger equation uses electron density to describe the system: a technique called Density Functional Theory (DFT)[13][19], which requires only 3 spatial co-ordinates. In terms of performance, DFT has a similar computational cost to Hartree-Fock theory. As will be demonstrated in later sections, DFT gives very good results for properties such as geometries, vibrational frequencies and reasonably good results can be produced for reaction energies. It can also sometimes produce reasonably good results for excited states providing the excited states involve excitations into low lying unoccupied MOs. Where DFT struggles is in modelling excited states where excitations are into high lying unoccupied MOs, reaction barriers, reaction rates, systems where weak interactions dominate, anionic systems, and charge transfer systems: essentially any system involving large displacement of electrons. Despite these problems however, DFT outperforms HF theory for a similar computational cost and has largely replaced HF as a standard computational tool. The benchmark for DFT comes from the G1 database of 55 molecules containing 1st and 2nd row atoms [56][57]. These molecules have experimental atomisation energies known to be correct to within 1 kcal mol^{-1}. The G2 procedure contains the current gold standard of *ab initio* calculations [58] on this same set of molecules and involves basis set corrections, perturbative corrections, quadratic configuration interaction corrections and fitted higher level corrections. It is against these standards that the performance of DFT methods are judged. It transpires that DFT methods perform very well against the G2 results although the G2 results are closer to experiment. DFT however is a vastly simpler method computationally. We now present a discussion of DFT, mapping the theory from its early days through to modern times.

1.15.1 The Thomas-Fermi-Dirac (TFD) Model

The use of electron density to describe chemical systems has its roots in the combined efforts of Thomas [59], Fermi [60] and Dirac [61] in the 1920's. The approach taken assumed that electron density played the central role in understanding the properties of interacting inhomogeneous gases. In particular, the electrons were treated like a classical liquid in an effort to understand atoms and impurities in metals.

Thomas was interested in methods of approximating the effective electric field within heavy atoms, in order to aid the determination of various atomic properties, in the absence of experimental data. Various approximations were made including the neglect of relativity, the assumption of $\frac{1}{r}$ dependence of the effective potential V on distance from the nucleus of the atom, the assumption of uniform distribution of electrons within the atom and the dependence of the potential V on both nuclear charge and electron distribution. These assumptions and approximations result in calculations which lose accuracy far from the nuclear centre and therefore the Thomas method was best suited to regions local to the nucleus where electron density is highest.

In a similar vein, Fermi regarded heavy atoms as a nucleus surrounded by a gaseous sea of electrons as a result of their large number in such heavy atoms. In this way, statistical methods could be deployed to obtain estimates of a variety of atomic properties. For example, elucidation of the electron distribution within the atom allowed the calculation of the full ionisation of those atoms. This involved progressively stripping all of the electrons from the atom under investigation until all the electrons were removed. Due to the fermionic nature of electrons and the requirement to fulfil the Pauli principle, classical statistical methods were unsuitable and Fermi derived his own statistical methods to aid his work. The ultimate aim of Fermi's work was to therefore determine the nature of the electric field binding the electrons within the atom and thus learn the relationship between the electric potential and the distance from the nucleus.

It was Dirac, however, who provided the mathematical and theoretical justification for the Thomas model, correcting for the exchange terms arising as a result of the requirement to fulfil the Pauli principle. In the process of this work, it was discovered that the entire nature of the atom can be deduced from the electron

density without having to specify the wavefunctions making up that total electron density. The 4N coordinates of the wavefunction were then able to be reduced to just 3. The Dirac model results in an exchange-correlation hole where an electron is less likely to be found. This hole occurs around each electron, causing problems for the approximation of uniform electron density. The exchange-correlation hole [13] can be considered conceptually as consisting of two parts - a Fermi (exchange) hole which deals with the reduced probability of finding another electron in the vicinity of one with the same spin and a Coulomb (correlation) hole which considers the probability of finding another electron in the vicinity of one with either the same or opposite spin. The Fermi contribution to the exchange-correlation hole, which varies as $\rho^{1/3}(\vec{r})$, dominates although it should be noted that it is the superposition of both effects which is real. Neither effect exists in isolation.

Although useful for atomic calculations local to the nucleus, the TFD approach outlined above suffers from qualitative errors in that chemical bonds are not predicted and oscillations due to shell structure are also not predicted. Additionally, the model predicts an infinite charge density at the nuclei with a subsequent decay of r^{-6} with respect to distance from the nucleus rather than exponential as desired. It is this featureless decay of charge density which causes the problems of lack of oscillations. One final problem with the model is the prediction that atomic size will shrink ($Z^{-1/3}$) with increasing nuclear charge instead of increasing. The TFD model therefore proved to be unsuitable for molecular calculations.

1.15.2 Hohenberg-Kohn Theory

The TFD model was adapted in the 1960's by Hohenberg and Kohn [62] to provide a potential solution to the Schrödinger equation for interacting, inhomogeneous systems in an external potential due to a nuclear framework. The initial work of Hohenberg and Kohn involved proof (the H-K Theorem) that a set of N interacting electrons within an external potential, υ, provided by the nuclear framework, will produce a non-degenerate ground state wavefunction, Ψ, and will have, associated with it, a unique electron density. Proof of this allowed a unique electron density to essentially be linked to a unique wavefunction representation of the non-degenerate ground state of the molecule. A knowledge of the exact electron density would,

therefore, contain all of the information about the system, including theoretically the exact ground state energy (as a functional of density), but at reduced complexity due to the vastly reduced number of degrees of freedom (3 instead of 4N). The proof of the unique relationship between the electron density and the wavefunction representing the non-degenerate ground state of the system is presented in the manner of *reducto ad absurdum*. Essentially to disprove the H-K Theorem, one needs to prove that if a unique external potential, υ, with associated non-degenerate ground state wavefunction, Ψ, gives rise to an electron density ρ, that a different external potential, $\upsilon^{'}$, with associated non-degenerate ground state wavefunction, $\Psi^{'}$ can give rise to the same electron density, ρ. Because the Hamiltonian contains the external potential due to the nuclear framework, we can define corresponding Hamiltonians, $\mathcal{H}$ and $\mathcal{H}^{'}$ for the two Schrödinger equations involving wavefunctions Ψ and $\Psi^{'}$ respectively. Letting Ψ be the ground state, the energy of the ground state is found as in equation 1.91. The energy of the state associated with wavefunction $\Psi^{'}$ is found as in equation 1.92.

$$E = \langle \Psi | \mathcal{H} | \Psi \rangle \tag{1.91}$$

$$E^{'} = \left\langle \Psi^{'} \middle| \mathcal{H}^{'} \middle| \Psi^{'} \right\rangle \tag{1.92}$$

By definition, for a non-degenerate ground state, $E < E^{'}$. Therefore, applying the ground state Hamiltonian to the wavefunction $\Psi^{'}$ will result in a higher energy than E. Mathematically this is described as in equation 1.93. Then, expressing $\mathcal{H} = \mathcal{H} + \mathcal{H}^{'} - \mathcal{H}^{'}$ leads through to equation 1.95.

$$E < \left\langle \Psi^{'} \middle| \mathcal{H} \middle| \Psi^{'} \right\rangle \tag{1.93}$$

$$E < \left\langle \Psi^{'} \middle| \mathcal{H} + \mathcal{H}^{'} - \mathcal{H}^{'} \middle| \Psi^{'} \right\rangle \tag{1.94}$$

$$E < \left\langle \Psi^{'} \middle| \mathcal{H}^{'} \middle| \Psi^{'} \right\rangle + \left\langle \Psi^{'} \middle| \mathcal{H} - \mathcal{H}^{'} \middle| \Psi^{'} \right\rangle \tag{1.95}$$

$$E < E^{'} + \left\langle \Psi^{'} \middle| \mathcal{H} - \mathcal{H}^{'} \middle| \Psi^{'} \right\rangle \tag{1.96}$$

The second term of 1.96 contains the differences between Hamiltonians $\mathcal{H}$ and $\mathcal{H}^{'}$. This is the difference between the external potentials υ and $\upsilon^{'}$ and therefore the second term can be written as an integral in terms of both external potentials and the electron density associated with both of these potentials (which we are attempting to show are equal in a bid to disprove the H-K theorem). Equation 1.97 results.

$$E < E^{'} + \int d\vec{r}\, \rho(\vec{r})(\upsilon - \upsilon^{'}) \tag{1.97}$$

Similarly we can apply $H^{'}$ to Ψ to obtain an energy E which must be higher than $E^{'}$ and follow a similar procedure to that described above arriving at equation 1.98.

$$E^{'} < E + \int d\vec{r}\, \rho(\vec{r})(\upsilon^{'} - \upsilon) \tag{1.98}$$

Adding equations 1.97 and 1.98 and noting that $(\upsilon - \upsilon^{'}) = -(\upsilon^{'} - \upsilon)$ leads us finally to equation 1.99 which is impossible.

$$E + E^{'} < E^{'} + E \tag{1.99}$$

By this method, proof was provided that there must be a one to one mapping between an external potential established by a nuclear framework and the associated electron density and that this is associated with a unique wavefunction although the exact energy functional which links them is as yet unknown. Subsequent to this initial proof, the application of the variational principle completed the theory. Applying the variational principle to H-K theory results in separation of the Born-Oppenheimer Hamiltonian into terms involving the external potential due to the nuclear framework and terms which include electron kinetic energy and electron-electron repulsion as shown in equation 1.100 where T is the kinetic energy of the electrons, E_{ee} is the electron-electron repulsion term and E_{ne} is the external potential term. Subject to the constraint that the integral of the electron density over all space is equal to the total number of electrons in the system, Hohenberg and Kohn showed

that a minimum exists for the correct ground state wavefunction, Ψ. If a different external potential under the same constraint was introduced, with corresponding wavefunction $\Psi^{'}$, then it was shown that the corresponding energy $E[\Psi^{'}] > E[\Psi]$. Therefore, in H-K theory, the energy was shown to be variational.

$$E[\rho] = E_{ne}[\rho] + T[\rho] + E_{ee}[\rho] \tag{1.100}$$

Whilst the first term in equation 1.100, which is the attraction of electrons to the nuclei, is known, the remaining two terms, which are the kinetic energies of the electrons and the electron-electron repulsion terms respectively, are not known exactly in DFT and subsequent research involved finding approximations to them. In order for this equation to be usable, the individual terms need to be expanded to demonstrate the nature of their dependence on the electron density ρ. The first term E_{ne} is shown in equation 1.101.

$$E_{ne}[\rho] = -\sum_{A}^{Nuc} \int d\vec{r} \frac{Z_A \rho(\vec{r})}{|R_A - r|} \tag{1.101}$$

The equation represents the interaction energy between the potential of the entire nuclear framework (hence the summation over all nuclei) and the electron density. This interaction is attractive, hence the minus sign, and the electron density is spread out across space, hence the requirement for the integral over $\vec{r}$. The relationship is understood as being one of Coulombic attraction. Next we consider the E_{ee} term. This can be split into two terms: one dealing with the Coulombic electron-electron repulsion, which shall be called $\hat{J}[\rho]$, and the other dealing with the exchange term necessary to comply with the Pauli principle. This is in direct analogy with HF Theory. The $\hat{J}[\rho]$ term is described as in equation 1.102 and the exchange term will be explained shortly.

$$\hat{J}[\rho] = \frac{1}{2} \int \int d\vec{r} d\vec{r}^{\,\prime} \frac{\rho(\vec{r})\rho(\vec{r}^{\,\prime})}{|r - r^{'}|} \tag{1.102}$$

Essentially this term describes the Coulombic repulsion of electron pair clouds which are smeared out over space. The factor of $\frac{1}{2}$ accounts for the double counting of repulsion terms.

1.15.3 Kohn-Sham Theory

Kohn and Sham [63] advanced the work of Hohenberg and Kohn to develop approximate methods for solving inhomogeneous systems of interacting electrons using wavefunctions and lifting the restriction of uniform electron density. Having developed DFT Theory to exclude the use of orbitals, these were re-introduced to allow computation of the electron kinetic energy term to a reasonable degree of accuracy. The rationale behind this is straightforward. The kinetic energy contribution dominates the energy of the system and it is therefore vital that this term is approximated as accurately as possible. In K-S Theory, the kinetic energy terms are considered as for quasi-non-interacting particles. In other words, the electrons are considered to experience the average field of the other electrons rather than be able to see the individual electrons. This is the same idea behind Hartree-Fock theory and therefore a similar kinetic energy term results as shown in equation 1.103.

$$T_s = \sum_{i=1}^{N} \langle \phi_i | -\frac{1}{2}\hat{\nabla}^2 | \phi_i \rangle \tag{1.103}$$

DFT is a theory of electron density and the link between these orbitals, called Kohn-Sham orbitals, is as shown in equation 1.104, with the density in practice being calculated at discrete points on a numerical grid.

$$\rho[\vec{r}] = \sum_{i=1}^{N} |\phi(\vec{r})|^2 \tag{1.104}$$

The electrons, in reality, are not non-interacting and this equation carries an error, $T[\rho] - T_s$, which needs to be corrected for, where $T[\rho]$ is the exact (but unknown) kinetic energy. The overall energy functional for DFT is therefore as described in equation 1.105.

$$E^{DFT}[\rho] = T_s[\rho] + E_{ne}[\rho] + J[\rho] + E_{xc}[\rho] \tag{1.105}$$

The first three terms are simple enough to evaluate and the majority of DFT functionals will share exactly the same terms. The major difference between the vast array of available DFT functionals then lies in how the final term, E_{xc}, is dealt with. This term contains the exchange contribution necessary for compliance with

the Pauli Principle (the equivalent of the $\hat{K}$ terms in HF theory) and also the error in the kinetic energy term as a result of approximating the electrons as quasi-non-interacting particles. It is common to see this E_{xc} split into two terms: one called the Exchange functional and the other called the Correlation functional as shown in equation 1.106. Equation 1.107 shows an alternative description of E_{xc} showing the source of the errors in the entire DFT equation 1.105.

$$E_{xc} = E_x + E_c \tag{1.106}$$

$$E_{xc} = (T[\rho] - T_s[\rho]) + (E_{ee}[\rho] - J[\rho]) \tag{1.107}$$

For the ground state of the system, the use of K-S orbitals leads to Hartree-Fock like equations, with Hamiltonian terms expressed in terms of electron density, see equations 1.108 to 1.110.

$$\hat{h}_{KS}\phi_i = \epsilon_i\phi_i \tag{1.108}$$

$$\hat{h}_{KS} = -\frac{1}{2}\hat{\nabla}^2 + V_{eff} \tag{1.109}$$

$$V_{eff} = V_{ne}(\vec{r}) + \int \frac{\rho^{'}}{|r - r^{'}|} d\vec{r}^{'} + V_{xc}(\vec{r}) \tag{1.110}$$

Here, V_{eff}, is the effective potential each electron feels and includes the attraction to the nuclei and the average field from the other electrons over all space. Also included are the corrections for the kinetic energy approximation and the exchange interaction combined under the term $V_{xc}(\vec{r})$. This final term is the main difference between Hartree-Fock and DFT. If E_{xc}, from equation 1.106 was known exactly, we could simply derive the potential V_{xc} from this potential energy as shown in equation 1.111.

$$V_{xc} = \frac{\partial E_{xc}[\rho]}{\partial \rho} \tag{1.111}$$

As described in equation 1.106 however, the exchange-correlation energy can be decomposed into exchange and correlation functionals, each of which can be expressed in terms of the exchange and correlation potential energies per electron, as shown in equations 1.112 and 1.113, where ϵ_x and ϵ_c are sometimes replaced by their exchange and correlation potentials in these equations.

$$E_x[\rho] = \int d\vec{r}\rho(\vec{r})\epsilon_x[\rho(\vec{r})] \tag{1.112}$$

$$E_c[\rho] = \int d\vec{r}\rho(\vec{r})\epsilon_c[\rho(\vec{r})] \tag{1.113}$$

Development of DFT functionals therefore tends to be split into construction of different exchange functionals and different correlation functionals, with combinations of each used in conjunction with each other to provide overall DFT functionals. Examples of these will be shown later.

1.15.4 Local Density Approximation (LDA)

We now turn to a discussion about how approximations are made for these exchange and correlation terms. The earliest attempt at this was the Local Density Approximation (LDA) [63] [64] [65], or the Local Spin Density Approximation (LSDA) for open shell systems where α and β spins are treated differently. Both LDA and LSDA invoke the uniform electron gas model which describes the electrons as being equally spaced to effect a uniform electron density everywhere. In reality, the electron density is highest near the nuclei, forming a cusp, before dropping away exponentially with distance from the nucleus (there is also the exchange-correlation hole which disrupts uniformity of electron density). Nevertheless, local to the nuclei, this approximation can be useful. The LDA exchange-correlation approximation is shown in equation 1.114 with the LSDA equivalent shown in equation 1.115. "Per electron" equivalent equations are shown in equations 1.116 and 1.117

$$E_x^{LDA} = -C_x \int d\vec{r}\rho^{4/3}(\vec{r}) \tag{1.114}$$

$$E_x^{LSDA} = -2^{1/3} C_x \int d\vec{r} \left(\rho_\alpha^{4/3}(\vec{r}) + \rho_\beta^{4/3}(\vec{r}) \right) \tag{1.115}$$

$$E_x^{LDA} = -C_x \rho^{1/3}(\vec{r}) \tag{1.116}$$

$$E_x^{LSDA} = -2^{1/3} C_x \left(\rho_\alpha^{1/3}(\vec{r}) + \rho_\beta^{1/3}(\vec{r}) \right) \tag{1.117}$$

As seen earlier, all of the terms in the Hamiltonian are expressible as functionals of electron density for various reasons: the number of electrons can be found as the integral over all space of the electron density, the position of cusps in the electron density identify the position of the nuclear centres and the slope at the cusps determines the nature of the nucleus at that point. The electron-nuclear attraction term and the electron-electron Coulombic repulsion terms can be expressed explicitly in terms of the electron density. The kinetic energy term can be described as an approximation (local density approximation derived from a consideration of the uniform density, particle in a box model) following the work of Thomas, Fermi and Dirac, detailed earlier, in terms of the integral of $\rho^{5/3}(\vec{r})$ over all space. Introducing the LDA approximation for the exchange contribution, the resulting LDA energy functional is thus described as equation 1.118, where $C_F = \frac{3}{10}(3\pi^2)^{2/3}$ and $C_x = \frac{3}{4}(\frac{3}{\pi})^{1/3}$.

$$\begin{aligned} E[\rho] = C_F \int d\vec{r} \rho(\vec{r})^{5/3} - \sum_A^M \int d\vec{r} \frac{\rho(\vec{r}) Z_A}{r - R_A} \\ + \frac{1}{2} \int d\vec{r} d\vec{r}' \frac{\rho(\vec{r}) \rho'(\vec{r})}{r - r'} - C_x \int \rho^{4/3}(\vec{r}) dr + E_C[\rho(\vec{r})] \end{aligned} \tag{1.118}$$

Although the LDA exchange approximation results from work by Dirac, it is sometimes referred to as Slater (or S) exchange. The final term $E_c[\rho(\vec{r})]$ in LDA has been approximated by Vosko, Wilk and Nusair and is termed the VWN correlation functional. It is a very complicated equation which will not be replicated here. The entire DFT functional using these LDA approximations is named after the exchange and correlation functionals because it is in these two approximations that most DFT functional differ from each other. In this case we have the amalgamation of the S

exchange and the VWN correlation to give us the so-called S-VWN functional. The term "local density" is used to describe DFT functionals such as these because the uniform electron density approximation is only accurate close to the centre of the electron density - i.e. close to the nucleus. This causes a problem when attempts are made to predict properties and features of molecular systems because bonding, for example, happens relatively far from the nuclei and involves overlap of the tails of exponentially decaying electron clouds.

1.15.5 Generalised Gradient Approximation (GGA)

For reasons just described, LDA calculations are necessarily inaccurate for molecular species. In order to improve on these results, consideration was given to the nature of the electron density far away from the nucleus, i.e. the non-local electron density. It was considered that the non-local electron density could be approximated by a power series of local electron density derivatives as described in equation 1.119, where ρ_{nloc} is the non-local electron density and ρ_{loc} is the local electron density.

$$\rho_{nloc} = \rho_{loc} + x\frac{\partial \rho_{loc}}{\partial \vec{r}} + x^2\frac{\partial^2 \rho_{loc}}{\partial \vec{r}^2} + ... \tag{1.119}$$

The use of just the first derivative of the local electron density as a correction to LDA is called the Generalised Gradient Approximation (GGA) [64]. This approximation is applied to E_{xc}. GGA calculations show good improvements over LDA techniques and are sometimes called Semi-Local Functionals because an attempt is being made to predict non-local behaviour. Some examples of Gradient-Corrected Exchange Functionals include PW91, B88 (usually just called B) and PW86. Examples of Gradient-Corrected Correlation Functionals include PW1, PBE and LYP. Examples of full DFT functionals with gradient-corrections for both exchange and correlation might therefore perhaps be BLYP, PW91PW91 or PW86PBE for example. Although specific DFT functionals will be described later, an example of what a gradient corrected functional looks like is provided for the gradient-corrected B exchange functional [66] shown in "per particle" form in equation 1.120, where $X = \frac{|\nabla\rho|}{\rho^{4/3}}$ is called the reduced gradient.

$$\epsilon_x^B[\rho] = \epsilon_x^{LDA} - \beta\rho^{1/3}\frac{X^2}{1+6\beta X sinh^{-1}X} \tag{1.120}$$

As can be seen, this functional uses the LDA exchange functional as a starting point and applies a gradient correction technique to improve on the result. The gradient is presented within the X term. Notice that no correlation correction is included. For this, a gradient-corrected correlation functional such as LYP would be required, thus combination of B and LYP would therefore give the BLYP DFT functional. Notice the single β parameter in equation 1.120. This parameter is determined by fitting to results obtained from other calculations on a test suite of atoms and molecules. This will be discussed further later.

1.15.6 Hybrid Functionals (Hyper GGA)

Previously we saw that LDA functionals were improved by the inclusion of gradient corrections of the local electron density using GGA functionals. By this approach, non-local electron density can be approximated with some degree of success providing the non-local area was not overly far from the nuclei. Both techniques are underpinned by the uniform electron density approximation which assumes the electrons are quasi-non-interacting. Of course, the real system is interacting and some technique is required to link both non-interacting and interacting systems together. A common technique is to use a perturbation parameter, λ as will be described now. The non-relativistic, Born-Oppenheimer Hamiltonians for the fully interacting and the non-interacting systems are as shown in equations 1.121 and 1.122 respectively. For a fully non-interacting system there are no electron-electron repulsion terms required.

$$\mathcal{H}_{inter} = \hat{T} + \hat{V}_{ne} + \hat{V}_{ee} \tag{1.121}$$

$$\mathcal{H}_{noninter} = \hat{T}_s + \hat{V}_{ne} \tag{1.122}$$

In order to reconcile both of these extreme cases a perturbative parameter λ is introduced to the fully interacting system described in equation 1.121. We are then presented with the following adapted equation 1.123. Here we allow λ to be a real

number between 0 and 1 including both limits. At $\lambda = 1$, the equation becomes the fully interacting Hamiltonian. For $\lambda = 0$, the equation collapses to the fully non-interacting Hamiltonian. λ therefore can be considered as a parameter which switches on Coulombic electron-electron interaction on a continuous range from fully off to fully on and all values inbetween. It is therefore of importance in general that any functionals employing this technique present smooth performance across this entire range of perturbation strengths, all displaying the same electron density in order to provide the link between the extremities of full non-interaction and full interaction.

$$\mathcal{H} = \hat{T} + \hat{V}_{ne}(\lambda) + \lambda \hat{V}_{ee} \tag{1.123}$$

For other values of λ between 0 and 1, the Hamiltonian can represent any intermediate system. The process here involves adjusting V_{ext} to produce the same electron density as found for both cases of $\lambda = 0$ and $\lambda = 1$. Mathematically, this technique of ensuring equivalence in terms of electron density as the perturbation strength, λ, is altered from 0 to 1 allows us to smoothly link the interacting and non-interacting systems. E_{xc} can be expressed using the Adiabatic Connection Formula [67] shown in equation 1.124. That is, we integrate over the exchange correlation energies at each value of λ over the range $0 \rightarrow 1$, where Ψ_λ is the wavefunction at each value of λ.

$$E_{xc} = \int \langle \Psi_\lambda | \hat{V}_{xc}(\lambda) | \Psi_\lambda \rangle \, d\lambda \tag{1.124}$$

This cannot be solved exactly but approximations can be made if V_{xc} is linear in λ. This can be shown to lead to the so called "half and half" expression [68] for E_{xc} shown in equation 1.125. Here the exchange-correlation functional is described as half of the non-interacting exchange-correlation functional ($\lambda = 0$) and half of the fully interacting exchange-correlation functional ($\lambda = 1$). It should be noted that for the non-interacting system ($\lambda = 0$), Ψ_0 is a single Slater Determinant. Ψ_1 is unknown and could be ascertained from LSDA.

$$E_{xc} = \frac{1}{2} \langle \Psi_0 | \hat{V}_{xc}(0) | \Psi_0 \rangle + \frac{1}{2} \langle \Psi_1 | \hat{V}_{xc}(1) | \Psi_1 \rangle \tag{1.125}$$

Because Ψ_0 is a Slater Determinant, this first term corresponding to $\lambda = 0$ is simply the Hartree-Fock exchange. Note that there is no Hartree-Fock correlation part because there is no electron correlation in Hartree-Fock and also for a fully non-interacting system, there will be no electron correlation anyway. For the situation where LSDA is used for the second term in equation 1.125, we are then left with the following equation 1.126. Other exchange-correlation functionals could be used in place of LSDA for the case where $\lambda = 1$. An example of B3LYP [69] [70] is shown in equation 1.127. As can be seen these functionals contain an element of exact Hartree-Fock exchange and are therefore categorised as Hybrid or Hyper-GGA DFT functionals [64].

$$E_{xc} = \frac{1}{2}E_x^{HF} + \frac{1}{2}(E_x^{LSDA} + E_c^{LSDA}) \tag{1.126}$$

$$E_{xc} = (1-a)E_x^{LSDA} + aE_x^{HF} + b\Delta E_x^B + (1-c)E_c^{VWN} + c\Delta E_c^{LYP} \tag{1.127}$$

Here we see a more complicated DFT functional which contains 3 variable parameters, a, b, and c. In addition, Hartree-Fock exchange, LSDA exchange, B gradient-corrected exchange, VWN correlation and finally gradient-corrected LYP correlation are included. The details of this functional will be covered later.

1.15.7 Meta GGA Functionals

After inclusion of first derivatives of the local electron density it is inevitable that inclusion of second order derivatives would be attempted in a bid to obtain more accuracy. This inclusion results in DFT functionals which are called meta GGA functionals [64]. An example of meta GGA functionals is M06L and this functional, amongst others, will be described later.

1.15.8 Dispersion Correction and Long Range Effects

Although DFT shows itself to model systems very well local to the source of electron density, a problem occurs at points further away from this source. In particular, molecules bound by weak van der Waals (VDW) bonding are poorly described by

DFT. VDW bonding originates in the correlation of electrons on different neighbouring atoms and is dominated by dispersion effects [71] [72]. In this region, the overlap of electron clouds of the bound species is very small. As described above, GGA techniques are essentially local electron density models where medium to long range density is approximated using gradient corrections of the local density. Although this leads to improved results over LDA/LSDA approaches, nevertheless to all extents and purposes, medium to long range effects are not captured well and this deterioration in performance is seen to become noticeable just short of the VDW radius of each atom [71]. In order to capture the correct behaviour at bonding distances in these weakly bound species it is necessary to correct for the neglect of, at least, the leading dispersion interaction term - C_6R^{-6}. Shortly, a description of the pertinent dispersion corrections within this work, GD3 and GD3BJ, will be discussed. First the common DFT functionals used in this work are considered.

1.16 DFT Functionals

A description of the key DFT functionals used in the course of this work is now presented covering a series of GGA, hybrid GGA, meta GGA functionals in addition to long range corrected functionals. Dispersion corrections are also considered.

1.16.1 BLYP, B1LYP and B3LYP

In this section we present an overview of the Becke-type DFT functionals. The original DFT exchange functional in this set is that of the B88 exchange functional, more commonly known simply as the B exchange functional [66]. This GGA functional was designed to correct errors in existing GGA functionals regarding displaying the correct asymptotic behaviour of the exchange energy density which, as described earlier when considering Hartree-Fock Theory, should be $-\frac{1}{r}$. The B exchange functional is shown in equation 1.128. It should be noted that this equation is the integral of equation 1.120 and includes both spin densities, $x = \frac{|\nabla\rho_\sigma|}{\rho_\sigma^{4/3}}$.

$$E_x^B = E_x^{LDA} - \beta \sum_\sigma \int d^3\vec{r}\, \rho_\sigma^{4/3} \frac{(x_\sigma)^2}{1 + 6\beta x_\sigma sinh^{-1} x_\sigma} \tag{1.128}$$

The value of $\beta = 0.0042$ au, was selected on a least squares fit to a range of exact atomic exchange results from Hartree-Fock calculations on the noble gases (He to Rn) and in this sense the B exchange functional is semi-empirical in nature. The value of β used allows the B functional to give a range of results deviating only 0.11% from the exact Hartree-Fock exchange results with just this single parameter. At the time, this represented the first GGA functional capable of properly describing the asymptotic behaviour of exchange density of finite many electron systems. Benchmarking of the B functional against the G1 and G2 test suites of atoms and molecules [73] showed that whilst LSDA techniques achieved average atomisation errors of around 36.2 kcal mol^{-1} compared to experiment, the B functional achieved errors of just 3.7 kcal mol^{-1}, simply by the addition of gradient corrected exchange only. Addition of the LYP [74] correlation functional gives BLYP.

Moving on from the B functional, the 3-parameter hybrid exchange functional B3 [69] and the introduction of exact exchange is presented. Here the exchange and correlation gradient corrections from the B functional and the PW91 correlation functional are brought into a modified LDA functional called B3PW91 which uses a portion of exact HF exchange. The B3PW91 functional results from this and is shown in equation 1.129.

$$E_{xc} = E_{xc}^{LSDA} + a(E_x^{exact} - E_x^{LSDA}) + b\Delta E_x^B + c\Delta E_c^{PW91} \tag{1.129}$$

In this equation, exact HF exchange from the fully non-interacting limit has replaced a portion of the LSDA exchange. This is done to ensure the lower λ limit is met from equation 1.124. In addition to LSDA and exact HF exchange, some gradient corrected B exchange is also introduced as well as gradient corrected PW91 correlation. The 3 parameters a, b and c are deduced from a fit to experimental data detailed in the G1 dataset and are therefore semi-empirical in nature. The respective values are 0.20, 0.72 and 0.81. The absolute average error in atomisation energies against the G1 data set is found to 2.4 kcal mol^{-1} which compares very favourably to the G2 procedure results of 1.2 kcal mol^{-1} on the same data set. Ionisation potential errors are shown to be 0.14 eV compared to 0.05 eV for G2 and proton affinities are 1.2 kcal mol^{-1} compared to 1.0 kcal mol^{-1} for G2. Substitution of PW91 correlation with LYP [70][74] gives the B3LYP functional. Here the gradient corrected

LYP correlation functional is split as follows, $\Delta E_c^{LYP} = E_c^{LYP} - E_c^{VWN}$ to allow for both non-local correlation (through LYP) and local correlation (through VWN). Substitution of this into the B3PW91 functional gives B3LYP which is described in equation 1.127 and reproduced for convenience in 1.130. Here the values of a, b and c are as for B3PW91 above.

$$E_{xc} = (1-a)E_x^{LSDA} + aE_x^{HF} + b\Delta E_x^B + (1-c)E_c^{VWN} + cE_c^{LYP} \tag{1.130}$$

The B1 functional [75], was designed to avoid the use of the three B3 adjustable parameters in determining the amount of Hartree-Fock exact exchange to include. This was performed using a more sound theoretical background to establish the optimal amount of exact exchange to include in advance, as opposed to the technique of fitting to experimental data as is the case with B3LYP. The B1 functional including LYP correlation is shown as the standalone B1LYP functional in equation 1.131.

$$E_{xc} = aE_x^{exact} + (1-a)(E_x^{VWN} + \Delta E_x^B) + E_c^{LYP} \tag{1.131}$$

The single parameter a is determined to be 0.25 using perturbation theory which establishes a firm theoretical description of the dependence of E_{xc} on λ from the Adiabatic Connection equation.

1.16.2 Dispersion Effects and B97D3

Finally, in this section, we consider dispersion effects with particular emphasis on DFT-D, GD3 and GD3BJ dispersion corrections and will reference the B97D3 functional which uses them [76][77].

The B97D3 functional introduced dispersion corrections into the Becke B97 functional [78] which is a non-hybrid GGA functional. B97 itself is based on a systematic fitting of B3PW91 to the G2 set of thermochemical data to produce optimised gradient correction for both exchange and correlation. As described earlier, dispersion corrections are necessary due to the almost complete neglect of the medium to long range effects by GGA functionals, which rely on a model of local electron density. The technique of simply adding C_6R^{-6} corrections to the B97 functional comes with

a problem: both the functional and the dispersion correction will attempt to correct for the lack of electron correlation in the same areas. An early example of this was the application of the DFT+D method of Grimme [79]. To fix this within B97D, re-parameterisation of the entire B97 functional was performed together with VDW effects included. This included the decision to partition up the correlation space by allowing the DFT functional to capture only short range correlation and using C_6R^{-6} to capture medium and longer range correlation. In this way the entire energy of the system can be captured as shown in equation 1.132, where E_{disp}, sometimes called DFT-D2 is defined in equation 1.133.

$$E_{B97D} = E_{B97} + E_{disp} \tag{1.132}$$

$$E_{disp} = -s_6 \sum_{i=1}^{M-1} \sum_{j=i+1}^{M} \frac{C_6^{ij}}{R_{ij}^6} f_{damp}(R_{ij}) \tag{1.133}$$

C_6^{ij} is the pairwise dispersion coefficient for atoms i and j, R_{ij}^6 is the sixth power of the distance between atoms i and j, $f_{damp}(R_{ij})$ is a damping function required to prevent singularities at small R_{ij} and s_6 is a scaling factor, the value of which is dependent on the DFT functional used. The coefficients C_6^{ij} can be further broken down as shown in equation 1.134, where C_6^a is defined for each atom as shown in equation 1.135. Here I_p^a is the ionisation potential for atom a, α^a is the polarisability of atom a and $N = 2, 10, 18, 36, 54$ for atoms from rows $1 - 5$ of the periodic table respectively. I_p^a and α^a are computed using *ab initio* techniques.

$$C_6^{ij} = \sqrt{C_6^i C_6^j} \tag{1.134}$$

$$C_6^a = 0.05 N I_p^a \alpha^a \tag{1.135}$$

f_{damp} is described as in equation 1.136, where R_r is the sum of atomic VDW radii calculated using *ab initio* electron density contour calculations and $d = 20$. As can be seen in equation 1.136, when R_{ij} becomes very small with respect to R_r, the denominator becomes approximately e^{20} and f_{damp} goes to zero, cancelling the effect of the singularity in the rest of equation 1.133. The gradient of the damping

function, controlled by the value of $d = 20$, is also steep enough to ensure that for distances well under the VDW limit, the corrections for dispersion are negligible, thus preventing unwanted double counting correlation effects.

$$f_{damp} = \frac{1}{1 + e^{-d((R_{ij}/R_r)-1)}} \tag{1.136}$$

It was found that using this set of equations, consistent results were found in terms of descriptions of elements across the periodic table without having to resort to any empirical fitting procedures. Some special cases were found regarding large differences between the free atom and the atom in molecular environments for groups I, II and transition metals which rendered direct calculations of parameters unreliable. In these circumstances the C_6 coefficients were obtained by averaging the coefficients found for the preceding noble gas and the subsequent group III element. Providing the number of such special case atoms were small relative to the number of other atoms within the system, this approximation could be considered reasonable with any loss in accuracy essentially lost in the noise.

In a bid to improve the accuracy of the dispersion correction and to broaden the range of applications which could benefit, attempts were made to modify the above dispersion scheme by replacing some of the empirical values used with more sound theoretical underpinnings [80]. In this new dispersion technique, called GD3 or DFT-D3, the C^{ij} and R_r values were targeted for such treatment. $C_8 R^{-8}$ terms were also included. Most importantly, the dependence on geometry of the dispersion coefficients was taken into account to allow for situations where the co-ordination sphere of the atom distorted the electron density. This allowed a more realistic dispersion correction for molecular and extended environments whereas previously isotropic isolated atom electron densities were assumed. This change also allowed chemical reactions to be treated more appropriately, especially where atoms are seen to have substantially changed co-ordination spheres. For ease of computation however, the dispersion coefficients are assumed to be independent of the electronic structure. Finally, 3-body dispersion terms were also included. The scaling factor s_6 is set to 1 for all DFT functionals with the exception of those functionals which are already designed to include some long range correction. For such functionals a value less than 1 was used. s_8 values however are DFT functional dependent. The

inclusion of a $C_8^{ij}R^{-8}$ correction causes problems however because, by definition, this has a shorter range effect than $C_6^{ij}R^{-6}$ corrections. As a result, this can interfere with the normal DFT functional short range correlation treatment causing double counting of correlation effects. The s_8 values therefore are used to help counter these effects. The modified GD3 dispersion correction is thus given in equation 1.137, where $E_{disp}^{(n)}$ is the n-body dispersion correction. Equation 1.138 is the GD3 modified version of 1.133, which is the DFT-D2 correction for B97D, taking into account the changes detailed above. The damping function has been changed to use a more convenient form following investigations which showed that the precise form of this function has less impact than first thought. This modified damping function is shown in equation 1.139.

$$E_{disp} = E_{disp}^{(2)} + E_{disp}^{(3)} \tag{1.137}$$

$$E_{disp}^{(2)} = -\sum_{A,B}\sum_{n=6,8} s_n \left(\frac{C_n^{AB}}{R_{AB}^n}\right) f_{d,n}(R_{AB}) \tag{1.138}$$

$$f_{d,n}(R_{AB}) = \frac{1}{1+6\left(\frac{R_{AB}}{S_{r,n}R_o^{AB}}\right)^{-\alpha_n}} \tag{1.139}$$

In the above damping equation, 1.139, $s_{r,n}$ is a scaling factor which determines the VDW cutoff radius, R_o^{AB}. It is DFT functional dependent for $n = 6$. $S_{r,6}$ replaces the global scaling factor S_6 from DFT-D2 and is set to ensure appropriate performance at short and medium ranges. $s_{r,8}$ is fixed at unity for all functionals. α_n is the steepness parameter which determines how quickly the dispersion correction is driven to zero at short range. At these distances, as discussed already, double counting of electron correlation can occur. The values of $\alpha_6 = 14$ and $\alpha_8 = 16$ have been explicitly fixed to ensure the GD3 dispersion correction falls under 1% of the total dispersion interaction at covalent bond distances, leaving the DFT functional to correct for the rest of the correlation. The dispersion coefficients, C_6^{ij} are calculated explicitly from averaged dipole polarisabilities using *ab initio* (Time-Dependent DFT) methods. These values are taken from the hydrides of each element from H through to Pu as opposed to free atom calculations and can be reduced to averaged multi-pole expectation values. The C_8^{ij} values are computed recursively from the C_6^{ij} values.

The reason for not explicitly calculating these higher order effects is once again related to the fact that they are short range and cause problems with the operation of DFT functionals at covalent bond lengths. Therefore calculating these higher order contributions exactly would be counter-intuitive. The atom pairwise cut-off radii are no longer approximated from electron density maps as with DFT-D2 dispersion. Instead, they are specifically calculated for all possible homonuclear diatomics in the range of H_2 to Pu_2, using DFT energies for each possible dimer. The cut-off radius is obtained by adjusting the bond length of the dimer until the energy reaches a certain reference value which was obtained for the C_2 dimer as part of the DFT-D2 work. This specifies where the dispersion corrections cut-off should occur. The GD3 dispersion correction also includes important changes to account for changes in the co-ordination environment of each atom where large changes to the dispersion coefficients can occur depending on the connectivity of the atom. Covalent bonding of the atom reduces the polarisability of the electron density around the atom and subsequently the dispersion coefficient. This lowers the energy of the orbitals and instigates a process called "quenching" of atomic states. This effect is approximated by assigning fractional co-ordination numbers for each atom and feeding these numbers back into the calculation of the C_6^{ij} coefficients using an interpolation procedure from known references values. The 3-body dispersion term is derived from a perturbation treatment for three atoms and this process will not be described in detail here other than to say that the dispersion coefficients for this contribution are approximated as the geometric mean of the relevant 2-body terms as shown in equation 1.140.

$$C_9^{ABC} = -\sqrt{C_6^{AB} C_6^{AC} C_6^{BC}} \tag{1.140}$$

One of the main problems with the GD3 dispersion correction is that it applies zero-damping below the VDW cutoff radius to prevent double counting effects in the covalent bond length range. There is however no theoretical justification for damping to zero. Additionally, this introduces an artefactual repulsive wall into calculations as a result of the rapid rise to zero as shown in figure 1.13 which shows the effect of damping on the dispersion curve for the argon dimer. This figure will be discussed shortly. The work of Becke *et al.* [81][82][83], suggested that "rational damping" might be a more appropriate way of treating short range dispersion. In

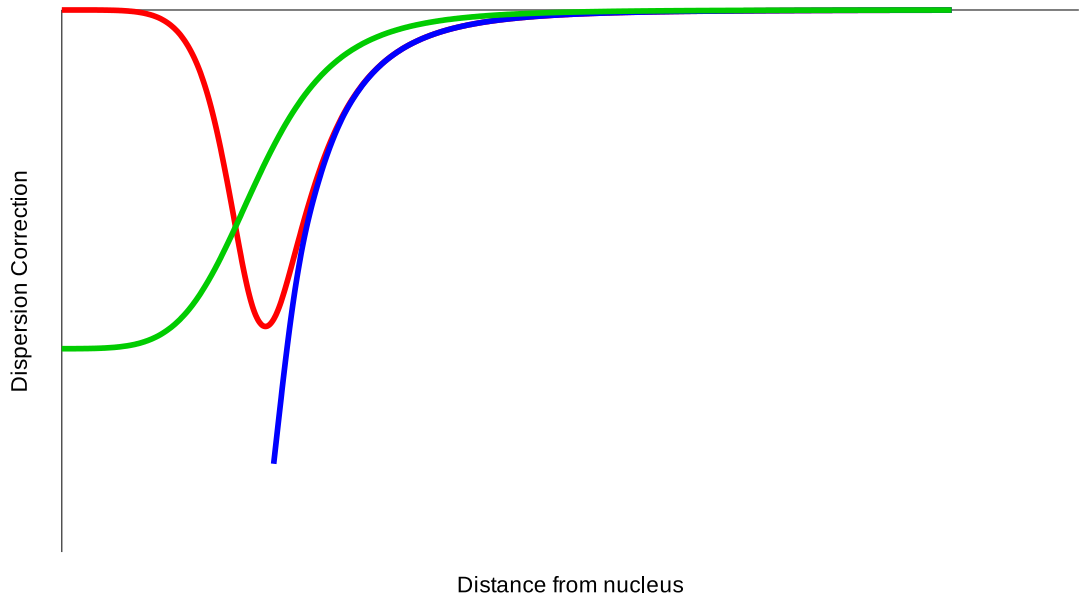

Figure 1.13: Qualitative example of dispersion damping. GD3 (red) and GD3BJ (green) methods are compared with the situation where no dispersion damping (blue) is applied at short range. GD3 dispersion is applied with only the two body dispersion corrections shown in equation 1.137, n is set to 6 only, C_6^{AB}, s_6 and the product term $R_o^{AB}S_{r,6}$ are all set to 1 and α_6 is set to 14. For the situation where no damping is provided, GD3 is shown with the damping term, $f_{d,6}(R_{AB})$, set to 1. For GD3BJ, shown in equation 1.141, n is set to 6 only, S_6, C_6^{AB}, a_2 and the product term $a_1R_o^{AB}$ are all set to 1.

this scheme, the damping correction is reduced to a certain value other than zero at short range. This is also demonstrated in figure 1.13. Incorporating this idea into GD3 dispersion results in what is known as GD3BJ dispersion.

In this figure, the undamped dispersion (blue line) clearly shows a singularity. The red line shows the effect of GD3 zero-damping on dispersion. Here the singularity is corrected but below 3.4 A a repulsive wall has been introduced by the desire to send the dispersion correction to zero. Counterintuitively, this can, in some cases, result in longer bond lengths when dispersion corrections are introduced with this type of damping. Finally, the green curve displays the effect of GD3BJ rational damping on the dispersion. Here the singularity has been fixed as with zero-damping but the repulsive wall has been removed. There is however the problem of non-zero damping correction at covalent bond lengths although it transpires that this is not a significant issue for the asymptotic fixed value approached by GD3BJ at short

range. Equation 1.141 shows the GD3BJ dispersion correction.

$$E_{disp} = -\frac{1}{2}\sum_{A\neq B} S_n \frac{C_n^{AB}}{R_{AB}^n + const} \tag{1.141}$$

It can be seen that in the limit of $R_{AB}^n \to 0$, this expression becomes a constant dispersion correction to the total correlation energy for covalent bonds. Because the BJ damping correction to GD3 is considered theoretically justified at short range, the focus now shifts to making corrections to the DFT correlation functionals themselves for their shortcomings in this region. The value of the nth order constant in equation 1.141 is as shown in equation 1.142. S_6 is set to unity for GGA and hybrid functionals with the value of S_8 determined by the functional. $a1$ and $a2$ are free-fit Becke-Johnson parameters. The expression for R_{AB}^0 can be reduced to a simple geometric mean of atomic multipole-type expectation values and can be described as $\frac{\langle r^4\rangle}{\langle r^2\rangle}$. There are therefore three free-fit parameters for GD3BJ: S_8, $a1$ and $a2$ and these parameters are fitted, via the least squares method to reference data from benchmark test sets of non-covalent interactions. Although GD3BJ outperforms GD3 for thermochemistry, it was found that both performed equally well on geometries.

$$const = f(R_{AB}^0)^n \tag{1.142}$$

$$f(R_{AB}^0)^n = a_1 R_{AB}^0 + a_2 \tag{1.143}$$

$$R_{AB}^0 = \sqrt{\frac{C_8^{AB}}{C_6^{AB}}} \tag{1.144}$$

As we final note we observe that we obtain the B97D3 functional by applying the above GD3BJ dispersion scheme to the B97 functional. This dispersion corrected GGA functional is seen to give enhanced accuracy in applications involving non-covalent interactions, thermochemistry and transition metals with respect to standard GGA functionals.

1.16.3 M06 and M06L

The Minnesota set of meta-GGA DFT functionals are briefly described here. M06L [84] is a local density functional (it does not contain any exact HF exchange) designed to improve performance for main group and transition metal systems with particular regard to non-covalent interactions. This functional was shown to be considerably faster than B3LYP for large and complex systems. It contains PBE exchange and exchange gradient corrections, with the addition of an LSDA exchange component and contains similar correlation to the group's earlier M05 functional which will not be described here. The functional is free of correlation self interaction. Testing against a range of standards, M06L was seen to produce lower mean errors than B3LYP and is intended for use in applications such as supramolecular chemistry and systems, where non-covalent interactions dominate but hybrid functionals are prohibitively expensive. M06 [85] is a hybrid-meta-GGA DFT functional and was designed for use in systems dominated by organometallic, inorganometallic and non-covalent interactions. It has the same functional form for exchange and correlation as M06L but with the inclusion of a portion of exact HF exchange. As with M06L, there are a number of parameters within the functional which are optimised by minimising a training function which describes a variety of types of mean error measures against a known set of standard databases. In particular, one of the parameters, X, describes the percentage amount of HF exchange to include. M06L contains 0% HF exchange whilst M06 contains 27%.

1.16.4 ωB97, ωB97X, ωB97XD

The ωB97 family of DFT functionals [86][87] attempts to correct the long range behaviour of the Becke B97 DFT functional described earlier (as the exchange part of the B97D3 functional). The B97 functional displays long range behaviour of $-C_X r^{-1}$ instead of $-r^{-1}$ which causes particular problems for charge transfer reactions and thermochemistry. The ωB97 family divides the Coulomb operator into short range and long range parts with a parameter, ω, describing the extent of each part. The short and long range parts are handled by DFT and wavefunction methods (WFT) respectively. DFT performs well at short range but has not yet been properly developed for long range. In this family of long range corrected function-

als, 100% HF exchange is used for the long range with the correlation correction from B97 remaining intact in both ωB97 and ωB97X. This eliminates self interaction in long range exchange. ωB97 contains 0% HF exchange at short range and ωB97X contains around 16% HF exchange at short range. These changes result in performance of these functionals which was shown to be significantly better for charge transfer systems, atomisation energies and a range of other properties. Short range self interaction is still a problem for these functionals however. A further problem is the omission of London interactions at long range and to correct this, the ωB97XD functional was introduced. This functional is based on the ωB97X functional described above but with 22% HF exchange at short range and an empirical atomic pairwise correction for dispersion effects which is simply added to the normal DFT calculated result. The form of this dispersion correction is similar to that described for GD3BJ. It is truncated to $C_6^{ij} R_{ij}^{-6}$ with zero damping included at short range. With the inclusion of dispersion corrections ωB97XD shows reasonable improvements over the other two functionals in this family.

1.16.5 CAM-B3LYP

The CAM-B3LYP functional [88] was designed to correct deficiencies in the standard B3LYP functional which prevent electron transfer reactions from being studied computationally along with issues over modelling the polarisability of long chains and TDDFT excitations using Rydberg states. Similarly to B97 in the discussion about the wB97 family above, B3LYP predicts long range behaviour of $-0.2r^{-1}$ instead of the desired $-r^{-1}$. In order to correct this error, the r_{12}^{-1} term is split into two: a short range term and a long range term, both described using standard error functions in a manner which allows the proportions of B88 and exact HF exchange to be altered to describe short range interactions through to long range interactions. In this functional, at short range, 19% HF exchange and 81% B88 exchange are used. At long range, this is altered to 65% HF exchange and 35% B88 exchange. At intermediate ranges, a single parameter $\mu = 0.33$ is used to determine the relative proportions of HF and B88 exchange thus smoothly linking short and long range corrections in a single equation. These changes result in improved description of VDW interactions, Rydberg excitation energies, charge transfer reactions and the 4s-3d interactions energies of 1st row transition metals (which B3LYP typically

underestimates).

1.17 CSFs and Spin Contamination

In order to describe the overall spin of a multi-electron system, two operators are required: one involving the spin angular momentum conventionally projected onto the z-axis - $\hat{S}_Z$, and the other involving the $\hat{S}^2$ operator. In this way, both magnitude and direction are able to be ascertained as appropriate for a full description of a vector quantity. The overall wavefunction should ideally be an eigenfunction of both of these operators as follows in equations 1.145 and 1.146.

$$\hat{S}_Z = M_S \left|\Psi\right\rangle \tag{1.145}$$

$$\hat{S}^2 = S(S+1) \left|\Psi\right\rangle \tag{1.146}$$

Whilst single Slater Determinants representing one electron configuration will always be eigenfunctions of $\hat{S}_Z$, they won't necessarily be eigenfunctions of $\hat{S}^2$. Restricted open shell singlets, for example, are not pure spin states and therefore will not be eigenfunctions of $\hat{S}^2$. Indeed, any restricted open shell configuration where the unpaired electrons are not all of the same spin states will be problematic in this way. This can be resolved by expressing the wavefunction using Configuration State Functions (CSFs) which are linear combinations of a small number of Slater Determinants [89][90]. In addition to forcing the wavefunction to be an eigenfunction of $\hat{S}^2$, there will be fewer CSFs than Slater Determinants in the wavefunction description, which should usually lead to an easing of the computational effort. Some of this computational saving however can be expended in attempting to create the CSFs in the first place. These competing effects mean that each case must be treated on its merit. For unrestricted calculations however, the problem is more severe. Because the α and β electron "pairs" are inhabiting different spatial orbitals, they cannot be spin adapted in this way to produce pure spin states. Instead, it is necessary to approximate these spin states using a linear combination of pure spin states with the spin manifold appropriate to the overall spin being approximated [91] [92]. An example of an approximate singlet is shown in equation 1.147 with an approximate doublet

shown in equation 1.148 and an approximate triplet shown in equation 1.149, where $|1\rangle$, $|2\rangle$ and $|3\rangle$ etc. represent pure singlet, doublet and triplet spin states.

$$\left|{}^1\Psi\right\rangle = a\,|1\rangle + b\,|3\rangle + c\,|5\rangle + ... \tag{1.147}$$

$$\left|{}^2\Psi\right\rangle = a\,|2\rangle + b\,|4\rangle + c\,|6\rangle + ... \tag{1.148}$$

$$\left|{}^3\Psi\right\rangle = a\,|3\rangle + b\,|5\rangle + c\,|7\rangle + ... \tag{1.149}$$

Note that only pure spin states starting from the desired approximate spin state are included in the linear expansion. The inclusion of these extra higher order pure spin states is called *spin contamination* and introduces an error in the expectation value of the $\hat{S}^2$ operator, resulting in energies which are usually artificially higher than desired. Additionally, spin contamination can cause problems of artefactual spin polarisation [93] which can cause problems in electronic structure calculations where the location of electrons are desired. The level of spin contamination can be shown, for an unrestricted Hartree-Fock calculation, to be as in equation 1.150, where $\langle\hat{S}^2\rangle_{pure}$ is shown in equation 1.151. In these equations, N^α and N^β are the number of alpha and beta spin electrons in the system and the summation of $S_{ij}^{\alpha\beta}$ is the summation over the overlap integrals.

$$\langle\hat{S}^2\rangle = \langle\hat{S}^2\rangle_{pure} + N^\beta - \sum_{i,j}^{N} \left|S_{ij}^{\alpha\beta}\right|^2 \tag{1.150}$$

$$\langle\hat{S}^2\rangle_{pure} = \left(\frac{N^\alpha - N^\beta}{2}\right)\left(\frac{N^\alpha - N^\beta}{2} + 1\right) \tag{1.151}$$

Spin contamination of more than around 10% causes serious problems for unrestricted calculations and if it cannot be reduced, another method must be found for modelling the system. When considering DFT however, no explicit wavefunction exists leading to problems defining $\langle\hat{S}^2\rangle$ [94][95]. Efforts to produce $\langle\hat{S}^2\rangle$ expectation values involve approximations which can be subjective in nature. Whilst it is imperative that spin contamination is reduced as much as possible for accurate calculations, care must be taken when relying on the numerical value calculated

by all DFT methods. Modern quantum chemistry tools will attempt to remove spin contamination through annihilation of the unwanted spin states using projection methods but the development of improved techniques with which to estimate accurate values of $\langle \hat{S}^2 \rangle$ is a continuing theme of research.

1.18 Wavefunction Stability

Hartree-Fock and DFT calculations attempt to minimise the energy of a wavefunction with respect to variation of the MO coefficients and this is usually performed under one or more constraints [96][97] , such as the use of real wavefunctions, the use of a truncated basis set, the use of spin-orbitals as simple single products of spatial and spin functions, symmetry restrictions or the use of restricted calculations for core electron pairs rather than fully unrestricted for example. There is no certainty that the minimised energy from such a heavily restricted wavefunction will satisfy the requirement of the final wavefunction being an eigenvalue of both the S_Z and S^2 operators, leading to a wavefunction instability. Most quantum chemical tools support features which seek to identify and rectify these wavefunction instabilities by progressively relaxing these constraints to identify solutions which may be more optimal. These instabilities manifest themselves in the following way: first derivatives of the energy, with respect to nuclear position, of the constrained system identify a stationary point, with second derivatives usually confirming this stationary point to be a local minimum. It may be possible that the calculation has converged on a solution containing one or more imaginary eigenvalues and this type of wavefunction instability can usually be easily rectified by displacing the geometry along the imaginary eigenvalue co-ordinate. The presence of further wavefunction instabilities are then tested by relaxing some of these wavefunction constraints and re-calculating to confirm that the energy remains as a local minimum, because it is entirely possible that, following the removal of the constraint, the energy becomes a stationary point other than a minimum, or it may even be that the energy is no longer a stationary point at all. The latter two conditions would mean that a lower energy solution would be available and it is then desirable to attempt to converge to this lower energy state correctly. How this is performed will depend on the tool used. For example, relaxing the constraint of double MO occupancy in a calculation

which results in a singlet being found, may identify the presence of a lower energy triplet for the system.

An example of a wavefunction instability is the use of RHF to calculate the planar allyl radical which results in a phenomenon known as symmetry breaking [93][98]. Symmetry breaking occurs when the wavefunction symmetry differs from the symmetry of the molecular geometry. In the case of the allyl radical, symmetry breaking is caused by the neglect of spin polarisation and results in a wavefunction symmetry of C_s instead of C_{2v}, as with the geometry. This can be seen to produce predictions of a double bond between two carbon atoms and a single electron localised on the third carbon atom in restricted calculations. Spin polarisation is important in this radical because of the presence of a node on the central carbon of the SOMO and also the presence of a pair of π electrons in the subjacent MO which can be easily polarised. Allowing the electrons the flexibility to occupy different spatial co-ordinates via an unrestricted calculation eases the problem with the result being that the unpaired electron is shared between the terminal carbons and the subjacent π system polarised with most electron density at the central carbon. It should be noted that because symmetry breaking occurs as a result of neglecting correlation between electrons of opposing spin, even unrestricted calculations can suffer from it. Unrestricted HF calculations can be shown to contain both some electron correlation and some spin contamination from higher spins, as a result of allowing flexibility in the spatial orbitals of pairs of electrons of opposing spin and from the inclusion of higher spin states to deal with the absence of pure spin states, respectively.

These two effects are in competition with each other. At smaller bond lengths, spin contamination is most important and hence an RHF solution is preferred in order to eliminate it. However, when a bond is stretched, the importance of electron correlation increases rapidly. When the importance of adding electron correlation exceeds the importance of removing the spin contamination, a RHF/UHF instability occurs [19]. It is at this point that a switch from a restricted approach to an unrestricted approach is required. Of course, it may be possible for geometric alterations to a molecule to occur such that the symmetry of the system is broken (as a result of Jahn-Teller effects for example), but if the wavefunction breaks symmetry then this is always considered to be artifactual [98]. Because symmetry breaking results in localisation of electron density, inspection of spin density and detection of spin

contamination can help identify situations where the results of the calculation have been rendered useless by this effect. Under these circumstances, another method for capturing the system must be sought.

1.19 Geometry Optimisation

The earlier discussion on the SCF procedure is focussed on optimising the wavefunction at a particular nuclear geometry. In order to determine properties such as equilibrium bond lengths it is necessary to find the stable nuclear geometries. This is done by identifying stationary points on the nuclear landscape. Two types are of importance in chemical applications. Energy minima represent stable species such as products, reactants and intermediates and first order saddle points represent transition states linking them. In order to find these stationary points, a process called Geometry Optimisation must take place. The nuclear framework is adjusted using analytical or numerical derivatives of the potential energy with respect to nuclear position. These derivatives indicate directions of increasing or reducing gradient. The second derivatives of energy with respect to nuclear position indicate the nature of any stationary points found. For computational purposes these second derivatives are stored in matrix form called the Hessian with eigenvalues of this Hessian indicating a minimum (all positive eigenvalues) or a transition state (a single imaginary eigenvalue with all other eigenvalues positive). At an energy minimum, the gradient will be zero in all directions, the physical interpretation of this being zero unbalanced forces between the atoms. Once an acceptable stationary point is reached, thermodynamic properties can be calculated as described in the next section.

The algorithm for finding stationary points in this work is the Berny algorithm using GEDIIS [99]. Here, energy minima can be found using a number of different methods, all essentially following a downhill energetic slope using the analytical gradients of the energy with respect to nuclear position. GEDIIS is a technique which creates a series of vectors representing different nuclear geometries which are calculated during each step of the optimisation process. The space spanned by these vectors is then searched for a local energy minimum with the new geometry adjusted accordingly to reach this minimum. A new set of geometry vectors is then extrapolated from this

new position and the process is repeated until the forces between the atoms and the displacement of the nuclear geometries between optimisation steps are all below a user-defined threshold which indicates convergence. It is important to recognise that at each geometry step, the wavefunction is re-optimised using the SCF procedure detailed earlier. In this way, the resulting solution represents a stationary point in the nuclear geometry landscape and an optimised wavefunction at that stationary point. In undertaking the optimisation process, the implementation of the Berny algorithm using GEDIIS takes advantage of an ability to overcome shallow potential energy wells combined with smooth and fast convergence near the energy minimum.

1.20 Thermodynamics

Once a local energy minimum is reached, a variety of properties of the system can be determined: an example of which would be thermodynamic properties. This requires accurate frequency analysis to be undertaken involving first and second derivatives of the energy with respect to nuclear position. In order to perform such frequency analyses or to determine free energies, an SCF calculation must be augmented with thermal corrections to account for the fact that the SCF calculations are performed at 0K rather than room temperature. In this work, Gaussian 09d has been the preferred tool and a short discussion of how Gaussian performs these thermal calculations follows [100]. Gaussian employs standard classical statistical thermodynamics approximations to account for thermal corrections to the SCF energy. An ideal gas is assumed, with non-interacting particles. Additionally, all excited electronic states are ignored and assumed to be inaccessible. Thermal corrections for vibration, rotation and translation are therefore deduced from these approximations. The key quantities for the thermal corrections are as shown in equations for entropy 1.152, internal energy 1.153 and heat capacity 1.154.

$$S = R\left[ln(qe) + T\left(\frac{\partial lnq}{\partial T}\right)_V\right] \tag{1.152}$$

$$E = Nk_BT^2\left(\frac{\partial lnq}{\partial T}\right)_V \tag{1.153}$$

$$C_V = \left(\frac{\partial E}{\partial T}\right)_{N,V} \tag{1.154}$$

These three equations are seen to be dependent on the partition function q and can be split down into the relevant contributions from vibration, rotation, electronic and translation contributions. The partition functions are constructed from standard approximation models: particle in a box (translational contributions), rigid rotor (rotational contributions) and simple harmonic oscillator (vibrational contributions).

First the translational contributions are considered. The quantum partition function is shown in equation 1.155 with the consequential translational contributions to entropy, internal energy and heat capacity shown in equations 1.156 1.157 and 1.158 respectively.

$$q_{tr} = \left(\frac{2\pi m k_B T}{h^2}\right)^{3/2} \frac{k_B T}{P} \tag{1.155}$$

$$S_{tr} = R\left(lnq_t + 1 + \frac{3}{2}\right) \tag{1.156}$$

$$E_{tr} = \frac{3}{2}RT \tag{1.157}$$

$$C_{tr} = \frac{3}{2}R \tag{1.158}$$

For the electronic contributions, things are a little easier. Because only the ground state is considered accessible, the partition function is simply the degeneracy of the ground state, g_o. As a result of the temperature independence of this partition function, there are no electronic contributions to either the internal energy or the heat capacity and both of these are zero. The electronic contribution towards the entropy however will not be zero. Equations 1.159 to 1.162 describe the relevant quantities.

$$q_{elec} = g_o \tag{1.159}$$

$$S_{elec} = Rlnq_e \tag{1.160}$$

$$E_{elec} = 0 \tag{1.161}$$

$$C_{elec} = 0 \tag{1.162}$$

For the vibrational contributions, Gaussian takes the bottom of the potential well as the zero of energy rather than the lowest vibrational level. The partition function is a product of contributions from each real vibrational mode, K and is shown in equation 1.163. The corresponding entropy, internal energy and heat capacity values are taken as the sum of contributions from each real vibrational mode and are shown in equations 1.164 to 1.166 where $\Theta_{V,K} = \frac{h\nu_K}{k_B}$ is the characteristic temperature of the vibrational mode.

$$q_{vib} = \Pi_K \left[\frac{e^{-\Theta_{V,K}/2T}}{1 - e^{-\Theta_{V,K}/T}} \right] \tag{1.163}$$

$$S_{vib} = R \sum_K \left[\frac{\Theta_{V,K}/T}{e^{\Theta_{V,K}/T} - 1} - ln\left(1 - e^{-\Theta_{V,K}/T}\right) \right] \tag{1.164}$$

$$E_{vib} = R \sum_K \Theta_{V,K} \left[\frac{1}{2} + \frac{1}{e^{\Theta_{V,K}/T - 1}} \right] \tag{1.165}$$

$$C_{vib} = R \sum_K e^{\Theta_{V,K}/T} \left[\frac{\Theta_{V,K}/T}{e^{-\Theta_{V,K}/T} - 1} \right]^2 \tag{1.166}$$

Finally, the contribution from rotations is considered. These contributions will be heavily dependent on the nature of the atom or molecule. For atoms, the partition function is 1 and consequently there is no temperature dependence at all. Under those circumstances the contributions to both internal energy and heat capacity are both zero. The entropic contribution will also be zero because of the value of the partition function, *ln(1) = 0*. For linear molecules, the values are as shown in equations 1.167 to 1.170 and for polyatomic molecules in general the contributions are as shown in equations 1.171 to 1.174. The parameter σ_r is called the symmetry number

of the molecule and is the number of indistinguishable orientations of the molecule. For example, a heteronuclear diatomic molecule would have one indistinguishable orientation whereas a homonuclear diatomic would have 2. In those circumstances σ_r would take the value 1 or 2 respectively.

$$q_{linearrot} = \frac{1}{\sigma_r}\frac{T}{\Theta_r} \tag{1.167}$$

$$S_{linearrot} = R(lnq_r + 1) \tag{1.168}$$

$$E_{linearrot} = RT \tag{1.169}$$

$$C_{linearrot} = R \tag{1.170}$$

$$q_{polyrot} = \frac{\pi^{1/2}}{\sigma_r}\left[\frac{T^{3/2}}{(\Theta_{r,x}\Theta_{r,y}\Theta_{r,z})^{1/2}}\right] \tag{1.171}$$

$$S_{polyrot} = R(lnq_r + 3/2) \tag{1.172}$$

$$E_{polyrot} = \frac{3}{2}RT \tag{1.173}$$

$$C_{polyrot} = \frac{3}{2}R \tag{1.174}$$

Now that these thermal corrections to entropy, internal energy and heat capacity have been determined, Gaussian then applies them to produce a range of corrected energy values for the calculation. The total thermochemical corrections for energy, enthalpy and Gibbs energy are then calculated as shown in equations 1.175 to 1.177 and can be added to the SCF energy in order to produce either energetically, enthalpic and Gibbs corrected energies for the system as required. It should be noted that in equation 1.177, $S_{corr} = S_{tr} + S_{elec} + S_{vib} + S_{rot}$.

$$E_{tot} = E_{tr} + E_{elec} + E_{vib} + E_{rot} \tag{1.175}$$

$$H_{corr} = E_{tot} + k_B T \tag{1.176}$$

$$G_{corr} = H_{corr} - TS_{corr} \tag{1.177}$$

References

[1] E. Schrodinger, "An Undulatory Theory of the Mechanics of Atoms and Molecules," *Physical Review*, vol. 28, no. 6, pp. 457–484, 1926.

[2] D. B. Cook, *Handbook of Computational Chemistry*. Dover Publications, 2005.

[3] M. Born and J. R. Oppenheimer, "On the Quantum Theory of Molecules (English Translation by S. M. Blinder, Jan 23, 2002)," *Annalen der Physik*, vol. 389, no. 20, pp. 457–484, 1927.

[4] A. Szabo and N. S. Ostlund, *Modern Quantum Chemistry*. pp. 31–38, Dover Publications, 1996.

[5] A. Szabo and N. S. Ostlund, *Modern Quantum Chemistry*. pp. 108–230, Dover Publications, 1996.

[6] C. J. Roothaan, "New Developments in Molecular Orbital Theory," *Reviews of Modern Physics*, vol. 23, no. 2, p. 69, 1951.

[7] C. J. Roothaan, "Self Consistent Field Theory for Open Shells of Electronic Systems," *Reviews of Modern Physics*, vol. 32, pp. 179–185, 1960.

[8] A. Szabo and N. S. Ostlund, *Modern Quantum Chemistry*. pp. 145–146, Dover Publications, 1996.

[9] C. Lanczos, "An Iteration Method for the Solution of the Eigenvalue Problem of Linear Differential and Integral Operators," *Journal of Research of the National Bureau of Standards*, vol. 45, no. 4, pp. 255–282, 1950.

[10] E. R. Davidson, "The Iterative Calculation of a Few of the Lowest Eigenvalues and Corresponding Eigenvectors of Large Real Symmetric Matrices," *Journal of Computational Physics*, vol. 17, no. 87, pp. 87–94, 1975.

[11] B. Liu, *The Simultaneous Expansion Method for the Iterative Solution of Several of the Lowest Eigenvalues and Corresponding Eigenvectors of Large Real-Symmetric Matrices, (Numerical Algorithms in Chemistry: Algebraic Methods)*. LBL-8158, Lawrence Berkley Laboratory, 1978.

[12] R. J. Boyd and C. A. Coulson, "The Fermi Hole in Atoms," *Journal of Physics B: Atomic Molecular Physics*, vol. 7, no. 14, pp. 1805–1816, 1974.

[13] W. Koch and M. C. Holthausen, *A Chemist's Guide to Density Functional Theory*. Wiley-VCH, 2000.

[14] D. Cremer, "Density Functional Theory: Coverage of Dynamic and Non-Dynamic Electron Correlation Effects," *Molecular Physics*, vol. 99, no. 23, pp. 1899–1940, 2001.

[15] P. J. Knowles and N. C. Handy, "A New Determinant-Based Full Configuration Interaction Method," *Chemical Physics Letters*, vol. 111, no. 4,5, pp. 315–321, 1984.

[16] P. J. Knowles and N. C. Handy, "A Determinant Based Full Configuration Interaction Program," *Computer Physics Communications*, vol. 54, pp. 75–83, 1989.

[17] A. Szabo and N. S. Ostlund, *Modern Quantum Chemistry*. pp. 261–265, Dover Publications, 1996.

[18] B. J. Rosenberg, W. C. Ermler, and I. Shavitt, "*Ab Initio* SCF and CI Studies on the Ground State of the Water Molecule. II. Potential Energy and Property Surfaces," *Journal of Chemical Physics*, vol. 65, no. 10, pp. 4072–4080, 1976.

[19] F. Jensen, *Introduction to Computational Chemistry, Second Edition*. Wiley-VCH, 2007.

[20] M. W. Schmidt and M. S. Gordon, "The Construction and Interpretation of MCSCF Wavefunctions," *Annual Review of Physical Chemistry*, vol. 49, pp. 233–266, 1998.

[21] B. O. Roos, P. R. Taylor, and P. E. M. Siegbahn, "A Complete Active Space SCF Method (CASSCF) Using a Density Matrix Formulated Super-CI Approach," *Chemical Physics*, vol. 48, pp. 157–173, 1980.

[22] P. J. Knowles and H. J. Werner, "An Efficient Second Order MCSCF Method for Long Configuration Expansions," *Chemical Physics Letters*, vol. 115, no. 3, pp. 259–267, 1985.

[23] H.-J. Werner and E.-A. Reinsch, "The Self-Consistent Electron Pairs Method for Multi-configuration Reference State Functions," *Journal of Chemical Physics*, vol. 76, no. 6, p. 3144, 1982.

[24] P. J. Knowles and H.-J. Werner, "An Efficient Method for the Evaluation of Coupling Coefficients in Configuration Interaction Calculations," *Chemical Physics Letters*, vol. 145, no. 6, pp. 514–522, 1988.

[25] H.-J. Werner and P. J. Knowles, "An Efficient Internally Contracted Multi-configuration Reference Configuration Interaction Method," *Journal of Chemical Physics*, vol. 89, no. 9, pp. 5803–5814, 1988.

[26] H. J. Werner, P. J. Knowles, G. Knizia, F. R. Manby, and M. Schutz *et al.* , "Molpro, version 2015. 1, a package of *ab initio* programs, see http://www. molpro. net," 2015.

[27] K. Andersson, P. A. Malmqvist, B. O. Roos, A. J. Sadlej, and K. Wolinksi, "Second-order Perturbation Theory with a CASSCF Reference Function," *Journal of Physical Chemistry*, vol. 94, no. 14, pp. 5483–5488, 1990.

[28] C. Angeli, R. Cimiraglia, S. Evangelisti, T. Leininger, and J. P. Malrieu, "Introduction of n-electron Valence States for Multireference Perturbation Theory," *Journal of Chemical Physics*, vol. 114, p. 10252, 2001.

[29] K. R. Shamasundar, G. Knizia, and H. J. Werner, "A New Internally Contracted Multi-reference Configuration Interaction Method," *Journal of Chemical Physics*, vol. 135, p. 054101, 2011.

[30] P. Celani and H. J. Werner, "Multireference Perturbation Theory for Large Restricted and Selected Active Space Reference Wave Functions," *Journal of Chemical Physics*, vol. 112, pp. 5546–5557, 2000.

[31] K. Sivalingam, M. Krupicka, A. Auer, and F. Neese, "Comparison of Fully Internally and Strongly Contracted Multireference Configuration Interaction Procedures," *Journal of Chemical Physics*, vol. 145, p. 054104, 2016.

[32] J. C. Greer, "Estimating Full Configuration Interaction Limits from a Monte Carlo Selection of the Expansion Space," *Journal of Chemical Physics*, vol. 103, no. 5, pp. 1821–1828, 1995.

[33] J. C. Greer, "Monte Carlo Configuration Interaction," *Journal of Computational Physics*, vol. 146, pp. 181–202, 1998.

[34] L. Tong, M. Nolan, T. Cheng, and J. C. Greer, "A Monte Carlo Configuration Generation Computer Program for the Calculation of Electronic States of Atoms, Molecules and Quantum Dots," *Computer Physics Communications*, vol. 131, pp. 142–163, 2000.

[35] J. P. Coe and M. J. Paterson, "Nobel Truncated and Stochastic Approaches to Configuration Interaction," *Recent Research Developments in Chemical Physics*, vol. 6, pp. 41–65, 2012.

[36] J. P. Coe and M. J. Paterson, "Open-Shell Systems Investigated with Monte Carlo Configuration Interaction," *International Journal of Quantum Chemistry*, vol. 116, pp. 1772–1782, 2016.

[37] H. Lischka, R. Shepard, I. Shavitt, M. Pitzer, M. Dallos, and T. Muller *et al.* , "Columbus, An *ab-initio* Electronic Structure Program, Release 5. 9. 2, available at http://www. univie. ac. at/columbus," 2008.

[38] J. P. Coe and M. J. Paterson, "Development of Monte Carlo Configuration Interaction: Natural Orbitals and Second-Order Perturbation Theory," *Journal of Chemical Physics*, vol. 137, p. 204108, 2012.

[39] T. Helgaker and P. R. Taylor, *Gaussian Basis Sets and Molecular Integrals Part 2.* Advanced Series in Physical Chemistry Vol 2, World Scientific Publishing, 1978.

[40] S. F. Boys, " Electronic Wave Functions. I. A General Method of Calculation for the Stationary States of Any Molecular System ," *Proceedings of the Royal Society of London. Series A: Mathematical and Physical Sciences*, vol. A200, pp. 542–554, 1950.

[41] W. J. Hehre, R. F. Stewart, and J. A. Pople, "Self Consistent Molecular Orbital Methods. I. Use of Gaussian Expansions of Slater Type Atomic Orbitals," *Journal of Chemical Physics*, vol. 51, no. 6, pp. 2657–2664, 1969.

[42] W. J. Pietro and W. J. Hehre, "Molecular Orbital Theory of the Properties of Inorganic and Organometallic Compounds. 3. STO-3G Basis Sets for First and Second Row Transition Metals," *Journal of Computational Chemistry*, vol. 4, no. 2, pp. 241–251, 1983.

[43] R. Ditchfield, W. J. Hehre, and J. A. Pople, "Self Consistent Molecular Orbital Methods. IX. An Extended Gaussian Type Basis for Molecular Orbital Studies of Organic Molecules," *Journal of Chemical Physics*, vol. 54, no. 7, pp. 724–728, 1971.

[44] W. J. Hehre, R. Ditchfield, and J. A. Pople, "Self Consistent Molecular Orbital Methods. XII. Further Extensions of Gaussian Type Basis Sets for Use in Molecular Orbital Studies of Organic Molecules," *Journal of Chemical Physics*, vol. 56, no. 5, pp. 2257–2261, 1972.

[45] M. M. Francl, W. J. Pietro, W. J. Hehre, J. S. Binkley, M. S. Head-Gordon, D. J. Defrees, and J. A. Pople, "Self consistent molecular orbital methods. XXIII. A polarization type basis set for second row elements," *Journal of Chemical Physics*, vol. 77, no. 7, pp. 3654–3665, 1982.

[46] V. A. Rassolov, J. A. Pople, M. A. Ratner, and T. L. Windus, "6-31G* basis set for atoms K through Zn," *Journal of Chemical Physics*, vol. 109, no. 4, pp. 1223–1229, 1998.

[47] R. Krishnan, J. S. Binkley, R. Seeger, and J. A. Pople, "Selfconsistent molecular orbital methods. XX. A basis set for correlated wave functions," *Journal of Chemical Physics*, vol. 72, no. 1, pp. 650–654, 1980.

[48] A. D. MacLean and G. S. Chandler, "Selfconsistent molecular orbital methods. XX. A basis set for correlated wave functions," *Journal of Chemical Physics*, vol. 72, no. 10, pp. 5639–5648, 1980.

[49] T. H. Dunning, "Gaussian Basis Sets for use in Correlated Molecular Calculations. I. The Atoms Boron Through Neon and Hydrogen," *Journal of Chemical Physics*, vol. 90, no. 2, pp. 1007–1023, 1989.

[50] R. A. Kendall and T. H. Dunning, "Electron Affinites of the First Row Atoms Revisited. Systematic Basis Sets and Wave Functions," *Journal of Chemical Physics*, vol. 96, no. 9, pp. 6796–6806, 1992.

[51] T. H. Dunning and D. E. Woon, "Gaussian Basis Sets for use in Correlated Molecular Calculations. III. The Atoms Aluminium Through Argon," *Journal of Chemical Physics*, vol. 98, no. 2, pp. 1358–1371, 1993.

[52] K. A. Peterson, D. E. Woon, and T. H. Dunning, "Benchmark Calculations with Correlated Molecular Wave Functions. IV. The Classical Barrier Height of the $H + H_2 \rightarrow H_2 + H$," *Journal of Chemical Physics*, vol. 100, no. 10, pp. 7410–7415, 1994.

[53] M. Dolg, U. Wedig, H. Stoll, and H. Preuss, "Energy-Adjusted *ab initio* Pseudopotentials for the First Row Transition Elements," *Journal of Chemical Physics*, vol. 86, no. 2, pp. 866–872, 1987.

[54] J. Kreutzer, P. Blaha, and U. Schubert, "Assessment of Different Basis Sets and DFT Functionals for the Calculation of Structural Parameters, Vibrational Modes and Ligand Binding Energies of Zr_4O_2(carboxylate)_12 Clusters," *Computational and Theoretical Chemistry*, vol. 1084, pp. 162–168, 2016.

[55] S. F. Boys and F. Bernardi, "Calculation of Small Molecular Interactions by Differences of Separate Total Energies - Some Procedures with Reduced Errors," *Molecular Physics*, vol. 19, pp. 553–566, 1970.

[56] J. A. Pople, M. Head-Gordon, D. J. Fox, K. Raghavachari, and L. A. Curtiss, "Gaussian-1 Theory: A General Procedure for Prediction of Molecular Energies," *Journal of Chemical Physics*, vol. 90, pp. 5622–5629, 1989.

[57] L. A. Curtiss, C. Jones, G. W. Trucks, K. Raghavachari, and J. A. Pople, "Gaussian-1 Theory of Molecular Energies for Second Row Compounds," *Journal of Chemical Physics*, vol. 93, pp. 2537–2545, 1990.

[58] L. A. Curtiss, K. Raghavachari, G. W. Trucks, and J. A. Pople, "Gaussian-2 Theory for Molecular Energies for First and Second Row Compounds," *Journal of Chemical Physics*, vol. 94, pp. 7221–7230, 1991.

[59] L. H. Thomas, "The Calculation of Atomic Fields," *Proceedings of the Cambridge Philosophical Society*, vol. 23, pp. 542–548, 1927.

[60] E. Fermi, "Un Metodo Statistico per la Determinazione di alcune Prioprietà dell'Atomo," *Rendiconti Accademia de Lincei*, vol. 66, pp. 602–607, 1927.

[61] P. A. M. Dirac, "Notes on Exchange Phenomena in the Thomas Atom," *Proceedings of the Cambridge Philosophical Society#*, vol. 26, pp. 376–385, 1930.

[62] P. Hohenberg and W. Kohn, "Inhomogeneous Electron Gas," *Physics Review*, vol. 136, p. B864, 1964.

[63] W. Kohn and L. J. Sham, "Self-Consistent Equations Including Exchange and Correlation Effects," *Physics Review*, vol. 140, p. A1133, 1965.

[64] A. D. Becke, "Perspective: Fifty Years of Density Functional Theory in Chemical Physics," *Journal of Chemical Physics*, vol. 140, p. 18A301, 2014.

[65] R. O. Jones and O. Gunnarsson, "The Density Functional Formalism, its Applications and Prospects," *Reviews of Modern Physics*, vol. 61, no. 3, pp. 689–746, 1989.

[66] A. D. Becke, "Density Functional Exchange Energy Approximation with Correct Asymptotic Behaviour," *Physical Review A*, vol. 38, no. 6, pp. 3098–3100, 1988.

[67] J. Harris, "Adiabatic Connection Approach to Kohn Sham Theory," *Physics Reviews A*, vol. 29, pp. 1648–, 1984.

[68] A. D. Becke, "A New Mixing of Hartree-Fock and Local Density Functional Theories," *Journal of Chemical Physics*, vol. 98, pp. 1372–, 1993.

[69] A. D. Becke, "Density Functional Thermochemistry. III. The Role of Exact Exchange," *Journal of Chemical Physics*, vol. 98, pp. 5648–5652, 1993.

[70] P. J. Stephens, F. J. Devlin, C. F. Chabalowski, and M. J. Frisch, "Ab Initio Calculation of Vibrational Absorption and Circular Dichroism Spectra Using Density Functional Force Fields," *Journal of Physical Chemistry*, vol. 98, no. 45, pp. 11623–11627, 1994.

[71] M. J. Allen and D. J. Tozer, "Helium Dimer Dispersion Forces and Correlation Potentials in Density Functional Theory," *Journal of Chemical Physics#*, vol. 117, no. 24, pp. 11113–11120, 2002.

[72] S. Grimme, "Seemingly Simple Stereoelectronic Effects in Alkane Isomers and the Implications for Kohn–Sham Density Functional Theory," *Angewandte Chemie International Edition*, vol. 45, pp. 4460–4464, 2006.

[73] A. D. Becke, "Density Functional Thermochemistry. I. The Effect of the Exchange-Only Gradient Correction," *Journal of Chemical Physics*, vol. 96, no. 3, pp. 2155–2160, 1992.

[74] C. Lee, W. Yang, and R. G. Parr, "Development of the Colle-Salvetti Correlation Energy Formula into a Functional of the Electron Density," *Physical Review B*, vol. 37, no. 20, pp. 785–789, 1988.

[75] C. Adamo and V. Barone, "Toward Reliable Connection Models Free from Adjustable Parameters," *Chemical Physics Letters*, vol. 274, pp. 242–250, 1997.

[76] S. Grimme, "Semiempirical GGA-type Density Functional Constructed with a Long-Range Dispersion Correction," *Journal of Computational Chemistry*, vol. 274, pp. 1787–1799, 2006.

[77] S. Grimme, S. Ehrlrich, and L. Goerigk, "Effect of the Damping Function in Dispersion Corrected Density Functional Theory," *Journal of Computational Chemistry*, vol. 32, pp. 1456–1465, 2011.

[78] A. D. Becke, "Density-functional thermochemistry. V. Systematic optimization of exchange- correlation functionals," *Journal of Chemical Physics*, vol. 107, pp. 8554–8560, 1997.

[79] S. Grimme, "Accurate Description of van der Waals Complexes by Density Functional Theory Including Empirical Corrections," *Journal of Computational Chemistry*, vol. 25, pp. 1463–1473, 2004.

[80] S. Grimme, J. Antony, S. Ehrlich, and H. Krieg, "A Consistent and accurate *ab-initio* Parameterization of Density Functional Dispersion Correction (DFT-D) for the 94 Elements H-Pu," *Journal of Chemical Physics*, vol. 132, p. 154104, 2010.

[81] A. D. Becke and E. R. Johnson, "Exchange-hole dipole moment and the dispersion interaction," *Journal of Chemical Physics*, vol. 122, p. 154101, 2005.

[82] E. R. Johnson and A. D. Becke, "A post-Hartree–Fock model of intermolecular interactions," *Journal of Chemical Physics*, vol. 123, p. 024101, 2005.

[83] E. R. Johnson and A. D. Becke, "A post-Hartree-Fock model of intermolecular interactions: Inclusion of higher-order corrections," *Journal of Chemical Physics*, vol. 124, p. 174104, 2006.

[84] Y. Zhao and D. G. Truhlar, "A New Local Density Functional for Main Group Thermochemistry, Transition Metal Bonding, Thermochemical Kinetics and Noncovalent Interactions," *Journal of Chemical Physics*, vol. 125, p. 194101, 2006.

[85] Y. Zhao and D. G. Truhlar, "The M06 Suite of Density Functionals for Main Group Thermochemistry, Thermochemical Kinetics, Noncovalent Interactions, Excited States and Transition Elements: Two New Functionals and Systematic Testing of Four M06-class Functionals and 12 Other Functionals," *Theoretical Chemistry Accounts*, vol. 120, pp. 215–241, 2008.

[86] J.-D. Chai and M. Head-Gordon, "Systematic Optimisation of Long-Range Corrected Hybrid Density Functionals," *Journal of Chemical Physics*, vol. 128, p. 084106, 2008.

[87] J.-D. Chai and M. Head-Gordon, "Long-Range Corrected Hybrid Density Functionals with Damped Atom-Atom Dispersion Corrections," *Physical Chemistry Chemical Physics*, vol. 10, pp. 6615–6620, 2008.

[88] T. Yanai, D. P. Tew, and N. C. Handy, "A New Hybrid Exchange-Correlation Functional Using the Coulomb-Attentuating Method (CAM-B3LYP)," *Chemical Physics Letters*, vol. 393, pp. 51–57, 2004.

[89] A. Szabo and N. S. Ostlund, *Modern Quantum Chemistry.* pp. 100–107, Dover Publications, 1996.

[90] R. Pauncz, *Spin Eigenfunctions.* Plenum, New York, 1979.

[91] J. C. Schug and D. H. Phillips, "Spin Contamination in Unrestricted Hartree-Fock Calculations," *Journal of Chemical Physics*, vol. 59, no. 4, pp. 1616–1624, 1973.

[92] F. Sasaki and K. Ohno, "Spin-Component Analysis of Single Determinant Wavefunctions," *Journal of Mathematical Physics*, vol. 4, no. 9, pp. 1140–1147, 1963.

[93] T. Bally and W. T. Borden, *Calculations on Open Shell Molecules: A Beginner's Guide, Reviews in Computational Chemistry*, vol. 13, ch. 1. John Wiley & Son, 1999.

[94] A. J. Cohen, D. J. Tozer, and N. C. Handy, "Evaluation of $\langle S^2 \rangle$ in Density Functional Theory," *Journal of Chemical Physics*, vol. 126, pp. 214104–1–214104–4, 2007.

[95] J. Baker, A. Scheiner, and J. Andzelm, "Spin Contamination in Density Functional Theory," *Chemical Physics Letters*, vol. 216, no. 3-6, pp. 380–388, 1993.

[96] R. Seeger and J. A. Pople, "Self-Consistent Molecular Orbital Methods. XVIII. Constraints and Stability in Hartree-Fock Theory," *Journal of Chemical Physics*, vol. 66, no. 7, pp. 3045–3050, 1977.

[97] R. Bauernschmitt and R. Ahlrichs, "Stability Analysis for Solutions of the Closed Shell Kohm-Sham Equations," *Journal of Chemical Physics*, vol. 104, no. 22, pp. 9047–9052, 1996.

[98] E. R. Davidson and W. T. Borden, "Symmetry Breaking in Polyatomic Molecules: Real and Artifactual," *Journal of Physical Chemistry*, vol. 87, pp. 4783–4792, 1983.

[99] X. Li and M. J. Frisch, "Energy-represented DIIS within a Hybrid Geometry Optimsation Method," *Journal of Chemical Theory and Computation*, vol. 2, pp. 835–839, 2006.

[100] J. W. Ochterski, "Thermochemistry in Gaussian," tech. rep., Gaussian Inc., 2000.

Chapter 2

MCCI - Metal Dimers

2.1 Chapter Abstract

In this chapter, a discussion is presented on the application of the Monte Carlo Configuration Interaction (MCCI) method to a variety of metal dimers in order to establish the efficacy of the technique in correctly describing systems exhibiting multi-reference character. The primary focus of this chapter is the analysis of the ScNi dimer as part of a wider project undertaken by other colleagues which included dimers such as the Sc_2, Cr_2 and Mo_2 systems. Potential energy surfaces are created for ScNi using MCCI and spectroscopic properties are estimated from the resulting curves. Both potential energy surfaces and properties are compared to experimental results and also previous computational studies using other techniques. An attempt is made to quantify the multi-reference nature of the wavefunction and to estimate the most important molecular orbitals in describing the system. The ScNi results are compared and contrasted with the dimers investigated as a part of the wider project.

2.2 Metal Dimer Background

For chemical systems consisting of more than one metal atom, state-of-the-art, multi-reference techniques are often required in order to successfully model the species. Although geometrically simple, there can be great complexity in the electronic structure of these molecules. In the case of transition metal dimers, for example, there are

usually many low lying excited states which results in the system becoming highly multi-reference at many geometries on the potential energy surface. The effect of this is that across the potential energy surface there are many important electron configurations which must be taken into account when attempting to describe the wavefunction at a particular geometry. For example, Hoyer *et al.* [1] describe challenges studying the Fe_2 molecule because predictions of ground and electronic excited states appear to be sensitive to the choice of quantum chemical method. CAS(16,12) with subsequent CASPT2 and MRCI(+Q) calculations predict the ground state for Fe_2 should be $^9\Sigma_g^-$ whilst increasing the active space to CAS(16,15) with subsequent CASPT2 calculations predicting $^7\Delta_u$ as the ground state. DFT with the OPBE exchange-correlation functional also experiences difficulties, predicting $^7\Delta_u$ as the ground state. Compounding the difficulty in predicting the correct ground state, predictions of the potential energy surfaces using NEVPT2 and NEVPT3 show large discontinuities across the surface clearly indicating the extreme difficulties in correctly capturing all of the necessary configurations involved. Other transition metal dimers are known to cause issues such as reported predictions of a double potential well for the ground state of the Cr_2 dimer [2]. It is proposed that the difficulty lies in the presence of a delicate balance between static and dynamic correlation as one progresses across the potential energy surface.

Single reference techniques such as Hartree-Fock theory (HF) and DFT struggle to deal with systems such as these. It is also possible that for heavier transition metals, relativistic effects need to be considered. Ideally a Full Configuration Interaction, (FCI) [3][4], calculation would be performed on the system, but as seen earlier, this can result in configuration vectors which are simply too large for all but the very smallest systems. FCI certainly would not be appropriate for systems involving transition metal dimers, as will be demonstrated. A first attempt to model such systems might then involve CASSCF. CASSCF is capable of recovering some static correlation by performing FCI on a small number of the most important orbitals for the system, but the technique requires prior knowledge of these orbitals. An additional problem is that this technique becomes computationally intractable for more than around 16 electrons and 15 orbitals and therefore is only suitable where a small number of electronic configurations are of importance. CASSCF nevertheless is capable of performing a first attempt at modelling the system. Subsequent capture of

the remaining dynamic correlation can be performed by multi-reference techniques such as Multi-reference Configuration Interaction (MRCI) [5] [6] [7] or perturbative methods such as CASPT2. Again these techniques become computationally infeasible for larger systems and even for smaller systems can result in wavefunctions which contain extremely large numbers of electronic configurations. Monte Carlo Configuration Interaction (MCCI) [8] [9] [10] attempts to resolve these problems and in the process produces highly compact wavefunctions which approximate the FCI solution. It does so by creating a configuration vector and augmenting it with randomly selected electronic configurations from the growing vector and routinely pruning the configurations which prove to be unimportant. This work attempts to gauge how successfully MCCI can balance the requirements for accuracy with the need for a compact wavefunction for metal dimer systems which are known to be challenging systems.

MCCI has been used in several applications. Gyorffy *et al.* [11] applied the technique to calculate a few singlet and triplet excitation energies of a number of small molecules such as CH_2 and H_2O. MCCI results for excitation energies for these molecules showed remarkable accuracy with just a few thousand CSFs, of around a few tenths of an eV compared to the FCI solutions which often required hundreds of millions of configurations. Across the range of molecules tested, results were essentially the same as those obtained using EOM-CCSDT. Ground state potential energies were also explored by Coe *et al.* [12] who investigated dissociation of small molecules such as N_2, F_2, HF and CH_4 and the H_{50} lattice. Ground state potential energy surfaces for systems such as NH_3 inversion and ethylene torsion were also considered with results approaching chemical accuracy in some cases. Following ground state potential energy work, Coe *et al.*[13] then found MCCI useful in finding accurate multipole moments for a variety of molecules such as NO (dipole), N_2 (quadrupole) and CH_4 (octupole) in addition to ionisation potentials for the first row atoms, Na and Mg, which came within 1.2% of the results for FCIQMC [14]. Electron affinities were found to be less accurate though, probably as a result of the small magnitude of these quantities relative to the stochastic noise inherent in a random technique. Coe also augmented the MCCI code to include the calculation of excited states using State Averaging to avoid the problem of root flipping and demonstrated that MCCI gave very good results for molecules such as H_3.

Coe *et al.* [15] developed MCCI to calculate higher order dipole properties up to hyper-polarisabilities of several small molecules including CO, H_4 and HF. Because hyperpolarisabilities require higher order derivatives of energy, excited states are required to calculate properties such as these. MCCI was developed to perform sum of states calculations using a form of state averaging. Essentially FCI-standard results were obtained for the hyperpolarisability of HF using 120 states whilst a result for H_4 using 40 states came to within 97% of the FCI solution. Further extension of the MCCI technique by Coe *et al.* [16] saw the technique developed to determine X-ray emission and absorption energies, with results for a range of molecules such as CO, HCN, HCl and NO, comparable with the more computationally expensive EOM-CCSD technique. Finally, Coe *et al.* [17] successfully undertook positronic wavefunction calculations on a range of atoms and molecules which were combined with positrons, such as positronium hydride, positronium hydroxide and lithium positride, obtaining essentially FCI standard results with a fraction of the space. All of the above used small molecules and atoms from the early part of the periodic table. It is therefore of interest to check whether MCCI is as useful for elucidating the ground state potential energies for transition metal dimers such as ScNi and a discussion of that molecule is now presented.

The thirteen valence electron ScNi early-late transition metal diatomic molecule has historically proven to be a difficult species to characterise in terms of both equilibrium bond length and dissociation energy. This species would therefore appear to be a good candidate on which to test the efficacy of MCCI as a computational technique. The stability of thirteen valence electron species such as ScNi was predicted [18][19] to be as a result of synergic bonding between Sc and Ni with $4s$ electron σ-donation from the Sc atom to Ni augmented with π-back donation from Ni to Sc. This σ-donation from the Sc atom is facilitated by the close proximity of the $4s^2 3d^8$ ground state configuration and the $4s^1 3d^9$ first excited state configuration of the Ni atom. Without this, the σ-donation would be an unimportant contribution to the bonding between the atoms. The π-back donation is facilitated by the virtually empty d orbitals of the Sc atom. In addition to σ and π bonding between the atoms, there is also δ bonding between the $3d_{x^2-y^2}$ and $3d_{xy}$ orbitals of both atoms. The ground state of this species is routinely accepted as $^2\Sigma^+$ after agreement between computational and experimental work [20][21][22][23][24][25][26] with

the single unpaired electron found to be mainly localised on Sc. The bonding can be represented by the molecular orbital configuration $1\sigma^2 2\sigma^2 1\pi^4 1\delta^4 3\sigma^{*1}$ where the 1σ MO was found to be a strongly bound $4s-4s$ interaction, the $2\sigma^2 1\pi^4 1\delta^4$ MOs found to be largely localised on the Ni atom with some delocalisation to the Sc atom and the $3\sigma^{*1}$ containing the unpaired electron found to be the antibonding equivalent of the 1σ MO. It is thought that the strength of the binding comes predominantly from the *d* orbitals with a bond order of around 5.5.

Experimentally, there is no data for either the dissociation energy or equilibrium bond length of ScNi. Arrington *et al.* [22] does however provide details of the vibrational wavenumber $\Delta G_{1/2} = \omega_e = 334.5$ +/- 1.0 cm^{-1} for the ground state (assuming simple harmonic oscillator behaviour at the bottom of the potential energy curve and neglecting anharmonicity). Various computational approaches have been attempted with regard to characterising the ground state of ScNi. Early models used by Miedema *et al.* [23] applied non-*ab initio* methods to a large range of heteronuclear metal dimers. The value of D_o(ScNi) = 3.28 eV is reported. Credence for this value of 3.28 eV was provided by experimental work [22], which indicated that a dissociation energy of D_o(ScNi) > 1.36 eV was expected with a value likely to be greater than 2.0 eV (based on extrapolation from the results of a database of thirteen-valence diatomics such as YNi). No firm experimental value for ScNi currently exists however. Faegri *et al.* [24] used a range of computational techniques to model ScNi including post-Hartree-Fock methods such as CASSCF and MRCI. CASSCF calculations predict R_e = 2.04 Å, whilst the more accurate MRCI calculations predict R_e = 2.13 Å, D_o = 1.55 eV and ω_e = 322 cm^{-1}. Mattar *et al.* [25] used LCAO-LDF techniques to investgate not only the $^2\Sigma^+$ ground state of ScNI, but also the lowest lying excited states A" $^2\Delta$, A' $^2\Pi$, A $^2\Sigma^+$ and B'$^2\Pi$, having shown promise as a technique in the modelling of challenging homonuclear diatomics such as Cr_2, V_2, Mn_2 and Mo_2. Spectroscopic values for the ground state of ScNi are reported as R_e = 2.019 Å, D_o = 5.95 eV and ω_e = 405.9 cm^{-1}. Whilst the value for R_e shows good agreement with Faegri's value of 2.04 Å and 2.13 Å for CASSCF and MRCI respectively, the values of D_o and ω_e are considerably different. The reason for this discrepancy is put down to the known problem of over-binding of the LCAO-LDF method. Of particular interest is the seemingly small energy gaps of around 0.5 eV to 1.5 eV between the ground state and excited states as this may

make it difficult to correctly model the ground state. Additionally, the potential energy surface has only been presented up to just 2.4 Å. Crossing of potential energy surfaces is demonstrated around the equilibrium bond length and it is reasonable to assume that further potential energy surface crossing will happen at long bond lengths as dissociation is approached, causing further computational challenges. It is interesting that Mattar does not report on this. Following the rise in popularity and efficacy of DFT methods, it is not surprising to find reports in the literature of an attempt to apply this technique to metal dimers. Gutsev *et al.* [26] investigated the bonding of ground and excited states of ScNi with emphasis on the nature of the bonding using the BPW91 method with 6-311+G* basis set and natural bond analysis. Findings included $R_e = 2.047$ Å, $D_o = 3.30$ eV and $\omega_e = 349$ cm^{-1}. The value for ω_e in particular is in excellent agreement with Arrington *et al.* [22] whilst the equilibrium bond length is in excellent agreement with the computational findings of Faegri *et al.* [24]. It is worthwhile noting that all of the computational calculations detailed here differ significantly from each other and with no reliable experimental data available, it is not possible to be certain which approach, if any, has resulted in the most accurate measurement for either R_e or ω_e

The series of findings above, with particular regard to low lying excited states and the lack of experimental data, highlight the nature of the challenges facing any computational technique which aims to successfully model the potential energy surface of the ground state for this diatomic molecule.

2.3 Computational Details - Metal Dimer

A detailed discussion of the operation of MCCI was given earlier but a summary is reproduced here for ease of following the work. Version 4 of the MCCI software is used throughout this work [8][27]. MCCI uses as an input, the molecular orbital integrals (both one and two electron) provided from the output of ROHF Molpro [28] calculations on the ScNi dimer using the STO-3G basis set. Basis sets larger than this proved computationally infeasible. These ROHF molecular orbital integrals were then transformed into a CSF within MCCI from the occupied molecular orbitals. Subsequently, this reference CSF was augmented with new CSFs which were formed from random single and double excitations. Each of these excitations

preserved both the spatial and spin symmetry of the reference CSF. In this way a growing vector of CSFs was produced which represented the entire wavefunction of the system. After this stage, the Hamiltonian matrix was constructed in a basis of these CSFs and diagonalised. Subsequent to this, any CSF with an absolute coefficient value below a specified c_{min} value was discarded. This process was repeated until convergence was achieved. Calculations were initially run at convergence values of 10^{-3} before tightening to 5x10^{-4}. c_{min} values were initially set at 5x10^{-4} before being reduced to lower values until a smooth potential energy curve was achieved. In order to measure spectroscopic values correctly, the LEVEL 8.0 program was used [29]. An approximation was made that at the lowest vibrational level, the potential energy surface could be reasonably modelled as a simple harmonic oscillator. This allowed an approximate value of ω_e to be calculated. Because MCCI is a truncated CI method, it suffers from size consistency issues. As a result, D_o is estimated by assuming the full dissociation is converged on at very long bond lengths and estimates are made of that converged value in the course of this work for the ScNi dimer. During this work, a quantitative measure of the multi-reference nature of the ScNi dimer is made using equation 2.1 and 2.2. Here it can be seen that for single reference systems, MR = 0 and for highly multi-reference systems, MR $\rightarrow$ 1.

$$MR = \sum_i |c_i|^2 - |c_i|^4 \tag{2.1}$$

$$\sum_i |c_i|^2 = 1 \tag{2.2}$$

Finally, the important molecular orbitals are estimated from an analysis of the percentage of CSFs in which they appear weighted by the $|c_i|^2$ value for each CSF.

2.3.1 Results and Discussion - Metal Dimer

For ScNi, the point group is C_{2v} for Molpro calculations and the required symmetry of A_1 and doublet spin is enforced in the wavefunction setup. Initially an MCCI convergence threshold of 10^{-3} is used along with c_{min} values of both 5x10^{-4} and 2x10^{-4}. 18 orbitals are frozen (36 electrons) with only the 4s and 3d orbitals and their respective electrons treated as valence for both Sc and Ni atoms in order to

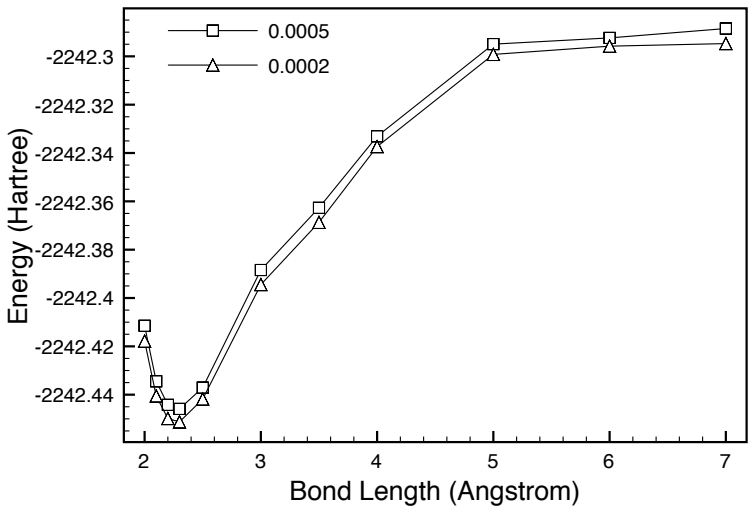

Figure 2.1: MCCI Energies for the ScNi dimer with c_{min} = 5x10^{-4} and c_{min} = 2x10^{-4} against bond length (Å) using the STO-3G basis set with 18 frozen orbitals and 36 frozen electrons.

minimise the computational effort. Single point energy ROHF calculations were made at a variety of internuclear distances from 2.00 Å to 7.00 Å with MCCI calculations subsequently performed at each of these points. In order to initially obtain a smooth ROHF potential energy curve, the wavefunction at 2.50 Å was used as the starting guess for 3.00 Å and the wavefunction at 4.00 Å was used as the starting guess at 3.50 Å. No other manipulations were necessary and all other data points were obtained in isolation from each other. The MCCI potential energy surface produced is shown in figure 2.1.

As can be seen, the reduction of c_{min} has shown very little difference in the potential energy surface. From this data, and subsequent spectroscopic analysis, the following results are reported for the ScNi MCCI calculations: R_e = 2.30 Å, D_o = 4.26 eV and ω_e = 329 cm^{-1} for c_{min} = 5x10^{-4} and R_e = 2.30 Å, D_o = 4.12 eV and ω_e = 309 cm^{-1} for c_{min} = 2x10^{-4}. There is no difference in equilibrium bond length for the tighter c_{min} criterion and a reduction in just 0.14 eV for D_o and a 20 cm^{-1} drop in ω_e. Results are summarised in table 2.1; experimental results are included for comparison.

Equilibrium bond lengths are seen to be slightly higher with MCCI than with MRCI and dissociation energies are around the middle of the range of results reported in the literature to date. In the absence of experimental data however, it is not possible

Table 2.1: ScNi MCCI Results. Calculations use STO-3G basis set and convergence at 10^{-3} Hartrees. Experimental errors are specified in brackets representing +/- that value. Error values listed as (-) indicate that no data was provided.

Property	$c_{min} = 5x10^{-4}$	$c_{min} = 2x10^{-4}$	MRCI	Experiment
R_e (Å)	2.30	2.30	2.13	-
Vib. ω_e (cm^{-1})	329	309	322	334.5(1)
D_o (eV)	4.26	4.12	1.55	>1.36(-)
Avg. Num MCCI CSFs	$7x10^3$	$2x10^4$	-	-
Num FCI SDs	10^8	10^8	-	-
Approx. Fraction	10^{-5}	10^{-4}	-	-
Num Important MOs	14	14	-	-

to be certain which technique is the most reliable. Of interest is that MCCI can obtain results which are very close to MRCI results for R_e and ω_e despite using a minimal basis set such as STO-3G. The ω_e results are in particularly good agreement with experiment and MRCI. In addition to the use of a minimal basis set, MCCI also obtains these results with, on average, only a fraction of the configuration space compared to the FCI solution. Nevertheless, the nature of the basis set used in this work means that results should be treated with caution.

The number of CSFs used across the potential energy surface is shown in figure 2.2.

This figure captures the main multi-reference characteristics across the potential energy surface of the ScNi dimer. As can be seen, the general trend is towards lower numbers of CSFs as the bond length is increased from equilibrium but with a spike around 3.00 Å for both values of c_{min}. When looking at the MR graph, which forms the inset in figure 2.2, this coincides with a peak in multi-reference character at the same bond length. Otherwise the CSF and MR curves would appear not to be particularly well correlated. Although the number of CSFs changes across the potential energy surface, the MR value indicates that the system is highly multi-reference across the range of bond lengths and is well above 0.9 in all cases. As a result, the difficulty for single reference methods in modelling systems such as the ScNi dimer is laid bare. Because of the multi-reference nature of the dimer, the importance of the CSF representing the original ROHF reference for the calculation drops away

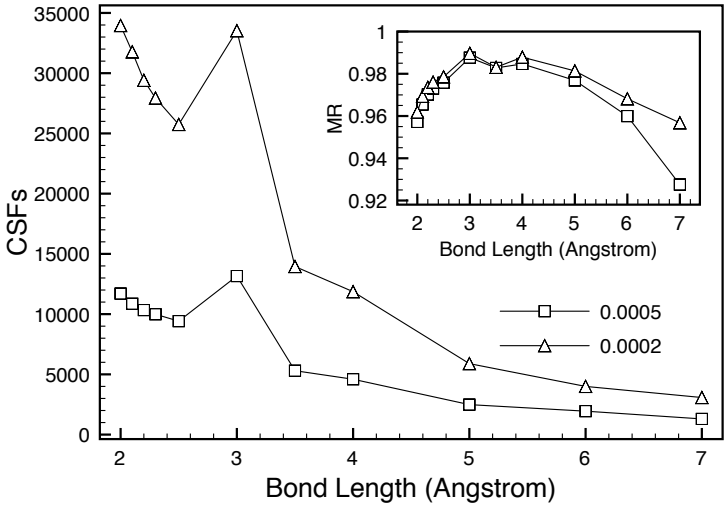

Figure 2.2: Number of CSFs at convergence for the MCCI wavefunction across the potential energy surface of ScNi with c_{min} = 5x10^{-4} and c_{min} = 2x10^{-4} using the STO-3G basis set with 18 frozen orbitals and 36 frozen electrons. Inset is the MR calculated result across the potential energy surface.

from 15% of the final wavefunction at bond lengths of 2.00 Å to zero at 3.50 Å. At the same time, single, double, triple and quadruple excited electron configurations take on significant importance, rising up 80% of the wavefunction across the same range as the importance of the ROHF reference drops away. Single reference methods which do not adequately capture this behaviour will over-emphasise the importance of the ROHF wavefunction and thus underestimate the value of R_e at equilibrium. Indeed, as described above, Faegri discovered a move towards longer equilibrium bond lengths when using MRCI compared to DFT calculations. It is reasonable to conclude therefore that the DFT results, and possibly also the CASSCF results, for R_e are underestimated. As already stated however, the use of a minimal basis set and the lack of experimental data means that conclusive statements cannot be made regarding whether MCCI is performing better than these two methods.

Analysis of the importance of the seven occupied active orbitals for ScNi was undertaken across the potential energy surface. All of these orbitals were shown to be of importance at all bond lengths. Seven other virtual orbitals are shown to also be of importance across the range of bond lengths and thus it is found that 14 orbitals are required in total. Further analysis of these orbitals could help to guide towards a more appropriate active space for CASSCF calculations which may eventually lead to an improved MRCI solution. By this method, the problem of prior knowledge of

Table 2.2: Comparison of dimer spectroscopic results at the lowest c_{min} value used for each species. Equilibrium bond lengths, ground state vibrational frequencies and zero-point energy corrected dissociation energies are provided. Experimental results are provided for comparison. Vibrational frequencies in cm^{-1}, bond lengths in (Å) and energies in eV. Experimental errors are specified in brackets representing +/- that value. Error values listed as (-) indicate that no data was provided.

Dimer	Basis	R_e	Vib. Freq.	D_o
Cr_2	cc-pVDZ	1.70	490	1.22
	cc-pVTZ	1.65	530	2.32
	Exp.	1.6788(-)	480.6(0.5)	1.53(0.06)
Sc_2	cc-pVDZ	2.7	216	2.09
	cc-pVTZ	2.7	222	2.02
	Exp.	-	239.9(-)	1.12(0.22)
Mo_2	STO-3G	1.9	467	6.40
	LANL2DZ	2.1	253	1.73
	Stuttgart	2.05	338	1.65
	Exp.	1.940(0.009)	449.1(0.2)	4.474(0.009)
ScNi	STO-3G	2.3	309	4.12
	Exp.	-	334.5(1.0)	>1.36(-)

the important orbitals which causes issues in CASSCF calculations could be avoided.

There is one final point to note regarding the use of the STO-3G basis set. Attempts to use 3-21G, cc-pVDZ and cc-pVTZ were made. All attempts to produce smooth potential energy curves with these basis sets failed. This was partly due to ROHF convergence issues and partly due to the size of the configuration space being 10^{13}, 10^{17} and 10^{20} respectively despite freezing 18 orbitals. For this reason, only STO-3G allowed any analysis of ScNi using MCCI.

Tables 2.2 and 2.3 provide a comparison of ScNi with the remaining dimers analysed by other colleagues within the wider context of this project. MCCI does appear to give reasonable results for predictions for the equilibrium bond lengths of the molecules studied. The technique has considerably more difficulty predicting dissociation energies. For all molecules with the exception of Mo_2, vibrational fre-

Table 2.3: Comparison of dimer multi-configuration features. Average number of CSFs, and the fraction of FCI space used are compared.

Dimer	Basis	MCCI CSFs	FCI SDs	Fraction
Cr_2	cc-pVDZ	1.2 x 10^5	10^{15}	10^{-10}
	cc-pVTZ	1.2 x 10^5	10^{18}	10^{-13}
Sc_2	cc-pVDZ	4.3 x 10^4	4 x 10^{10}	10^{-6}
	cc-pVTZ	5.1 x 10^4	3 x 10^{12}	10^{-8}
Mo_2	STO-3G	1.3 x 10^4	4 x 10^7	10^{-4}
	LANL2DZ	2.7 x 10^4	10^{11}	10^{-7}
	Stuttgart	2.7 x 10^4	7 x 10^{14}	10^{-11}
ScNi	STO-3G	2 x 10^4	10^8	10^{-4}

quencies are in good agreement with experiment. For all of these results however it should be borne in mind that the fraction of the FCI space being used to make these predictions is extremely small in all cases as shown in table 2.3.

As can be seen, ScNi represents a considerably more difficult system than the homonuclear diatomic molecules: the latter capable of being calculated using up to triple zeta basis sets. Two reasons are proposed for this. The homonuclear diatomic molecules are likely to be able to take computational advantage of symmetry in the molecule to reduce the numbers of configurations required to produce a smooth potential energy curve at comparable basis sets. Secondly, in order to obtain a smooth potential energy curve for the particular basis set, the c_{min} value must be lowered to an appropriate amount to cover all points along the surface. Failure to do this results in discontinuities in the surface. ScNi was found to suffer from these problems even at basis sets such as 3-21G. The level of c_{min} required was too low to be computationally viable. It is likely then that the current limit of MCCI in terms of use for transition metal dimers rests with homonuclear diatomic molecules.

2.4 Summary and Conclusions - Metal Dimer

Despite the use of a minimal basis set, MCCI showed reasonable performance during the calculations of various properties of the ScNi dimer. In particular, the

equilibrium bond length compared reasonably well against MRCI calculations and ω_e values were very close to experimental values. MCCI produces these results with a very compact wavefunction compared to more computationally expensive techniques. Further analysis of the wavefunction shows that MCCI holds potential for the elucidation of the important orbitals required for a better specification of the active space of subsequent CASSCF calculations without requiring prior knowledge of those orbitals.

References

[1] C. E. Hoyer, G. L. Manni, D. G. Truhlar, and L. Gagliardi, "Controversial Electronic Structures and Energies of Fe_2, Fe_2^+ and Fe_2^- Resolved by RASPT2 Calculations," *Journal of Chemical Physics*, vol. 141, p. 204309, 2014.

[2] J. P. Coe, P. Murphy, and M. J. Paterson, "Applying Monte Carlo Configuration Interaction to Transition Metal Dimers: Exploring the Balance Between Static and Dynamic Correlation," *Chemical Physics Letters*, vol. 604, pp. 46–52, 2014.

[3] P. J. Knowles and N. C. Handy, "A New Determinant-Based Full Configuration Interaction Method," *Chemical Physics Letters*, vol. 111, no. 4,5, pp. 315–321, 1984.

[4] P. J. Knowles and N. C. Handy, "A Determinant Based Full Configuration Interaction Program," *Computer Physics Communications*, vol. 54, pp. 75–83, 1989.

[5] H.-J. Werner and E.-A. Reinsch, "The Self-Consistent Electron Pairs Method for Multi-configuration Reference State Functions," *Journal of Chemical Physics*, vol. 76, no. 6, pp. 3144–, 1982.

[6] P. J. Knowles and H.-J. Werner, "An Efficient Method for the Evaluation of Coupling Coefficients in Configuration Interaction Calculations," *Chemical Physics Letters*, vol. 145, no. 6, 1988.

[7] H.-J. Werner and P. J. Knowles, "An Efficient Internally Contracted Multi-configuration Reference Configuration Interaction Method," *Journal of Chemical Physics*, vol. 89, no. 9, 1988.

[8] J. C. Greer, "Estimating Full Configuration Interaction Limits from a Monte Carlo Selection of the Expansion Space," *Journal of Chemical Physics*, vol. 103, no. 5, pp. 1821–1828, 1995.

[9] J. C. Greer, "Monte Carlo Configuration Interaction," *Journal of Computational Physics*, vol. 146, pp. 181–202, 1998.

[10] L. Tong, M. Nolan, T. Cheng, and J. C. Greer, "A Monte Carlo Configuration Generation Computer Program for the Calculation of Electronic States of Atoms, Molecules and Quantum Dots," *Computer Physics Communications*, vol. 131, pp. 142–163, 2000.

[11] W. Gyorffy, R. J. Bartlett, and J. C. Greer, "Monte Carlo configuration interaction predictions for the electronic spectra of Ne, CH2, C2, N2, and H2O compared to full configuration interaction calculations. ," *Journal of Chemical Physics*, vol. 129, p. 064103, 2008.

[12] J. P. Coe, D. J. Taylor, and M. J. Paterson, " Calculations of potential energy surfaces using Monte Carlo configuration interaction ," *Journal of Chemical Physics*, vol. 137, p. 194111, 2012.

[13] J. P. Coe, D. J. Taylor, and M. J. Paterson, "Monte Carlo configuration interaction applied to multipole moments, ionisation energies and electron affinities. ," *Journal of Computational Physics*, vol. 34, pp. 1083–1093, 2013.

[14] G. H. Booth, A. J. W. Thom, and A. Alavi, "Fermion Monte Carlo without fixed nodes: a Game of Life, death and annihilation in Slater Determinant space," *Journal of Chemical Physics*, vol. 131, p. 054106, 2009.

[15] J. P. Coe and M. J. Paterson, "Approaching Exact Hyperpolarisabilities via Sum-Over-States Monte Carlo Configuration Interaction," *Journal of Chemical Physics*, vol. 141, no. 12, p. 124118, 2014.

[16] J. P. Coe and M. J. Paterson, "Multireference X-ray Emission and Absorption Spectroscopy Calculations from Monte Carlo Configuration Interaction," *Theoretical Chemistry Accounts*, vol. 134, p. 58, 2015.

[17] J. P. Coe and M. J. Paterson, "Positronic Molecule Calculations Using Monte Carlo Configuration Interaction," *Chemical Physics Letters*, vol. 645, pp. 106–111, 2016.

[18] N. Engel, "Bonding in transition metals and alloys," *Acta Metallica*, vol. 15, pp. 557–560, 1967.

[19] L. Brewer, "A most striking confirmation of the Engel metallic correlation ," *Acta Metallica*, vol. 15, pp. 553–556, 1967.

[20] R. J. V. Zee and W. Weltner, "ScNi and TiCo Molecules," *High Temperature Science*, pp. 181–191, 1984.

[21] R. J. V. Zee and W. Weltner, "Isovalent transition metal diatomic molecules: ScNi, ScPd, YNi, YPd," *Chemical Physics Letters*, vol. 150, no. 3,4, pp. 329–333, 1988.

[22] C. A. Arrington and M. D. Morse, "Spectroscopy of mixed early–late transition metal diatomics: ScNi, YPd, and ZrCo," *Journal of Chemical Physics*, vol. 102, no. 5, pp. 1895–1904, 1995.

[23] A. Miedema, "Model Predictions of the Dissociation Energies of Homonuclear and Heteronuclear Diatomic Molecules of Two Transition Metals," *Faraday Symposium Chemical Society*, vol. 14, pp. 136–148, 1980.

[24] K. Faegri and C. W. Bauschlicher, "Heteronuclear transition metal diatomics: The bonding and electronic structure of ScNi, YNi, ScPd, and YPd," *Journal of Chemical Physics*, vol. 153, pp. 399–408, 1991.

[25] S. M. Mattar and W. D. Hamilton, "Electronic structure, bonding, geometry, and some spectroscopic properties of the scandium-nickel molecule," *Journal of Physical Chemistry*, vol. 96, pp. 8277–8282, 1992.

[26] G. L. Gutsev, P. Jena, B. K. Rao, and S. N. Khanna, "Electronic structure and chemical bonding of 3d-metal dimers ScX, X= Sc-Zn," *Journal of Chemical Physics*, vol. 114, no. 24, pp. 10738–10748, 2001.

[27] L. Tong, M. Nolan, T. Cheng, and J. C. Greer, "A Monte Carlo configuration generation computer program for the calculation of electronic states of atoms,

molecules, and quantum dots," *Computer Physics Communications*, vol. 131, pp. 142–, 2000.

[28] H. J. Werner, P. J. Knowles, G. Knizia, F. R. Manby, and M. Schutz *et al.* , "Molpro, version 2012. 1, a package of *ab initio* programs, see http://www. molpro. net," 2012.

[29] R. J. L. Roy, "Level 8. 0: A computer program for solving the radial Schrodinger equation for bound and quasibound levels, see http://leroy. uwaterloo. ca/programs," 2008.

Chapter 3

Development of Spin-Orbit Coupling for Stochastic Configuration Interaction Techniques

3.1 Chapter Abstract

In this chapter a discussion is presented of the application of MCCI to the prediction of the effect of spin-orbit coupling on the lowest degenerate energy states of a variety of small atoms and molecules: B, C, O, F, S, Si, Cl, OH, CN, C_2 and NO. Spin-orbit coupling is shown to remove the degeneracy of these ground states and quantitative measurements of this were attempted. In order to achieve this, the MCCI software has been modified to accept spin-orbit coupling integrals from the Molpro program and to subsequently compute spin-orbit coupling matrix elements, using direct methods, in the basis of degenerate states. Software was also developed to allow the translation of the spin-orbit coupling integrals from Molpro format into a format suitable for MCCI for all Abelian subgroups. Details of the software development required for both tasks are provided along with details of how to perform the calculations in a stepwise procedure, followed by a discussion of the results from the MCCI calculations themselves.

3.2 Spin-Orbit Coupling Theory

A bound electron in an atom will exhibit two forms of angular momentum. The first is orbital angular momentum and relates to the angular motion of the negatively charged electron in the vicinity of the nucleus. This orbital angular momentum gives rise to a magnetic dipole moment. Classically [1], this magnetic moment can be understood to be derived from a charge moving in a circle, as shown in figure 3.1 although in reality, the electron is not orbiting the nucleus in a classical manner. Assuming the electron orbits in a perfect circle at radius r, the distance travelled in one circuit will be $s = 2\pi r$ and the time to complete this circuit will be $t = s/v = 2\pi r/v$. The current flowing will be the amount of charge, $-e$, per unit time: i.e. $I = -e/t = -ev/2\pi r$. The magnetic moment generated by this current is then given by equation 3.1, where A is the area enclosed by the orbit, πr^2. Therefore, $m = -evr/2$. In vector form, the angular momentum is defined by the cross product of the displacement and the linear momentum vectors as shown in equation 3.2, with linear momentum defined as $\vec{p} = m_e\vec{v}$. Substituting this into equation 3.2, leads to definition of the induced magnetic dipole moment shown by equation 3.3. The convention is to express this magnetic dipole moment in component form in the direction z and converting to quantum mechanical form by recognising that l_z is quantised as $l_z = m_l\hbar$, equation 3.4 results for the magnetic dipole moment due to orbital angular momentum. Here m_l can take integer values $l \rightarrow -l$. The second form of angular momentum is spin angular momentum. Because it has no classical equivalent, the magnetic moment deriving from spin angular momentum is presented here as equation 3.5 where m_s can take values of $+\frac{1}{2}$ and $-\frac{1}{2}$. Notice that the direction of the magnetic moment is opposite that of the angular momentum in both cases.

$$m = IA \tag{3.1}$$

$$\vec{l} = \vec{r} \times \vec{p} \tag{3.2}$$

$$\vec{m} = (-e/2m_e)\vec{l} \tag{3.3}$$

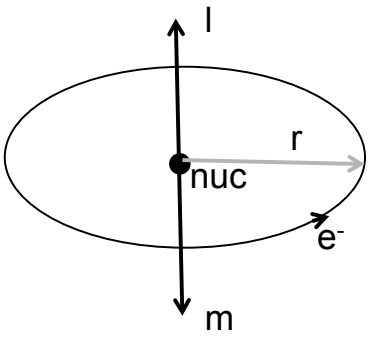

Figure 3.1: An electron orbiting a nucleus at radius r, induces a magnetic dipole moment at the nucleus. This magnetic dipole moment induces a magnetic field which is detected at the electron and interacts with the electron's spin magnetic dipole moment.

$$m_z(orb) = -\left(\frac{e}{2m_e}\right)m_l\hbar \tag{3.4}$$

$$m_z(spin) = -g_e\left(\frac{e}{2m_e}\right)m_s\hbar \tag{3.5}$$

The orbital magnetic dipole moment can be considered as a tiny bar magnet. As such a magnetic field is induced. The spin magnetic moment of the electron is able to energetically interact with this magnetic field (spin-orbit interaction).

Having described the source of the spin and orbital magnetic moments from classical arguments, it is now time to consider the impact of spin-orbit coupling on the electronic state. It is clear that in order for the spin and orbital angular magnetic moments to interact, both must be present. For that to happen, the electronic state in question must have the necessary non-zero spin and orbital angular momentum. To illustrate this, the ^3P ground state of the carbon atom is considered, with spin angular momentum $S = 1$ and orbital angular momentum $L = 1$. Using the Russell-Saunders coupling scheme, these angular momenta can align either in parallel or in opposite directions to give the resultant overall angular momentum J where $J = L + S$ or $J = L - S$ for the parallel and anti-parallel arrangements respectively. Alternatively, one electron can align parallel with the orbital angular momentum and the other anti-parallel to give the resultant overall angular momentum J where $J = L + S - 1$ as shown in figure 3.2. The differing alignment of

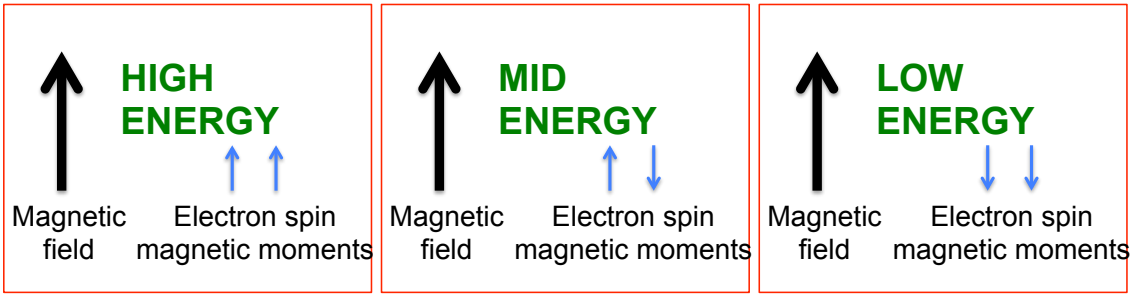

Figure 3.2: The set of permutations of alignment between orbital angular momentum and spin angular momentum vectors for the C atom. In the ^3P ground state, only the spin angular momenta of the two p electrons interact with the orbital angular momentum

the corresponding magnetic moments causes a difference in interaction energy between the three arrangements and this is the source of the spin-orbit coupling effect. Without this spin-orbit coupling effect, there would be no interaction between the magnetic momenta and all three of these relative orientations would be energetically degenerate. Therefore, spin-orbit coupling removes any degeneracy in the affected electronic state. This is shown in figure 3.3.

In order to proceed further, the fully relativistic Dirac equation, equation 3.6 [2], shown in time independent form in the presence of an electric field but in the absence of a magnetic field, normally replaces the Schrödinger Equation. Here c is the speed of light, $\hat{\alpha}$ and $\hat{\beta}$ are four component matrices shown in equations 3.7 and 3.8 and $\hat{V}$ is the external potential provided by the nuclear framework. In equation 3.7, $\hat{\sigma}_{x,y,z}$, refers to the Pauli spin matrices shown in equations 3.9, 3.10 and 3.11. In equation 3.8, I is the two by two unit matrix.

$$[c\hat{\alpha} \cdot \hat{p} + \hat{\beta}mc^2 + \hat{V}]\Psi = E\Psi \tag{3.6}$$

$$\hat{\alpha} = \begin{pmatrix} 0 & \hat{\sigma}_{x,y,z} \\ \hat{\sigma}_{x,y,z} & 0 \end{pmatrix} \tag{3.7}$$

$$\hat{\beta} = \begin{pmatrix} I & 0 \\ 0 & -I \end{pmatrix} \tag{3.8}$$

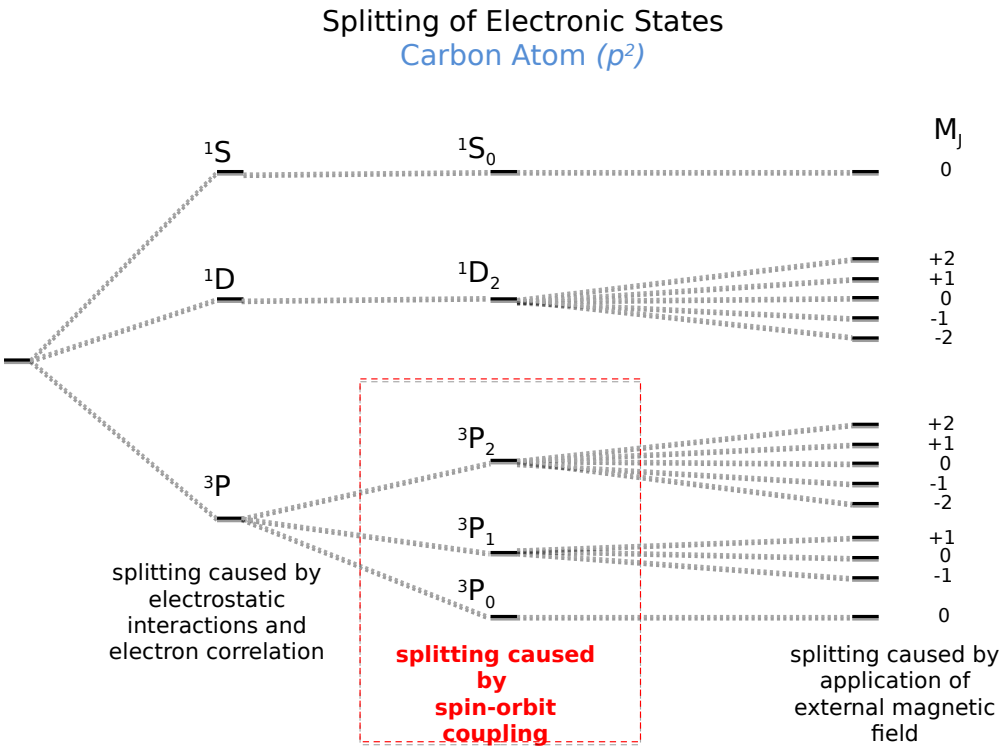

Figure 3.3: Diagram showing the removal of degeneracy of the ^3P ground state of the C atom. Spin-orbit coupling splits this state into three different energy levels according to the value of total angular momentum J. Further application of a magnetic field fully resolves these J levels into the respective M_J levels but this latter effect is not considered further in this work.

$$\hat{\sigma}_x = \begin{pmatrix} 0 & 1 \\ 1 & 0 \end{pmatrix} \tag{3.9}$$

$$\hat{\sigma}_y = \begin{pmatrix} 0 & -i \\ i & 0 \end{pmatrix} \tag{3.10}$$

$$\hat{\sigma}_z = \begin{pmatrix} 1 & 0 \\ 0 & -1 \end{pmatrix} \tag{3.11}$$

The wavefunction solutions to the Dirac equation turn out to be four component spinors which describe both electronic and positronic states: positronic states being identified as a continuum of negative energy states [2]. The wavefunction is split into large and small components, Ψ_L and Ψ_S, with each of these further split into α and β spins. The large components are associated with electronic solutions and the small components with positronic solutions. Ignoring the different spin parts, the Dirac equation can be factored into large and small wavefunction parts as shown in equation 3.12 and 3.13.

$$c(\hat{\sigma} \cdot \hat{p})\Psi_S + (mc^2 + V)\Psi_L = E\Psi_L \tag{3.12}$$

$$c(\hat{\sigma} \cdot \hat{p})\Psi_L - (mc^2 - V)\Psi_S = E\Psi_S \tag{3.13}$$

Solving for Ψ_S in equation 3.13 and substituting into equation 3.12, reveals equation 3.14 where K is defined in equation 3.15. Here the desired two component electronic part of the wavefunction has been separated out from the positronic part and it is now possible to continue the discussion without further reference to the positronic components.

$$\left[K\frac{(\hat{\sigma} \cdot \hat{p})^2}{2m} + \hat{V}\right]\Psi = E\Psi \tag{3.14}$$

$$K = \left(1 + \frac{E - V}{2mc^2}\right)^{-1} \tag{3.15}$$

In the non-relativistic case where $c \to \infty$ and $K \to 1$. equation 3.14 collapses to the non-relativistic Schrödinger equation. Otherwise, K can be approximated by a Taylor expansion as shown in equation 3.16

$$K = 1 - \frac{E - V}{2mc^2} \tag{3.16}$$

In the Dirac equation, there is the problem of the interaction term, V, representing electron-electron repulsion and electron-nuclear attraction. This interaction occurs instantaneously and therefore violates the limit of the speed of light. A retardation correction from quantum electrodynamics is therefore introduced in order to correct for this. Introducing this into the Dirac equation results in problems because the equation for the potential energy cannot be described in closed form and there is no accepted way of resolving this issue. Fortunately, approximations can be made as a series in 1/c. Including the effects of electric fields produced by the nuclear framework and magnetic fields produced by the movement of electrons, converting the linear momentum $\hat{p}$ to a more generalised momentum operator which interacts with the magnetic field and quantum electrodynamics corrections approximated up to $1/c^2$, a series of corrective terms are produced, the leading terms of which form the Breit-Pauli approximation which will be described shortly. If the relativistic effects are a small part of the overall energy of the chemical system, these terms can be included in the non-relativistic Hamiltonian as a perturbation [3]. Compared to the difference in energy between electronic states (*ca.* 10,000 cm^{-1}), spin-orbit coupling energies are in the order of 1-1000 cm^{-1} for systems including atoms from the top of the periodic table and so for the first three rows of the periodic table a perturbative treatment is justified. This simplifies matters computationally because perturbative modifications can be made to standard non-relativistic software codes. The first order correction can be represented as the expectation of the perturbation operator acting on the ground state wavefunction, represented in general by equation 3.17 where Φ_o is the ground state wavefunction, $\hat{P}$ is the perturbation operator and E_1 is the first order correction for the perturbation which acts on the ground state wavefunction. In this work, the perturbation operator is the Breit-Pauli Hamiltonian, $\mathcal{H}^{so}$. Equation 3.17 can then be restated more specifically as in equation 3.18.

$$E_1 = \langle \Phi_o | \hat{P} | \Phi_o \rangle \tag{3.17}$$

$$E_{so} = \langle \Phi_o | \mathcal{H}^{so} | \Phi_o \rangle \tag{3.18}$$

For spin-orbit coupling, first order degenerate perturbation theory must be used and therefore the wavefunction in equation 3.18 must be expressed in the basis of a linear combination of all of the degenerate states to prevent singularities in the first order correction to the wavefunction and zero first order correction to the energy due to symmetry as the spin-orbit coupling operator is not totally symmetric for the point group. As stated earlier, only the leading contributions to the spin-orbit coupling interaction are considered in this work and the relevant terms of the Breit-Pauli Hamiltonian [2][4][5] described as shown in equations 3.19, 3.20, 3.21 and 3.22 are used, where atomic units are used throughout. Other corrections for effects such as spin-spin, orbit-orbit, mass-velocity and Darwin terms are omitted as they are considerably smaller than the terms in this work and thus considered negligible.

$$\mathcal{H}^{so} = \mathcal{H}^{so}_{ne} + \mathcal{H}^{so}_{ee} + \mathcal{H}^{soo}_{ee} \tag{3.19}$$

$$\mathcal{H}^{so}_{ne} = \frac{1}{2c^2} \sum_{i=1}^{N_{elec}} \sum_{A=1}^{N_{nuc}} Z_A \frac{\hat{s}_i \cdot (\hat{r}_{iA} \times \hat{p}_i)}{r^3_{iA}} \tag{3.20}$$

$$\mathcal{H}^{so}_{ee} = -\frac{1}{2c^2} \sum_{i=1}^{N_{elec}} \sum_{j \neq i}^{N_{elec}} \frac{\hat{s}_i \cdot (\hat{r}_{ij} \times \hat{p}_i)}{r^3_{ij}} \tag{3.21}$$

$$\mathcal{H}^{soo}_{ee} = -\frac{1}{c^2} \sum_{i=1}^{N_{elec}} \sum_{j \neq i}^{N_{elec}} \frac{\hat{s}_i \cdot (\hat{r}_{ij} \times \hat{p}_j)}{r^3_{ij}} \tag{3.22}$$

Here $\mathcal{H}^{so}_{ne}$ is the one-electron operator which captures the interaction between the spin of an electron and its orbital angular momentum around the nuclei. $\mathcal{H}^{so}_{ee}$ is the two-electron operator which captures the interaction between the spin of an electron and the magnetic field induced by the movement of itself as it moves around other electrons. $\mathcal{H}^{soo}_{ee}$ is the two-electron operator which captures the interaction between the spin of an electron and magnetic field induced by the movement of the other

electrons around it. The first of these three interactions has the most significant impact and the other two terms can sometimes be neglected. The larger the system, the smaller the effect of including these two-electron terms and in this work, only the first term $\mathcal{H}_{ne}^{so}$ is considered.

3.3 Spin-Orbit Coupling Background

Spin-orbit coupling effects play a vital role in a range of applications from the removal of degeneracy of energy levels to phosphorescence in living animals through intersystem crossings. When electronic excited states are close in energy to the ground state, spin-orbit coupling of these states can allow chemical reactions to proceed through these excited states when normal thermal processes would not allow such a reaction [6]. Exact calculation of spin-orbit effects involves solving the fully relativistic Dirac equation shown in equation 3.6. This proves cumbersome computationally and efforts to find solutions to this problem rely on using the Breit-Pauli Hamiltonian which approximates these effects shown in equations 3.19, 3.20, 3.21 and 3.22.

Blume *et al.* [7][8] modified the Breit-Pauli Hamiltonian to derive four components from HF Theory with the aim of allowing more accurate predictions of the spin-orbit coupling constant for a range of atoms with 2p, 3p and 3d valence electrons than had been hitherto possible. These four components are as follows: a one electron interaction between the spin and the potential provided by the nuclear framework, a two electron interaction between the electron spin and the potential due to movement of the other electrons, a two electron term for the interaction between the spin of each electron and the field due to its own movement and finally a two electron term for the interaction between the spins of pairs of electrons. It was found that the interaction between the unpaired electrons and the core electrons was an effective one-particle spin-orbit interaction which caused screening of the nucleus from the electrons, reducing the spin-orbit coupling constant. The value of the spin-orbit coupling constant was found by diagonalising the Hamiltonian matrix in the basis of the Hartree-Fock wavefunction. Good agreement with experiment was found in most cases. In particular, results of the spin-orbit coupling constant were obtained with an average error of around 6.11% from experiment for B(^2P): 9.74 cm^{-1} ,

C(^3P): 13.4 cm^{-1}, O(^3P): -79.6 cm^{-1}, F(^2P): -265 cm^{-1}, Si(^3P): 64.0 cm^{-1}, S(^3P): -184 cm^{-1}, and Cl(^2P): -545 cm^{-1}.

In much the same way that Slater developed general rules for solving matrix elements involving the standard energetic Hamiltonian [9], Cooper and McWeeny [10] developed an analogous set of rules for spin coupled functions including the terms present in the Breit-Pauli Hamiltonian. These rules are general in the sense that they do not depend on the nature of the wavefunction. This approach was found to significantly ease the computational effort involved in more complicated systems including those where excited electron configurations are involved.

Walker *et al.* [11] used the Breit-Pauli Hamiltonian described by Blume *et al.* [7][8] earlier and applied this to hydrides of the first row of the period table and other small molecules such as BO and CO. For molecules such as CO where there was more equality between the masses of the atoms, the two electron integrals were more important but the team still found that good results could be achieved by ignoring them. Again, the two electron integral terms were interpreted as providing shielding of the valence electrons from the core. For OH, the spin-orbit coupling constant was found to be -141.4 cm^{-1}.

Cooper *et al.* [12] used fully relativistic calculations on first and second row atoms in order to compare the accuracy of the Breit-Pauli Hamiltonian. A technique called Multi-Configuration Dirac-Fock-Extended Average Level (MCDF-EAL) was used which consists of two steps. Firstly, an SCF calculation was performed on the system and subsequently a matrix in the basis of CSFs representing the necessary electron configurations for the degenerate states was diagonalised. Results on the atoms B, C, O, F, Si, S and Cl showed that the Breit-Pauli approximation was extremely accurate and that higher order corrections were essentially negligible until the late second row atoms were attempted. At this point it became clear that it was necessary to include second and higher order corrections to the Breit-Pauli Hamiltonian. More importantly, it was found to be necessary to include a correction for the anomalous magnetic moment. This is described as the magnetic moment discrepancy caused by the incorrect assumption that the Lande g factor is equal to exactly 2. By the end of the second row of atoms, this error was found to cause deviations of up to 2cm^{-1} for Cl splittings.

The use of MCSCF wavefunctions via CASSCF using the 6-31G(d,p) basis set to determine spin-orbit coupling constants was attempted by Koseki *et al.* [13] in 1992. The active space included all valence electrons and orbitals. Of interest was the spin-orbit coupling constants relevant to the mixing of singlet and triplet states of small diatomic molecules. Because of the complexity and computational intractability of using two electron integrals, only the one electron part of the Breit-Pauli Hamiltonian was used. The nuclear charge term, Z_A however was replaced by an effective nuclear charge, Z_{eff}. The idea was to determine a value of Z_{eff} for each atom in the first two rows, using calculations from $^2\Pi$ terms of A-H diatomics and adjusting Z_{eff} to obtain the correct fine structure splitting from experiment. Because the two electron terms are interpreted as performing the task of shielding the electrons from the nuclear charge, this "semi empirical" inclusion of Z_{eff} was thought to negate the need for the two electron terms. Results for A-H diatomic molecules suggested that with only a couple of exceptions, results using one-electron integrals with Z_{eff} were within 10 cm^{-1} of experimental results. Using these values of Z_{eff} for more general diatomics resulted in calculated fine structure splitting values which were largely within 20 cm^{-1} of experiment. For this work, the pertinent results for the spin-orbit coupling constant are OH (-144.12 cm^{-1}), NO(128.52 cm^{-1}) and CN(-54.62 cm^{-1}).

Bearpark *et al.* [14] used non-orthogonal sets of orbitals for each state of a spin-orbit calculation as opposed to the more common method of using an MCSCF approach with a single set of common orbitals between the states. The Breit-Pauli approximation was again used. Of interest was the application of this technique to the $^2\Pi_{1/2}$ and $^2\Pi_{3/2}$ degenerate states of the OH molecule. The basis of electronic configurations which represent the fourfold degeneracy are described as:

$$(1\sigma)^2(2\sigma)^2(3\sigma)^2(1\pi_y)^2(1\pi_x)^\alpha$$
$$1\sigma)^2(2\sigma)^2(3\sigma)^2(1\pi_y)^2(1\pi_x)^\beta$$
$$(1\sigma)^2(2\sigma)^2(3\sigma)^2(1\pi_x)^2(1\pi_y)^\alpha$$
$$(1\sigma)^2(2\sigma)^2(3\sigma)^2(1\pi_x)^2(1\pi_y)^\beta$$

The spin-orbit coupling constant was calculated as the bond length was increased from 1.3 Å through to 2.75 Å with longer bond lengths ignored as SCF wavefunctions become inappropriate descriptions of dissociating molecular bonds. Good agreement was found between these results and those found using CI wavefunctions across the

potential energy surface. Around the equilibrium bond length, results very close to experiment were achieved.

The problem of how to handle the two electron terms was reviewed by Hess *et al.* [15] in 1996 when attempting to use CI techniques with spin-orbit coupling calculations. The two electron part of the spin-orbit matrix elements were restricted to having only one centre terms and the electrons i and j were allowed to move in the mean field of the other k electrons. These k electrons were those present in at least one of the CI electron configurations. This resulted in a set of effective one electron operators with multi-centre two electron integrals neglected entirely. The error introduced by the neglect of these multi-centre two electron integrals was found to be just 2 cm^{-1} for palladium complexes such as PdCl and Pd_2^+ and the overall accuracy with just the effective one electron operator approximation was found to be excellent.

A new FCI algorithm was developed by Mitrushenkov *et al.* [16] which included spin-orbit components of the Hamiltonian. The aim of this new algorithm, implemented in Molpro [17], was to reduce the number of matrix elements requiring calculation. It was found that a certain, relatively small, number of the matrix elements could be calculated directly, after which a "recurrence relationship" could be used to derive the others. This allowed efficient evaluation of matrix elements. Additionally, the use of light atoms permitted the application of a perturbative treatment to determine spin-orbit coupling properties. Results for the ^3P state of the oxygen atom indicated a spin-orbit coupling constant value within 1.0 cm^{-1} of experiment.

Nicklass *et al.* [18] used the Breit-Pauli Hamiltonian to predict the $^2P_{3/2} -^2 P_{1/2}$ spin-orbit splitting on the atoms F, Cl and Br using an internally contracted multi-reference CI method (MRCI). Attempts were made to establish the effect of increasing basis set, tight functions, and higher angular momentum functions on the splitting. It was noted that some spin-orbit operations were not bound from below and would therefore give problems if included in a variational treatment. Additionally, it was difficult, computationally, to include spin-orbit contributions to the standard energetic Hamiltonian for the variational procedure. It was therefore deemed that the spin-orbit coupling splitting should be calculated by means of a perturbation treatment after the variational procedure was completed. Correlation consistent basis sets were used. This is important as spin-orbit coupling affects the electrons closest to the core. In these calculations the anomalous magnetic moment effects

were neglected. Diffuse basis functions were found to have a negligible impact on the spin-orbit splitting and were not investigated further. Using basis sets in which the core electrons were correlated was found to be important for high levels of accuracy: more so than correlating the valence electrons. The inclusion of a single tight p basis function was found to improve the convergence of the F atom with increased basis set although this did not affect Cl or Br in the same way: both of these converging rapidly with or without the extra p basis function. Recovering more correlation energy by expanding the active space to include more virtual orbitals was found to have relatively negligible effect.

The procedure by which Nicklass performed these calculations is detailed by Berning *et al.* [5], who introduced a method for evaluating the matrix elements for the Breit-Pauli Hamiltonian for internally contracted MRCI wavefunctions. The most important two electron integrals were approximated using an effective one-electron operator thus easing the computational effort. Here the effective one electron integrals are created from electron densities, derived directly from the two electron integrals, rather than semi-empirical methods described by Koseki *et al.* [13], see above. These effective one electron integrals are created as weighted sums of the most important two electron spin-orbit interactions with virtually no loss in accuracy. The recommended process of performing large CASSCF calculations on the system and then using this CASSCF wavefunction as a zeroth order wavefunction for a subsequent MRCI calculation ensure that both static (from CASSCF) and dynamic (from MRCI) correlation energy are recovered. Additionally, direct methods of integral evaluation are performed which allows large configuration spaces to be used without the computational overhead of storing the integral values themselves. It was found that two electron effects can be large for lighter atoms, diminishing as the size of the atom increases. For the Cl atom using a cc-pV5Z basis set, the neglect of two electron integrals entirely results in 20% error in the spin-orbit coupling constant calculation for the ^{2}P state. The two electron effects have their greatest impact on core electrons and therefore the inclusion of the most important two electron integrals via the effective one electron operator captures much of this. The residual two electron integrals involve the valence electrons and it was therefore found that neglect of these two electron integrals resulted in errors less than 1%. Where double excitations feature prominently in a wavefunction however, the inclusion of

all two electron integrals can be switched on because this would be the only way of capturing their contribution to the spin-orbit coupling constant, remembering that for one-electron operators, only single differences in configurations are non-zero. As found by Nicklass *et al.* [18], the effect of adding angular momentum functions had minimal effect and that it was found to be more important to correctly characterise the orbitals near the nucleus (s and p) rather than introducing more virtual orbitals into the active space. For 2nd row atoms, correlating $2p$ orbitals in the MRCI calculation led to dramatic improvements. Best results for the atoms C(^3P), O(^3P), F(^2P), Si(^3P), S(^3P) and Cl(^2P) were obtained using the cc-pV5Z basis set with maximum angular momentum of f functions used, full valence active space for CASSCF calculations and all electrons correlated for subsequent MRCI calculations; most results falling within 1-2 cm^{-1} of experiment. Spin-orbit coupling constants were found to be 13.31 cm^{-1} for C, -77.26 cm^{-1} for O, -132.86 cm^{-1} for F, 72.48 cm^{-1} for Si, -196.37 cm^{-1} for S and -294.06 cm^{-1} for Cl. Small diatomic molecules were also investigated: OH($^2\Pi$), $C_2(a^3\Pi_u)$, CN($A^2\Pi$) and NO($X^2\Pi$). Here full valence CASSCF calculations were performed followed by valence-only correlated MRCI and all electron correlated MRCI. Again excellent results were obtained with respect to experiment when the cc-pV5Z basis set was used. Also, the inclusion of core correlation had a greater impact on diatomics with atoms from the 2nd row. The impact of using the effective one-electron operator in place of the two electron operator was negligible. Results for the spin-orbit coupling constants for the diatomic molecules which relate to this work were found to be -136.98 cm^{-1} for OH, -14.68 cm^{-1} for C_2, -51.25 cm^{-1} for CN and 123.36 cm^{-1} for NO.

Other applications of spin-orbit coupling include mixing of singlet and triplet states. Furlani *et al.* [19] used CASSCF as the baseline for spin-orbit coupling constants between singlet and triplet states of the trimethylene biradical. When mixing triplet and singlet states, only $M_s = 0$ of the triplet state will mix with the singlet; the remaining matrix elements will be zero by symmetry. Using this technique, the spin-orbit coupling constant was found to be sensitive to the geometry of the molecule. The role of spin-orbit coupling in the process of inter-system crossing (ISC) in conjugated polymers was investigated by Beljonne *et al.* [20] using correlated methods (SCI) based on semi-empirical geometry optimisations. The matrix elements once again were treated as first order perturbation and rates of inter-system crossings

were able to be evaluated with consideration given to the effect of the geometry of the system on these rates. Although quantitative details were not able to be made, several mechanisms were elucidated showing how the ISCs could be realised.

Potential energy surfaces for several diatomic molecules have been investigated by Li *et al.* [21][22][23] using the MRCI+Q method to provide insight into species which are known to be involved in stratospheric ozone depletion. The lowest lying electronic states of CS were treated using the aug-cc-pwCV5Z basis set taking spin-orbit coupling effects into account. This allowed for elucidation of several avoided crossings, spectroscopic constants and radiative lifetimes of triplet states. Similar calculations were performed on BrF, BrF^+ IBr and IBr^+ all of which resulted in good agreement with experiment.

Finally it is noted that state of the art techniques such as DMRG can now be supplemented with spin-orbit coupling calculations [24]. This will not be discussed further here other than to mention that the technique shows promise for investigating the spin-orbit coupling effects on larger systems containing metals. In particular, results on the spin-orbit splitting in atoms such as Cu and Au show significantly better performance than CASSCF-SO methods and in many cases also CASPT2-SO.

3.4 Implementation of Spin-Orbit Coupling

A range of atoms and molecules were tested in this work in order to investigate the efficacy of using MCCI to determine the spin-orbit coupling interactions between degenerate electronic states of each system. In order to perform this, several tasks must be undertaken. Initially, a series of ROHF calculations were performed to identify all of the necessary degenerate wavefunctions of each of the following: B(^{2}P), C(^{3}P), O(^{3}P), F(^{2}P), Si(^{3}P), S(^{3}P), Cl(^{2}P) atoms and OH($X^2\Pi$), CN($A^2\Pi$), C_2($a^3\Pi_u$) and NO($X^2\Pi$) molecules. These represent the lowest energy states for which degeneracy is exhibited by these species bearing in mind that, for spin-orbit coupling, it is necessary to have non-zero overall spin and non-zero overall orbital angular momentum. Basis sets cc-pVDZ, cc-pVTZ, cc-pVQZ and cc-pV5Z were used on all systems.

In order to improve the zeroth order ROHF wavefunctions and capture electron

correlation, MCCI calculations were performed on the degenerate states of the test-bed atoms and molecules, using Slater Determinants. For each basis set, the effect of lowering the c_{min} value was investigated and calculations were performed at c_{min} values of 0.001, 0.0005, 0.0002 and 0.0001. All calculations were performed at a convergence threshold of 0.001. Having calculated the MCCI wavefunction for each of the degenerate states, with close agreement in energy between them as expected, a file containing details of the wavefunction for each of the degenerate states is produced by MCCI. These files contain the list of Slater Determinants representing the electronic configurations deemed to be important in capturing the new and improved MCCI zeroth order wavefunction of each degenerate state. These files are then collected and submitted to spin-orbit coupling calculations in the x, y and z directions within MCCI, code for which has been written as part of this work. The spin orbit code must calculate the expectation value of the Breit-Pauli operator in the basis of all degenerate states as shown in equation 3.23, where $\mathcal{H}^{so}$ is factored into a product of L and S terms described in equations 3.24 and 3.25.

$$\langle\Phi|\mathcal{H}^{so}|\Phi\rangle = \sum_{x,y,z} \langle\Phi|\mathcal{H}_L^{so}|\Phi\rangle \ \langle\Phi|\mathcal{H}_S^{so}|\Phi\rangle \tag{3.23}$$

$$\mathcal{H}_L^{so} = -\sum_{i=1}^{Elec}\sum_{K=1}^{Nuc} \frac{Z_K[\hat{r}_{iK} \times \hat{p}(i)]}{r_{iK}^3} \tag{3.24}$$

$$\mathcal{H}_S^{so} = -\sum_{i=1}^{Elec}\sum_{K=1}^{Nuc} \frac{1}{2c^2}\hat{s}(i) \tag{3.25}$$

Integrals of the $\mathcal{H}_L^{so}$ operator in the basis of molecular orbitals are provided by Molpro and are available in the x, y and z directions, all of which are required. These integrals are hereafter referred to as LSq integrals where q = x,y,z and are defined in equation 3.26 and it should be noted that the presence of the linear momentum operator, $\hat{p} = -i\nabla$, in the $\mathcal{H}_L^{so}$ operator means these integrals are complex.

$$LSq = \langle\psi_i|\mathcal{H}_{Lq}^{so}|\psi_j\rangle \tag{3.26}$$

The MCCI code developed as part of this work must convert the integrals into a format suitable for MCCI and then generate a spin-orbit coupling matrix in the

basis of states which in general form is shown equation 3.27 for a two-by-two matrix using direct methods, where the matrix elements are as defined in equation 3.28. It should be noted that the degenerate states are expanded in a linear combination of electron configurations in the form of Slater Determinants (shown in equation 3.29) and each Slater Determinant is an antisymmetrised product of MOs (shown in equation 3.30). Overall then the spin-orbit coupling state matrix is defined in equation 3.31.

$$H^{so} = \begin{pmatrix} H^{so}_{aa} & H^{so}_{ab} \\ H^{so}_{ba} & H^{so}_{bb} \end{pmatrix} \tag{3.27}$$

$$H^{so}_{ab} = \langle \Phi_a | \mathcal{H}^{so} | \Phi_b \rangle \tag{3.28}$$

$$|\Phi\rangle = \sum_{\nu}^{Cfgs} c_\nu \, |\Psi_\nu\rangle \tag{3.29}$$

$$|\Psi_\nu\rangle = \frac{1}{\sqrt{N!}} \sum_{n=1}^{N!} (-1)^{q_n} P_n \, |\chi_i \chi_j \ldots . \chi_k\rangle \tag{3.30}$$

$$H^{so}_{ab} = \sum_{\mu}^{Cfgs} \sum_{\nu}^{Cfgs} c^*_\mu c_\nu \sum_{i,j}^{MOs} \left\langle \Psi^i_\mu \middle| \mathcal{H}^{so}_L \middle| \Psi^j_\nu \right\rangle \left\langle \Psi^i_\mu \middle| \mathcal{H}^{so}_S \middle| \Psi^j_\nu \right\rangle \tag{3.31}$$

The result of these calculations are the spin-orbit coupling matrix elements expressed in both atomic units and cm^{-1} in the basis of degenerate states for the directions x, y and z. From this, the relative splitting of the degenerate energy levels as a result of spin-orbit coupling can be ascertained by diagonalising a matrix of these spin-orbit coupling matrix elements in the basis of degenerate symmetry and spin states.

3.4.1 Conversion of Molpro Integrals

For this work, Molpro was used to undertake the ROHF calculations and to produce the LSq integrals. It is therefore necessary to consider how Molpro handles molecular orbitals and symmetry. Molpro converts point groups of molecules into the highest Abelian subgroup for computational efficiency. For example, the CO molecule with

point group $C_{\infty v}$ is converted to use point group C_{2v} in Molpro. Within the point group, the irreducible representations labels are converted into symmetry numbers using a mapping described in tables 3.1 for the C_{2v} point group and 3.2 for the D_{2h} point group.

Table 3.1: Symmetry Numbers used in Molpro for Irreducible Representations of the Point Group C_{2v}

Molpro Sym. Num.	Irreducible Rep.	Function
1	A_1	z
2	B_1	x, R_y
3	B_2	y, R_x
4	A_2	R_z

Table 3.2: Symmetry Numbers used in Molpro for Irreducible Representations of the Point Group D_{2h}

Molpro Sym. Num.	Irreducible Rep.	Function
1	A_g	
2	B_{3u}	x
3	B_{2u}	y
4	B_{1g}	R_z
5	B_{1u}	z
6	B_{2g}	R_y
7	B_{3g}	R_x
8	A_u	

Molecular orbitals in Molpro are numbered $i \cdot j$ where j is the symmetry of the molecular orbital and i is the i-th molecular orbital of symmetry j in order of increasing energy. Molpro therefore orders molecular orbitals by symmetry and then by increasing energy within that symmetry. For example, a system with two orbitals of symmetry 1 and one of symmetry 3 would order the molecular orbitals in the following way: MO 1 = 1·1, MO 2 = 2·1, MO 3 = 1·3. Note that this does not necessarily mean that MO 2 is lower in energy than MO 3 or that MO 1 is lower in energy than MO 3. Molpro therefore, has symmetry at the heart of its operation.

The one-electron Molpro LSq integrals are written in a format based on symmetry blocks where each integral, in the MO basis, is as shown in equation 3.26 where $\mathcal{H}_L^{so}$ is defined in equation 3.24 and χ_i and χ_j are molecular integrals. It should be remembered that these integrals do not contain the required factor of $\frac{1}{2c^2}$ from the Breit-Pauli Hamiltonian. Neither is the spin component included. That means that when handling these integrals, both α and β spins of a doublet, for example, must be taken into account as well as the pre-factor in atomic units. It also needs bearing in mind that these integrals are complex numbers. In order for MCCI to be able to read these LSq integrals they must first be converted to the format *"integral value; i; j; k; l"*. Because these LSq integrals are one-electron only, the values of k and l are zero. The file must end with a row containing an integral value of zero and all orbital indices zero.

Selection rules govern the result of these molecular integrals. The result of these integrals are only non-zero when the overall symmetry of the result contains the totally symmetric irreducible representation of the point group of the molecule. In other words, this can be written as shown in equation 3.32.

$$\Gamma_i = \Gamma_{LSq} \otimes \Gamma_j \tag{3.32}$$

Molpro stores the LSq integrals in symmetry blocks which contain only the permutations of orbitals i and j allowed by the selection rules for the particular type of spin-orbit coupling operator in the x, y or z direction in equation 3.32. The blocks are numbered in increasing symmetry number of the point group. Each block is presented in a tabular format where each row is a molecular orbital of symmetry Γ_i listed in increasing order of MO number. The columns are molecular orbitals of symmetry determined by the irreducible representation symmetry required to make the direct product with the spin-orbit coupling operator equivalent to the row symmetry of that block. Again these column molecular orbitals are listed in increasing energy from left to right. The number stored at the intersection between a column molecular orbital and a row molecular orbital is the value of the LSq integral shown in equation 3.26. The number of columns and rows in any one symmetry block is the number of molecular orbitals of symmetry type i and j respectively. The symmetry of the spin-orbit coupling operators transform as R_x, R_y, and R_z for the x, y and

z directions respectively and the irreducible representation of each of these will be specific to the point group.

The software designed, written, tested and maintained, as part of this work, to perform the conversion of these symmetry blocks of integrals into a form suitable for MCCI is called **conv_molp_prop_ints** and is written in Fortran 90. Before running this code, an ROHF Molpro calculation of the chemical system must be performed, followed by a calculation of the LSq integrals. The inputs for **conv_molp_prop_ints** are the Molpro files FCIDUMP, which contains the standard energetic Hamiltonian one- and two-electron integrals for the ROHF calculation; the Molpro output file which must be manually renamed molp.out and a file called prop_ints which contains the LSq integrals from Molpro. Now the **conv_molp_prop_ints** software can be described in detail:

1) The files molp.out, prop_ints and FCIDUMP are opened. The point group is ascertained from the molp.out file and checked to make sure that it is one of the supported point groups. All Abelian subgroups are supported in this code. From the point group, the maximum number of irreducible representations can be deduced. This sets the maximum number of symmetry blocks produced by Molpro in the LSq integrals file.

2) Depending on the point group and the subsequent maximum number of irreducible representations, an appropriate direct product table can be allocated from memory and set up for the point group. Various other lookup/mapping tables are allocated for future use, such as mapping tables for the reversible transformation between molecular orbital numbers and symmetry formats, a table of selection rules and a table listing the number of MOs per irreducible symmetry for the point group.

3) From FCIDUMP, the number of molecular orbitals of each symmetry number is read and stored as well as the total number of molecular orbitals.

4) The operator symmetry is retrieved from the prop_ints file.

5) A mapping table is made to link the molecular orbital X·Y symmetry format to a molecular orbital number. This mapping has been described earlier in this section. For readability, this table is a two-dimensional array with columns representing the Y irreducible symmetry numbers, for the point group and the rows listing the X molecular orbitals, of that symmetry. The entry stored against each of these is the

molecular orbital number. A reverse mapping is also constructed which links the molecular orbital number back to the X·Y symmetry format.

6) A lookup table linking the direct product of the operator symmetry and each irreducible representation is created which represents the right hand side of equation 3.32, $\Gamma_{LSq} \otimes \Gamma_j$. This lookup table essentially links the symmetry allowed Γ_i and Γ_j permutations for the operator symmetry.

7) Now the symmetry blocks of spin-orbit integrals are read, in order, from the prop_ints file. For each symmetry block the symmetry of the rows is known because the blocks are listed in order of Molpro symmetry number. Each row corresponds to a different molecular orbital of that symmetry number in increasing energy for that symmetry. Because the operator symmetry is known and the symmetry of molecular orbitals arranged in rows of the symmetry block is also known, the symmetry of the molecular orbitals arranged in the columns is determined from step 6 above (there is a one-to-one mapping between the column and row symmetries). The number of rows and columns is also known for each symmetry block because those are the numbers of molecular orbitals of the particular symmetry numbers read in from the FCIDUMP file as detailed earlier. It is then a simple matter to step through the rows of each symmetry block and read in the integral values between each molecular orbital pairing from $\Gamma_i \otimes \Gamma_{LSq} \otimes \Gamma_j$. Once the relevant molecular orbitals in X·Y symmetry format are converted to molecular orbital number format using step 5 above, these integrals are then stored in an array where the rows and columns are ordered molecular orbital numbers.

8) The final task therefore remains for the integrals to now be written to file MCCI_PROP_INTS_DUMP in a format ready to be read by MCCI. Details of the required file format for this can be found in the literature [25][26].

Pseudo-code for the above **conv_molp_prop_ints** file is now shown. In bold are the major steps, variables and filenames in the code:

Step 1:

do read ***molp.out*** *file*

if "Point Group" found

set ***max_num_irreps*** *for point group*

endif ("Point Group")

enddo (read ***molp.out****)*

Step 2:

allocate ***sel_rule_allowed[max_num_irreps]*** *lookup table*

allocate ***num_mos_per_sym[max_num_irreps]***

allocate ***irrep_dp_table[max_num_irreps][max_num_irreps]***

construct ***irrep_dp_table*** *for point group*

Step 3:

read ***FCIDUMP*** *header*

extract MOs to ***num_mos_per_sym****[irrep_sym_type]*

extract ***norb***

Step 4:

do read ***prop_ints*** *file*

if "Symmetry" found

set ***operator_symmetry***

endif ("Symmetry")

enddo (read ***prop_ints****)*

Step 5:

allocate ***mo_integral_store[norb][norb]***

allocate ***mosym_to_monum[norb][max_num_irreps]***

allocate ***mo_to_irrep_conv[norb][2]***

Set ***mo_num*** $\rightarrow$ *1*

do i:1 $\rightarrow$ ***max_num_irreps***

do j:1 $\rightarrow$ ***num_mos_per_sym[i]***

mo_to_irrep_conv[mo_num][1] $= j$

mo_to_irrep_conv[mo_num][2] $= i$

mosym_to_monum[j][i] $=$ ***mo_num***

increment ***mo_num***

enddo (j)

enddo (i)

Step 6:

do i:1 $\rightarrow$ ***max_num_irreps***

get $j =$ ***operator_symmetry*** $\otimes\ i$

sel_rule_allowed[j] $= i$

enddo (i)

Step 7:

*do i:1 → **max_num_irreps** (step through symmetry blocks one at a time)*

*   ***num_mos_per_sym[i]** → **num_rows***

*   ***sel_rule_allowed[i]** → **col_sym***

*   ***num_mos_per_sym[col_sym]** → **num_cols***

*   *ignore symmetry blocks where either **col_sym** or **row_sym** are zero*

*   *do j:1 → **num_rows***

*   *get **mo_num_row** from **mosym_to_monum[j][i]***

*   *columns for each row are in blocks of 5*

*   ***phys_rows_per_row** (for row j) → (**num_cols** % 5)*

*   *add extra row if (num_cols % 5) gt 0*

*   *do k:1 → **phys_rows_per_row***

*   *read integrals from **prop_ints** file*

*   *get **mo_num_col** from **mosym_to_monum** for column entry file*

*   *store integral in **mo_integral_store[mo_num_row][mo_num_col]***

*   *enddo (k)*

*   *enddo (j)*

enddo(i)

Step 8:

*do i:1 → **norb***

*   *do j:1 → i*

*   *write **mo_integral_store[i][j]** → **MCCI_PROP_INTS_DUMP** file*

*   *enddo (j)*

enddo (i)

*write "zeros" line to **MCCI_PROP_INTS_DUMP***

3.4.2 Development of Spin-Orbit Coupling Property Calculations Using MCCI

Having run the Molpro ROHF calculations for one of the degenerate states of interest (described in the next section), the corresponding FCIDUMP files is used in the next stage as is the MCCI_PROP_INTS_DUMP file, produced by running the **conv_molp_prop_ints** script above. A standard MCCI calculation is run to estab-

lish the MCCI wavefunction for the state using an MCCI input file called **mcci.in** as part of this process [27]. The MCCI wavefunctions for the other states are now required. The necessary occupied molecular orbitals for the valence electrons for each state are hand crafted into a modified version of **mcci.in** and now MCCI calculations are run on all of these states. The FCIDUMP file is common to all of the calculations and Slater Determinants are used throughout. Once all MCCI wavefunction calculations are complete, each of the degenerate states will have a file called **civ_out_state**. These **civ_out_state** files are now used alongside the common **MCCI_PROP_INTS_DUMP** file and the **mcci.in** file is modified once more to perform a Spin-Orbit Coupling calculation on these n states. This process which was designed as part of this work is now described:

1) The LSq integrals are read in from the file **MCCI_PROP_INTS_DUMP**. Only one electron integrals are available from Molpro. Although these integrals would be expected to be in a two dimensional array, in practice they are stored in a single dimension array called **e1ints** for computational performance reasons. This format is described in the literature [27].

2) The **civ_out_state** files for each state are now read into the **icij** array which stores each electron configuration, including the molecular orbitals and spin state, present in each Slater Determinant for each state. The **icij** array exists in the standard MCCI code but in this work it has been partitioned to store the details of more than one state.

3) The **prop_state_matrix** is the LSq integral matrix in the basis of electronic states (one state per **civ_out_state** file). Each off-diagonal matrix element is the spin-orbit coupling interaction between the two respective states. Note that due to the selection rules, the symmetry of the spin-orbit coupling operator means that all diagonal elements in this matrix are necessarily zero. The matrix elements are calculated as shown in equation 3.31. Here, a and b are the various electronic states detailed by the **civ_out_state** files. It should be noted that although the H^{so} matrix shown in equation 3.27 is calculated explicitly, each matrix element is the combination of spin-orbit interactions in the basis of appropriate Slater Determinants and ultimately in the basis of MOs. The individual Hamiltonian matrices in the basis of both Slater Determinants and molecular orbitals are not explicitly constructed. Instead each element is summed "on the fly" with only the final value of H^{so}_{ab} being stored explicitly

in the final matrix **prop_state_matrix**. This is done for computational storage reasons, similar to the CASSCF and MRCI techniques discussed in the theory section of this work. When evaluating the matrix element value in the basis of Slater Determinants, the usual Slater rules can be employed. Because the symmetry of the spin-orbit operator is not totally symmetric, the bra and ket Slater Determinants cannot have the same symmetry. Therefore all matrix elements where there are no orbital differences between the determinants must be zero. Equally, because only one electron integrals are supported, the Slater rules determine that where there are differences of two or more orbitals the matrix element must also be zero. It is therefore only situations where there is precisely one orbital difference between the Slater Determinants that a non-zero matrix element can exist and $\hat{S}$ operators can be treated as one-electron operators. The MCCI code has been specially modified to handle these three scenarios specifically for the spin-orbit coupling code. The course of action taken when one orbital difference is found depends on the symmetry of the spin-orbit operator. The spin-orbit operators require MCCI to take account of the spin part of the Breit-Pauli Hamiltonian. This means calculation of $\mathcal{H}^{so}$ in the x, y and z directions. Therefore the value of $\langle\Psi_i|\mathcal{H}_S^{so}|\Psi_j\rangle$, in x and y directions requires the spin of the differing i and j orbitals to be different for a non-zero matrix element to occur. This is because neither $\hat{S}_x$ nor $\hat{S}_y$ form eigenvalue equations with the ket vector. For the z direction, the spins must be the same because $\hat{S}_z$ does form an eigenvalue equation with the ket vector. The effect of the relevant $\hat{S}$ operators on the possible spin states of the differing orbital is summarised in equations 3.33 to 3.38.

$$\hat{S}_x\,|\alpha\rangle = \frac{1}{2}\,|\beta\rangle \tag{3.33}$$

$$\hat{S}_x\,|\beta\rangle = \frac{1}{2}\,|\alpha\rangle \tag{3.34}$$

$$\hat{S}_y\,|\alpha\rangle = \frac{i}{2}\,|\beta\rangle \tag{3.35}$$

$$\hat{S}_y\,|\beta\rangle = -\frac{i}{2}\,|\alpha\rangle \tag{3.36}$$

$$\hat{S}_z \left|\alpha\right\rangle = \frac{1}{2} \left|\alpha\right\rangle \tag{3.37}$$

$$\hat{S}_z \left|\beta\right\rangle = -\frac{1}{2} \left|\beta\right\rangle \tag{3.38}$$

Two added complexities require mentioning. Firstly, as menioned earlier, all of the LSq integrals are purely imaginary. Secondly, the $\hat{S}_y$ operator is also complex. This means that all matrix elements in the y direction are of the wrong sign and need to be negated. The calculated value of $\langle\chi_i|\hat{S}_q|\chi_j\rangle$ is then multiplied by the LSq integral between the same two molecular orbitals. The contribution for the LSq matrix element in the basis of the respective states is thus the sum of all such molecular orbital permutations for all of the configurations in each state. Because the LSq integrals involve complex quantities, integral matrix is Hermitian. The MCCI code has been modified to allow complex matrices by simply negating the lower triangle matrix element integral when the corresponding upper triangle matrix element integral is required. The final H^{so} matrix values for x and z directions are purely imaginary and those of the y direction purely real. This must be reflected in the final state matrix which requires diagonalisation to reveal the spin-orbit coupling line splitting values.

Because Slater Determinants are used, MCCI by default will orthonormalise the configurations and hence the overlap matrix, S, will be the unit matrix. It is therefore not necessary to divide the H_{AB} matrix elements by a normalisation factor. The final step is to multiply each matrix element H_{AB} by a factor of $1/2c^2$, taken in atomic units, to produce a spin-orbit coupling matrix element between the respective electronic states in the units of cm^{-1} before printing this to the MCCI output log file **properties_output**. This entire process must be repeated until all values of the spin-orbit coupling matrix elements for the x, y and z directions are obtained. From here a matrix of spin-orbit coupling matrix elements for the full set of spin-orbit operators is constructed in the basis of the degenerate states bearing in mind that this will be a complex matrix. Diagonalisation of this matrix will reveal the extent of spin-orbit coupling on the removal of degeneracy of the original states by detailing the energy shift of each individual state under this interaction.

Pseudo-code for the above MCCI Spin-Orbit Coupling work is now shown. In bold

are the major steps, variables and filenames in the code:

Step 1:

do read ***MCCI_PROP_INTS_DUMP*** *file*

get storage index for integral, ij, from ***ipoint*** *lookup table*

store integral → ***one_e_propints[ij]***

*enddo (****read MCCI_PROP_INTS_DUMP****)*

Step 2:

do i:1 → num states

do j:start → EOF

read configs from ***civ_out_state_i*** *file*

store each config in ***icij*** *matrix sector for state*

store coeff of each config in ***ctemp****[j][i]*

enddo (j)

store num configs for state in ***state_civec_len****[i]*

enddo

Step 3: *copy* ***one_e_propints*** *to* ***e1ints***

init ***prop_state_matrix*** *(H_{ij}^{so} state matrix elements) to zero*

do ***bra_state****:1 → num_states*

do ***ket_state****:1 → num_states*

calculate range of configs (ici and jci) for each bra and ket state

do ici:start_ici_config → end_ici_config

do jci:start_jci_config → end_jci_config

want $H_{ij}^{so} = \langle ici|\mathcal{H}^{so}|jci\rangle \forall$ ici and jci permutations

calc num MO diffs between ici and jci configs

if ndiff = 1 (all others give zero H_{ij}^{so})

get spins of differing MOs (spini and spinj)

get MO numbers of differing MOs iorb and jorb

if parallel spins

if iorb gt jorb (lower triangle)

spin_contribution *= spinj/2*

if LSZ

kk = integral index for iorb and jorb permutation

energy += ***e1ints[kk]*spin_contribution***

endif (LSZ)

- *else (upper triangle)*

spin_contribution *= spinj/2*

if LSZ

kk = integral index for iorb and jorb permutation

energy -= ***e1ints[kk]*spin_contribution***

endif (LSZ)

endif (iorb gt jorb)

else (differing spins)

if iorb gt jorb(lower triangle)

kk = integral index for iorb and jorb permutation

if LSY

spin_contribution = -spinj/2

elseif LSX

spin_contribution *= 1/2 (always positive)*

endif (LSY, LSX)

energy += ***(e1ints[kk]*spin_contribution)***

else (upper triangle)

kk = integral index for iorb and jorb permutation

if LSY

spin_contribution *= -spinj/2*

energy -= ***(e1ints[kk]*spin_contribution)***

else LSX

spin_contribution *= 1/2*

energy -= ***(e1ints[kk]*spin_contribution)***

endif (LSY, LSX)

endif (iorb gt jorb)

endif (parallel spins)

endif (ndiff=1)

*SOC property value += ici coeff * energy * jci coeff*

enddo (jci)

enddo (ici)

prop_state_matrix*[bra_state][ket_state] = SOC property value * 1/2c*^{2} *(au)*

enddo (ket_state)

enddo (bra_state)

3.5 Results and Discussion - Spin-Orbit Coupling

Boron Atom

The first atom considered is the ^2P ground state of the boron atom. The point group for all atoms in this work within Molpro is D_{2h}. This ground state has six-fold degeneracy. The following six electron configurations are therefore required:

$$[\mathrm{He}]2\mathrm{s}2\mathrm{p}^1_{x\alpha} \text{ (symmetry } \mathrm{B}_{3u})$$
$$[\mathrm{He}]2\mathrm{s}2\mathrm{p}^1_{y\alpha} \text{ (symmetry } \mathrm{B}_{2u})$$
$$[\mathrm{He}]2\mathrm{s}2\mathrm{p}^1_{z\alpha} \text{ (symmetry } \mathrm{B}_{1u})$$
$$[\mathrm{He}]2\mathrm{s}2\mathrm{p}^1_{x\beta} \text{ (symmetry } \mathrm{B}_{3u})$$
$$[\mathrm{He}]2\mathrm{s}2\mathrm{p}^1_{y\beta} \text{ (symmetry } \mathrm{B}_{2u})$$
$$[\mathrm{He}]2\mathrm{s}2\mathrm{p}^1_{z\beta} \text{ (symmetry } \mathrm{B}_{1u})$$

Under the influence of spin-orbit coupling, this six-fold degenerate ^2P state splits into 2 levels: a four-fold degenerate $^2P_{3/2}$ level and a two-fold degenerate $^2P_{1/2}$ level. The symmetries of the spin-orbit operators, which transform as rotations in the appropriate direction, are: x direction = B_{3g}; y direction = B_{2g} and z direction = B_{1g}. Applying selection rules, only the following spin-orbit coupling matrix elements, involving the levels above, will be non-zero:

$$\langle B_{1u}|\hat{H}^{so}_x|B_{2u}\rangle \;\; \langle B_{2u}|\hat{H}^{so}_x|B_{1u}\rangle$$
$$\langle B_{1u}|\hat{H}^{so}_y|B_{3u}\rangle \;\; \langle B_{3u}|\hat{H}^{so}_y|B_{1u}\rangle$$
$$\langle B_{2u}|\hat{H}^{so}_z|B_{3u}\rangle \;\; \langle B_{3u}|\hat{H}^{so}_z|B_{2u}\rangle$$

Carbon Atom

The ^3P ground state of the carbon atom is used in this work. In this case a triplet ground state exists and the degeneracy of this ground state is nine. The following nine electron configurations are required:

$$[\mathrm{He}]2\mathrm{s}2\mathrm{p}^1_{x\alpha}2\mathrm{p}^1_{y\alpha} \text{ (symmetry } \mathrm{B}_{1g})$$
$$[\mathrm{He}]2\mathrm{s}2\mathrm{p}^1_{x\alpha}2\mathrm{p}^1_{z\alpha} \text{ (symmetry } \mathrm{B}_{2g})$$
$$[\mathrm{He}]2\mathrm{s}2\mathrm{p}^1_{y\alpha}2\mathrm{p}^1_{z\alpha} \text{ (symmetry } \mathrm{B}_{3g})$$
$$[\mathrm{He}]2\mathrm{s}2\mathrm{p}^1_{x\beta}2\mathrm{p}^1_{y\beta} \text{ (symmetry } \mathrm{B}_{1g})$$
$$[\mathrm{He}]2\mathrm{s}2\mathrm{p}^1_{x\beta}2\mathrm{p}^1_{z\beta} \text{ (symmetry } \mathrm{B}_{2g})$$
$$[\mathrm{He}]2\mathrm{s}2\mathrm{p}^1_{y\beta}2\mathrm{p}^1_{z\beta} \text{ (symmetry } \mathrm{B}_{3g})$$

$$[\mathrm{He}]2\mathrm{s}2\mathrm{p}^1_{x\alpha}2\mathrm{p}^1_{y\beta}\ (\text{symmetry } \mathrm{B}_{1g})$$
$$[\mathrm{He}]2\mathrm{s}2\mathrm{p}^1_{x\alpha}2\mathrm{p}^1_{z\beta}\ (\text{symmetry } \mathrm{B}_{2g})$$
$$[\mathrm{He}]2\mathrm{s}2\mathrm{p}^1_{y\alpha}2\mathrm{p}^1_{z\beta}\ (\text{symmetry } \mathrm{B}_{3g})$$

For the $\mathrm{M}_s = 0$ states of the triplet, only those states which give an overall symmetry which will result in a non-zero spin-orbit coupling matrix element with one of the $\mathrm{M}_s = +1$, -1 states are chosen. Spin-orbit coupling splits this nine-fold degenerate state into three levels: a five fold ${}^3P_2$ level, a three-fold ${}^3P_1$ level and finally a single non-degenerate ${}^3P_0$ level. Applying the selection rules, only the following spin-orbit coupling matrix elements, involving the levels above, will be non-zero:

$$\langle B_{1g}|\hat{H}^{so}_x|B_{2g}\rangle\ \ \langle B_{2g}|\hat{H}^{so}_x|B_{1g}\rangle$$
$$\langle B_{1g}|\hat{H}^{so}_y|B_{3g}\rangle\ \ \langle B_{3g}|\hat{H}^{so}_y|B_{1g}\rangle$$
$$\langle B_{2g}|\hat{H}^{so}_z|B_{3g}\rangle\ \ \langle B_{3g}|\hat{H}^{so}_z|B_{2g}\rangle$$

Oxygen Atom

The ${}^3P$ ground state of the oxygen atom is used in this work. This atom is handled in the same way as the carbon atom. The following nine electron configurations are required:

$$[\mathrm{He}]2\mathrm{s}2\mathrm{p}^2_z2\mathrm{p}^1_{x\alpha}2\mathrm{p}^1_{y\alpha}\ (\text{symmetry } \mathrm{B}_{1g})$$
$$[\mathrm{He}]2\mathrm{s}2\mathrm{p}^2_y2\mathrm{p}^1_{x\alpha}2\mathrm{p}^1_{z\alpha}\ (\text{symmetry } \mathrm{B}_{2g})$$
$$[\mathrm{He}]2\mathrm{s}2\mathrm{p}^2_x2\mathrm{p}^1_{y\alpha}2\mathrm{p}^1_{z\alpha}\ (\text{symmetry } \mathrm{B}_{3g})$$
$$[\mathrm{He}]2\mathrm{s}2\mathrm{p}^2_z2\mathrm{p}^1_{x\beta}2\mathrm{p}^1_{y\beta}\ (\text{symmetry } \mathrm{B}_{1g})$$
$$[\mathrm{He}]2\mathrm{s}2\mathrm{p}^2_y2\mathrm{p}^1_{x\beta}2\mathrm{p}^1_{z\beta}\ (\text{symmetry } \mathrm{B}_{2g})$$
$$[\mathrm{He}]2\mathrm{s}2\mathrm{p}^2_x2\mathrm{p}^1_{y\beta}2\mathrm{p}^1_{z\beta}\ (\text{symmetry } \mathrm{B}_{3g})$$
$$[\mathrm{He}]2\mathrm{s}2\mathrm{p}^2_z2\mathrm{p}^1_{x\alpha}2\mathrm{p}^1_{y\beta}\ (\text{symmetry } \mathrm{B}_{1g})$$
$$[\mathrm{He}]2\mathrm{s}2\mathrm{p}^2_y2\mathrm{p}^1_{x\alpha}2\mathrm{p}^1_{z\beta}\ (\text{symmetry } \mathrm{B}_{2g})$$
$$[\mathrm{He}]2\mathrm{s}2\mathrm{p}^2_x2\mathrm{p}^1_{y\alpha}2\mathrm{p}^1_{z\beta}\ (\text{symmetry } \mathrm{B}_{3g})$$

The non-zero matrix elements are the same as for the carbon atom.

Fluorine Atom

The ${}^2P$ ground state of the fluorine atom is used in this work. This atom is handled in exactly the same way as for the boron atom. The six required electron configurations are:

$$[\mathrm{He}]2\mathrm{s}2\mathrm{p}^2_y2\mathrm{p}^2_z2\mathrm{p}^1_{x\alpha}\ (\text{symmetry } \mathrm{B}_{3u})$$
$$[\mathrm{He}]2\mathrm{s}2\mathrm{p}^2_x2\mathrm{p}^2_z2\mathrm{p}^1_{y\alpha}\ (\text{symmetry } \mathrm{B}_{2u})$$
$$[\mathrm{He}]2\mathrm{s}2\mathrm{p}^2_x2\mathrm{p}^2_y2\mathrm{p}^1_{z\alpha}\ (\text{symmetry } \mathrm{B}_{1u})$$

$$[\mathrm{He}]2\mathrm{s}2\mathrm{p}_y^2 2\mathrm{p}_z^2 2\mathrm{p}_{x\beta}^1 \text{ (symmetry } \mathrm{B}_{3u})$$
$$[\mathrm{He}]2\mathrm{s}2\mathrm{p}_x^2 2\mathrm{p}_z^2 2\mathrm{p}_{y\beta}^1 \text{ (symmetry } \mathrm{B}_{2u})$$
$$[\mathrm{He}]2\mathrm{s}2\mathrm{p}_x^2 2\mathrm{p}_y^2 2\mathrm{p}_{z\beta}^1 \text{ (symmetry } \mathrm{B}_{1u})$$

The non-zero matrix elements are the same as for the boron atom.

Silicon Atom

The ^3P ground state of the silicon atom is used in this work. This atom is handled in the same way as the carbon atom with the difference being that the [Ne]3s3p shells are now required. The following nine electron configurations are required:

$$[\mathrm{Ne}]3\mathrm{s}3\mathrm{p}_{x\alpha}^1 3\mathrm{p}_{y\alpha}^1 \text{ (symmetry } \mathrm{B}_{1g})$$
$$[\mathrm{Ne}]3\mathrm{s}3\mathrm{p}_{x\alpha}^1 3\mathrm{p}_{z\alpha}^1 \text{ (symmetry } \mathrm{B}_{2g})$$
$$[\mathrm{Ne}]3\mathrm{s}3\mathrm{p}_{y\alpha}^1 3\mathrm{p}_{z\alpha}^1 \text{ (symmetry } \mathrm{B}_{3g})$$
$$[\mathrm{Ne}]3\mathrm{s}3\mathrm{p}_{x\beta}^1 3\mathrm{p}_{y\beta}^1 \text{ (symmetry } \mathrm{B}_{1g})$$
$$[\mathrm{Ne}]3\mathrm{s}3\mathrm{p}_{x\beta}^1 3\mathrm{p}_{z\beta}^1 \text{ (symmetry } \mathrm{B}_{2g})$$
$$[\mathrm{Ne}]3\mathrm{s}3\mathrm{p}_{y\beta}^1 3\mathrm{p}_{z\beta}^1 \text{ (symmetry } \mathrm{B}_{3g})$$
$$[\mathrm{Ne}]3\mathrm{s}3\mathrm{p}_{x\alpha}^1 3\mathrm{p}_{y\beta}^1 \text{ (symmetry } \mathrm{B}_{1g})$$
$$[\mathrm{Ne}]3\mathrm{s}3\mathrm{p}_{x\alpha}^1 3\mathrm{p}_{z\beta}^1 \text{ (symmetry } \mathrm{B}_{2g})$$
$$[\mathrm{Ne}]3\mathrm{s}3\mathrm{p}_{y\alpha}^1 3\mathrm{p}_{z\beta}^1 \text{ (symmetry } \mathrm{B}_{3g})$$

The non-zero matrix elements are the same as for the carbon atom.

Sulfur Atom

The ^3P ground state of the sulfur atom is used in this work. This atom is handled in the same way as the carbon atom with the difference being that the [Ne]3s3p shells are now required. The following nine electron configurations are required:

$$[\mathrm{Ne}]3\mathrm{s}3\mathrm{p}_z^2 3\mathrm{p}_{x\alpha}^1 3\mathrm{p}_{y\alpha}^1 \text{ (symmetry } \mathrm{B}_{1g})$$
$$[\mathrm{Ne}]3\mathrm{s}3\mathrm{p}_y^2 3\mathrm{p}_{x\alpha}^1 3\mathrm{p}_{z\alpha}^1 \text{ (symmetry } \mathrm{B}_{2g})$$
$$[\mathrm{Ne}]3\mathrm{s}3\mathrm{p}_x^2 3\mathrm{p}_{y\alpha}^1 3\mathrm{p}_{z\alpha}^1 \text{ (symmetry } \mathrm{B}_{3g})$$
$$[\mathrm{Ne}]3\mathrm{s}3\mathrm{p}_z^2 3\mathrm{p}_{x\beta}^1 3\mathrm{p}_{y\beta}^1 \text{ (symmetry } \mathrm{B}_{1g})$$
$$[\mathrm{Ne}]3\mathrm{s}3\mathrm{p}_y^2 3\mathrm{p}_{x\beta}^1 3\mathrm{p}_{z\beta}^1 \text{ (symmetry } \mathrm{B}_{2g})$$
$$[\mathrm{Ne}]3\mathrm{s}3\mathrm{p}_x^2 3\mathrm{p}_{y\beta}^1 3\mathrm{p}_{z\beta}^1 \text{ (symmetry } \mathrm{B}_{3g})$$
$$[\mathrm{Ne}]3\mathrm{s}3\mathrm{p}_z^2 3\mathrm{p}_{x\alpha}^1 3\mathrm{p}_{y\beta}^1 \text{ (symmetry } \mathrm{B}_{1g})$$
$$[\mathrm{Ne}]3\mathrm{s}3\mathrm{p}_y^2 3\mathrm{p}_{x\alpha}^1 3\mathrm{p}_{z\beta}^1 \text{ (symmetry } \mathrm{B}_{2g})$$
$$[\mathrm{Ne}]3\mathrm{s}3\mathrm{p}_x^2 3\mathrm{p}_{y\alpha}^1 3\mathrm{p}_{z\beta}^1 \text{ (symmetry } \mathrm{B}_{3g})$$

The non-zero matrix elements are the same as for the carbon atom.

Chlorine Atom

The ^2P ground state of the chlorine atom is used in this work. This atom is handled in exactly the same way as the fluorine atom with the difference being that the [Ne]3s3p shells are now required. The required electron configurations are

$$[\text{Ne}]3\text{s}3\text{p}_y^2 3\text{p}_z^2 3\text{p}_{x\alpha}^1 \text{ (symmetry } \text{B}_{3u})$$
$$[\text{Ne}]3\text{s}3\text{p}_x^2 3\text{p}_z^2 3\text{p}_{y\alpha}^1 \text{ (symmetry } \text{B}_{2u})$$
$$[\text{Ne}]3\text{s}3\text{p}_x^2 3\text{p}_y^2 3\text{p}_{z\alpha}^1 \text{ (symmetry } \text{B}_{1u})$$
$$[\text{Ne}]3\text{s}3\text{p}_y^2 3\text{p}_z^2 3\text{p}_{x\beta}^1 \text{ (symmetry } \text{B}_{3u})$$
$$[\text{Ne}]3\text{s}3\text{p}_x^2 3\text{p}_z^2 3\text{p}_{y\beta}^1 \text{ (symmetry } \text{B}_{2u})$$
$$[\text{Ne}]3\text{s}3\text{p}_x^2 3\text{p}_y^2 3\text{p}_{z\beta}^1 \text{ (symmetry } \text{B}_{1u})$$

The non-zero matrix elements are the same as for the fluorine atom.

OH radical. The OH radical is the first of the small molecules considered here. The ground state of $\text{X}^2\Pi$ is modelled at a bond length of 0.96966 Å. The ground state has four-fold degeneracy and spin-orbit coupling causes these degenerate levels to be split into a two fold $\text{X}^2\Pi_{3/2}$ level and a two fold $\text{X}^2\Pi_{1/2}$ level. The following four electron configurations are required:

$$1\sigma^2 2\sigma^2 3\sigma^2 1\pi_x^2 1\pi_{y\alpha}^1 \text{ (symmetry } \text{B}_2)$$
$$1\sigma^2 2\sigma^2 3\sigma^2 1\pi_x^2 1\pi_{y\beta}^1 \text{(symmetry } \text{B}_2)$$
$$1\sigma^2 2\sigma^2 3\sigma^2 1\pi_y^2 1\pi_{x\alpha}^1 \text{ (symmetry } \text{B}_1)$$
$$1\sigma^2 2\sigma^2 3\sigma^2 1\pi_y^2 1\pi_{x\beta}^1 \text{ (symmetry } \text{B}_1)$$

The point group for this molecule, as with all molecules in this study within Molpro is C_{2v}, with the exception of C_2, and the symmetries of the spin-orbit operators, which transform as rotations in the appropriate direction, are: x direction = B_2; y direction = B_1 and z direction = A_2. Applying selection rules, only the following spin-orbit coupling matrix elements, for the levels listed above, will be non-zero for the ground state of the OH radical:

$$\langle B_1|\hat{H}_z^{so}|B_2\rangle \;\; \langle B_2|\hat{H}_z^{so}|B_1\rangle$$

NO radical. The NO radical ground state is $\text{X}^2\Pi$ at a bond length of 1.15077 Å and is four-fold degenerate. It is handled in the same way as the OH radical and the following four configurations are required:

$$1\sigma^2 2\sigma^2 3\sigma^2 4\sigma^2 5\sigma^2 1\pi^4 2\pi_{x\alpha}^1 \text{ (symmetry } \text{B}_1)$$
$$1\sigma^2 2\sigma^2 3\sigma^2 4\sigma^2 5\sigma^2 1\pi^4 2\pi_{x\beta}^1 \text{ (symmetry } \text{B}_1)$$
$$1\sigma^2 2\sigma^2 3\sigma^2 4\sigma^2 5\sigma^2 1\pi^4 2\pi_{y\alpha}^1 \text{ (symmetry } \text{B}_2)$$
$$1\sigma^2 2\sigma^2 3\sigma^2 4\sigma^2 5\sigma^2 1\pi^4 2\pi_{y\beta}^1 \text{ (symmetry } \text{B}_2)$$

Under the influence of spin-orbit coupling the four-fold degenerate ground state splits into two levels: a doubly degenerate $^2\Pi_{3/2}$ state and a doubly degenerate $^2\Pi_{1/2}$ state. The non-zero matrix elements are the same as for the OH radical but for the NO radical.

CN radical. The ground state of the CN radical is $X^2\Sigma$. Because this has no orbital angular momentum there will be no spin-orbit coupling. Instead, the first excited state $A^2\Pi$ is used instead at a bond length of 1.2333 Å. It is handled in the same way as the OH radical and the following four electron configurations are required:

$$1\sigma^2 2\sigma^2 3\sigma^2 1\pi^4 4\sigma^2 5\sigma^0 2\pi^1_{x\alpha} \text{ (symmetry } B_1)$$
$$1\sigma^2 2\sigma^2 3\sigma^2 1\pi^4 4\sigma^2 5\sigma^0 2\pi^1_{x\beta} \text{ (symmetry } B_1)$$
$$1\sigma^2 2\sigma^2 3\sigma^2 1\pi^4 4\sigma^2 5\sigma^0 2\pi^1_{y\alpha} \text{ (symmetry } B_2)$$
$$1\sigma^2 2\sigma^2 3\sigma^2 1\pi^4 4\sigma^2 5\sigma^0 2\pi^1_{y\beta} \text{ (symmetry } B_2)$$

The non-zero matrix elements are the same as for the OH radical.

C_2 radical. The final molecule in this study is the C_2 radical. The ground state of the C_2 radical is $X^1\Sigma^+$ which has neither orbital angular momentum nor spin angular momentum and therefore there will be no spin-orbit coupling. Instead, the first excited triplet state a $^3\Pi_u$ is used instead at a bond length of 1.3119 Å. This state has eight-fold degeneracy and spin-orbit coupling will split this into three levels: a $^3\Pi_{u(2)}$ level, a $^3\Pi_{u(1)}$ and a $^3\Pi_{u(0)}$ level. The point group for this molecule is D_{2h} and the symmetries of the spin-orbit operators, which transform as rotations in the appropriate direction, are: x direction = B_{3g}; y direction = B_{2g} and z direction = B_{1g}. The following six electron configurations are required by MCCI:

$$1\sigma^2 2\sigma^2 3\sigma^2 4\sigma^2 1\pi^2_x 1\pi^1_{y\alpha} 5\sigma^1_\alpha \text{ (symmetry } B_{2u})$$
$$1\sigma^2 2\sigma^2 3\sigma^2 4\sigma^2 1\pi^2_x 1\pi^1_{y\beta} 5\sigma^1_\beta \text{ (symmetry } B_{2u})$$
$$1\sigma^2 2\sigma^2 3\sigma^2 4\sigma^2 1\pi^2_x 1\pi^1_{y\alpha} 5\sigma^1_\beta \text{ (symmetry } B_{2u})$$
$$1\sigma^2 2\sigma^2 3\sigma^2 4\sigma^2 1\pi^2_y 1\pi^1_{x\alpha} 5\sigma^1_\alpha \text{ (symmetry } B_{3u})$$
$$1\sigma^2 2\sigma^2 3\sigma^2 4\sigma^2 1\pi^2_y 1\pi^1_{x\beta} 5\sigma^1_\beta \text{ (symmetry } B_{3u})$$
$$1\sigma^2 2\sigma^2 3\sigma^2 4\sigma^2 1\pi^2_y 1\pi^1_{x\alpha} 5\sigma^1_\beta \text{ (symmetry } B_{3u})$$

The non-zero matrix elements are as follows:

$$\langle B_{2u}|\hat{H}^{so}_z|B_{3u}\rangle \;\; \langle B_{3u}|\hat{H}^{so}_z|B_{2u}\rangle$$

Energy Convergence

In order to determine an appropriate basis set to use for spin-orbit coupling calcula-

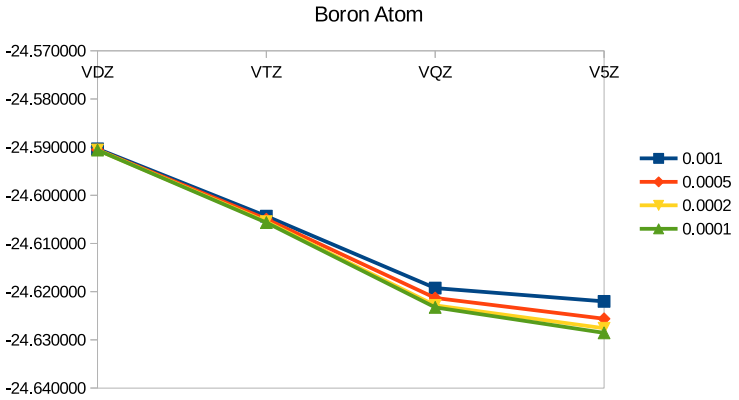

Figure 3.4: MCCI Energies for the boron atom with a variety of c_{min} values from 0.001 to 0.0001. Energy convergence is 0.001 in all cases. All energies in Hartrees.

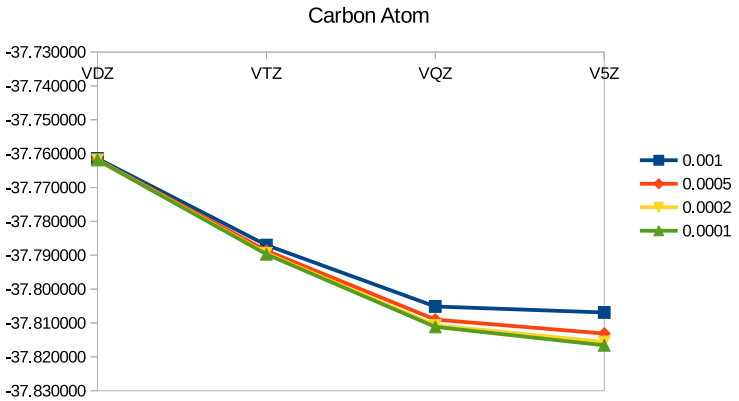

Figure 3.5: MCCI Energies for the carbon atom with a variety of c_{min} values from 0.001 to 0.0001. Energy convergence is 0.001 in all cases. All energies in Hartrees.

tions, the convergence of the energy of the $|B_{3u}, \alpha\rangle$ state of the B, F and Cl atoms, the $|B_{2g}, \alpha\alpha\rangle$ state of the C, O, Si and S atoms, the $|B_1, \alpha\rangle$ state of the OH, NO and CN radicals and the $|B_{2u}, \alpha\alpha\rangle$ state for C_2 was calculated in MCCI using a series of basis sets from cc-pVDZ to cc-pV5Z and a variety of c_{min} values. The results are detailed in figures 3.4 to 3.14.

Here it can be seen that rapid convergence appears to occur once the cc-pVQZ basis set is used, with the exception of the Si, S and Cl atoms. The molecules CN and NO show increases in energy as the basis set is improved but the reason for this is clear from the figures. As the basis set is improved, the c_{min} value must be reduced accordingly. Looking at the energy obtained with the cc-pV5Z basis set, it is seen that reducing the c_{min} value steadily from 0.001 to 0.0001 corrects for this problem. In most cases however the extra effort in obtaining convergence at the cc-pV5Z level

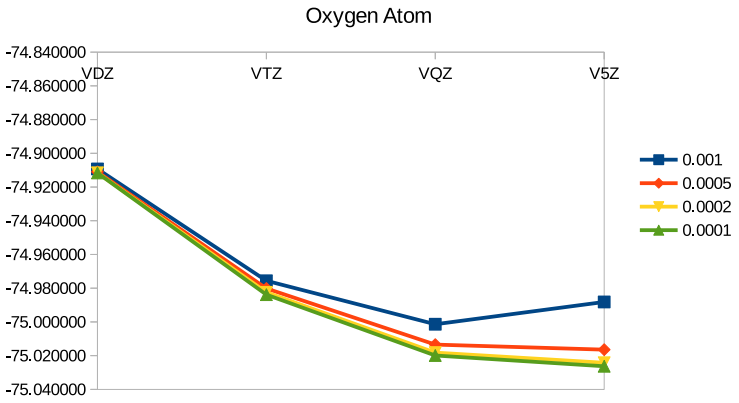

Figure 3.6: MCCI Energies for the oxygen atom with a variety of c_{min} values from 0.001 to 0.0001. Energy convergence is 0.001 in all cases. All energies in Hartrees.

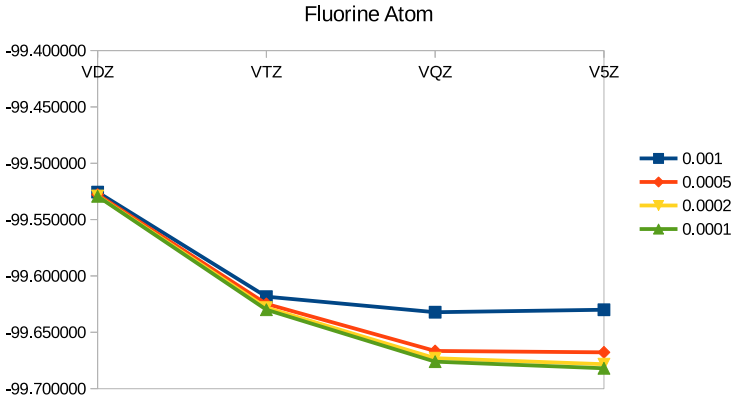

Figure 3.7: MCCI Energies for the fluorine atom with a variety of c_{min} values from 0.001 to 0.0001. Energy convergence is 0.001 in all cases. All energies in Hartrees.

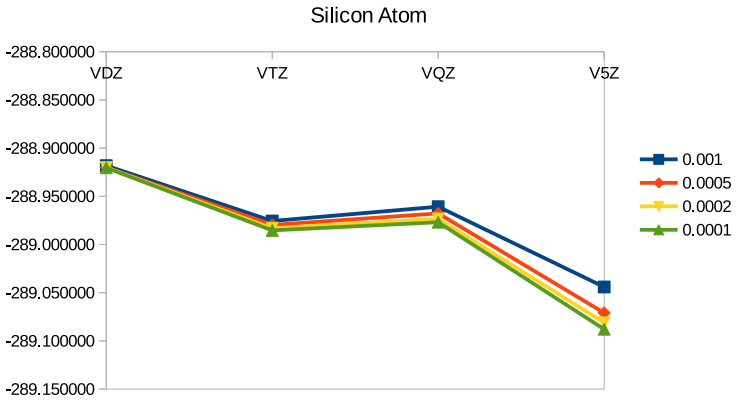

Figure 3.8: MCCI Energies for the silicon atom with a variety of c_{min} values from 0.001 to 0.0001. Energy convergence is 0.001 in all cases. All energies in Hartrees.

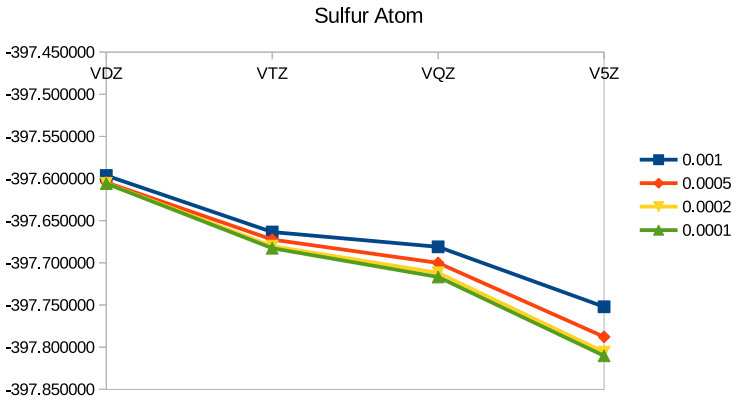

Figure 3.9: MCCI Energies for the sulfur atom with a variety of c_{min} values from 0.001 to 0.0001. Energy convergence is 0.001 in all cases. All energies in Hartrees.

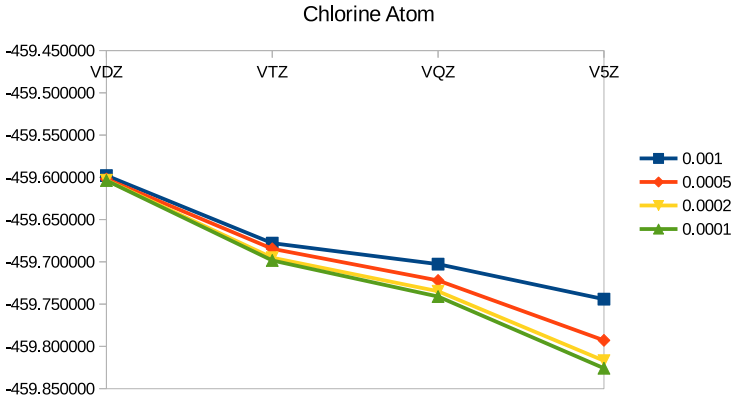

Figure 3.10: MCCI Energies for the chlorine atom with a variety of c_{min} values from 0.001 to 0.0001. Energy convergence is 0.001 in all cases. All energies in Hartrees.

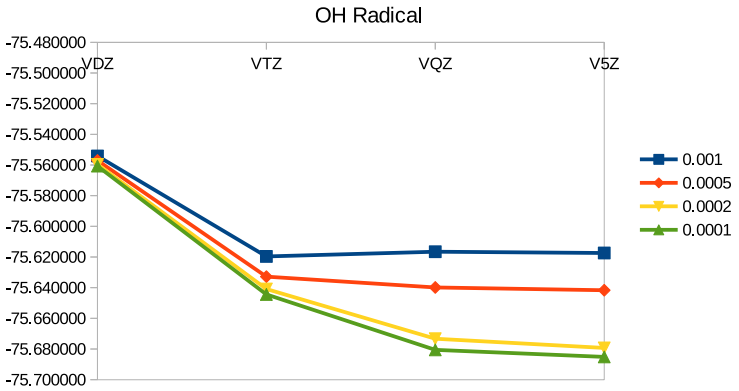

Figure 3.11: MCCI Energies for the OH radical with a variety of c_{min} values from 0.001 to 0.0001. Energy convergence is 0.001 in all cases. All energies in Hartrees.

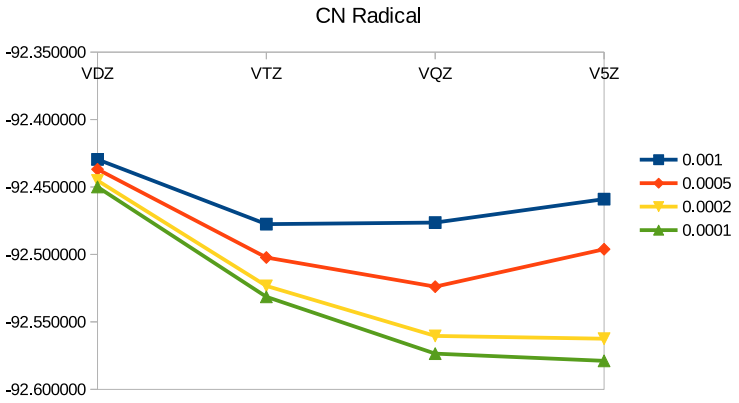

Figure 3.12: MCCI Energies for the CN radical with a variety of c_{min} values from 0.001 to 0.0001. Energy convergence is 0.001 in all cases. All energies in Hartrees.

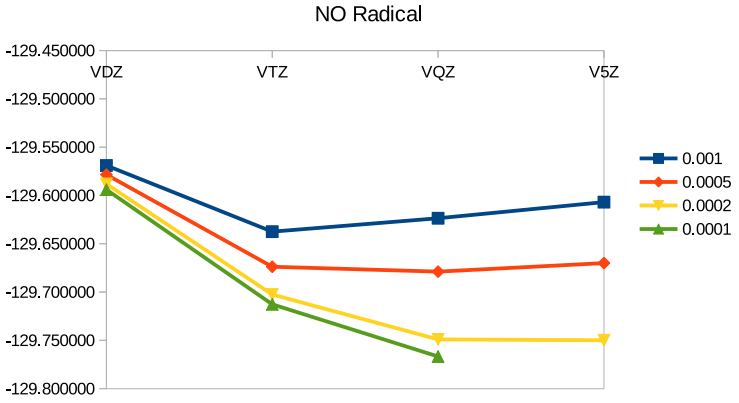

Figure 3.13: MCCI Energies for the NO radical with a variety of c_{min} values from 0.001 to 0.0001. Energy convergence is 0.001 in all cases. All energies in Hartrees.

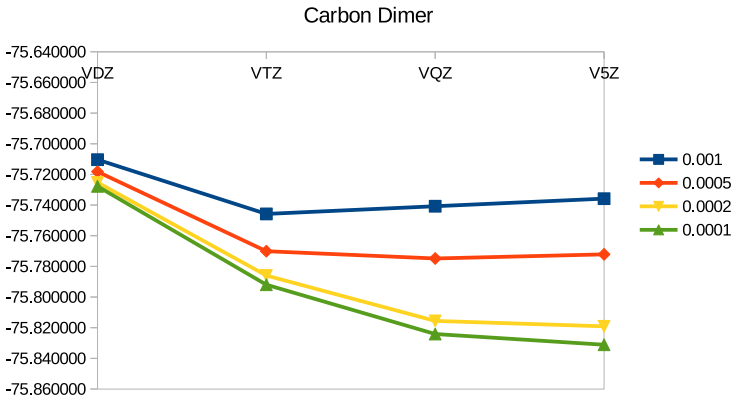

Figure 3.14: MCCI Energies for the C_2 radical with a variety of c_{min} values from 0.001 to 0.0001. Energy convergence is 0.001 in all cases. All energies in Hartrees.

outweighs the absolute energy gain compared to using cc-pVQZ. At the cc-pVQZ level therefore, a reasonable compromise between accuracy and computational ease would appear to be obtained. From these initial graphs, it would appear that there is worthwhile improvement in energy stabilisation using smaller values of c_{min}. The absolute energy however is not the crucial parameter: of higher importance is the variation of spin-orbit coupling matrix element. The convergence of the magnitude of the spin-orbit coupling matrix elements was therefore investigated for each species. Results are shown for the $\mathcal{H}_z^{so}$ operator using a range of basis sets and c_{min} values and are shown in figures 3.15 to 3.25. Once again, good convergence is seen once cc-pVQZ is used with the exception of the Si, S and Cl atoms. This is not surprising given that within the computational resources available, these atoms had not displayed energy convergence with basis set. It should be noted however that the value of c_{min}, with the exception of 0.001, did not affect the reported spin-orbit coupling matrix element for the S or Cl atoms at these higher basis sets. The problem with the Si atom spin-orbit matrix element at the cc-pV5Z basis set is explained by the need to drop the value of c_{min} below 0.0001. Within the computational resources available, this was not a viable solution and for this atom, the cc-pV5Z basis set was discarded. Additionally, it is clear that using c_{min} values smaller than 0.0005 produces very little change in the spin-orbit coupling matrix element on any of the species in this study. Given the severe computational cost of using the cc-pV5Z basis set and the invariance of the spin-orbit coupling constant beyond cutoff values of 0.0005 it was therefore decided to use the cc-pVQZ basis set with c_{min} values of 0.0005 on all doublet species. Unfortunately, for triplet species, a problem arose with the energy calculations of the remaining electron configurations. All of these electron configurations for a species should have degenerate energy values. For the triplet species however, the $M_s = 0$ electron configurations did not converge to the M_s = -1,1 configuration energies. This was a result of the c_{min} value being too low. For the C and O atoms, reducing c_{min} to 0.0001 with the cc-pVQZ basis set proved sufficient to achieve degeneracy. Unfortunately for the remaining atoms and molecules: Si, S and C_2, this was not sufficient. Reducing this value below 0.0001 was not computationally feasible, the only recourse was to reduce the quality of the basis set and convergence was only found when the cc-pVDZ basis set was used with a c_{min} cutoff of 0.0001. In summary therefore, the cc-pVQZ basis set with c_{min} = 0.0005 was used for the B, F, Cl, NO, CN and OH species, the cc-VQZ basis set

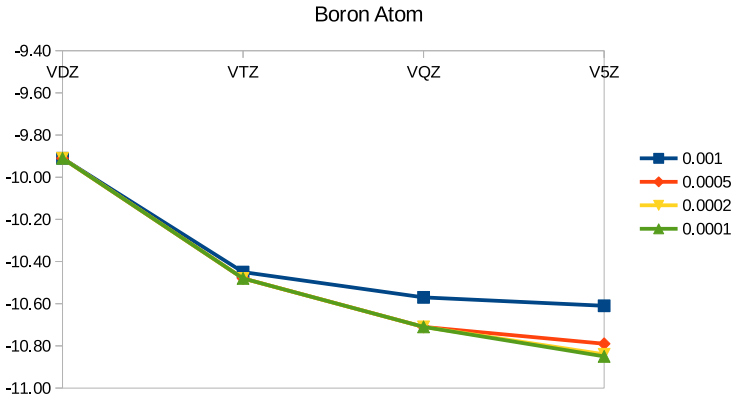

Figure 3.15: MCCI spin-orbit coupling matrix element magnitudes for the boron atom with a variety of c_{min} values from 0.001 to 0.0001. All spin-orbit coupling matrix element values are in cm^{-1}

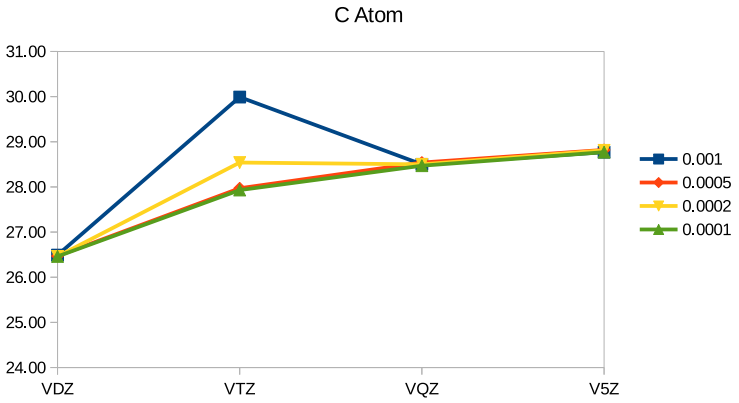

Figure 3.16: MCCI spin-orbit coupling matrix element magnitudes for the carbon atom with a variety of c_{min} values from 0.001 to 0.0001. All spin-orbit coupling matrix element values in cm^{-1}

with $c_{min} = 0.0001$ was used for the C and O atoms and finally the cc-pVDZ basis set with $c_{min} = 0.0001$ was used for the Si, S and C_2 species.

Following this initial benchmarking work, the full set of spin-orbit coupling matrix elements were calculated for each species. Calculations for the operators $\mathcal{H}_x^{so}$, $\mathcal{H}_y^{so}$ and $\mathcal{H}_z^{so}$ were performed using MCCI in the basis of electron configurations listed earlier for the atoms and diatomic molecules.

In order to show the removal of degeneracy of the energy levels by spin-orbit coupling, the individual matrix element results for the $\mathcal{H}^{so}$ operator calculations are formed into a matrix in the basis of degenerate states and spins for each species. This matrix is then required to be diagonalised and the eigenvalues will be the en-

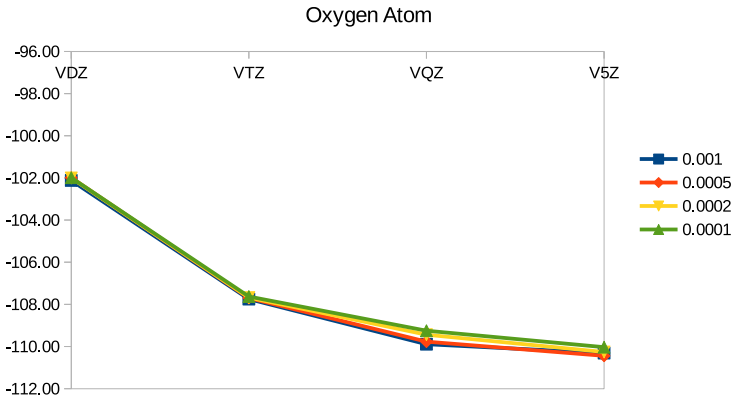

Figure 3.17: MCCI spin-orbit coupling matrix element magnitudes for the oxygen atom with a variety of c_{min} values from 0.001 to 0.0001. All spin-orbit coupling matrix element values in cm^{-1}

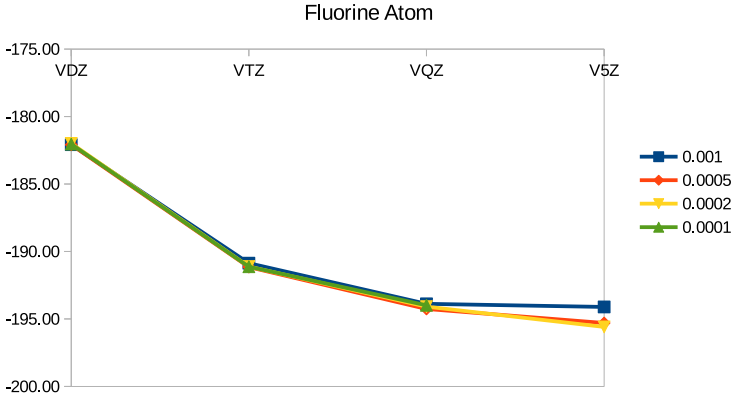

Figure 3.18: MCCI spin-orbit coupling matrix element magnitudes for the fluorine atom with a variety of c_{min} values from 0.001 to 0.0001. All spin-orbit coupling matrix element values in cm^{-1}

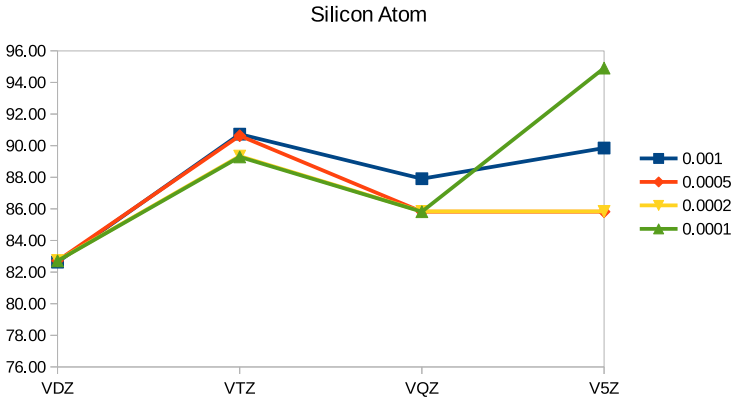

Figure 3.19: MCCI spin-orbit coupling matrix element magnitudes for the silicon atom with a variety of c_{min} values from 0.001 to 0.0001. All spin-orbit coupling matrix element values in cm^{-1}

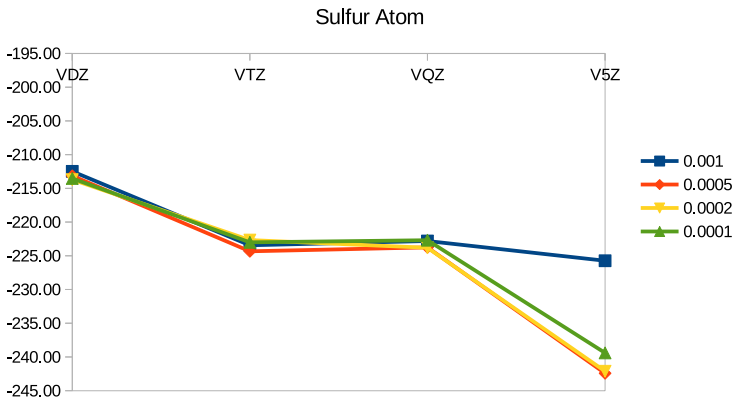

Figure 3.20: MCCI spin-orbit coupling matrix element magnitudes for the sulfur atom with a variety of c_{min} values from 0.001 to 0.0001. All spin-orbit coupling matrix element values in cm^{-1}

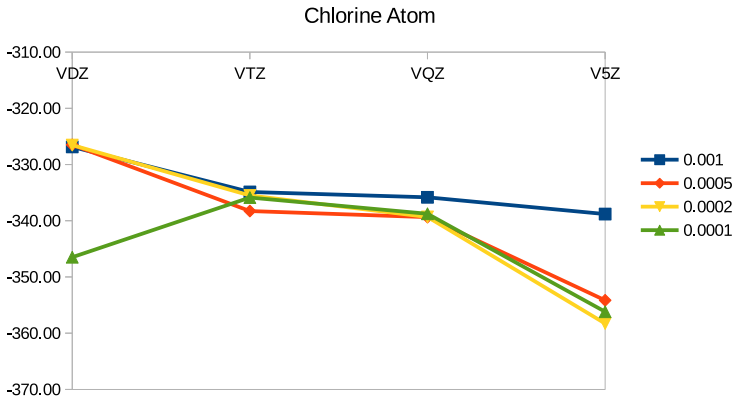

Figure 3.21: MCCI spin-orbit coupling matrix element magnitudes for the chlorine atom with a variety of c_{min} values from 0.001 to 0.0001. All spin-orbit coupling matrix element values in cm^{-1}

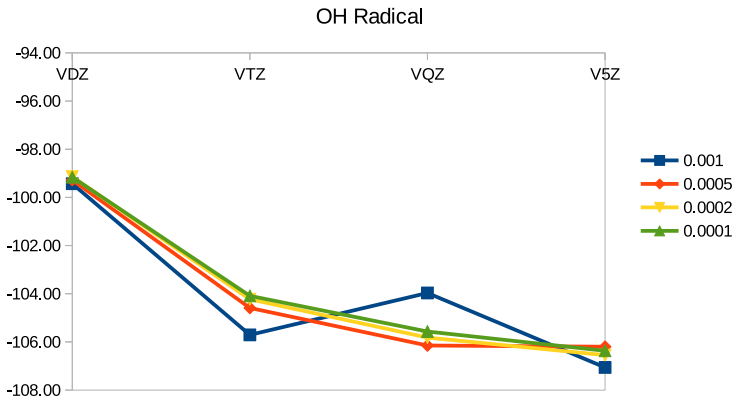

Figure 3.22: MCCI spin-orbit coupling matrix element magnitudes for the OH radical with a variety of c_{min} values from 0.001 to 0.0001. All spin-orbit coupling matrix element values in cm^{-1}

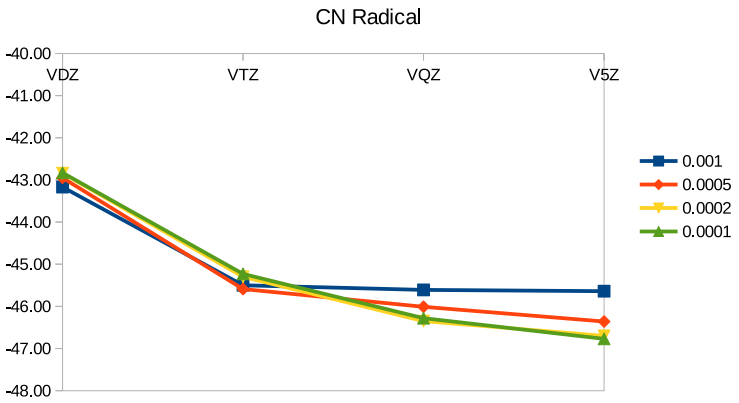

Figure 3.23: MCCI spin-orbit coupling matrix element magnitudes for the CN radical with a variety of c_{min} values from 0.001 to 0.0001. All spin-orbit coupling matrix element values in cm^{-1}

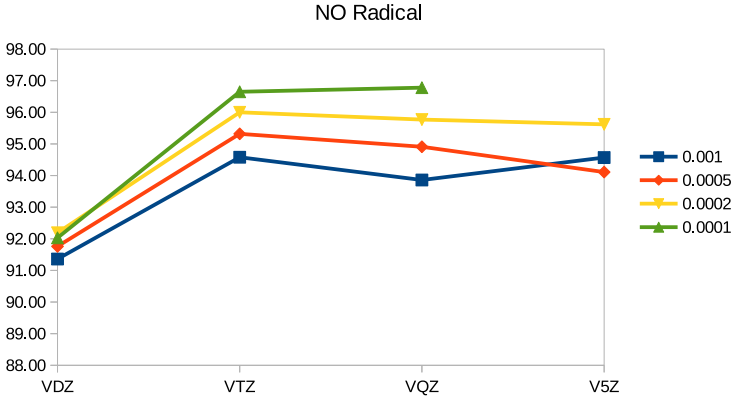

Figure 3.24: MCCI spin-orbit coupling matrix element magnitudes for the NO radical with a variety of c_{min} values from 0.001 to 0.0001. All spin-orbit coupling matrix element values in cm^{-1}

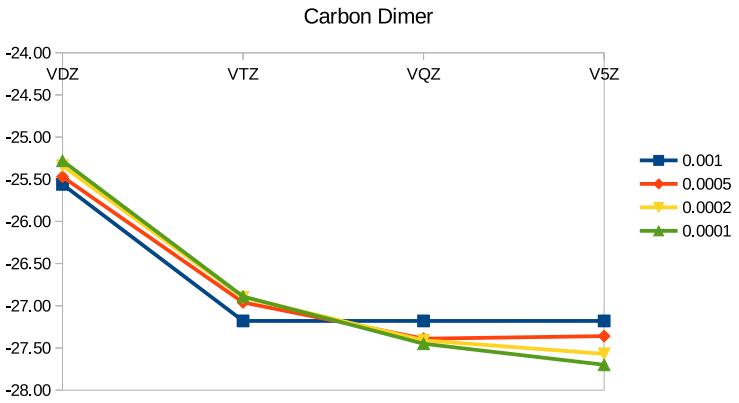

Figure 3.25: MCCI spin-orbit coupling matrix element magnitudes for the C_2 radical with a variety of c_{min} values from 0.001 to 0.0001. All spin-orbit coupling matrix element values in cm^{-1}

ergy level splittings. The general matrix for the atoms exhibiting a doublet ground state is shown in equation 3.39.

$$H^{so} = \begin{pmatrix} 0.00 & 0.00 & a & 0.00 & 0.00 & b \\ 0.00 & 0.00 & 0.00 & c & d & 0.00 \\ e & 0.00 & 0.00 & 0.00 & 0.00 & f \\ 0.00 & g & 0.00 & 0.00 & h & 0.00 \\ 0.00 & i & 0.00 & j & 0.00 & 0.00 \\ k & 0.00 & l & 0.00 & 0.00 & 0.00 \end{pmatrix} \tag{3.39}$$

Here, the following matrix elements are defined:

$$\begin{aligned} \text{a} &= \langle B_{3u}, \alpha | \mathcal{H}_z^{so} | B_{2u}, \alpha \rangle \\ \text{b} &= \langle B_{3u}, \alpha | \mathcal{H}_y^{so} | B_{1u}, \beta \rangle \\ \text{c} &= \langle B_{3u}, \beta | \mathcal{H}_z^{so} | B_{2u}, \beta \rangle \\ \text{d} &= \langle B_{3u}, \beta | \mathcal{H}_y^{so} | B_{1u}, \alpha \rangle \\ \text{e} &= \langle B_{2u}, \alpha | \mathcal{H}_z^{so} | B_{3u}, \alpha \rangle \\ \text{f} &= \langle B_{2u}, \alpha | \mathcal{H}_x^{so} | B_{1u}, \beta \rangle \\ \text{g} &= \langle B_{2u}, \beta | \mathcal{H}_z^{so} | B_{3u}, \beta \rangle \\ \text{h} &= \langle B_{2u}, \beta | \mathcal{H}_x^{so} | B_{1u}, \alpha \rangle \\ \text{i} &= \langle B_{1u}, \alpha | \mathcal{H}_y^{so} | B_{3u}, \beta \rangle \\ \text{j} &= \langle B_{1u}, \alpha | \mathcal{H}_x^{so} | B_{2u}, \beta \rangle \\ \text{k} &= \langle B_{1u}, \beta | \mathcal{H}_y^{so} | B_{3u}, \alpha \rangle \\ \text{l} &= \langle B_{1u}, \beta | \mathcal{H}_x^{so} | B_{2u}, \alpha \rangle \end{aligned}$$

Recall the matrix elements for the $\mathcal{H}_x^{so}$ and $\mathcal{H}_z^{so}$ operators are pure complex numbers and the $\mathcal{H}_y^{so}$ elements are pure real numbers.

For atoms exhibiting a triplet ground state, the general matrix is as shown in equation 3.40

$$H^{so} = \begin{pmatrix} 0.00 & 0.00 & 0.00 & 0.00 & a & 0.00 & 0.00 & b & 0.00 \\ 0.00 & 0.00 & 0.00 & c & 0.00 & d & e & 0.00 & f \\ 0.00 & 0.00 & 0.00 & 0.00 & g & 0.00 & 0.00 & h & 0.00 \\ 0.00 & j & 0.00 & 0.00 & 0.00 & 0.00 & k & 0.00 & 0.00 \\ l & 0.00 & m & 0.00 & 0.00 & 0.00 & 0.00 & 0.00 & 0.00 \\ 0.00 & n & 0.00 & 0.00 & 0.00 & 0.00 & 0.00 & 0.00 & p \\ 0.00 & q & 0.00 & r & 0.00 & 0.00 & 0.00 & 0.00 & 0.00 \\ s & 0.00 & t & 0.00 & 0.00 & 0.00 & 0.00 & 0.00 & 0.00 \\ 0.00 & u & 0.00 & 0.00 & 0.00 & v & 0.00 & 0.00 & 0.00 \end{pmatrix} \tag{3.40}$$

Here, the following matrix elements are defined:

$$\begin{aligned}
\text{a} &= \langle B_{1g}, \alpha\alpha | \mathcal{H}_x^{so} | B_{2g}, \alpha\beta + \beta\alpha \rangle \\
\text{b} &= \langle B_{1g}, \alpha\alpha | \mathcal{H}_y^{so} | B_{3g}, \alpha\beta + \beta\alpha \rangle \\
\text{c} &= \langle B_{1g}, \alpha\beta + \beta\alpha | \mathcal{H}_x^{so} | B_{2g}, \alpha\alpha \rangle \\
\text{d} &= \langle B_{1g}, \alpha\beta + \beta\alpha | \mathcal{H}_x^{so} | B_{2g}, \beta\beta \rangle \\
\text{e} &= \langle B_{1g}, \alpha\beta + \beta\alpha | \mathcal{H}_y^{so} | B_{3g}, \alpha\alpha \rangle \\
\text{f} &= \langle B_{1g}, \alpha\beta + \beta\alpha | \mathcal{H}_y^{so} | B_{3g}, \beta\beta \rangle \\
\text{g} &= \langle B_{1g}, \beta\beta | \mathcal{H}_x^{so} | B_{2g}, \alpha\beta + \beta\alpha \rangle \\
\text{h} &= \langle B_{2g}, \beta\beta | \mathcal{H}_y^{so} | B_{3g}, \alpha\beta + \beta\alpha \rangle \\
\text{j} &= \langle B_{2g}, \alpha\alpha | \mathcal{H}_x^{so} | B_{1g}, \alpha\beta + \beta\alpha \rangle \\
\text{k} &= \langle B_{2g}, \alpha\alpha | \mathcal{H}_z^{so} | B_{3g}, \alpha\alpha \rangle \\
\text{l} &= \langle B_{2g}, \alpha\beta + \beta\alpha | \mathcal{H}_x^{so} | B_{1g}, \alpha\alpha \rangle \\
\text{m} &= \langle B_{2g}, \alpha\beta + \beta\alpha | \mathcal{H}_x^{so} | B_{1g}, \beta\beta \rangle \\
\text{n} &= \langle B_{2g}, \beta\beta | \mathcal{H}_x^{so} | B_{1g}, \alpha\beta + \beta\alpha \rangle \\
\text{p} &= \langle B_{2g}, \beta\beta | \mathcal{H}_z^{so} | B_{3g}, \beta\beta \rangle \\
\text{q} &= \langle B_{3g}, \alpha\alpha | \mathcal{H}_y^{so} | B_{1g}, \alpha\beta + \beta\alpha \rangle \\
\text{r} &= \langle B_{3g}, \alpha\alpha | \mathcal{H}_z^{so} | B_{2g}, \alpha\alpha \rangle \\
\text{s} &= \langle B_{3g}, \alpha\beta + \beta\alpha | \mathcal{H}_y^{so} | B_{1g}, \alpha\alpha \rangle \\
\text{t} &= \langle B_{3g}, \alpha\beta + \beta\alpha | \mathcal{H}_y^{so} | B_{1g}, \beta\beta \rangle \\
\text{u} &= \langle B_{3g}, \beta\beta | \mathcal{H}_y^{so} | B_{1g}, \alpha\beta + \beta\alpha \rangle \\
\text{v} &= \langle B_{3g}, \beta\beta | \mathcal{H}_z^{so} | B_{2g}, \beta\beta \rangle
\end{aligned}$$

Recall the matrix elements for the $\mathcal{H}_x^{so}$ and $\mathcal{H}_z^{so}$ operators are purely imaginary numbers and the $\mathcal{H}_y^{so}$ elements are purely real numbers.

For the diatomic molecules other than C_2, which have a doublet state, the general matrix is shown in equation 3.41. All of these numbers are pure complex numbers.

$$H^{so} = \begin{pmatrix} 0.00 & 0.00 & m & 0.00 \\ 0.00 & 0.00 & 0.00 & n \\ o & 0.00 & 0.00 & 0.00 \\ 0.00 & p & 0.00 & 0.00 \end{pmatrix} \tag{3.41}$$

Here, the following matrix elements are defined:

$$\begin{aligned} \mathrm{m} &= \langle B_1, \alpha | \mathcal{H}_z^{so} | B_2, \alpha \rangle \\ \mathrm{n} &= \langle B_1, \beta | \mathcal{H}_z^{so} | B_2, \beta \rangle \\ \mathrm{o} &= \langle B_2, \alpha | \mathcal{H}_z^{so} | B_1, \alpha \rangle \\ \mathrm{p} &= \langle B_2, \beta | \mathcal{H}_z^{so} | B_1, \beta \rangle \end{aligned}$$

All of these numbers are purely imaginary numbers because only the matrix elements for the $\mathcal{H}_z^{so}$ operator are non-zero.

Finally, for the triplet C_2, the general matrix is shown in equation 3.42. All of these numbers are purely imaginary numbers because, once more, only the matrix elements for the $\mathcal{H}_z^{so}$ operator are non-zero.

$$H^{so} = \begin{pmatrix} 0.00 & 0.00 & 0.00 & a & 0.00 & 0.00 \\ 0.00 & 0.00 & 0.00 & 0.00 & 0.00 & 0.00 \\ 0.00 & 0.00 & 0.00 & 0.00 & 0.00 & b \\ c & 0.00 & 0.00 & 0.00 & 0.00 & 0.00 \\ 0.00 & 0.00 & 0.00 & 0.00 & 0.00 & 0.00 \\ 0.00 & 0.00 & d & 0.00 & 0.00 & 0.00 \end{pmatrix} \tag{3.42}$$

Here, the following matrix elements are defined:

$$\begin{aligned} \mathrm{a} &= \langle B_{3u}, \alpha\alpha | \mathcal{H}_z^{so} | B_{2u}, \alpha\alpha \rangle \\ \mathrm{b} &= \langle B_{3u}, \beta\beta | \mathcal{H}_z^{so} | B_{2u}, \beta\beta \rangle \\ \mathrm{c} &= \langle B_{2u}, \alpha\alpha | \mathcal{H}_z^{so} | B_{3u}, \alpha\alpha \rangle \\ \mathrm{d} &= \langle B_{2u}, \beta\beta | \mathcal{H}_z^{so} | B_{3u}, \beta\beta \rangle \end{aligned}$$

The specific matrices for each species are now presented along with the eigenvalues of those matrices which represent the energetic splitting. Where degenerate eigenvalues

exist, values are reported as averages as there are slight energy differences between them due to the stochastic nature of MCCI.

The matrix for the boron atom is shown in equation 3.43.

$$H_B^{so} = \begin{pmatrix} 0.00 & 0.00 & -10.71i & 0.00 & 0.00 & +10.71 \\ 0.00 & 0.00 & 0.00 & +10.70i & +10.71 & 0.00 \\ +10.71i & 0.00 & 0.00 & 0.00 & 0.00 & -10.71i \\ 0.00 & -10.71i & 0.00 & 0.00 & +10.70i & 0.00 \\ 0.00 & +10.71 & 0.00 & -10.70i & 0.00 & 0.00 \\ +10.71 & 0.00 & +10.71i & 0.00 & 0.00 & 0.00 \end{pmatrix} \tag{3.43}$$

Diagonalisation of this complex matrix results in six eigenvalues split into a group of two and four as expected. Two eigenvalues of -21.42 cm^{-1} represent the lower energy two-fold $^2P_{1/2}$ level and the four eigenvalues of +10.71 cm^{-1} represent the higher energy four-fold $^2P_{3/2}$ level. This leaves $\Delta_{so} = 32.13$ cm^{-1} compared to the experimental value [28] of 15.29cm^{-1}, an error of 110%.

The matrix for the carbon atom is shown in equation 3.44.

$$H_C^{so} = \begin{pmatrix} 0.00 & 0.00 & 0.00 & 0.00 & -20.05i & 0.00 & 0.00 & +20.17 & 0.00 \\ 0.00 & 0.00 & 0.00 & +20.17i & 0.00 & -20.06i & -20.06 & 0.00 & -20.18 \\ 0.00 & 0.00 & 0.00 & 0.00 & -20.17i & 0.00 & 0.00 & -20.05 & 0.00 \\ 0.00 & -20.17i & 0.00 & 0.00 & 0.00 & 0.00 & -28.47i & 0.00 & 0.00 \\ +20.05i & 0.00 & +20.17i & 0.00 & 0.00 & 0.00 & 0.00 & 0.00 & 0.00 \\ 0.00 & +20.06i & 0.00 & 0.00 & 0.00 & 0.00 & 0.00 & 0.00 & +28.47i \\ 0.00 & -20.06 & 0.00 & +28.47i & 0.00 & 0.00 & 0.00 & 0.00 & 0.00 \\ +20.17 & 0.00 & -20.05 & 0.00 & 0.00 & 0.00 & 0.00 & 0.00 & 0.00 \\ 0.00 & -20.18 & 0.00 & 0.00 & 0.00 & -28.47i & 0.00 & 0.00 & 0.00 \end{pmatrix} \tag{3.44}$$

Diagonalisation of this complex matrix results in nine eigenvalues split into groups of five, three and one as expected. A single non-degenerate eigenvalue of -56.91 cm^{-1} represents the lowest energy $^3P_0$ level, three eigenvalues of energy -28.45 cm^{-1} represent the higher energy $^3P_1$ level and the five eigenvalues of +28.45 cm^{-1} represent the highest energy five-fold degenerate $^3P_2$ level. This leaves $\Delta_{so} = 85.36$ cm^{-1} compared to the experimental value [28] of 43.40 cm^{-1}, an error of 97%.

The matrix for the oxygen atom is shown in equation 3.44.

$$H_O^{so} = \begin{pmatrix} 0.00 & 0.00 & 0.00 & 0.00 & +77.63i & 0.00 & 0.00 & -77.97 & 0.00 \\ 0.00 & 0.00 & 0.00 & +77.79i & 0.00 & -77.30i & +77.32 & 0.00 & +77.79 \\ 0.00 & 0.00 & 0.00 & 0.00 & -77.45i & 0.00 & 0.00 & -77.09 & 0.00 \\ 0.00 & -77.79i & 0.00 & 0.00 & 0.00 & 0.00 & -109.25i & 0.00 & 0.00 \\ -77.63i & 0.00 & +77.45i & 0.00 & 0.00 & 0.00 & 0.00 & 0.00 & 0.00 \\ 0.00 & +77.30i & 0.00 & 0.00 & 0.00 & 0.00 & 0.00 & 0.00 & +109.22i \\ 0.00 & +77.32 & 0.00 & +109.25i & 0.00 & 0.00 & 0.00 & 0.00 & 0.00 \\ -77.97 & 0.00 & -77.09 & 0.00 & 0.00 & 0.00 & 0.00 & 0.00 & 0.00 \\ 0.00 & +77.79 & 0.00 & 0.00 & 0.00 & -109.22i & 0.00 & 0.00 & 0.00 \end{pmatrix} \quad (3.45)$$

Diagonalisation of this complex matrix results in nine eigenvalues split into groups of five, three and one as expected. A single non-degenerate eigenvalue of +219.05 cm^{-1} represents the highest energy $^3P_0$ level, three eigenvalues of energy +109.51 cm^{-1} represent the lower energy $^3P_1$ level and the five eigenvalues of -109.52 cm^{-1} represent the lowest energy five-fold degenerate $^3P_2$ level. This leaves $\Delta_{so} = 328.57$ cm^{-1} compared to the experimental value [28] of 226.98 cm^{-1}, an error of 45%.

The matrix for the fluorine atom is shown in equation 3.46.

$$H_F^{so} = \begin{pmatrix} 0.00 & 0.00 & +194.26i & 0.00 & 0.00 & -195.30 \\ 0.00 & 0.00 & 0.00 & -194.32i & +195.34 & 0.00 \\ -194.26i & 0.00 & 0.00 & 0.00 & 0.00 & -195.26i \\ 0.00 & +194.32i & 0.00 & 0.00 & +195.30i & 0.00 \\ 0.00 & +195.34 & 0.00 & -195.30i & 0.00 & 0.00 \\ +195.30 & 0.00 & +195.26i & 0.00 & 0.00 & 0.00 \end{pmatrix} \quad (3.46)$$

Diagonalisation of this complex matrix results in six eigenvalues split into a group of two and four as expected. Two eigenvalues of +389.93 cm^{-1} represent the upper energy two-fold $^2P_{1/2}$ level and the four eigenvalues of -194.96 cm^{-1} represent the lower energy four-fold $^2P_{3/2}$ level. This leaves $\Delta_{so} = 584.89$ cm^{-1} compared to the experimental value [28] of 404.10 cm^{-1}, an error of 45%.

The matrix for the silicon atom is shown in equation 3.47.

$$H_{Si}^{so} = \begin{pmatrix} 0.00 & 0.00 & 0.00 & 0.00 & +58.41i & 0.00 & 0.00 & +58.39 & 0.00 \\ 0.00 & 0.00 & 0.00 & +58.38i & 0.00 & +58.35i & +58.35 & 0.00 & +58.38 \\ 0.00 & 0.00 & 0.00 & 0.00 & +58.33i & 0.00 & 0.00 & -58.37 & 0.00 \\ 0.00 & -58.38i & 0.00 & 0.00 & 0.00 & 0.00 & +82.71i & 0.00 & 0.00 \\ -58.41i & 0.00 & -58.33i & 0.00 & 0.00 & 0.00 & 0.00 & 0.00 & 0.00 \\ 0.00 & -58.35i & 0.00 & 0.00 & 0.00 & 0.00 & 0.00 & 0.00 & +82.78i \\ 0.00 & +58.35 & 0.00 & -82.71i & 0.00 & 0.00 & 0.00 & 0.00 & 0.00 \\ +58.39 & 0.00 & -58.37 & 0.00 & 0.00 & 0.00 & 0.00 & 0.00 & 0.00 \\ 0.00 & +58.38 & 0.00 & 0.00 & 0.00 & -82.78i & 0.00 & 0.00 & 0.00 \end{pmatrix} \quad (3.47)$$

Diagonalisation of this complex matrix results in nine eigenvalues split into groups of five, three and one as expected. A single non-degenerate eigenvalue of -164.03

cm^{-1} represents the lowest energy $^3P_0$ level, three eigenvalues of energy -83.64 cm^{-1} represent the higher energy $^3P_1$ level and the five eigenvalues of +82.38 cm^{-1} represent the highest energy five-fold degenerate $^3P_2$ level. This leaves $\Delta_{so} = 246.41$ cm^{-1} compared to the experimental value [28] of 223.16 cm^{-1}, an error of 10%.

The matrix for the sulfur atom is shown in equation 3.48.

$$H_S^{so} = \begin{pmatrix} 0.00 & 0.00 & 0.00 & 0.00 & +151.06i & 0.00 & 0.00 & +151.06 & 0.00 \\ 0.00 & 0.00 & 0.00 & +150.96i & 0.00 & +150.92i & +150.99 & 0.00 & +150.99 \\ 0.00 & 0.00 & 0.00 & 0.00 & -150.92i & 0.00 & 0.00 & +150.96 & 0.00 \\ 0.00 & -150.96i & 0.00 & 0.00 & 0.00 & 0.00 & -213.53i & 0.00 & 0.00 \\ -151.06i & 0.00 & +150.92i & 0.00 & 0.00 & 0.00 & 0.00 & 0.00 & 0.00 \\ 0.00 & -150.92i & 0.00 & 0.00 & 0.00 & 0.00 & 0.00 & 0.00 & -213.54i \\ 0.00 & +150.99 & 0.00 & +213.53i & 0.00 & 0.00 & 0.00 & 0.00 & 0.00 \\ +151.06 & 0.00 & +150.96 & 0.00 & 0.00 & 0.00 & 0.00 & 0.00 & 0.00 \\ 0.00 & +150.99 & 0.00 & 0.00 & 0.00 & +213.54i & 0.00 & 0.00 & 0.00 \end{pmatrix} \quad (3.48)$$

Diagonalisation of this complex matrix results in nine eigenvalues split into groups of five, three and one as expected. A single non-degenerate eigenvalue of +427.49 cm^{-1} represents the highest energy $^3P_0$ level, three eigenvalues of energy +213.54 cm^{-1} represent the lower energy $^3P_1$ level and the five eigenvalues of -213.62 cm^{-1} represent the lowest energy five-fold degenerate $^3P_2$ level. This leaves $\Delta_{so} = 641.11$ cm^{-1} compared to the experimental value [28] of 573.64 cm^{-1}, an error of 12%.

The matrix for the chlorine atom is shown in equation 3.49.

$$H_{Cl}^{so} = \begin{pmatrix} 0.00 & 0.00 & +339.36i & 0.00 & 0.00 & -339.39 \\ 0.00 & 0.00 & 0.00 & -339.00i & -339.39 & 0.00 \\ -339.36i & 0.00 & 0.00 & 0.00 & 0.00 & +339.33i \\ 0.00 & +339.00i & 0.00 & 0.00 & -339.39i & 0.00 \\ 0.00 & -339.39 & 0.00 & +339.39i & 0.00 & 0.00 \\ -339.39 & 0.00 & -339.33i & 0.00 & 0.00 & 0.00 \end{pmatrix} \quad (3.49)$$

Diagonalisation of this complex matrix results in six eigenvalues split into a group of two and four as expected. Two eigenvalues of +678.62 cm^{-1} represent the upper energy two-fold $^2P_{1/2}$ level and the four eigenvalues of -339.31 cm^{-1} represent the four-fold $^2P_{3/2}$ level. This leaves $\Delta_{so} = 1017.93$ cm^{-1} compared to the experimental value [28] of 882.35 cm^{-1}, an error of 15%.

Moving onto the molecules, the matrix for the OH radical is shown in equation 3.50.

$$H_{OH}^{so} = \begin{pmatrix} 0.00 & 0.00 & +106.15i & 0.00 \\ 0.00 & 0.00 & 0.00 & -105.53i \\ -106.15i & 0.00 & 0.00 & 0.00 \\ 0.00 & +105.53i & 0.00 & 0.00 \end{pmatrix} \tag{3.50}$$

Diagonalisation of this complex matrix results in four eigenvalues split into two groups of two as expected. Two eigenvalues of +105.84 cm^{-1} represent the upper energy two-fold level and the two eigenvalues of -105.84 cm^{-1} represent the two-fold lower energy level. This leaves Δ_{so} = 211.68 cm^{-1} compared to the experimental value [29] of 139.21 cm^{-1}, an error of 52%.

The matrix for the CN radical is shown in equation 3.51.

$$H_{CN}^{so} = \begin{pmatrix} 0.00 & 0.00 & +46.01i & 0.00 \\ 0.00 & 0.00 & 0.00 & +46.02i \\ -46.01i & 0.00 & 0.00 & 0.00 \\ 0.00 & -46.02i & 0.00 & 0.00 \end{pmatrix} \tag{3.51}$$

Diagonalisation of this complex matrix results in four eigenvalues split into two groups of two as expected. Two eigenvalues of +46.02 cm^{-1} represent the upper energy two-fold level and the two eigenvalues of -46.02 cm^{-1} represent the two-fold lower energy level. This leaves Δ_{so} = 92.04 cm^{-1} compared to the experimental value [29] of 52.64 cm^{-1}, an error of 75%.

The matrix for the NO radical is shown in equation 3.52.

$$H_{NO}^{so} = \begin{pmatrix} 0.00 & 0.00 & -94.91i & 0.00 \\ 0.00 & 0.00 & 0.00 & +94.80i \\ +94.91i & 0.00 & 0.00 & 0.00 \\ 0.00 & -94.80i & 0.00 & 0.00 \end{pmatrix} \tag{3.52}$$

Diagonalisation of this complex matrix results in four eigenvalues split into two groups of two as expected. Two eigenvalues of +94.86 cm^{-1} represent the upper energy two-fold level and the two eigenvalues of -94.86 cm^{-1} represent the two-fold lower energy level. This leaves Δ_{so} = 189.72 cm^{-1} compared to the experimental value [29] of 123.16 cm^{-1}, an error of 54%.

Finally, the matrix for the C_2 radical is shown in equation 3.53.

$$H^{so}_{C_2} = \begin{pmatrix} 0.00 & 0.00 & 0.00 & -25.28i & 0.00 & 0.00 \\ 0.00 & 0.00 & 0.00 & 0.00 & 0.00 & 0.00 \\ 0.00 & 0.00 & 0.00 & 0.00 & 0.00 & -25.29i \\ +25.28i & 0.00 & 0.00 & 0.00 & 0.00 & 0.00 \\ 0.00 & 0.00 & 0.00 & 0.00 & 0.00 & 0.00 \\ 0.00 & 0.00 & +25.29i & 0.00 & 0.00 & 0.00 \end{pmatrix} \tag{3.53}$$

Diagonalisation of this complex matrix results in six eigenvalues split into three groups of two. Two eigenvalues of +25.29 cm^{-1} represent the upper energy two-fold level, two eigenvalues of 0.00 cm^{-1} represent a two-fold lower energy level and two eigenvalues of -25.29 cm^{-1} represent the two-fold lowest energy level. This leaves Δ_{so} = 50.58 cm^{-1} compared to the experimental value [29] of 15.25 cm^{-1}, an error of 232%.

The energy level splitting is summarised in figures 3.26 and 3.27 with experimental values shown in red.

The calculated spin-orbit coupling constants are summarised in table 3.3 with all experimental data collected from references [28], [29], [30], [31] and [32].

It is very clear from table 3.3 that the neglect of two-electron effects, either directly or via an effective one-electron operator causes significant deviation from experimental results given the agreement between the results of this work and the one electron results from SEHF. As found by Blume *et al.* [7][8] and others, the neglect of two electron effects clearly has a greater impact on smaller atoms in this study: 110% error for the B atom but reducing to 15% error for the Cl atom. for molecules, the error is seen to increase substantially once more as expected considering the errors on the C and O atoms. Nevertheless, the calculated results are in reasonable enough agreement with experiment to suggest that, upon inclusion of the two-electron effects, MCCI could be used as an alternative method for investigating spin-orbit coupling effects with the method's inherent advantage of the formation of highly compact wavefunctions.

The advantage of MCCI over other techniques is the ability of the method to accurately predict energies and properties of systems using compact wavefunctions

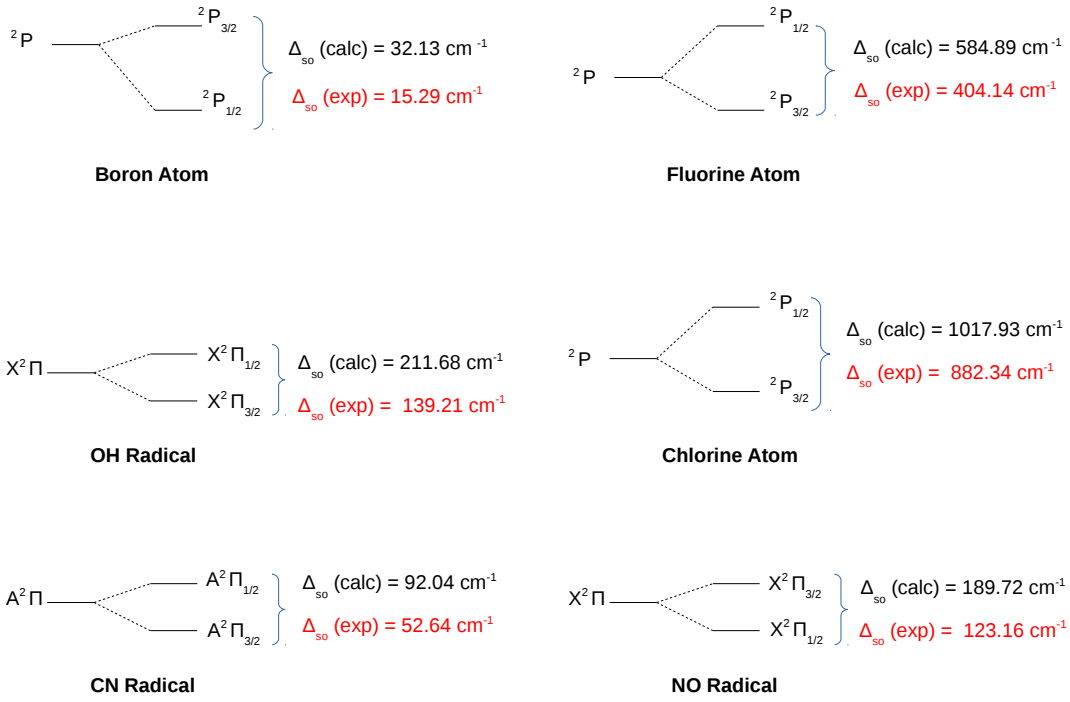

Figure 3.26: MCCI spin-orbit coupling splitting for the doublet state atoms and molecules. Energy convergence is 0.001 in all cases.

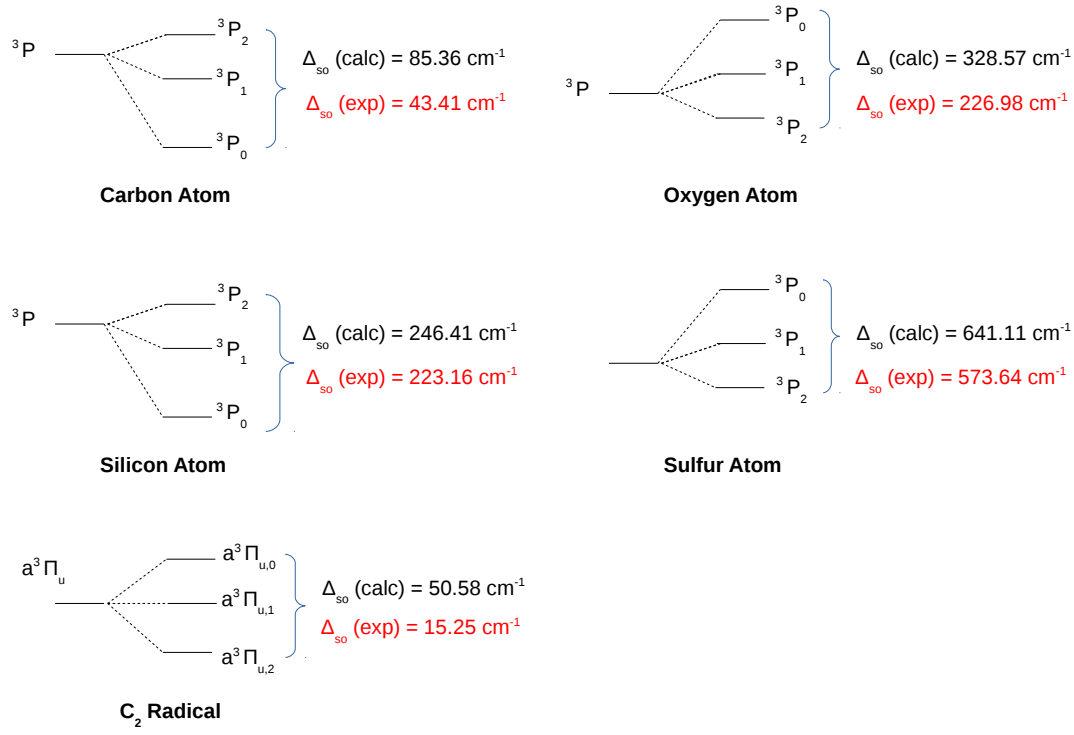

Figure 3.27: MCCI spin-orbit coupling splitting for the triplet state atoms and molecules. Energy convergence is 0.001 in all cases.

Table 3.3: MCCI spin-orbit coupling constant results. All spin-orbit coupling constant values in cm^{-1}. SEHF (1e) is the comparative one electron contribution to the spin orbit coupling using Spin Extended Hartree Fock calculations. SEHF (Full) is the corrected spin orbit coupling constant when two electron terms are subsequently taken into account. SEHF results obtained from references [31] and [32]. Experimental results from reference [28], [29] and [30]. Where available, experimental errors have been provided in parentheses.

Atom/Molecule	SOC Constant	SEHF (1e)	SEHF (Full)	Exp
B atom	+21.42	+23.10	+10.29	+10.19(3.33)
C atom	+28.45	+30.09	+13.99	+14.47(3.33)
O atom	-109.52	-110.14	-76.36	-75.66(3.67)
F atom	-389.92	-395.87	-269.10	-269.4(1)
Si atom	+82.14			-74.39(-)
S atom	-213.70			-191.21(-)
Cl atom	-678.62			-588.23(-)
OH radical	-211.68	-215.77	-140.83	-139.21(-)
CN radical	-92.04			-52.64(-)
NO radical	+189.72			+123.16(-)
C2 radical	-50.58			-15.25(-)

compared to other more computationally intensive methods. Table 3.4 lists the relative numbers of electron configurations required compared to those required for an FCI solution. As can be seen, for all systems, MCCI achieves reasonable results compared with experiment using just a fraction of the available FCI space.

3.5.1 Summary and Conclusions - Development of Spin-Orbit Coupling for Stochastic Configuration Interaction Techniques

MCCI has shown promise as a technique for calculating spin-orbit coupling properties using highly compact wavefunctions subsequent to the development of supporting software as part of this thesis. Reasonable results are obtained compared to experiment in this first proof-of-concept work although it is clear that the values of

Table 3.4: Comparison of approximate number of electron configurations generated between MCCI and FCI

System	Basis	cmin	MCCI SDs	FCI SDs	Fraction
B	cc-pVQZ	0.0005	1.2×10^{3}	3.9×10^{7}	3.1×10^{-5}
C	cc-pVQZ	0.0001	5.4×10^{3}	5.1×10^{8}	1.1×10^{-5}
O	cc-pVQZ	0.0001	1.1×10^{4}	9.1×10^{10}	1.2×10^{-7}
F	cc-pVQZ	0.0005	3.1×10^{3}	1.2×10^{12}	2.6×10^{-9}
Si	cc-pVDZ	0.0001	1.9×10^{3}	8.1×10^{8}	2.3×10^{-6}
S	cc-pVDZ	0.0001	3.1×10^{3}	1.6×10^{9}	2.0×10^{-6}
Cl	cc-pVQZ	0.0005	5.2×10^{3}	2.8×10^{19}	1.9×10^{-16}
OH	cc-pVQZ	0.0005	6.8×10^{3}	6.6×10^{13}	1.0×10^{-10}
C_2	cc-pVDZ	0.0001	4.3×10^{4}	1.2×10^{11}	3.7×10^{-7}
CN	cc-pVQZ	0.0005	1.4×10^{4}	6.8×10^{19}	2.1×10^{-16}
NO	cc-pVQZ	0.0005	1.8×10^{4}	1.3×10^{22}	3.1×10^{-5}

spin-orbit coupling constant for the species in this study suffer from the neglect of two electron terms in the Breit-Pauli Hamiltonian as demonstrated by the excellent agreement of the results in this work with the one-electron results from SEHF.

As discussed in the theory section, CASSCF and MRCI techniques require the specification of the important orbitals in order to properly describe the system. This clearly makes both of these techniques rely heavily on the skill of the user in establishing the correct active space. Additionally, the active space may be larger than can be handled computationally. CASSCF, for example, has the restriction of performing FCI in the active space when this may not be desirable. Other techniques such as RASSCF allow the active space to be further partitioned but this clearly enhances the problem of setting up the correct space in advance. MCCI avoids these problems and requires the user to select only a single parameter: a c_{min} cutoff value, with no knowledge of the important orbitals. Clearly this is an advantage for MCCI but there are disadvantages in this approach. CASSCF and MRCI calculations partition the resulting orbital space into clear sections. This partitioning has the potential to ease further calculations on the orbitals as it may, for instance, be possible to identify integrals or derivatives which may be zero in subsequent property calculations without having to explicitly make those calculations. MCCI does not

partition the orbital space and so is unable to take advantage of these simplifications - all derivatives for example would have to be explicitly calculated. Therefore, like all techniques, MCCI has advantages and disadvantages and these must be weighed up when using the method.

Future work in this regard must be focussed on adopting some form of inclusion of two-electron terms, perhaps via effective one electron operators, before more advanced studies such as singlet-triplet mixing can be reliably attempted.

References

[1] P. Atkins and R. Friedman, *Molecular Quantum Mechanics*. 5th Edition, Oxford University Press, 2011.

[2] F. Jensen, *Introduction to Computational Chemistry, Second Edition*. Wiley-VCH, 2007.

[3] S. Coriani, T. Helgaker, P. Jorgensen, and W. Klopper, "A closed-shell coupled-cluster treatment of the Breit–Pauli first-order relativistic energy correction," *Journal of Chemical Physics*, vol. 121, pp. 6591–6598, 2004.

[4] H. A. Bethe and E. E. Salpeter, *Quantum Mechanics of One and Two Electron Atoms*. Berlin: Springer-Verlag, 1957.

[5] A. Berning, M. Schweizer, H.-J. Werner, P. J. Knowles, and P. Palmieri, "Spin-Orbit Matrix Elements for Internally Contracted Multireference Configuration Interaction Wavefunctions," *Molecular Physics*, vol. 98, no. 21, pp. 1823–1833, 2000.

[6] G. Chambaud, H. Gritli, P. Rosmus, H. J. Werner, and P. J. Knowles, "The ion-molecule reaction O^+ (^4S) + $N_2(X^{1+})$ NO+ (X^{1+}, ν) + N(^4S) and the predissociation of the A^{2+} and $B^2\Pi$ states of N_2O^+," *Molecular Physics*, vol. 98, pp. 1793–1802, 2000.

[7] M. Blume and R. E. Watson, "Theory of Spin-Orbit Coupling in Atoms. I. Derivation of the Spin-Orbit Coupling Constant," *Proceedings of the Royal Society of London. Series A, Mathematical and Physical Sciences*, vol. 270, no. 1340, pp. 127–143, 1962.

[8] M. Blume and R. E. Watson, "Theory of Spin-Orbit Coupling in Atoms. II. Comparison of Theory with Experiment," *Proceedings of the Royal Society of London. Series A, Mathematical and Physical Sciences*, vol. 271, no. 1347, pp. 565–578, 1963.

[9] A. Szabo and N. S. Ostlund, *Modern Quantum Chemistry*. Dover Publications, 1996.

[10] I. L. Cooper and R. McWeeny, "Studies in Configuration Interaction. I. Matrix Elements between Spin-Coupled Functions," *Journal of Chemical Physics*, vol. 45, no. 1, pp. 226–234, 1966.

[11] T. E. H. Walker and W. G. Richards, "*Ab Initio* Computation of Spin-Orbit Coupling Constants in Diatomic Molecules," *Symposia of the Faraday Society*, vol. 2, pp. 64–68, 1968.

[12] D. L. Cooper, J. Hata, and I. P. Grant, "On the Accuracy of the Breit-Pauli Approximation for Fine-Structure Intervals in Light Atoms: Significance for Molecular Calculations," *Journal of Physics B: Atomic and Molecular Physics*, vol. 17, pp. L499–L503, 1984.

[13] S. Koseki, M. W. Schmidt, and M. S. Gordon, "MCSCF 6-31g(d,p) Calculations of One Electron Spin-Orbit Coupling Constants in Diatomic Molecules," *Journal of Physical Chemistry*, vol. 96, no. 26, pp. 10768–10772, 1992.

[14] M. J. Bearpark, N. C. Handy, P. Palmieri, and R. Tarroni, "Spin-Orbit Interactions from SCF Wavefunctions," *Molecular Physics*, vol. 80, no. 3, pp. 479–502, 1993.

[15] B. A. Hess, C. M. Marian, U. Wahlgren, and O. Gropen, "A Mean-Field Spin-Orbit Method Applicable to Correlated Wavefunctions," *Chemical Physics Letters*, vol. 251, pp. 365–371, 1996.

[16] A. O. Mitrushenkov and P. Palmieri, "A New Configuration Interaction Algorithm for Electron Spin Dependent Properties," *Molecular Physics*, vol. 92, no. 3, pp. 511–522, 1997.

[17] H. J. Werner, P. J. Knowles, G. Knizia, F. R. Manby, and M. Schutz *et al.* , "Molpro, version 2015. 1, a package of *ab initio* programs, see http://www. molpro. net," 2015.

[18] A. Nicklass, K. A. Peterson, A. Berning, H.-J. Werner, and P. J. Knowles, "Convergence of Breit-Pauli Spin Orbit Matrix Elements with Basis Set Size and Configuration Interaction Space: The Halogen atoms F, Cl and Br," *Journal of Chemical Physics*, vol. 112, no. 13, pp. 5624–5632, 2000.

[19] T. R. Furlani and H. F. King, "Theory of Spin-Orbit Coupling. Application to Singlet-Triplet Interaction in the Trimethylene Biradical," *Journal of Chemical Physics*, vol. 82, no. 12, pp. 5577–5583, 1985.

[20] D. Beljonne, Z. Shuai, G. Pourtois, and J. L. Bredas, "Spin-Orbit Coupling and Intersystem Crossing in Conjugated Polymers: A Configuration Interaction Description," *Journal of Physical Chemistry A*, vol. 105, pp. 3899–3907, 2001.

[21] R. Li, C. Wei, Q. Sun, E. Sun, H. Xu, and B. Yan, "*Ab initio* MRCI+Q Study on Low Lying States of CS Including Spin-Orbit Coupling," *Journal of Physical Chemistry A*, vol. 117, pp. 2373–2382, 2013.

[22] R. Li, X. Zhang, W. Feng, Y. Jiang, D. Fei, M. Jin, B. Yan, and H. Xu, "*Ab initio* CI Calculations on Potential Energy Curves of Low Lying States of BrF and its Cation Including Spin-Orbit Coupling," *Computational and Theoretical Chemistry*, vol. 1032, pp. 20–26, 2014.

[23] R. Li, C. Wei, Q. Sun, E. Sun, M. Jin, H. Xu, and B. Yan, "*Ab initio* MRCI+Q Study on Low Lying States of CS Including Spin-Orbit Coupling," *Journal of Quantitative Spectroscopy and Radiative Transfer*, vol. 133, pp. 271–280, 2014.

[24] E. R. Sayfutyarova and G. K.-L. Chan, "A State Interaction Spin-Orbit Coupling Density Matrix Renormalisation Group Method," *Journal of Chemical Physics*, vol. 144, p. 234301, 2016.

[25] P. J. Knowles and N. C. Handy, "A New Determinant-Based Full Configuration Interaction Method," *Chemical Physics Letters*, vol. 111, no. 4,5, pp. 315–321, 1984.

[26] P. J. Knowles and N. C. Handy, "A Determinant Based Full Configuration Interaction Program," *Computer Physics Communications*, vol. 54, pp. 75–83, 1989.

[27] L. Tong, M. Nolan, T. Cheng, and J. C. Greer, "A Monte Carlo Configuration Generation Computer Program for the Calculation of Electronic States of

Atoms, Molecules and Quantum Dots," *Computer Physics Communications*, vol. 131, pp. 142–163, 2000.

[28] J. E. Sansonetti and W. C. Martin, "Handbook of Basic Atomic Spectroscopic Data," *Journal of Physical Chemistry Reference Data*, vol. 34, no. 4, pp. 1559–2259, 2005.

[29] K. P. Huber and G. Herzberg, *Constants of Diatomic Molecules*. Litton Educational Publishing Inc., 1979.

[30] L. Veseth, "Spin-extended Hartree-Fock calculations of Atomic Fine Structure," *Journal of Physics B: Atomic and Molecular Physics*, vol. 14, pp. 795–802, 1981.

[31] D. L. Cooper and S. Wilson, "*Ab initio* Calculation of Atomic Spin-Orbit Coupling Constants using a Universal Systematic Sequenvce of Even-Tempered Eexpontential-type Basis Sets," *Journal of Physics B: Atomic and Molecular Physics*, vol. 15, pp. 493–501, 1982.

[32] D. L. Cooper and S. Wilson, "Ab initio calculation of molecular spin-orbit coupling constants using a universal even- tempered basis set of exponential functions," *Journal of Chemical Physics*, vol. 76, pp. 6088–6090, 1982.

Chapter 4

Ring Inversion of Biscalix[4]arene, Preferential Binding of Transition Metals at Lower Rim of Calix[4]arene and Preferential Binding of Small Guest Molecules at Upper Rim of Calix[4]arene

4.1 Chapter Abstract

In this chapter, a body of computational work on calixarenes using Density Functional Theory is presented. The Dalgarno group at Heriot Watt University has an active interest in the synthesis of novel polymetallic clusters using a variety of calixarene structures. As part of an ongoing collaboration with this group, a range of computational insights into various properties of these calixarenes has been provided. Although geometrically more complex than smaller molecules, the electronic structure of such species turns out to be simpler than expected, despite the presence of open-shell metals. The metal-free biscalixarene structure is investigated first and involves the elucidation of the ring inversion of one of the calixarene moieties to allow a favourable conformation for interesting polymetallic cluster formation. This work

involved a detailed analysis of the ring inversion mechanism, the identification of the lowest energy pathway and ultimately the energy barrier associated with that pathway. The second piece of work is an in-depth analysis of the preferential binding of calix[4]arene (C4) at the lower rim towards 1st row transition metals. In particular, an investigation was undertaken to determine whether the calixarene had a preference for any particular transition metal and whether the oxidation state or spin state had any effect on any preference displayed. The final piece of work in this section considers the binding preferences at the upper rim of the calix[4]arene towards small guest molecules to identify whether the formation of polymetallic clusters made a difference to the binding of these guests compared to metal-free C4.

4.2 Calixarene Background

Calix[n]arenes [1][2] are macrocyclic oligomers consisting of n phenolic rings connected by methylene bridges to form a cup shaped molecule. An example, p-tert-butylcalix[4]arene (TBC4), is shown in figure 4.1 in the four possible stable conformers: cone, partial cone, 1,2-alternate and 1,3-alternate with the cone conformation found to be the most thermodynamically stable (although there is some dependence on both solvent and the nature of substituents on the phenyl rings [3]). TBC4 will however undergo interconversion between the various different conformations by rotation of the phenol rings whereby the OH groups pass through the annulus of the molecule. The history of these fascinating molecules begins with the work of Zinke who first postulated their existence in 1941 [4]. It was not until the mid 1950s however, that formal validation of Zinke's predictions about calixarenes was achieved, through the work of Cornforth *et al.* [5][6] to gauge the antituberculous properties of the phenolic-rich calixarene. In particular, Cornforth was able to show that Zinke's method of synthesis was producing tetramers. Subsequent research then saw the discovery of a variety of four membered rings, during attempts to synthesise phenol-based resins, by industrial company Bakelite [7][8]. Synthesis of these molecules proved challenging however, with the workers having to rely on the use of complicated protection groups in an attempt to direct and control the reaction. Despite these advances, the molecules themselves remained relatively obscure until the development of a one-pot synthesis involving condensation oligomerisation of

phenols in the presence of formaldehyde and a suitably strong base such as KOH [9]. This ease of synthesis resulted in the field of calixarenes gaining much prominence in the literature with an explosion of activity including substitution at the *para* position and the methylene bridges in addition to changes at the tetraphenolic pocket [3][10][11]. Work by Carroll *et al.* [12] showed that a biscalixarene could be formed by displacing one of the protons at a methylene bridge by another calixarene moiety using a strong lithiated base which exploited the acidic $\alpha\alpha$ position.

Several attempts have been made to ascertain the energies associated with full ring inversion of calixarenes. These attempts primarily consist of Molecular Mechanics techniques to determine overall barrier heights [13][14][15][16] although a little work has been done using DFT [17][18] to determine the relative stabilities of each of the four conformations. It is interesting to note however that no in-depth analysis has been performed on the mechanism involved in full inversion of calixarenes and no studies have been performed on the biscalixarene mentioned earlier. This is addressed in this work.

As can be seen from figure 4.1, the cone conformation possesses a lower rim constructed as a tetraphenolic pocket which forms a ring of four hydrogen bonds. These hydrogen bonds pull the lower rim atoms together with consequent opening up of the upper rim to produce an overall cup-like shape. This cone conformation opened up the possibility of forming polymetallic clusters using TBC4 and several successful attempts were made to bind metal atoms to the tetraphenolic pocket using transition metal and/or lanthanide salts [19][20][21][22][23][24]. These polymetallic clusters were subsequently shown to display a range of properties including refrigeration and magnetism and hence have potential for use in applications such as single molecule magnets, data storage, metal organic frameworks and refrigerants. Two examples of polymetallic clusters are shown in figures 4.2 and 4.3. The Fe(III) structure shown in figure 4.2 is the first example of a structure of this type, containing as it does both a transition metal and a lanthanide (Gd) and provided a synthetic route towards the formation of $3d$-$4f$ bound clusters. The Cu(II) structure on the other hand, shown in figure 4.3, demonstrates how flexible the structures of polymetallic clusters involving calixarenes can be: in this case an enneanuclear tricapped trigonal prism Cu(III) centre. Both structures demonstrate important capabilities in the search for techniques to better direct and control cluster formation. It is expected that the

ability to exert fine control over the geometric structure of the cluster will open up the possibility of fine tuning of cluster properties such as magnetism.

The fact that metals have been shown to bind to the lower rim also raises the question of whether calixarenes can find application as scavenging agents for contaminated land and water. Studies show a number of heavy metals as well as metals from groups I and II of the periodic table can indeed be trapped by calixarenes [18][22][25][26][27] suggesting potential for use in environmental chemistry.

From the structure of the calixarenes shown in figure 4.1, one might also consider that calixarenes can be used for host-guest chemistry and indeed this is the case. Early attempts at gas storage using calixarenes [28] employed bridging ligands across the upper rim of TBC4 to enforce a cone conformation and facilitate capture of small organic solvents such as alcohols, esters, ketones, benzene and MeCN. As with many early attempts at gas storage using such structures, fracturing of the substrate was commonplace. Removal of the bridging ligands from the upper rim was found to prevent fracturing when storing vinyl bromides [29][30] in a crystal of TBC4. This was thought to be as a result of a process called Dynamic Transport which occurs when one or more phenyl rings from the calixarene rotates out of position, unhindered now that the upper rim bridging ligand has been removed. The gas, therefore, is not stored statically in one calixarene molecule but moves from calixarene to calixarene in a dynamic manner. Other groups however found that when storage increased, structural changes re-occurred, evidenced using techniques such as XRD and ^{13}C NMR [31][32][33]. Of course, whilst gas storage is an important concept, it is equally important for the stored gases to be released in a controlled manner in order to recycle the material. Such reversible storage was demonstrated for TBC4 for a range of gases such as Xe, NO, air, SO_2 and CH_4 [34][35][36][37]. The ability to trap guest molecules at the upper rim has seen calixarenes used in a variety of practical uses such as transport agents for toxic or unstable guest molecules [38] and gas phase optical detectors [39]. Very little quantitative analysis has been performed into the nature of binding of guest molecules. Some molecular dynamics work has estimated the binding energies of small molecules [40][41] although these seem to underestimate bindings and crucially they incorrectly predict that H_2 will not bind to the upper rim of calixarenes. From some of these results however, it is apparent that tethering the lower rim of calixarenes to a metal substrate such as gold

strengthens binding energies of guest molecules at the upper rim by around 1.58 kcal mol^{-1} [42]. More accurate methods were used by Hontama *et al.* [43] who applied MP2/aug-cc-pVQZ to investigate the strength of binding of H_2O to the upper rim of TBC4. The results showed a calculated binding energy of -8.94 kcal mol^{-1} against the experimental value of -8.98 kcal mol^{-1}. Kaneko *et al.* [44] followed this work up by using the MP2/CBS on TBC4 and calculated binding energies for NH_3 as -11.09 kcal mol^{-1}. This compared with experimental values of -8.00 kcal mol^{-1} for NH_3. For H_2O, they calculated a binding energy of -8.10 kcal mol^{-1}. Finally, Ozbek *et al.* [45] discovered that doping calixarenes with iron led to a substantially increased uptake of CO gas.

Coletta *et al.* [46] developed the theme of biscalixarenes by changing the tethering between the two C4 moieties. A series of polymetallic clusters were created by using alkyl chain (from propyl up to octyl) tethering between the methylene bridges of the C4 entities rather than connecting them directly as described earlier in this work. From these biscalixarenes, several polymetallic clusters were created involving 3d, and combined 3d/4f metal ions such as Mn_2^{III}/Mn_2^{II} and Mn_4^{III}/Gd_4^{III}. Further control over 3d/4f metal ion cluster formation was demonstrated [47] by alteration of the stoichiometric ratio of Mn_xLn_y resulting in different polymetallic structures. In the meantime, research into the use of calixarenes as guest capture devices, sensors and detectors continues apace and a few recent examples are briefly mentioned here. C4 derivatives are currently being used as sensors for detection of silver ions in the environment [48], fluoride ions [49], arsenic [50], NADH [51] and dopamine [52].

4.3 Biscalix[4]arene Ring Inversion Mechanism

The relevant published paper covering the work described in this section is provided in reference [53]. Following the work of Carroll *et al.* in discovering the biscalixarene molecule [12], a DFT analysis is now presented of this important addition to the family of calixarenes. Of particular interest is the mechanism by which one of the calixarene moieties undergoes full ring inversion to produce a conformation in which the two calixarenes adopt a position which is *syn* to each other from the more thermodynamically stable *anti* arrangement as shown in figures 4.4 and 4.5. This conformational change leads to these biscalixarenes forming polymetallic clusters

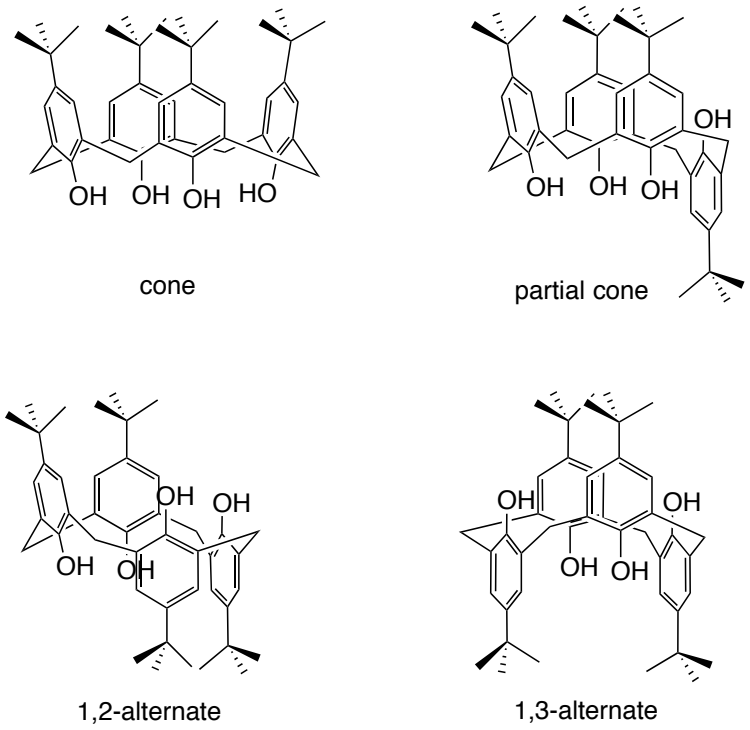

Figure 4.1: TBC4 and stable conformations

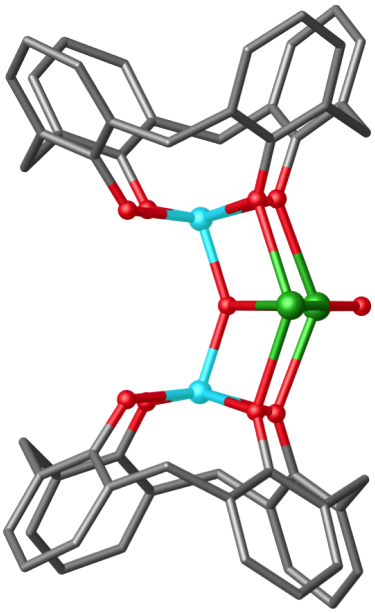

Figure 4.2: $Fe^{3+}Gd^{3+}$ polymetallic cluster based on C4. H atoms hidden for clarity

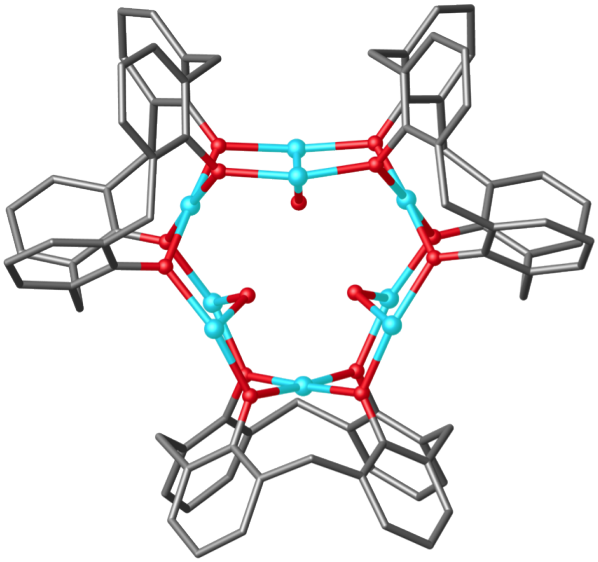

Figure 4.3: Cu^{2+} polymetallic cluster based on C4. H atoms hidden for clarity

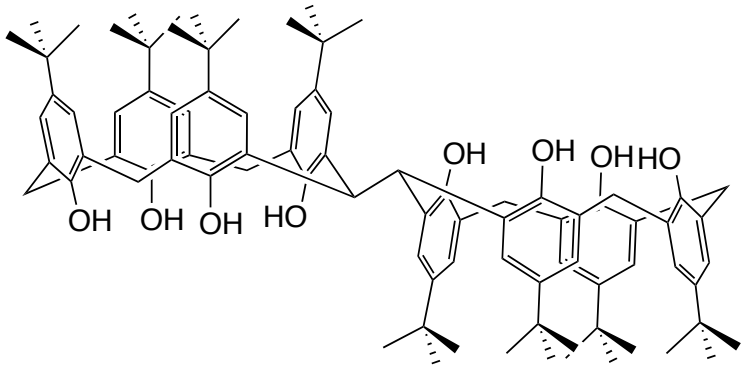

Figure 4.4: Biscalix[4]arene *anti* conformation

involving octadentate ligation via the two tetraphenolic pockets. As can be seen in figure 4.4, whilst the *anti* arrangement would not facilitate clustering (possibly preferring to form chains), the *syn* arrangement in figure 4.5 would allow for such a construction. All key intermediate species are identified along with transition state structures, relative stabilities of the various stable conformations and identification of the lowest energy pathway.

4.3.1 Computational Details - Biscalixarene Ring Inversion

All calculations for the work in this subsection were performed using Gaussian 09 D01 [54] Geometry optimisations and all thermal corrections were performed using B3LYP/6-31G** [55][56]. All energy values are reported as Gibbs energies taken from subsequent B3LYP/6-311G** single point calculations at these optimised ge-

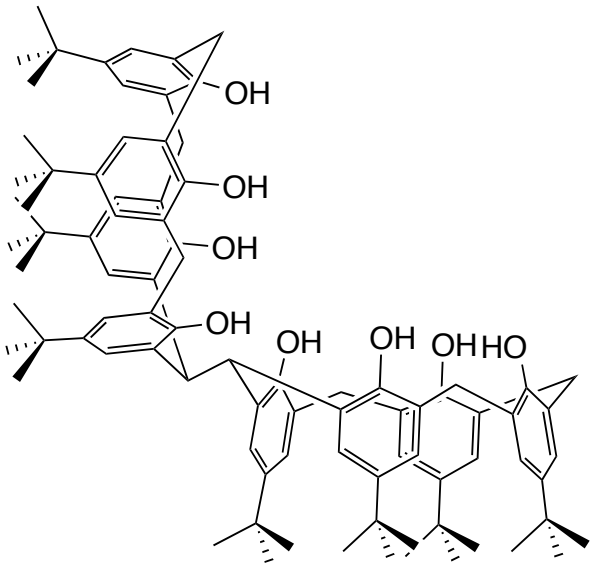

Figure 4.5: Biscalix[4]arene *syn* conformation

ometries at 298.15K and are zero-point corrected. All thermodynamic quantities are calculated using standard statistical thermodynamics as described earlier in this thesis. Empirical dispersion GD3BJ [57] was included with all calculations where supported by the method. Benchmark calculations were performed using AM1 [58], SVWN [59][60][61] and BP86 [62][63] in order to compare the performance of semi empirical, LSDA, GGA and hybrid GGA methods in modelling parts of the potential energy surface. Analysis of analytical Hessian computations confirmed the nature of critical points as either transition states (with one imaginary eigenvalue) or minima (all positive eigenvalues). Intrinsic reaction co-ordinate (IRC) methods were attempted in order to link transition states to the corresponding minima either side of the transition state but were unsuccessful as a result of flat potential energies around the transition state. An alternative strategy was therefore necessary and is described as follows: a small displacement was induced in both directions along the transition state reaction co-ordinate and the geometry was optimised starting from these displacements to confirm that the subsequent minima found were as expected. Finally, the need to account for long range bulk solvent on the calculations were checked using B3LYP/6-31G** with the PCM (with and without SMD) and CPCM solvent models [64][65][66][67] using both DMF and methanol solvents (solvents routinely used in the synthesis of biscalixarenes). These solvation models allow the inclusion of bulk solvent effects without having to perform explicit solvation calculations [68]. The *anti*-biscal structure shown in figure 4.4 was used

as the starting point for geometry optimisation with all *p*-tert-Butyl substituents replaced by H atoms for computational ease. All other structures were identified by performing potential energy scans via rotation of individual phenyl rings in a stepwise manner, previous studies having ruled out a concerted mechanism as being energetically unfavourable [16].

4.3.2 Results and Discussion - Biscalixarene Ring Inversion

Because of the size of the bicalixarene molecule, comparison of the optimised *anti* structure using semi-empirical (AM1), LSDA (SVWN), GGA (BP86) and hybrid GGA (B3LYP) methods was performed. In the absence of a biscalixarene crystal structure, TBC4 crystal data [69] was used as a guide to suitability of these methods and displayed measurements are averaged over all similar bonds and angles. Table 4.1 shows the results. AM1 calculations resulted in a highly distorted geometry of the entire molecule and the method is therefore not considered further.

Table 4.1: Biscal lower rim geometries predictions

Property	Crystal	SVWN	BP86	B3LYP
phenolic C-O distance (Å)	1.3854	1.3666	1.3905	1.3819
O-O cis distance (Å)	2.6704	2.4850	2.6192	2.6732
O-O distal distance (Å)	3.7766	3.5144	3.7041	3.7798
phenolic C-C distance (Å)	3.7203	3.6359	3.7307	3.7389
phenolic C-C distal distance (Å)	5.2613	5.1412	5.2764	5.2876
tetraphenolic pocket geometry	sq. planar.	sq. planar	sq. planar	sq.plan.

As can be seen, SVWN shows significant overbinding as evidenced by the shorter bond lengths in all areas of the lower rim. This is to be expected from a LSDA method. BP86 shows significant improvement with errors of 1.9% in the O-O measurements and 0.3% in all other bond lengths. B3LYP shows the closest match to the crystal structure with deviations of just 0.1% on the O-O measurements and under 0.5% elsewhere. The choice of B3LYP for the remainder of this work is therefore justified.

In order to describe the ring inversion process, figure 4.6 is considered. Of interest is the lowest pathway to full inversion of one calixarene to obtain the *syn* arrangement.

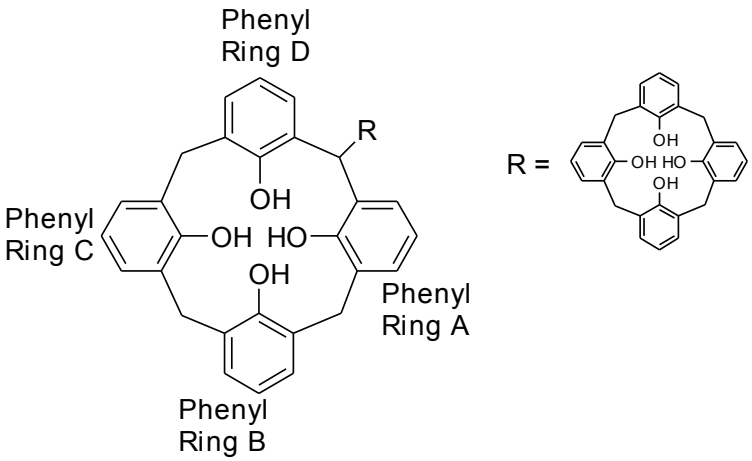

Figure 4.6: Top view of biscalix[4]arene looking into upper rim.

Only the inversion of a single calixarene is required. Because several conformers of calixarene have been identified as shown in figure 4.1, the process of inversion is likely to be stepwise and not concerted. Calculations as part of this work confirm that the barrier involved in inverting more than one phenyl ring at a time is too large to be practical at room temperature. Considering then, a stepwise mechanism, there are four phenyl rings to be inverted: one after another. This gives 4! possible pathways to full inversion, each with at least 4 energy barriers (one for each phenyl ring). That leaves 24 pathways and a minimum of 96 transition states to capture. Figure 4.6 shows symmetry elements however, which can reduce the computational effort. Phenyl rings A and B are symmetrically equivalent to phenyl rings D and C respectively. It is therefore only necessary to consider inversion of phenyl rings A or B as the first phenyl ring to invert. Additionally, matched pathways result in duplication which can also be ignored from the calculations. For example, if phenyl rings A and B are already inverted, the subsequent inversion of phenyl ring C doesn't depend on which order A and B were inverted. One of these pathways can be ignored. By identifying and eliminating such pathways, the computational effort is seen to be dramatically reduced.

The convention for naming structures in this work is now described. The *anti* structure is called **Start** and the *syn* structure called **End**. The suffixes **_TS** and **_prod** indicates the structure is a transition state or an intermediate respectively. Intermediate and transition states are named after the route by which they were obtained. For example, the transition state found after inverting phenyl ring B and attempting to invert phenyl ring A is called **BA_TS**. After overcoming this

transition state, the intermediate **BA_prod** is formed. If in the process of fully inverting phenyl ring A a second transition state is found then it is named **BA_2_TS**. There are places where pathways cross and in this case the lettering may change. This is done for overall convenience. For example, after **BA_2_TS**, full inversion of phenyl ring A results in **AB_2_prod** instead of **BA_2_prod**. The convention for naming the overall pathway itself follows the order of phenyl ring inversion. Therefore pathway **ABDC** indicates that the order of phenyl ring inversion was A first, followed by B then D and finally C. All mechanistic pathways are shown in figures 4.7, 4.8, 4.9, 4.10, 4.11, 4.12, 4.13, 4.14, 4.15, 4.16, 4.17, 4.18, 4.19 and 4.20. Each structure is labelled following the convention described above and all calculated structures can be found in figures 4.21, 4.22 and 4.23.

With a barrier height of 19.31 kcal mol^{-1}, figure 4.7 shows the lowest energy pathway, **BADC**. The structural changes, including all transition states and intermediates, along this lowest energy pathway are shown in figure 4.21 and a discussion of this mechanism is now considered. The first step is to invert phenyl ring B of the *anti* conformer. The resultant barrier height of 15.84 kcal mol^{-1} to the transition state **B_TS** consists of the breaking of two hydrogen bonds and an increase in angle strain on the methylene bridges on either side of phenyl ring B (123.5° and 120.9°) with the latter angle strain the dominant contributor to the barrier height. Note that the breaking of the hydrogen bonds cannot be computationally separated from the angle strain increase and both steps present as a single transition state. This is the single highest energy barrier (SHEB) in the pathway. Partial relief of the angle strain to 117.8° and 116.3°, results in **B_prod**, a structure which has full inversion of phenyl ring B and is 6.93 kcal mol^{-1} above the *anti* structure. The next phenyl ring to be inverted is ring A. This results in hydrogen bond breaking between phenolic rings A and D and a combined increase in angle strain on the surrounding methylene bridges resulting in **BA_TS** a barrier of 9.14 kcal mol^{-1} above **B_prod**. At 119.8° and 118.1°, this angle strain is less than that experienced in the B_TS transition state. Further slight relief in the angle strain to 119.3° and 115.7° sees a stabilisation of 1.48 kcal mol^{-1} at **BA_prod**. The transition state **BA_2_TS** is a result of the steric hindrance caused by a deviation of the angle between the calixarene moieties from 180° for the *anti* arrangement to 163.2° which increases steric hindrance. This deviation results from attempts to reduce the angle strain

around the rotating phenyl ring A. These two competing effects almost balance each other out and the resulting transition state is only 2.84 kcal mol^{-1} above **BA_prod**. Subsequent recovery of the dihedral angle to 180° plus formation of a hydrogen bond between phenyl rings A and B results in a drop in energy of 4.00 kcal mol^{-1} to **AB_2_prod**. The stabilisation is limited due to an increase in angle strain at the methylene bridge between phenyl rings B and C. Note that AB and BA pathways are symmetry equivalent and **AB_2_prod** is chosen as the name for this intermediate. The third phenyl ring to invert in this mechanism is ring D. A number of things happen at once here. Angle strain between phenyl rings D and A builds up to 117.6° with further angle strain of 118.7° appearing between phenyl rings B and C, the dihedral angle between the calixarenes becomes severely deformed to 145.1° and the hydrogen bond between phenyl ring D and C is broken. An increase in energy of 5.55 kcal mol^{-1} to **ABD_TS** is observed. Further rotation of phenyl ring D sees some recovery of both the angle strain between A and D to 115.1° and the dihedral angle between the calixarenes although there is an increase in angle strain between D and C to 119.2°. The net result of these changes sees a stabilisation of 5.11 kcal mol^{-1} to **ABD_prod**. Here the inverting calixarene has now rotated to about 110° with respect to the second calixarene. An increase in angle strain of 121.7° between rings C and D is then observed as the system moves to **ABD_2_TS**, an increase in energy of 2.07 kcal mol^{-1} from **AB_2_prod**. Following this, there is relief of the angle strain between rings C and D and also between rings B and C. Additionally, a hydrogen bond between rings D and A is formed. This is however, matched by an increase in angle strain at the bridge to the second calixarene of 117.0°. The net result is a stabilisation of 6.25 kcal mol^{-1} to **ABD_2_prod**. Finally, ring C is inverted. Although the angle strain at the bridge is relieved to 111.6°, very large angle strain develops between rings B and C of 121.6° and between rings C and D of 123.6°. This causes a large energy increase of 9.62 kcal mol^{-1} to **ABDC_TS** from **ABD_2_prod**. This transition state sits at 19.31 kcal mol^{-1} above the *anti* structure and represents the overall energy barrier for the pathway. Once ring C has fully inverted, the angle strain around ring C is relieved, all four hydrogen bonds are now reformed and a large stabilisation of energy to the required *syn* structure is obtained. In the *syn* structure, the two tetraphenolic pockets form a clam-like geometry which is ideal for forming polymetallic clusters.

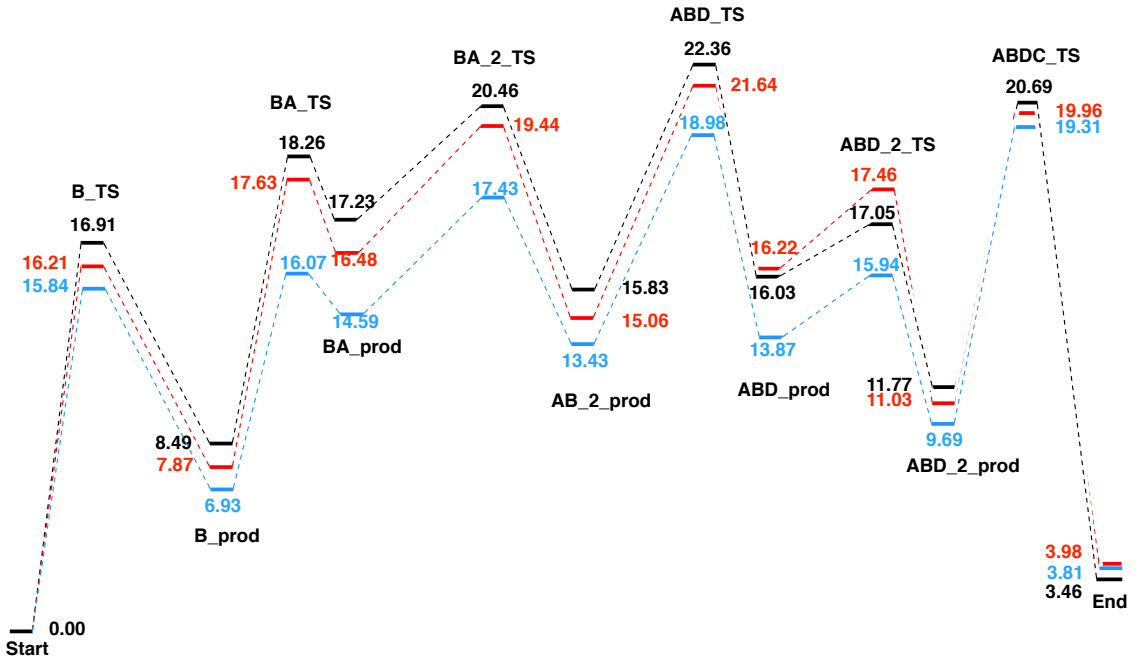

Figure 4.7: Biscalix[4]arene ring inversion: lowest Energy BADC Pathway. All energies are in kcal mol^{-1} relative to the **Start** structure. (a)B3LYP/6-31G** (black). (b)B3LYP/6-311G** (red). (c)B3LYP/6-311G**/GD3BJ Empirical Dispersion (blue).

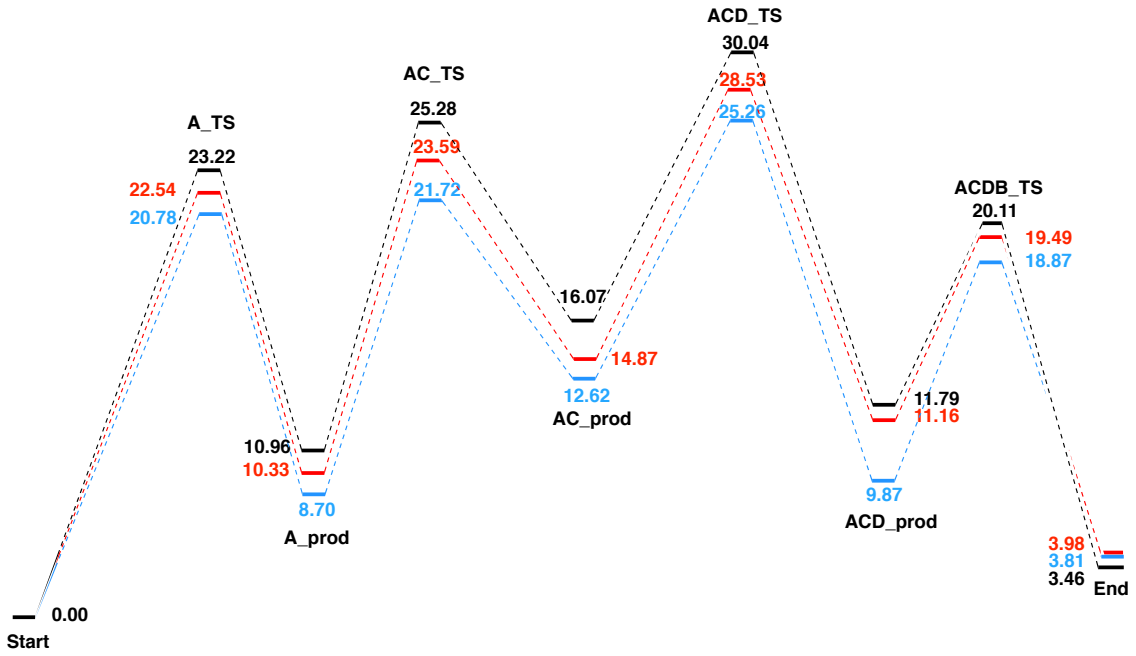

Figure 4.8: Biscalix[4]arene ring inversion: ACDB Pathway. All energies are in kcal mol^{-1} relative to the **Start** structure. (a)B3LYP/6-31G** (black). (b)B3LYP/6-311G** (red). (c)B3LYP/6-311G**/GD3BJ Empirical Dispersion (blue).

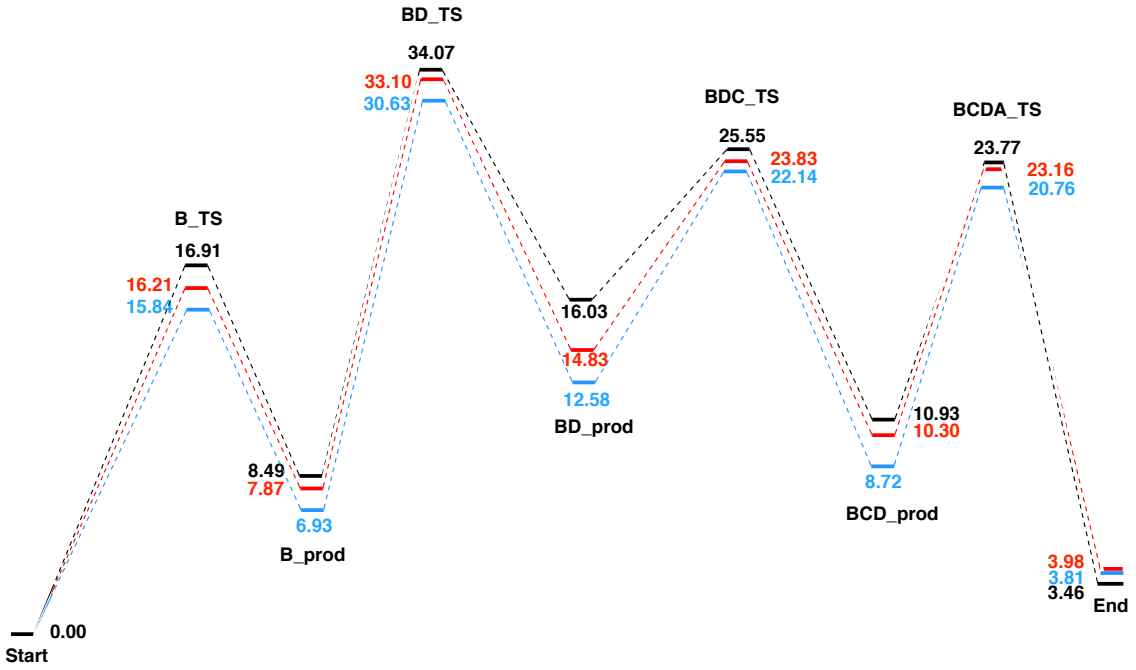

Figure 4.9: Biscalix[4]arene ring inversion: BDCA Pathway. All energies are in kcal mol^{-1} relative to the **Start** structure. (a)B3LYP/6-31G** (black). (b)B3LYP/6-311G** (red). (c)B3LYP/6-311G**/GD3BJ Empirical Dispersion (blue).

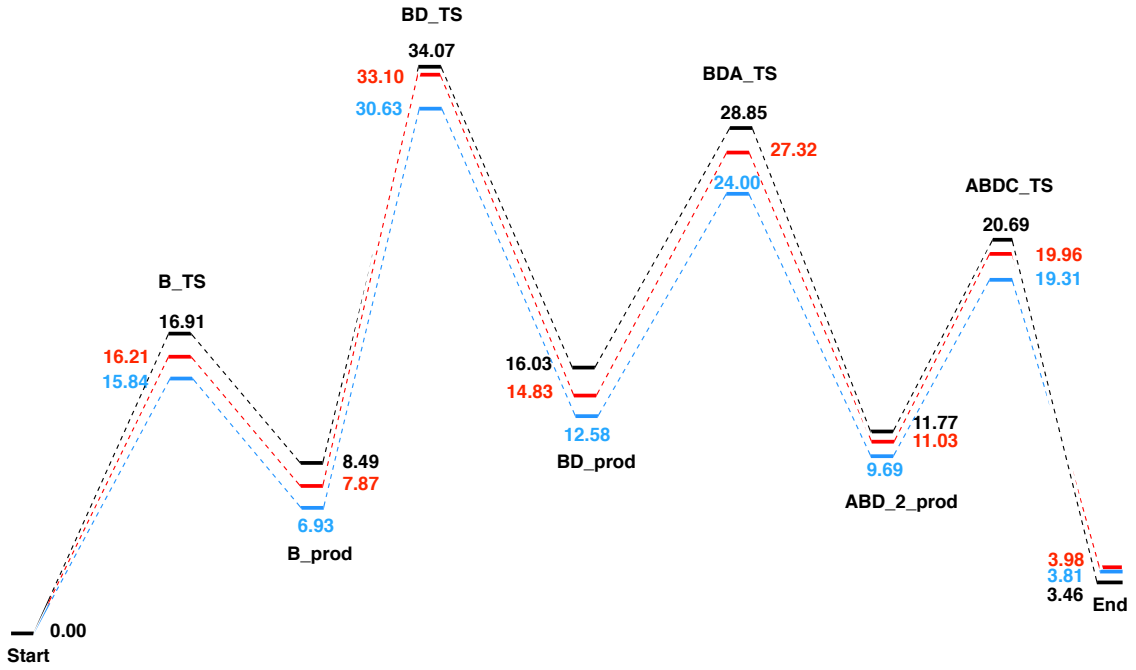

Figure 4.10: Biscalix[4]arene ring inversion: BDAC Pathway. All energies are in kcal mol^{-1} relative to the **Start** structure. (a)B3LYP/6-31G** (black). (b)B3LYP/6-311G** (red). (c)B3LYP/6-311G**/GD3BJ Empirical Dispersion (blue).

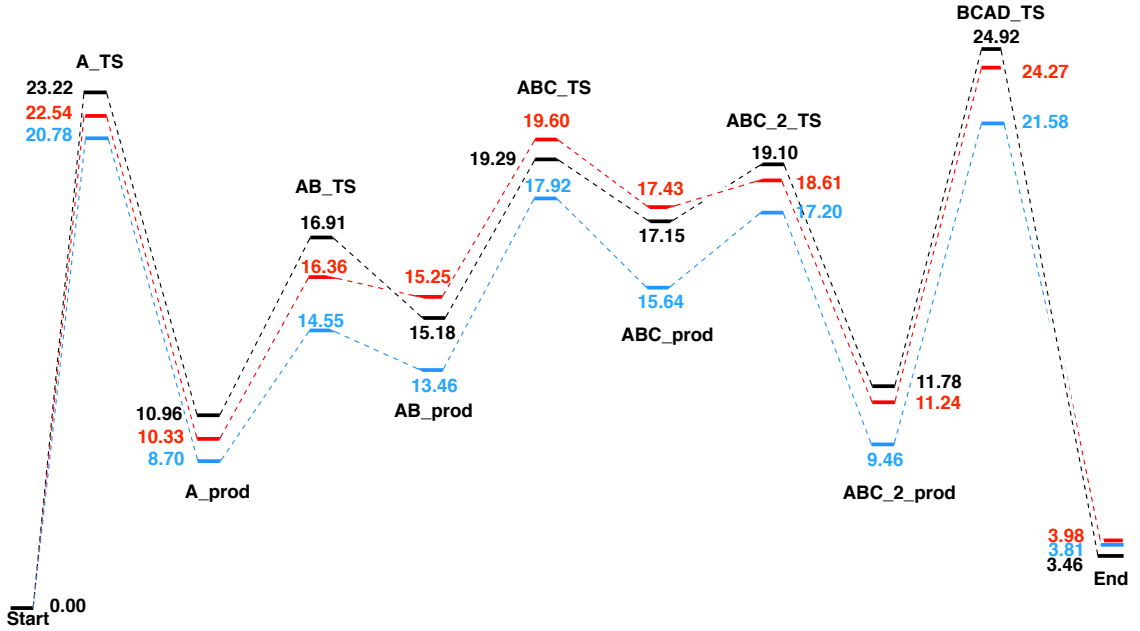

Figure 4.11: Biscalix[4]arene ring inversion: ABCD_1 Pathway. All energies are in kcal mol^{-1} relative to the **Start** structure. (a)B3LYP/6-31G** (black). (b)B3LYP/6-311G** (red). (c)B3LYP/6-311G**/GD3BJ Empirical Dispersion (blue).

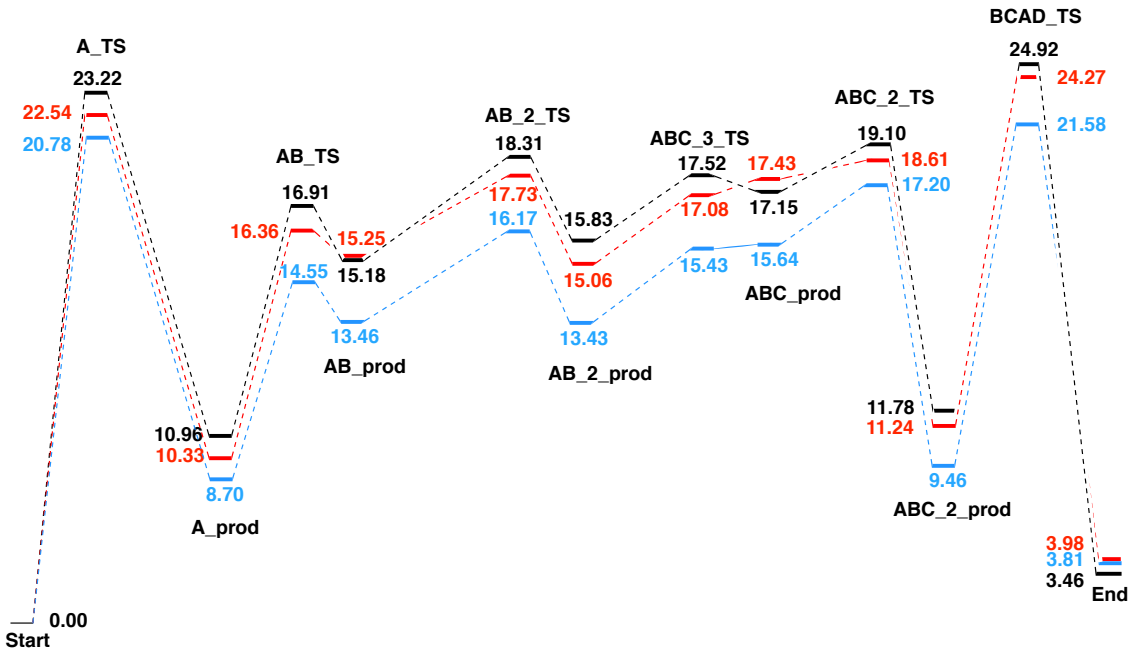

Figure 4.12: Biscalix[4]arene ring inversion: ABCD_2 Pathway. All energies are in kcal mol^{-1} relative to the **Start** structure. (a)B3LYP/6-31G** (black). (b)B3LYP/6-311G* (red). (c)B3LYP/6-311G**/GD3BJ Empirical Dispersion (blue).

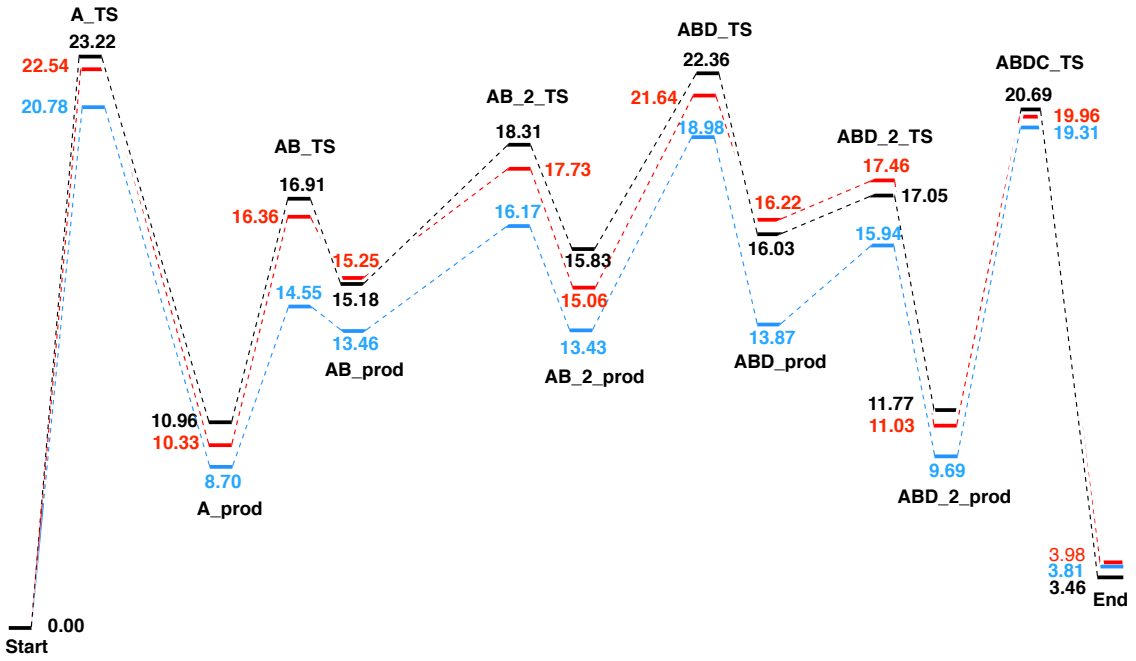

Figure 4.13: Biscalix[4]arene ring inversion: ABDC Pathway. All energies are in kcal mol^{-1} relative to the **Start** structure. (a)B3LYP/6-31G** (black). (b)B3LYP/6-311G** (red). (c)B3LYP/6-311G**/GD3BJ Empirical Dispersion (blue).

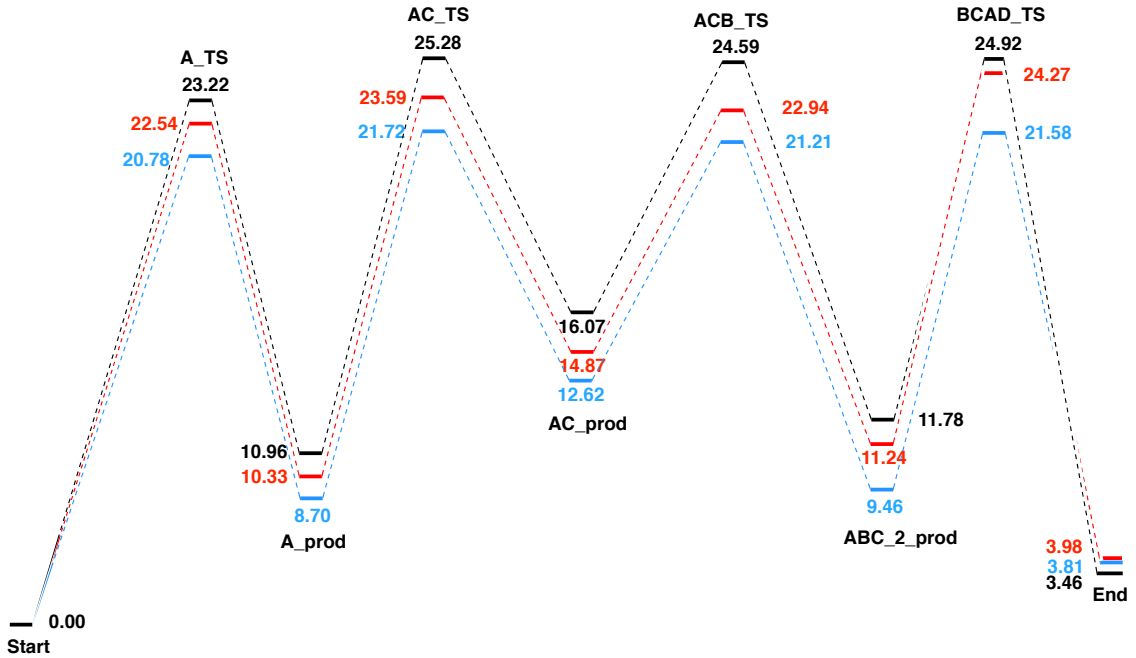

Figure 4.14: Biscalix[4]arene ring inversion: ACBD Pathway. All energies are in kcal mol^{-1} relative to the **Start** structure. (a)B3LYP/6-31G** (black). (b)B3LYP/6-311G** (red). (c)B3LYP/6-311G**/GD3BJ Empirical Dispersion (blue).

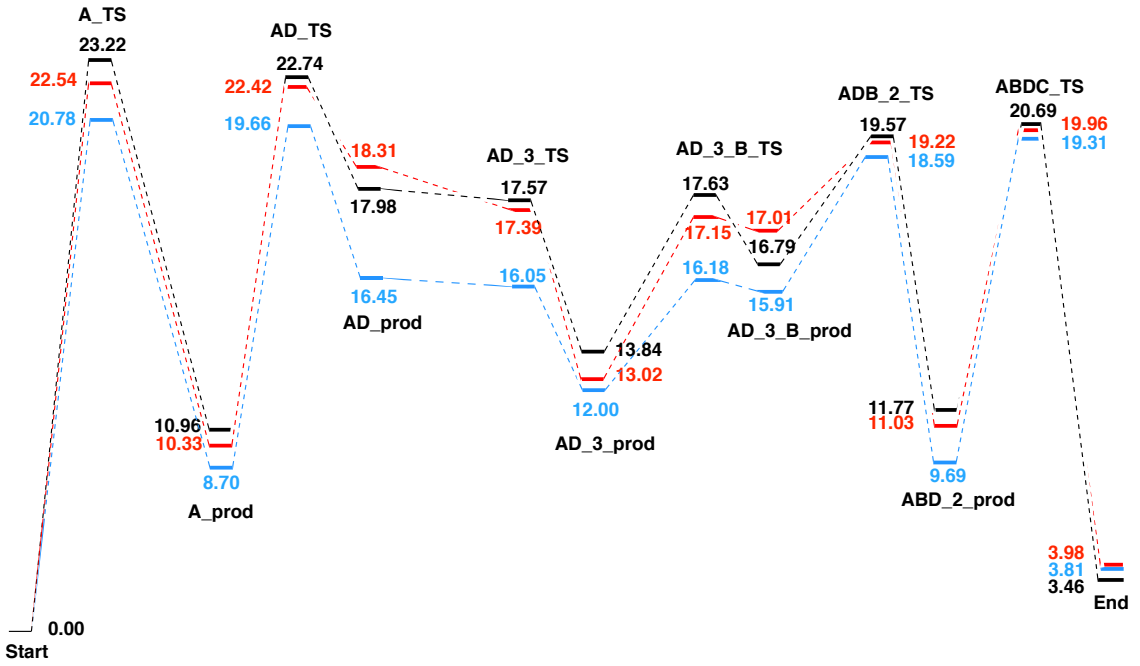

Figure 4.15: Biscalix[4]arene ring inversion: ADBC Pathway. All energies are in kcal mol^{-1} relative to the **Start** structure. (a)B3LYP/6-31G** (black). (b)B3LYP/6-311G** (red). (c)B3LYP/6-311G**/GD3BJ Empirical Dispersion (blue).

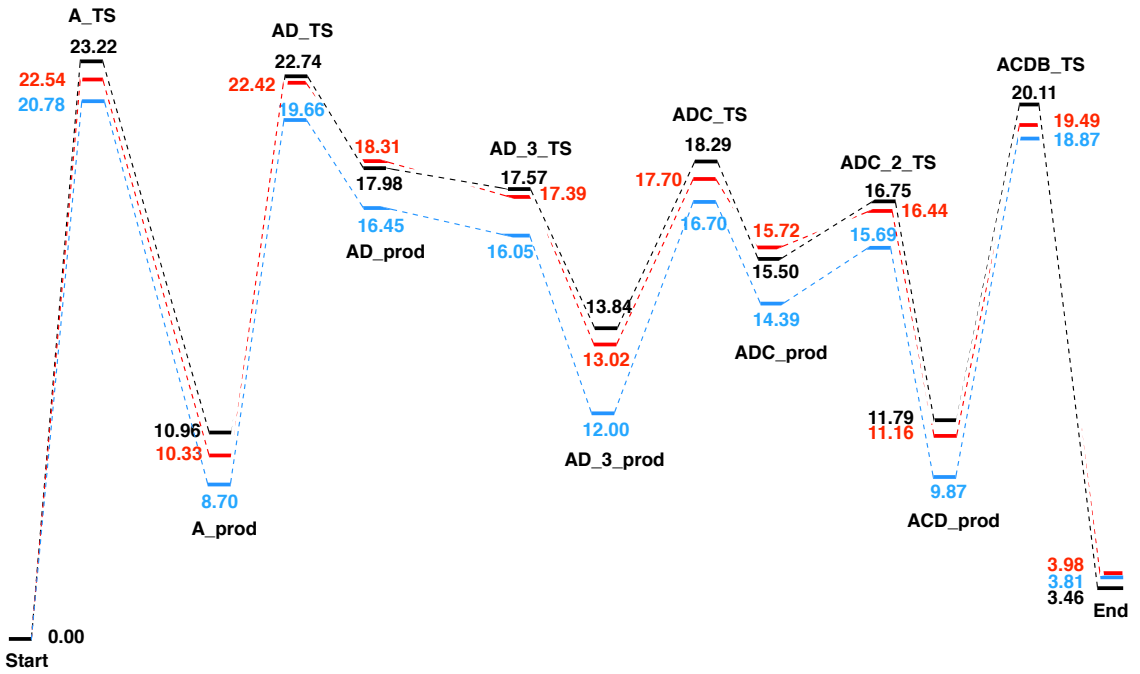

Figure 4.16: Biscalix[4]arene ring inversion: ADCB Pathway. All energies are in kcal mol^{-1} relative to the **Start** structure. (a)B3LYP/6-31G** (black). (b)B3LYP/6-311G** (red). (c)B3LYP/6-311G**/GD3BJ Empirical Dispersion (blue).

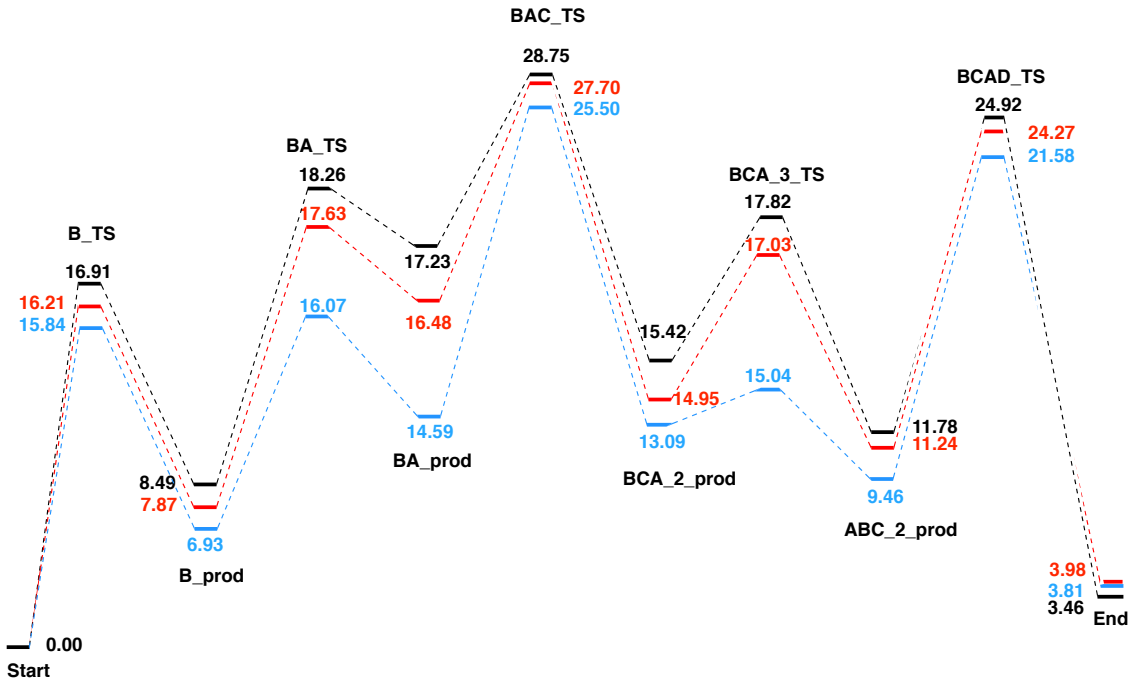

Figure 4.17: Biscalix[4]arene ring inversion: BACD Pathway. All energies are in kcal mol^{-1} relative to the **Start** structure. (a)B3LYP/6-31G** (black). (b)B3LYP/6-311G** (red). (c)B3LYP/6-311G**/GD3BJ Empirical Dispersion (blue).

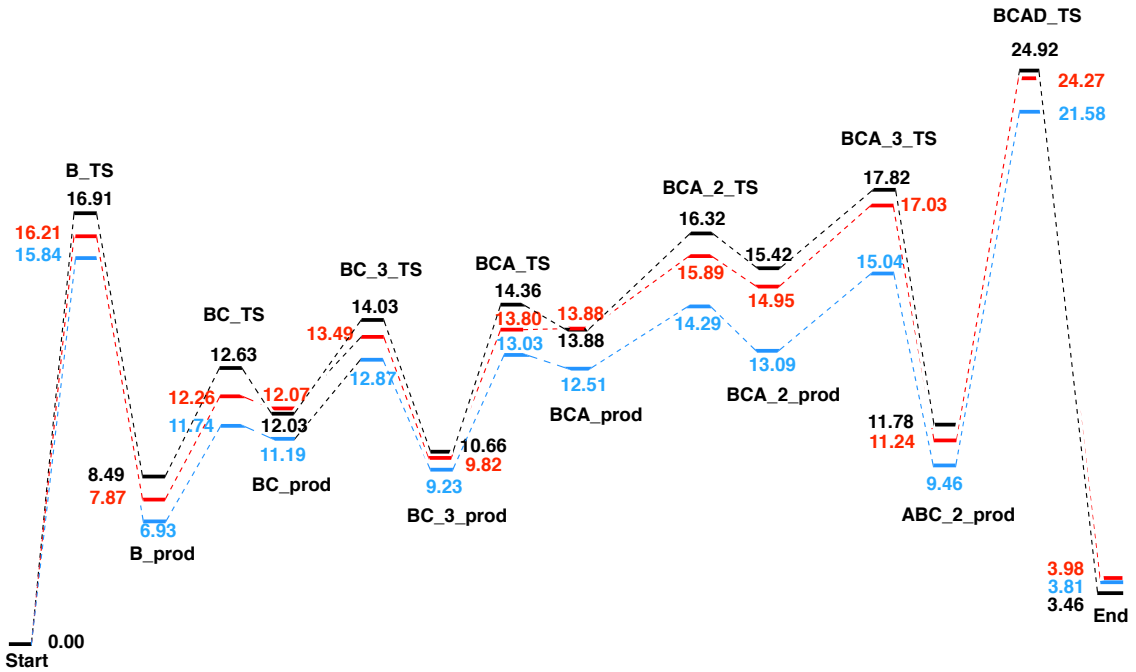

Figure 4.18: Biscalix[4]arene ring inversion: BCAD Pathway. All energies are in kcal mol^{-1} relative to the **Start** structure. (a)B3LYP/6-31G** (black). (b)B3LYP/6-311G** (red). (c)B3LYP/6-311G**/GD3BJ Empirical Dispersion (blue).

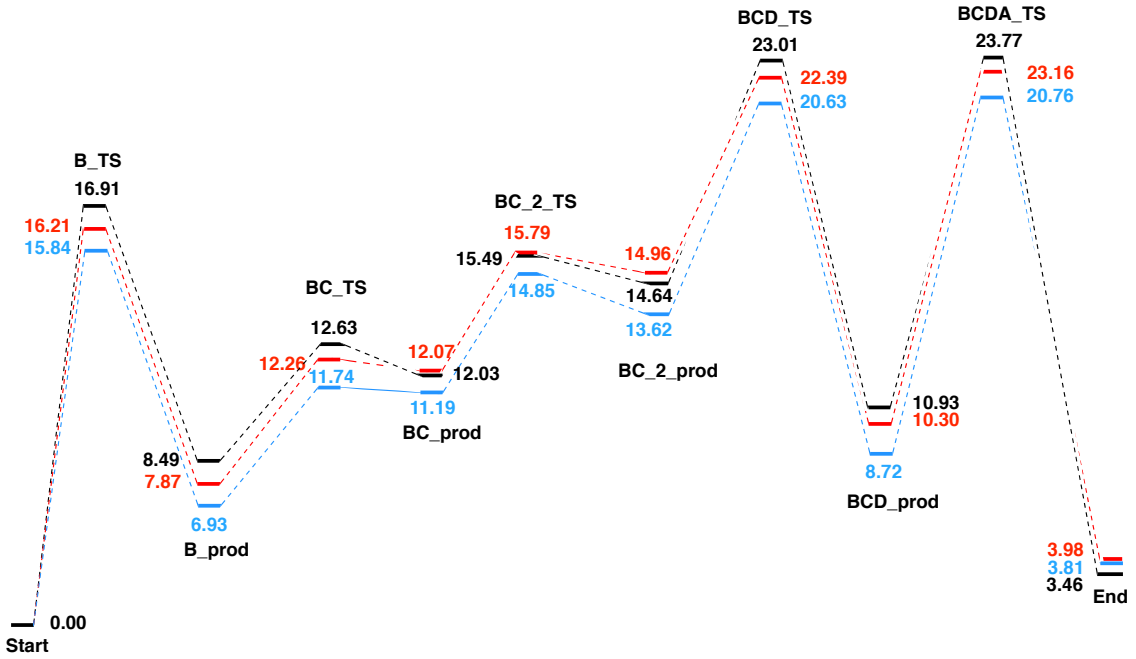

Figure 4.19: Biscalix[4]arene ring inversion: BCDA_1 Pathway. All energies are in kcal mol^{-1} relative to the **Start** structure. (a)B3LYP/6-31G** (black). (b)B3LYP/6-311G** (red). (c)B3LYP/6-311G**/GD3BJ Empirical Dispersion (blue).

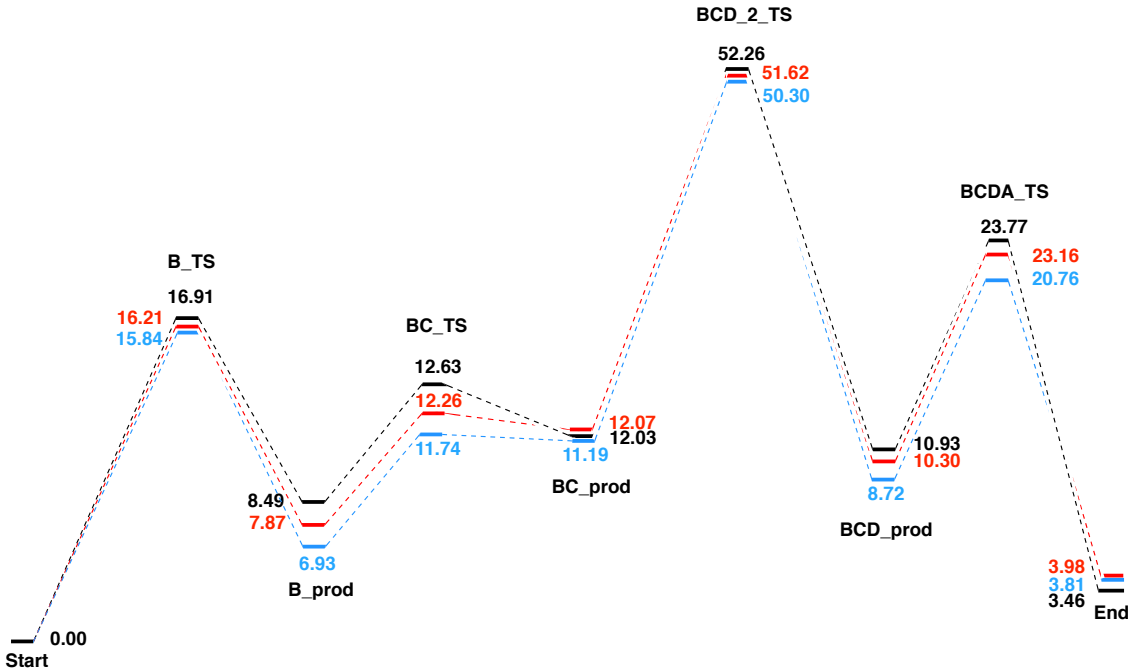

Figure 4.20: Biscalix[4]arene ring inversion: BCDA_2 Pathway. All energies are in kcal mol^{-1} relative to the **Start** structure. (a)B3LYP/6-31G** (black). (b)B3LYP/6-311G** (red). (c)B3LYP/6-311G**/GD3BJ Empirical Dispersion (blue).

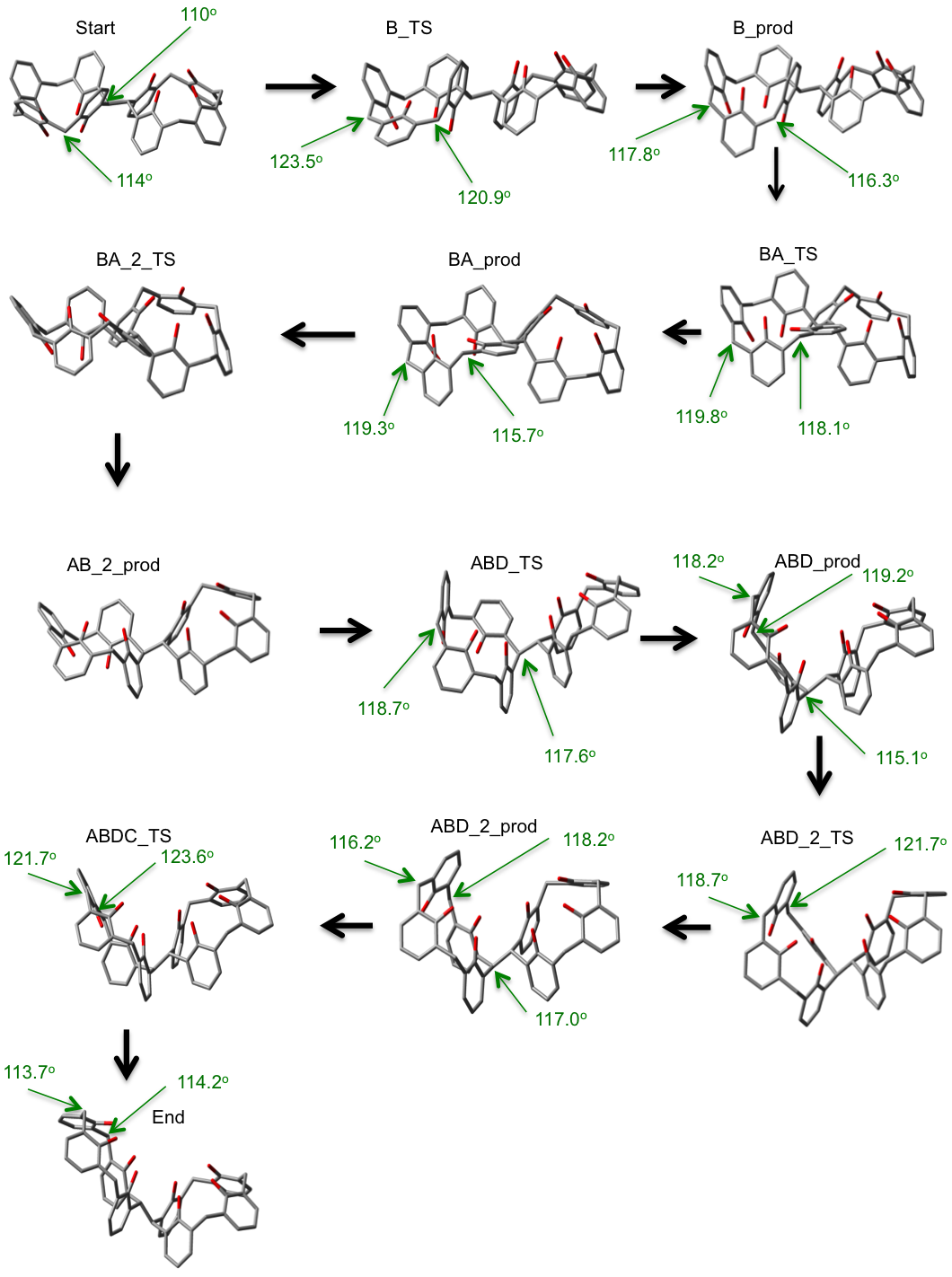

Figure 4.21: Biscalix[4]arene ring inversion: structures involved in the lowest energy BADC pathway

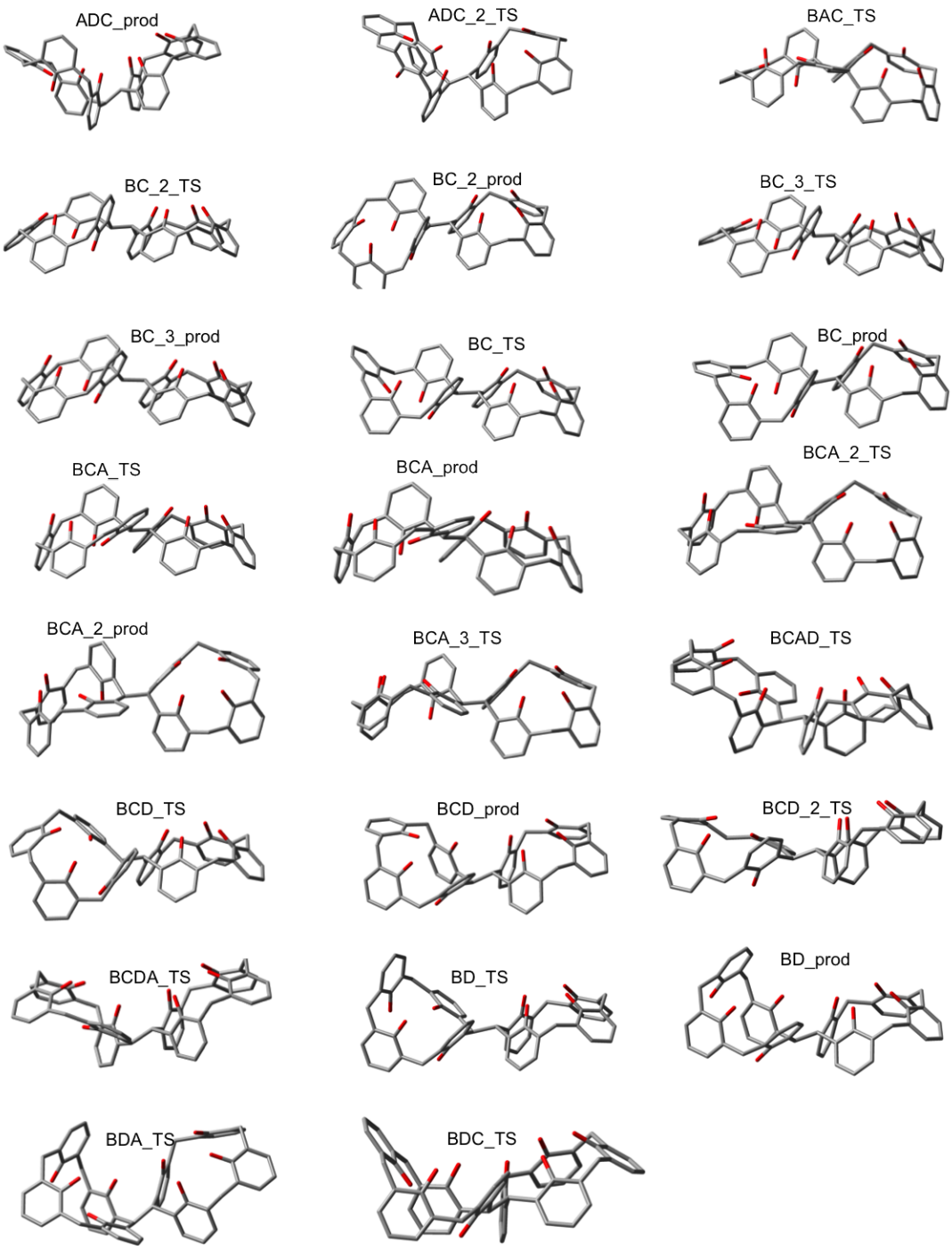

Figure 4.22: All structures involved in full inversion of biscalix[4]arene

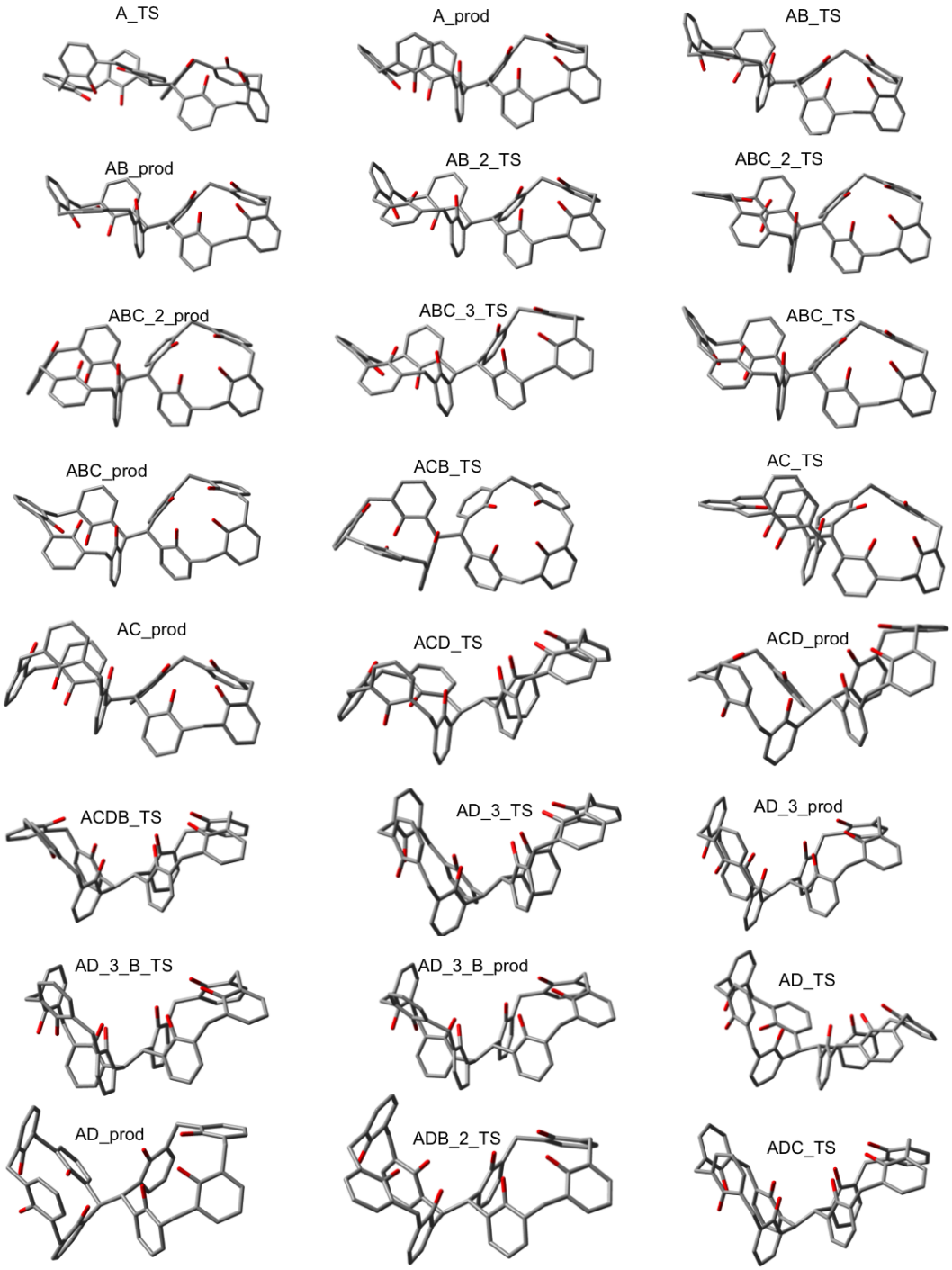

Figure 4.23: All structures involved in full inversion of biscalix[4]arene (contd.)

Table 4.2 shows the SHEB and the energy barriers for all of the mechanistic pathways discovered in this work. For most pathways the SHEB is the rotation of the first phenyl ring. The exceptions are pathways **BDAC**, **BDCA** and **BCDA Path 2** where the rotation of ring D is the SHEB. These three exceptions are explained as follows: After rotating ring B, the next most difficult ring to rotate is ring D because two hydrogen bonds need to be broken, angle strain needs to be overcome and steric effects at the bridge cause issues due to the second calixarene. It is therefore to be expected that ring D is the SHEB for these pathways. The problem with pathway **BCDA Path 2** stems from the fact that ring D attempts to invert before ring C has completely rotated. This essentially mimics the situation where more than one ring attempts to rotate in a concerted fashion. Under these circumstances, the relevant structure **BCD_2_TS** shows significant angle strain of 119.1° at the bridge but a more serious problem appears at the methylene moiety linking rings C and D where angle strain of 136.9° occurs. This leads to the very large barrier to this transition state. It is this very large level of angle strain which which occurs when more than one ring attempts to rotate at the same time, which provides some proof that the full ring inversion must be a step-wise process rather than concerted mechanism.

Relative energies of the major stable calixarene conformations are shown in table 4.3 in addition to the lowest barrier heights to each of them as the quality of the basis set is improved and empirical dispersion is added. Note that biscalix[4]arene has reduced symmetry in comparison to C4 because of the replacement of one of the methylene H atoms with a second C4 moiety and therefore there are two different partial cone conformations (paco), three different 1,2-alternate possibilities and two 1,3-alternate possibilities.

As can be seen, the inclusion of a dispersion correction has at least the same effect as increasing the basis set and in several cases is significantly more important, lowering the energy in all cases. This is to be expected from systems for which non-covalent bonding is a vital part of the structure. The two *paco* structures, **A_prod** with energy 8.70 kcal mol^{-1} and barrier height 20.78 kcal mol^{-1} and **B_prod** with energy 6.93 kcal mol^{-1} and barrier height 15.84 kcal mol^{-1}, are reached by the breaking of two hydrogen bonds and by overcoming some angle strain around the methylene bridges neighbouring the inverting phenyl moiety, but the rotation of phenyl ring A is more sterically hindered by the second calixarene than phenyl ring B resulting

Table 4.2: Single Highest Energy Barrier (SHEB) and energy barriers of all mechanistic pathways in the ring inversion of biscalix[4]arene. All calculations use B3LYP/6-311G** and GD3BJ empirical dispersion. All energies are kcal mol^{-1} and relative to *anti* biscal **Start** structure.

Pathway	Inversion Barrier	SHEB	SHEB Barrier
BADC	19.31	Inversion of ring B	15.84
BCDA Path 1	20.76	Inversion of ring B	15.84
ABDC	20.78	Inversion of ring A	20.78
ADBC	20.78	Inversion of ring A	20.78
ADCB	20.78	Inversion of ring A	20.78
ACDB	25.26	Inversion of ring A	20.78
BACD	25.50	Inversion of ring B	15.84
BCAD	21.58	Inversion of ring B	15.84
ABCD Path 1	21.58	Inversion of ring A	20.78
ABCD Path 2	21.58	Inversion of ring A	20.78
ACBD	21.72	Inversion of ring A	20.78
BDAC	30.63	Inversion of ring D	23.70
BDCA	30.63	Inversion of ring D	23.70
BCDA Path 2	50.30	Inversion of ring D	39.11

Table 4.3: Calculated energies of major stable biscalix[4]arene conformers: paco, 1,2-alternate, 1,3-alternate. All calculations use B3LYP and energies are kcal mol^{-1} and relative to *anti* biscal **Start** structure. Dispersion is GD3BJ. Barrier height uses 6-311G** and dispersion.

Structure	6-31G**	6-311G**	6-311G**/Disp	Barrier
anti biscal (**Start**)	0.00	0.00	0.00	0.00
paco 1 (**A_prod**)	10.96	10.33	8.70	20.78
paco 2 (**B_prod**)	8.49	7.87	6.93	15.84
1,2-alternate 1 (**AB_2_prod**)	15.83	15.06	13.43	20.78
1,2-alternate 2 (**AD_3_prod**)	13.84	13.02	12.00	20.78
1,2-alternate 3 (**BC_3_prod**)	10.66	9.82	9.23	15.84
1,3-alternate 1 (**AC_prod**)	16.07	14.87	12.62	21.72
1,3-alternate 2 (**BD_prod**)	16.03	14.83	12.58	30.63
syn biscal (**End**)	3.46	3.98	3.81	19.31

in the higher barrier towards formation of **A_prod** and also the greater relative stability of **B_prod**. It is therefore predicted that the *paco* variant **B_prod** will be more prevalent on both thermodynamic and kinetic grounds.

The three 1,2-alternate structures are **BC_3_prod** with energy 9.23 kcal mol^{-1} and barrier height 15.84 kcal mol^{-1}, **AD_3_prod** with energy 12.00 kcal mol^{-1} and barrier height 20.78 kcal mol^{-1} and **AB_2_prod** with energy 13.43 kcal mol^{-1} and barrier height 20.78 kcal mol^{-1}. **BC_3_prod** is expected to be more stable because the phenyl ring inversions are far away from the bridge to the second calixarene. This also explains the lower barrier height. **AD_3_prod** inverts two phenyl rings at the bridge to the second calixarene. In theory that would give the least stable structure but **AB_2_prod** results in the hydrogen atoms of one calixarene encroaching on second calixarene. **AD_3_prod** avoids this in the final structure by rotating both phenyl rings A and D in a symmetrical manner and thus **AB_2_prod** is the least stable conformer. It is predicted that **BC_3_prod** will be the most prevalent form of 1,2-alternate conformer on both thermodynamic and kinetic grounds.

The two 1,3-alternate structures are **AC_prod** with energy 12.62 kcal mol^{-1} and barrier height 21.72 kcal mol^{-1} and **BD_prod** with energy 12.58 kcal mol^{-1} and

barrier height 30.63 kcal mol^{-1}. By symmetry, both of these intermediates are matched paths of each other and therefore from a thermodynamic point of view expected to be of the same energy. **AC_prod** does however show a much lower barrier height because the second inversion is of the phenyl ring furthest from the bridge to the second calixarene and thus experiences less steric hindrance compared to **BD_prod** which inverts phenyl ring D which is right next to the bridge. It is predicted therefore that **AC_prod** will be the most prevalent form of 1,3-alternate conformer on kinetic grounds.

The *syn* structure is the end point of the full ring inversion and adopts a double cone conformation. From a thermodynamic stability point of view, it is only 3.81 kcal mol^{-1} above the starting *anti* structure.

Finally, the effect of long range solvent effects on the inversion mechanism is considered. To do this, two transitions are modelled: **Start→A_TS→A_prod** and **ABD_2_prod→ABDC_TS→End**, both of which are part of the **ADBC** pathway shown in figure 4.15. To mimic the synthetic environment for calixarene synthesis, the commonly used solvents methanol and DMF are tested in these calculations. The results are shown in tables 4.4 and 4.5. Gas phase calculations are provided for comparison. As can be seen, for methanol, the solvent results show a stabilisation of most species of between 0.75 to 1.19 kcal mol^{-1} compared to the gas phase results. A similar story emerges from the DMF calculations which shows very similar results to methanol. CPCM and PCM results show relative invariance between the two solvents whilst PCM/SMD shows much more variation. Nevertheless, the effect on all structures is relatively minimal compared to the gas phase predictions. It is therefore considered that long range bulk solvent effects are relatively minor for the ring inversion mechanism and they are therefore not considered further.

4.3.3 Summary and Conclusions - Biscalixarene Ring Inversion

In summary, the minimum global energy pathway is predicted to be **BADC** with an energy barrier of 19.31 kcal mol^{-1}. The SHEB is 15.84 kcal mol^{-1} corresponding to inversion of the phenyl ring B. Most other pathways are energetically achievable however and all show a range of low barriers separating intermediates suggesting

Table 4.4: Comparative energies from methanol solvation applied to two transitions from pathway **ADBC** of biscalix[4]arene ring inversion. All calculations use B3LYP and energies are kcal mol^{-1} and relative to *anti* biscal **Start** structure. All energies use B3LYP/6-31G** and GD3BJ dispersion.

Structure	Gas Phase	PCM	PCM/SMD	CPCM
Start	0.00	0.00	0.00	0.00
A_TS	23.22	23.52	23.08	23.19
A_prod	10.96	10.76	10.49	10.56
ABD_2_prod	11.77	11.46	10.98	11.05
ABDC_TS	20.69	19.90	18.68	19.50
End	3.46	2.98	3.20	2.47

Table 4.5: Comparative energies from DMF solvation applied to two transitions from pathway **ADBC** of biscalix[4]arene ring inversion. All calculations use B3LYP and energies are kcal mol^{-1} and relative to *anti* biscal **Start** structure. All energies use B3LYP/6-31G** and GD3BJ dispersion.

Structure	Gas Phase	PCM	PCM/SMD	CPCM
Start	0.00	0.00	0.00	0.00
A_TS	23.22	23.48	23.39	23.19
A_prod	10.96	10.73	10.81	10.55
ABD_2_prod	11.77	11.41	10.99	11.04
ABDC_TS	20.69	19.85	19.48	19.49
End	3.46	2.91	3.28	2.46

rapid interconversion between the various conformations. The *syn* conformation is predicted to be just 3.81 kcal mol^{-1} above the *anti* conformation and thus expected to be thermodynamically stable and kinetically available enough to be a suitable arrangement for polymetallic cluster formation. Other major stable conformations were found corresponding to paco, 1,2-alternate and 1,3-alternate and the relative stabilities of each species were elucidated. Energetic barriers to access these conformations was also found. **B_prod** was predicted to be the most thermodynamically and kinetically favoured paco conformation, **BC_3_prod** was predicted to be the most prevalent 1,2-alternate conformation on kinetic and thermodynamic grounds and **AC_prod** the most prevalent 1,3-alternate structure on kinetic grounds.

Because crystallisation of these species requires stable species, the predicted rapid interconversion between the various conformers is likely to cause problems for synthetic chemists attempting to produce polymetallic cluster crystals using biscalix[4]arene. It is therefore recommended that such crystallisations are attempted in conditions which mitigate these rapid interconversions such as using cooler temperatures or by augmenting the bis[4]calixarene structure with substituents which force the structure into the required conformation and resist interconversion altogether. Variable temperature NMR might indicate the temperature required to prevent interconversion for example. Variation of the amount of base used to deprotonate the tetraphenolic pockets may also aid in crystallisation efforts for clusters involving non-*syn* conformations of the biscalixarene. For example, stoichiometric ratios of 8:1 base:biscalixarene would be required to deprotonate all eight protons of the biscalixarene forcing the *syn* structure, whereas 7:1 base:biscalixarene might promote a paco arrangement on one of the calixarene moieties. In this way, the base can be used to effect control over the polymetallic cluster growth.

Finally, it was found that long range bulk solvent effects did not unduly influence the mechanism of biscalixarene ring inversion.

4.4 Calix[4]arene Lower Rim Binding

The relevant published paper covering the work described in this section is provided in reference [70]. As described earlier, the known ability for calixarenes to bind to

heavy metals and metals from Groups I and II of the periodic table suggest that calixarenes could find practical use in environmental applications for the remediation of metal-polluted land or water, in addition to having potential for data storage. To that extent, a detailed study is provided, within this section, of the preferential binding of calixarenes to the first row of transition metals to determine whether or not a preference for one type of metal over another exists and whether the oxidation and spin states of the metals make a difference. Several oxidation and spin states of each metal are included. Predictions are also made for the binding preferences for transition metals which have not yet been successfully bound to calixarenes synthetically.

4.4.1 Computational Details - Lower Rim Binding

All calculations in this subsection were performed using Gaussian 09 D01 [54]. Geometry optimisations were performed using 6-31G** basis set in conjunction with DFT functionals BLYP [62][71], B3LYP [55][56][71] and B97D3 [57][72] for non metal atoms. SDD [73] was used for all metal atoms with 10 electrons included as core. All energy values are reported as Gibbs energies taken from subsequent B3LYP/6-311G** single point calculations at these optimised geometries at 298.15K and are zero-point corrected. All thermodynamic quantities are calculated using standard statistical thermodynamics [74]. Empirical dispersion GD3BJ [57] was included with all calculations with the exception of B97D3 which already includes this correction. After geometry optimisation was performed on each compound, wavefunction stability tests [75][76] were carried out. In the presence of instabilities, a new more stable wavefunction was found and used to re-optimise the structure until no further instabilities were uncovered. Analysis of analytical Hessian computations confirmed the nature of critical points as minima (all positive eigenvalues). No symmetry constraints were applied to the calculations.

Binding energies were calculated using the model approach shown in figure 4.24 and equation 4.1, where E_{C4} is the energy of the geometry optimised metal-free tetra-anionic calixarene ligand. Metals atoms were placed in the centre of the tetraphenolic pocket at the lower rim of the calixarene. For metals such as Mn and Fe, which prefer octahedral or square pyramidal co-ordination spheres respectively, wa-

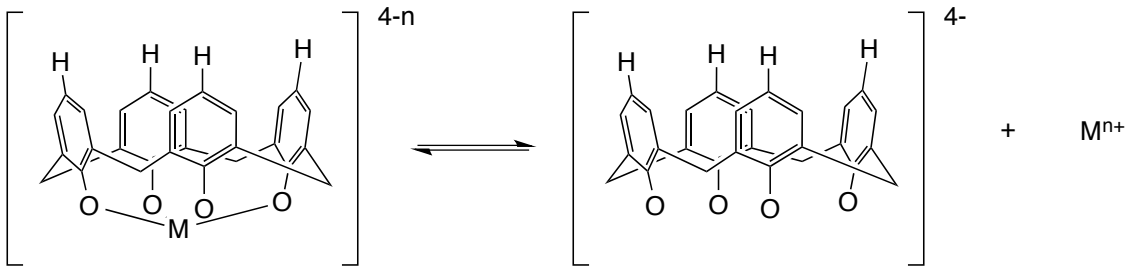

Figure 4.24: Binding energy calculation process for the binding of transition metals to the lower rim of calix[4]arene.

ter molecules were bound in axial positions to mimic the alcohol solvent molecules which normally occupy those positions in the crystal structures. For Mn, both axial positions were occupied with water whilst for Fe, just one water molecule was bound underneath the metal. Tests were carried out on Mn^{3+} and Fe^{3+} and binding energies compared with the situation where no water molecules were used. It was found that the presence of water molecules added just 1-3 kcal mol^{-1} to the binding energies and thus all metals were used in four-coordinate square planar arrangement for computational ease.

$$E_{bind} = E_{complex} - E_{cation} - E_{C4} \tag{4.1}$$

DFT is essentially a single reference method with some recovery of dynamic correlation. The technique is therefore ill-suited to systems which show too much multi-reference character. To test the efficacy of DFT for systems such as the calixarenes in this study, which are prone to be multi-reference in nature due to the presence of transition metals, Truhlar's multi-reference B1 test has been employed [77]. Using figure 4.24, a value B_1 is calculated as shown in equation 4.2 where BE_{LYP} is the binding energy of the geometry optimised complex at the BLYP/6-31G** level, $BE_{B1LYP//BLYP}$ is the B1LYP/6-31G** single point binding energy at the BLYP/6-31G** geometries and n is the number of bonds to be broken in order to remove the metal from the calixarene (in this work, $n = 4$). The value of B_1 has units of kcal mol^{-1} and gives a numerical feel for the multi-reference nature of the system. Truhlar argues that a value of much greater than 10 kcal mol^{-1} indicates a multi-reference system for which the use of hybrid DFT functionals may not be suitable. The method is justified as follows: It is known that DFT recovers some static

correlation via the exchange functional and dynamic correlation via the correlation functional [55][78][79]. It is also known that Hartree Fock is very poor at describing multi-reference systems and that as systems display a greater multi-reference nature, static correlation becomes more important as near degeneracy effects increase. A multi-reference system would therefore likely show large differences in binding energy depending on the amount of exact HF exchange included. Truhlar found that pure DFT functionals such as BLYP (containing 0% HF exchange) performed better with multi-reference systems whilst hybrid functionals such as B1LYP (containing 28% HF exchange) performed worse with the same system. The B_1 test is therefore comparing the difference in binding energies per bond broken, calculated by BLYP and B1LYP, and making a judgment that significant differences between them indicates a multi-reference system. BLYP is considered relatively invariant to the multi-reference nature of the system whereas B1LYP tends to drift. For values much greater than 10 kcal mol^{-1}, it would be considered better to use pure DFT functionals. By way of an example, the B_1 test, using the cc-pVDZ basis set, predicts a value of around 98 kcal mol^{-1} for the ScNi metal dimer discussed earlier in this work. A closely related multi-reference test is the A_λ test [80] which uses DFT functionals with differing levels of exact HF exchange, showing that this type of test can provide a reasonable indication of the multi-reference nature of systems.

$$B_1 = (BE_{BLYP} - BE_{B1LYP//BLYP})/n \tag{4.2}$$

Solvation was performed using the CPCM solvent model [66][67] with water solvent at the B3LYP/6-311G** level with GD3BJ empirical dispersion. All calculations were checked for spin contamination [81][82][83][84][85]. The tetra-anionic metal-free calixarene is modelled as a -4 charged anion. Once solvation is included in the calculations, the electrons are all bound to the ligand as shown by the charged ligand having a lower energy than the closed shell neutral version. For gas phase calculations, the anion appears in every calculation and therefore the net result of analysing the relative binding energy differences between metals sees any error in this regard cancelled out. Despite modelling anionic species, diffuse functions were found to make no overall difference to binding calculations and for computational ease were not used.

Spin density calculations were performed using an isovalue of 0.002 on all complexes. Finally, NBO 3.0 calculations were performed at the B3LYP/6-311++G** level with GD3BJ empirical dispersion.

NBO (Natural Bond Orbital) calculations analyse the wavefunction in terms of localised bonds involving electron pairs in order to provide population analysis and aid in the analysis of the nature of bonding between particular atoms. It is integrated seamlessly into the Gaussian package, taking, as input, a keyword in the Gaussian input file, the one electron density matrix in the basis of atomic orbitals, the atomic orbital overlap matrix, the symmetry and location of each atomic orbital and the nuclear charge of each atom. The output from this program is a text file containing details or natural populations, natural bond orbitals and analysis of localised molecular orbitals of the wavefunction.

4.4.2 Results and Discussion - Lower Rim Binding

B_1 test results for each bound metal are shown in table 4.6. In almost all cases, the values are below the 10 kcal mol^{-1} mark with only the Cr^{4+} singlet complex exceeding this value by 1.13 kcal mol^{-1}. This shall be borne in mind later when considering the binding energies, however it seems reasonable on the basis of these results to use DFT functionals such as B3LYP for such systems given that most results are under 5 kcal mol^{-1}.

In order to determine the best functional for these systems, calculations are performed on a selected range of metal-bound calixarenes where known crystal structures are available for comparison. The performance of BLYP, B3LYP and B97D3 are compared with respect to predicted optimised geometries and compared to experiment. Results are shown in table 4.7. It should be borne in mind that these calculations can never exactly match the crystal structure, due to the nature of the structural approximations used. Nevertheless, good agreement is found for all geometric properties for all functionals compared to the crystal data. The average errors across all geometric calculations for the chosen functionals are 1.91% for BLYP, 2.52% for B3LYP and 2.18% for B97D3 and all three functionals appear to be subsequently justified for use in this work.

For the purposes of this work, no assumption was made regarding the most likely

Table 4.6: Results of B_1 diagnostic tests on all metal-bound C4 complexes. All energies are magnitudes in kcal mol^{-1} and are shown per bond broken, where n=4 in all cases.

Metal	Spin	B_1	Metal	Spin	B_1
Sc^{3+}	singlet	0.76	Mn^{4+}	quartet	6.43
Ti^{2+}	triplet	0.05		doublet	9.91
	singlet	1.42	Fe^{2+}	quintet	0.17
Ti^{3+}	doublet	1.72		triplet	2.42
Ti^{4+}	singlet	5.96		singlet	2.31
V^{2+}	quartet	0.33	Fe^{3+}	sextet	5.55
	doublet	1.02		quartet	5.27
V^{3+}	triplet	3.03		doublet	6.79
	singlet	3.29	Co^{2+}	quartet	0.71
V^{4+}	doublet	8.66		doublet	2.29
Cr^{2+}	quintet	0.82	Co^{3+}	quintet	7.88
	triplet	0.84		triplet	-6.01
	singlet	1.13		singlet	-7.20
Cr^{3+}	quartet	4.09	Ni^{2+}	triplet	1.57
	doublet	4.12		singlet	-3.77
Cr^{4+}	triplet	9.47	Ni^{3+}	quartet	9.02
	singlet	11.13		doublet	-8.90
Mn^{2+}	sextet	1.24	Cu^{2+}	doublet	1.39
	quartet	1.94	Cu^{3+}	triplet	5.95
	doublet	2.37		singlet	6.83
Mn^{3+}	quintet	2.92			
	triplet	4.68			
	singlet	4.83			

Table 4.7: Predicted geometries of selected metal-bound C4 complexes using a variety of DFT functionals. All distances are averaged and are in angstroms. Crystal results[20][23][24][86][87] are averaged over all similar bonds and angles. All angles are in degrees. Values in parenthesis indicate percentage deviation from crystal data. All functionals use 6-31G** basis set for non-metal atoms and SDD for metal atoms.

Metal	Property	Crystal	BLYP	B3LYP	B97D3
Ti^{4+} singlet	M-O distance	1.9630	1.877 (4.4)	1.851 (5.7)	1.866 (4.9)
	C-O distance	1.3550	1.361 (0.4)	1.351 (0.4)	1.352 (0.4)
	O-M-O angle	155.5	158.3 (1.8)	157.4 (1.2)	158.7 (2.1)
V^{3+} triplet	M-O distance	1.9404	1.911 (1.5)	1.893 (2.4)	1.903 (1.9)
	C-O distance	1.3733	1.351 (1.6)	1.338 (2.6)	1.340 (2.4)
	O-M-O angle	172.7	168.0 (2.7)	168.1 (2.7)	169.0 (2.1)
Mn^{3+} quintet	M-O distance	1.9362	1.921 (0.8)	1.905 (1.6)	1.933 (0.2)
	C-O distance	1.3557	1.350 (0.4)	1.339 (1.2)	1.337 (1.4)
	O-M-O angle	175.4	179.2 (2.2)	179.4 (2.3)	178.3 (1.7)
Fe^{3+} sextet	M-O distance	1.9763	1.956 (1.0)	1.929 (2.4)	1.966 (0.5)
	C-O distance	1.3633	1.336 (2.0)	1.329 (2.5)	1.326 (2.7)
	O-M-O angle	162.6	165.7 (1.9)	169.7 (4.4)	168.4 (3.6)
Cu^{2+} doublet	M-O distance	1.9661	2.007 (2.1)	1.928 (1.9)	2.016 (2.5)
	C-O distance	1.3838	1.324 (4.3)	1.312 (5.2)	1.313 (5.1)
	O-M-O angle	175.9	178.8 (1.6)	178.4 (1.4)	178.0 (1.2)

spin state of the bound metal although it might be expected, *a priori* from application of Hund's Rule, that spin of maximum multiplicity would be the most thermodynamically stable. Results of calculations on the thermodynamic stability and binding energy of each metal complex are shown in tables 4.8 and 4.9. As expected, in most cases the complex containing spin of maximum multiplicity is the most thermodynamically stable. This is however not observed in six complexes.

Complexes involving Ti^{2+}, Fe^{3+}, Co^{3+}, Ni^{2+}, Ni^{3+} and Cu^{3+} favour spin configurations other than high spin. Ti^{2+} favours the singlet over the triplet, Fe^{3+} favours the quartet over the sextet, Co^{3+} favours the triplet over the quintet, Ni^{2+} favours the singlet over the triplet, Ni^{3+} favours the doublet over the quartet and Cu^{3+} favours the singlet over the triplet. This pattern is observed across all functionals used in this study. Because moving from one functional to another affects all of the spin state energies to the same extent, the issue is not thought to be caused by the inability of DFT to predict the correct ground state of these species. The functionals used present a range of HF exchange from 0% to around 20% and thus the issue is invariant to both the functional used and the amount of non-local exchange. Removing dispersion from the BLYP and B3LYP functionals (results not detailed in this work) also makes no difference to either the order of stability of these complexes or the relative stability of the energy levels and this can therefore be ruled out as a source of error. The multi-reference nature of the complex was also considered and ruled out as a source of error: the issue affects complexes with both high and low B_1 values. Interestingly, the complex with the highest B_1 value, Cr^{4+} favours the triplet over the singlet as expected by application of Hund's Rule. In the absence of the ability to verify these conclusions by performing MRCI calculations on these large systems, it can reasonably be concluded that the effect is real. In this case, one possible explanation might be that the ligand is of intermediate crystal field strength: in other words, strong enough to invoke stabilisation of the quartet over the sextet in the Fe^{3+} complex for example, but not strong enough to allow the doublet to be the most stable arrangement. Essentially the ligand destabilises the $d_{x^2-y^2}$ orbital just enough that the pairing energy becomes lower than the energy required to overcome this splitting energy. The observed very small energy gap between the most stable spin arrangement and the maximum multiplicity arrangement of around 6-12 $kcal^{-1}$ in each of these cases lends weight to this theory.

Table 4.8: Calculated ground state energies of C4-metal complexes (Sc to Mn). Energies in Hartrees. All calculations use 6-311G** basis set. BLYP and B3LYP also include GD3BJ empirical dispersion. B97D3 contains dispersion and no further corrections are used.

Metal	Spin	BLYP Energy	B97D3 Energy	B3LYP Energy
Sc^{3+}	singlet	-1426.6307	-1426.2054	-1427.1407
Ti^{2+}	triplet	-1438.0866	No Results	-1438.5848
	singlet	-1438.0962	-1437.6956	-1438.5925
Ti^{3+}	doublet	-1438.1808	-1437.7747	-1438.6775
Ti^{4+}	singlet	-1438.0892	-1437.6847	-1438.5680
V^{2+}	quartet	-1451.4332	-1451.0661	-1451.9384
	doublet	-1451.4210	-1451.0427	-1451.9194
V^{3+}	triplet	-1451.5015	-1451.1296	-1451.9947
	singlet	-1451.4920	-1451.1138	-1451.9814
V^{4+}	doublet	-1451.4177	-1451.0420	-1451.8844
Cr^{2+}	quintet	-1466.7442	-1466.4279	-1467.2573
	triplet	-1466.7092	-1466.3774	-1467.2169
	singlet	-1466.6996	-1466.3514	-1467.1992
Cr^{3+}	quartet	-1466.7841	-1466.4631	-1467.2761
	doublet	-1466.7611	-1466.4186	-1467.2483
Cr^{4+}	triplet	-1466.6763	-1466.3474	-1467.1444
	singlet	-1466.6600	-1466.3154	-1467.1117
Mn^{2+}	sextet	-1484.0819	-1483.8237	-1484.6036
	quartet	-1484.0760	-1483.7993	-1484.5762
	doublet	-1484.0383	-1483.7413	-1484.5365
Mn^{3+}	quintet	-1484.1378	-1483.8706	-1484.6382
	triplet	-1484.1008	-1483.8105	-1484.5841
	singlet	-1484.0893	No Results	-1484.5708
Mn^{4+}	quartet	-1484.0205	-1483.7455	-1484.5050
	doublet	-1483.9847	-1483.6960	-1484.4523

Table 4.9: Calculated ground state energies of C4-metal complexes (Fe to Cu). Energies in Hartrees. All calculations use 6-311G** basis set. BLYP and B3LYP also include GD3BJ empirical dispersion. B97D3 contains dispersion and no further corrections are used.

Metal	Spin	BLYP Energy	B97D3 Energy	B3LYP Energy
Fe^{2+}	quintet	-1503.6427	-1503.4241	-1504.1552
	triplet	-1503.6223	-1503.3871	-1504.1223
	singlet	-1503.6037	-1503.3533	-1504.0888
Fe^{3+}	sextet	-1503.6610	-1503.4468	-1504.1558
	quartet	-1503.6849	-1503.4572	-1504.1716
	doublet	-1503.6514	-1503.4023	-1504.1275
Co^{2+}	quartet	-1525.5432	-1525.3709	-1526.0525
	doublet	-1525.5354	-1525.3515	-1526.0332
Co^{3+}	quintet	-1525.5634	-1525.3957	-1526.0420
	triplet	-1525.5742	-1525.4017	-1526.0653
	singlet	-1525.5589	-1525.3704	-1526.0348
Ni^{2+}	triplet	-1550.6328	-1550.5277	-1551.1368
	singlet	-1550.6468	-1550.5367	-1551.1414
Ni^{3+}	quartet	-1550.6492	-1550.5411	-1551.1286
	doublet	-1550.6682	-1550.5584	-1551.1472
Cu^{2+}	doublet	-1577.0186	-1576.9890	-1577.5249
Cu^{3+}	triplet	-1577.0269	-1576.9932	-1577.5157
	singlet	-1577.0500	-1577.0160	-1577.5300

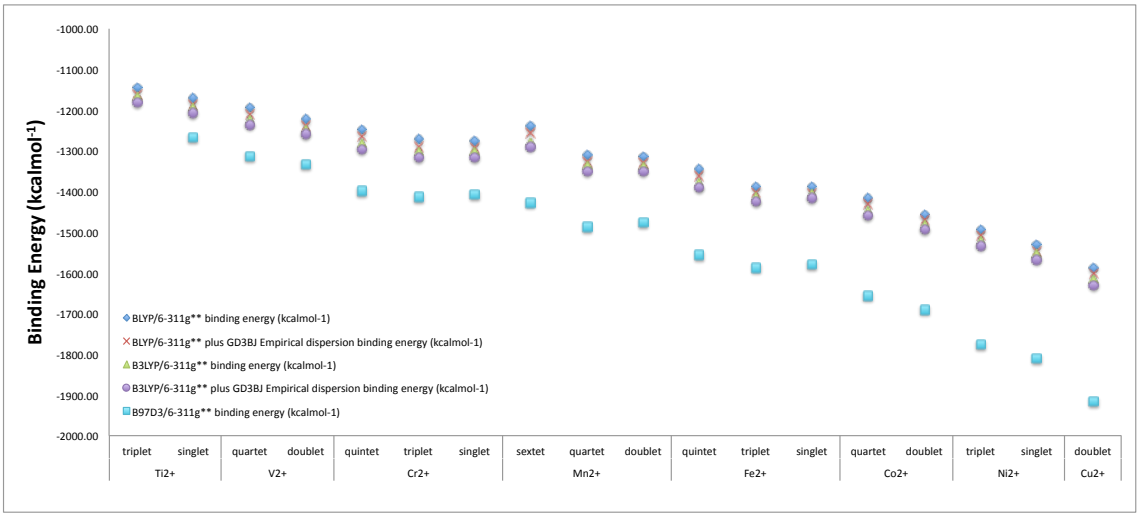

Figure 4.25: Gas phase binding energies for 2+ metal-bound C4 species. Energies in kcal mol^{-1}. All calculations use 6-311G** basis set. BLYP and B3LYP also include GD3BJ empirical dispersion. B97D3 contains dispersion and no further corrections are used.

Following analysis of the thermodynamic stability of these complexes, the binding energies of the calixarene to the metals are considered. The results are presented in tables 4.10 (Sc to Mn) and 4.11 (Fe to Cu). Trends across the various oxidations states are in figures 4.25 (oxidation state 2+), 4.26 (oxidation state 3+) and 4.27 (oxidation state 4+) for gas phase calculations.

For all oxidation state graphs, the same trend appears, of increasing magnitude of binding energy across the row of transition metals. It seems clear that the M-O bonds are primarily electrostatic in nature given the very large increase in binding energies from oxidation state 2+ to 3+ and then again for oxidation state 4+ in the gas phase calculations with no overlap between the graphs. The increase in magnitude of binding energy from the oxidation 2+ graph to the oxidation 3+ graph ranges from 600 to 1000 kcal mol^{-1} for each metal with a similar jump from oxidation 3+ graphs to that of oxidation state 4+. The slope of the graphs increases with oxidation state. From oxidation state 2+ to 3+ an increase in the slope of 30% is observed whilst the oxidation state 4+ graph is almost twice that of the oxidation 3+ graph. As the oxidation state of a metal increases, the atomic radius decreases, resulting in a harder acid. That this harder acid should then form progressively stronger bonds to the relatively hard base of the calixarene suggests that Hard-Soft Acid-Base (HSAB) theory may explain this increase in magnitude of binding energy

Table 4.10: Calculated binding energies of C4-metal complexes (Sc to Mn). Energies in kcal mol^{-1}. All calculations use 6-311G** basis set. BLYP and B3LYP also include GD3BJ empirical dispersion. B97D3 contains dispersion and no further corrections are used.

Metal	Spin	BLYP Binding	B97D3 Binding	B3LYP Binding
Sc^{3+}	singlet	-1713.12	-1779.25	-1741.78
Ti^{2+}	triplet	-1160.82	No Results	-1182.07
	singlet	-1186.94	-1268.51	-1206.97
Ti^{3+}	doublet	-1837.35	-1915.51	-1857.61
Ti^{4+}	singlet	-2760.36	-2839.57	-2769.46
V^{2+}	quartet	-1211.04	-1313.69	-1236.69
	doublet	-1238.25	-1333.90	-1259.61
V^{3+}	triplet	-1910.37	-2009.95	-1928.46
	singlet	-1928.76	-2024.43	-1944.50
V^{4+}	doublet	-2926.94	-3024.20	-2928.40
Cr^{2+}	quintet	-1264.32	-1398.85	-1294.93
	triplet	-1289.21	-1413.98	-1316.41
	singlet	-1293.77	-1408.26	-1315.93
Cr^{3+}	quartet	-1979.42	-2110.95	-1996.76
	doublet	-2006.43	-2124.49	-2020.76
Cr^{4+}	triplet	-3033.09	-3159.69	-3035.46
	singlet	-3050.90	-3167.65	-3042.93
Mn^{2+}	sextet	-1255.24	-1426.17	-1291.20
	quartet	-1326.87	-1486.21	-1349.36
	doublet	-1329.86	-1476.49	-1351.14
Mn^{3+}	quintet	-2046.04	-2211.39	-2068.69
	triplet	-2079.15	-2229.94	-2091.01
	singlet	-2084.58	No Results	-2095.34
Mn^{4+}	quartet	-3150.29	-3310.76	-3162.98
	doublet	-3175.18	-3326.97	-3177.23

Table 4.11: Calculated binding energies of C4-metal complexes (Fe to Cu). Energies in kcal mol^{-1}. All calculations use 6-311G** basis set. BLYP and B3LYP also include GD3BJ empirical dispersion. B97D3 contains dispersion and no further corrections are used.

Metal	Spin	BLYP Binding	B97D3 Binding	B3LYP Binding
Fe^{2+}	quintet	-1361.02	-1556.78	-1391.23
	triplet	-1402.99	-1588.35	-1425.35
	singlet	-1403.90	-1579.80	-1416.95
Fe^{3+}	sextet	-2029.31	-2227.82	-2048.35
	quartet	-2132.88	-2322.95	-2146.87
	doublet	-2143.37	-2320.02	-2150.72
Co^{2+}	quartet	-1430.04	-1654.89	-1458.27
	doublet	-1471.67	-1689.26	-1492.67
Co^{3+}	quintet	-2166.70	-2394.47	-2175.68
	triplet	-2236.86	-2461.57	-2253.65
	singlet	-2241.90	-2456.59	-2249.09
Ni^{2+}	triplet	-1508.00	-1775.04	-1532.91
	singlet	-1547.22	-1811.11	-1566.24
Ni^{3+}	quartet	-2276.80	-2541.97	-2286.24
	doublet	-2342.13	-2606.18	-2351.29
Cu^{2+}	doublet	-1602.96	-1917.39	-1629.28
Cu^{3+}	triplet	-2399.77	-2711.58	-2415.08
	singlet	-2448.24	-2759.93	-2458.06

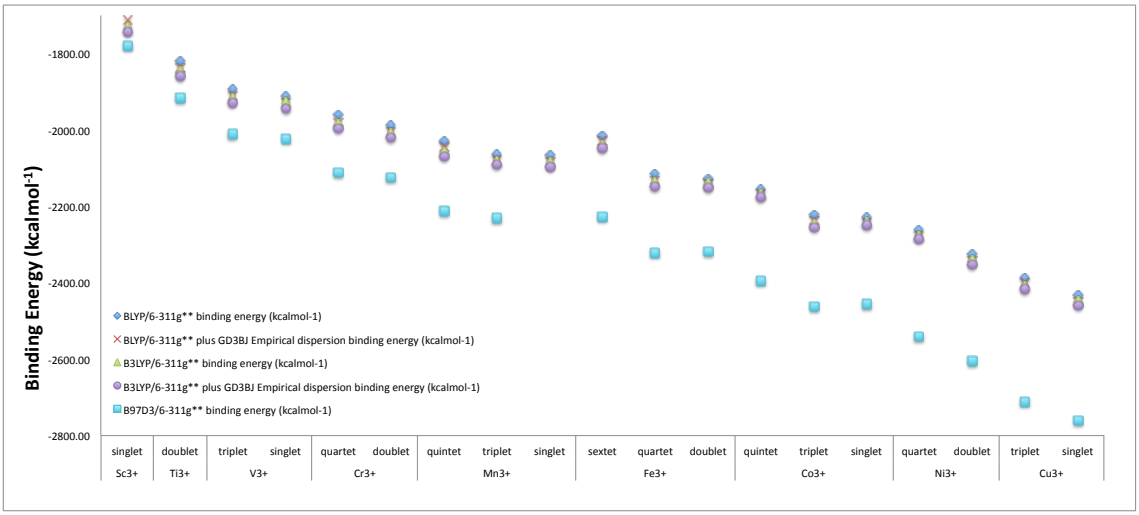

Figure 4.26: Gas phase binding energies for 3+ metal-bound C4 species. Energies in kcal mol^{-1}. All calculations use 6-311G** basis set. BLYP and B3LYP also include GD3BJ empirical dispersion. B97D3 contains dispersion and no further corrections are used.

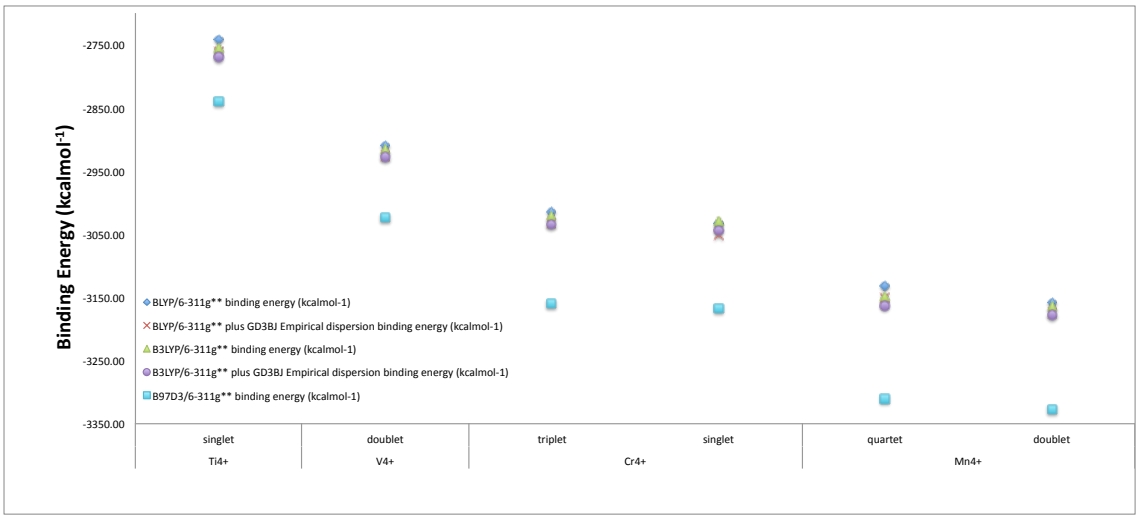

Figure 4.27: Gas phase binding energies for 4+ metal-bound C4 species. Energies in kcal mol^{-1}. All calculations use 6-311G** basis set. BLYP and B3LYP also include GD3BJ empirical dispersion. B97D3 contains dispersion and no further corrections are used.

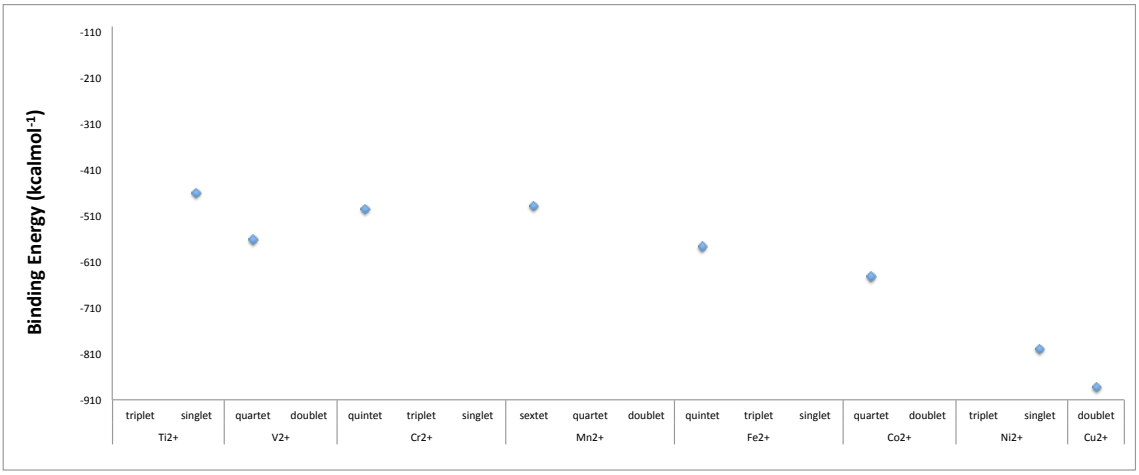

Figure 4.28: Solvent (water) Phase binding energies for 2+ metal-bound C4 species. Energies in kcal mol^{-1}. All calculations use B3LYP/6-311G** with GD3BJ empirical dispersion.

with oxidation state. It is unlikely that HSAB theory can explain the trend for one oxidation state across the transition metals though. The hardness of the acid is related to its atomic radius but this is not linear across the transition metals. Instead, the trend of atomic radii [88] is a curve with a minimum around Mn with increases on either side to Sc and Cu. Of interest is that despite the large variation of exact HF exchange from 0% to 20%, the binding energy trend across any oxidation state appears relatively invariant to the functional. B97D3 is seen to diverge a little as the transition metal series is traversed but absolute binding energies are less important than differences between metal species. In that light, all three functionals are seen to perform similarly to each other. In all cases, the trend is towards increased binding energy as the transition metal series is crossed. It is therefore predicted that calixarenes will adopt a preference for late transition metals over early transition metals and will also preferentially bind to higher oxidation species.

The effect of long range bulk solvent effects is now considered using CPCM model with water as the solvent. As a result of the relative invariance to the DFT functional used, B3LYP/6-311G** with GD3BJ empirical dispersion was arbitrarily chosen to investigate solvation effects. Only the most thermodynamically stable species for each metal oxidation state, as detailed in tables 4.8 and 4.9, were analysed for this purpose. The results are shown in figures 4.28, 4.29 and 4.30.

As expected, solvation results in considerable reduction in the magnitude of binding

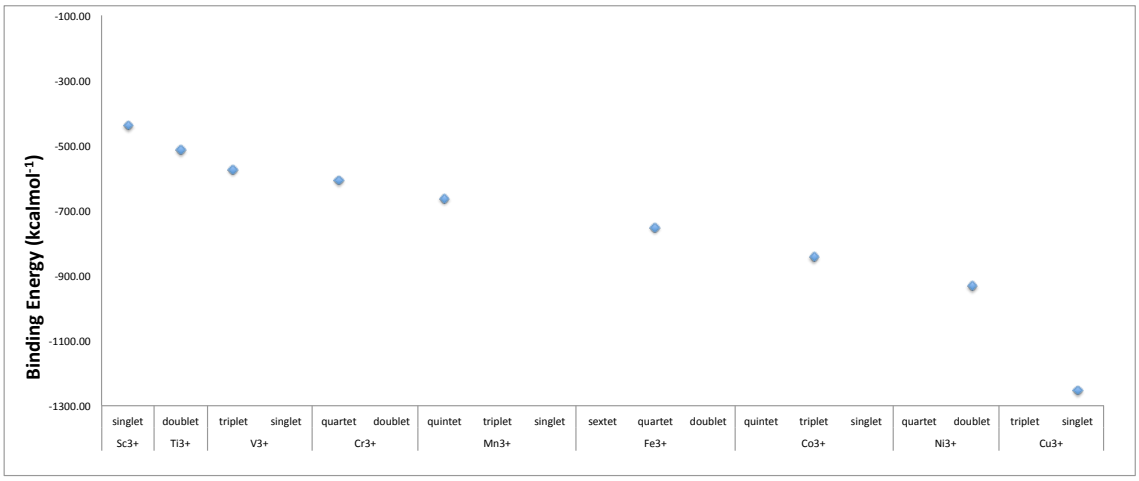

Figure 4.29: Solvent (water) Phase binding energies for 3+ metal-bound C4 species. Energies in kcal mol^{-1}. All calculations use B3LYP/6-311G** with GD3BJ empirical dispersion.

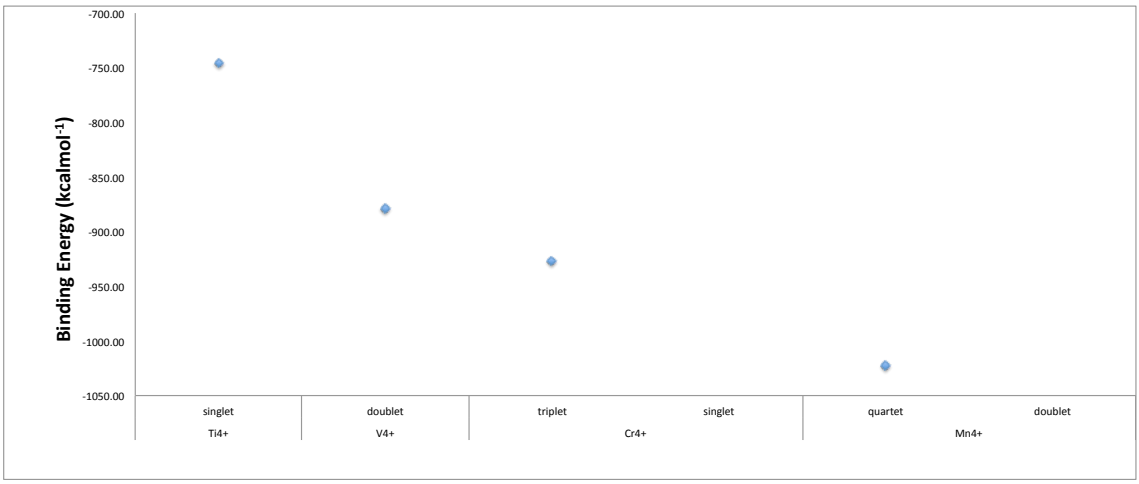

Figure 4.30: Solvent (water) Phase binding energies for 4+ metal-bound C4 species. Energies in kcal mol^{-1}. All calculations use B3LYP/6-311G** with GD3BJ empirical dispersion.

energies in all cases as a result of the increased stability of all charged species. The reduction in magnitude of binding energy for oxidation state 2+ is in the order of 600 to 1000 kcal mol^{-1}, for oxidation state 3+, the reduction is much more pronounced at 1400-1500 kcal mol^{-1} and for oxidation state 4+, reductions of over 2000 kcal mol^{-1} are observed. Because the introduction of solvation is likely to have a greater effect on higher charged species, this finding is not surprising. Qualitatively, the solvent phase graphs are no different to the gas phase graphs however. The same trends appear for each oxidation state. Quantitatively, there is a reduction in the trend slope of the oxidation state 4+ graph but the 2+ and 3+ slopes are unaffected by the introduction of solvation. At this stage it is noted that the earlier B_1 tests showed some species which indicated borderline multi-reference nature. For these species, spin contamination was shown to be present in the calculations. The calculations presented here show that the spin contaminated species, when included, fit the overall trend very well. This indicates that although spin contaminated species have to be treated with care as regards calculations made on them, in the case of this work, it appears that spin contamination is not a significant factor in the calculation of binding energies and does not unduly introduce errors in the process. It could simply be that the scale of the absolute energies involved here simply swamps the spin contamination error. The inclusion of solvation has however brought about a significant change in that the various oxidation state graphs now overlap each other. Some late transition metals such as Ni^{2+} and Cu^{2+} are now seen to be more favoured than early transition metals such as Ti^{4+} by approximately 50 kcal mol^{-1} and 140 kcal mol^{-1} respectively. In fact, only late transition metals beyond Co^{3+} are more favoured. Cu^{3+} is the most favoured species and binds preferentially compared to any other species in this work. This indicates that whilst electrostatics are important in the metal-calixarene binding, other factors are also involved. Of course this work has only established preferential binding for transition metal cations from a thermodynamic stability point of view. Kinetic factors should also be considered before more accurate predictions can be made about the likely outcome of experimental competitive binding exercises. Although Cu^{3+} is predicted to preferentially bind before Mn^{2+}, early unpublished tests suggest that in fact Mn^{2+} bound C4 crystals are exclusively formed in a mixture of Mn^{2+} and Cu^{3+} salts. This work is not yet complete and will not be discussed further.

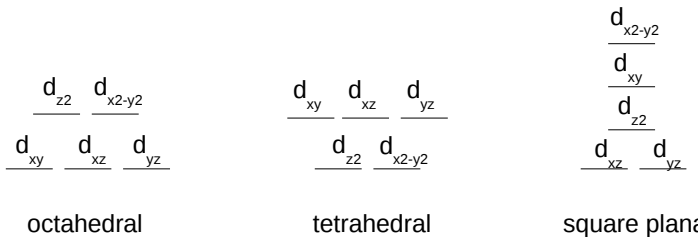

Figure 4.31: The crystal field theory d-splitting diagrams for octahedral, tetrahedral and square planar geometries around a transition metal centre.

Next, consideration is given to the comparison between crystal field theory predictions of d-orbital splitting patterns and those obtained during studies such as this using DFT. Crystal field theory predicts that when metals are co-ordinated in octahedral, tetrahedral and square planar fashion, d-orbital splitting is expected as shown in figure 4.31. This picture changes for the molecules in this study largely because the restrictions on paired electrons sharing the same spatial orbital are removed. Figures 4.32 and 4.33 show the Mn^{3+} (quintet spin) co-ordinated C4 as an example. Here the geometry around the metal atom is square planar and the actual d-splitting pattern is as shown in figure 4.34.

It can be seen that the orbitals are arranged with the z co-ordinate pointing up through the C4 ring and the x and y co-ordinates pointing along the M-O bonds at the tetraphenolic pocket. The spin density for this species is as specified in table 4.13. The $d_{x^2-y^2}$ orbitals are virtually unoccupied and also point directly along the M-O bonds. For both reasons, this orbital is the highest in energy as expected. The remaining d-orbitals contain a single alpha electron. d_{z^2} points upwards into the upper cavity of the molecule. This represents a relatively high energy position compared to the remaining occupied d-orbitals and the d_{z^2} orbital is therefore the highest occupied d-orbital. The most stable d orbital is that of d_{xy} as this orbital point between the M-O bonds and also does not extend into the upper rim cavity space. Finally, the d_{xz} and d_{yz} orbitals have a component which points partially into the upper cavity and are thus higher in energy than the d_{xy} orbital but lower in energy than the d_{z^2} orbital because they intrude less into the cavity. Both are degenerate as expected as their spatial extent into the cavity are equivalent. Thus, all of the orbitals are ordered in energy as would be expected.

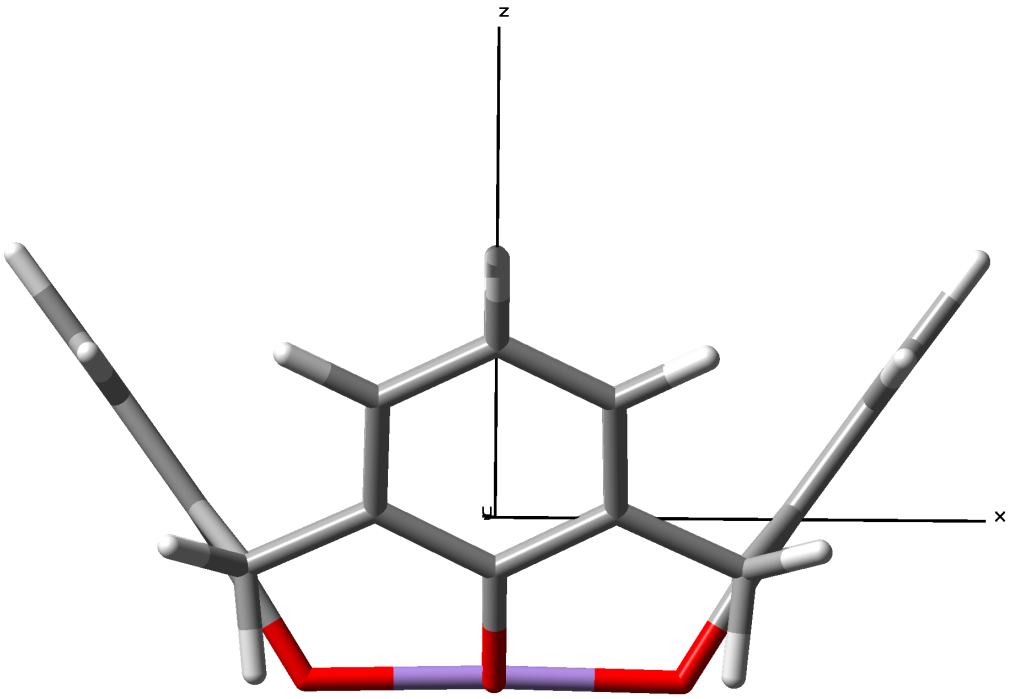

Figure 4.32: Side view of Mn^{3+} (quintet spin) co-ordinated C4 showing cartesian axes superimposed on the structure.

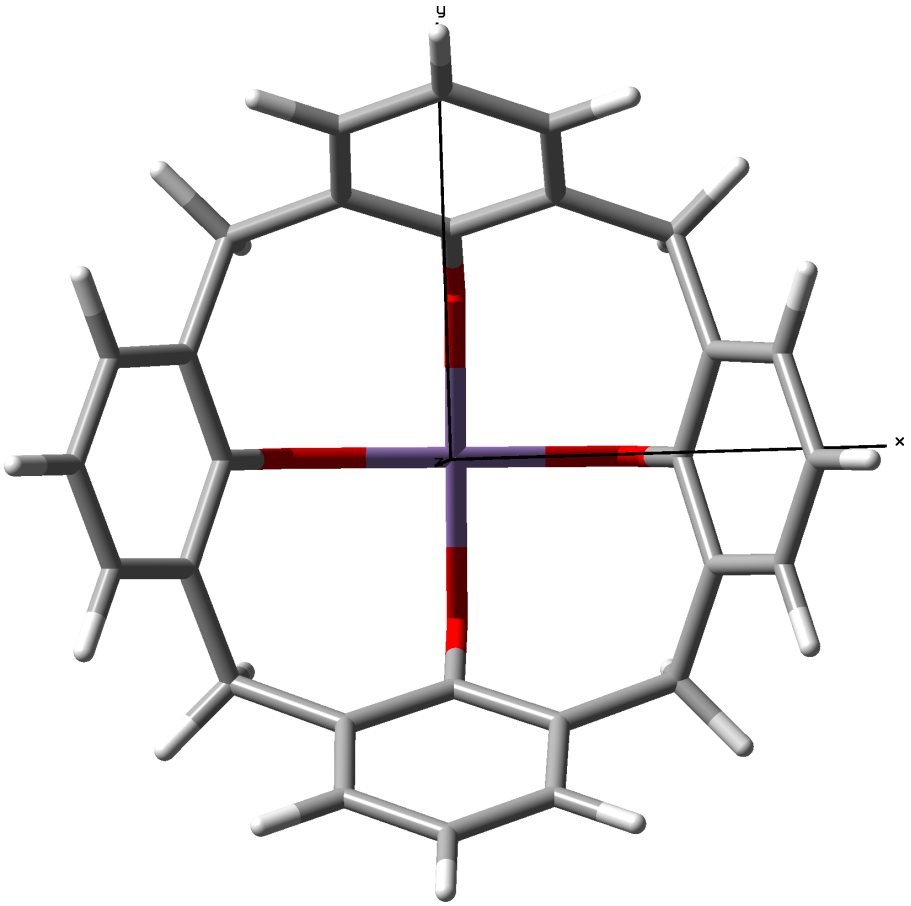

Figure 4.33: Top view of Mn^{3+} (quintet spin) co-ordinated C4 showing cartesian axes superimposed on the structure.

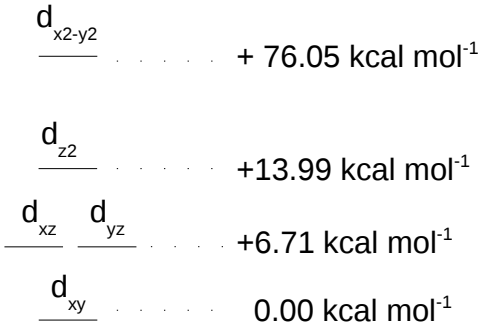

Figure 4.34: The d-splitting diagrams for Mn^{3+} (quintet spin) co-ordinated C4. Here the geometry is square planar. Energies are relative to the d_{xy} orbital energy. Alpha spin-orbitals shown only. All beta spin d-orbitals are unoccupied and are considerably destabilised relative to the alpha spin-orbitals and are not presented here.

Finally, consideration is given to the use of spin density calculations of each species in order to determine the location of the unpaired electrons in the system. Results are shown in figure 4.35 and tables 4.12, 4.13 and 4.14. Results for Sc^{3+} (singlet), Ti^{4+} (singlet), Ti^{2+} (singlet) and Ni^{2+} (singlet) all show zero spin density and are therefore not detailed. As can be seen, most complexes do not show significant levels of spin density away from the metal centre. More specifically, the bulk of spin density is found in the metal 3d orbitals. Some minor spin polarisation, evidenced by the presence of β spin density into the tetraphenolic oxygen atoms and the conjugated aromatic ring, is exhibited by Ni^{3+} (doublet), Mn^{3+} (quintet), Fe^{3+} (quartet), Cu^{2+} (doublet) and Co^{3+} (triplet). There is however no spin contamination in the calculations for these complexes. Two complexes do stand out however: Mn^{4+} (quartet) and Cr^{4+} (triplet). Spin polarisation in both of these complexes is significant and results in β spin density well into the aromatic ring system in the calixarene. There is also a resultant increase in spin contamination in the calculation of around 10%. Although this is a significant amount of spin contamination, it is at the limit of what is deemed acceptable for calculations [89] and we therefore include these results in our work.

4.4.3 Summary and Conclusions - Lower Rim Binding

It was found that calixarenes are predicted to have a preference for late transition metals over early transition metals with regard to binding to the tetraphenolic pocket. From thermodynamic stability considerations, Cu^{3+} was predicted to preferentially bind ahead of all other first row transition metals regardless of oxidation state or spin and it is expected that this is due to largely electrostatic effects. The trend for each oxidation state was seen to be a linear increase in magnitude of binding energy across the transition metals. The level of exact HF exchange was not found to be an important factor in these trends indicating that these systems may be adequately described as relatively single reference in nature. This view is backed by the results of B_1 tests. Whilst solvation was shown to reduce the absolute energies of each complex, the qualitative trends were unaffected with respect to the gas phase calculations. Significant overlap between trends was made possible though by solvation allowing more meaningful and realistic predictions to be made about preferential binding of calixarenes towards metals of different oxidation and spin states.

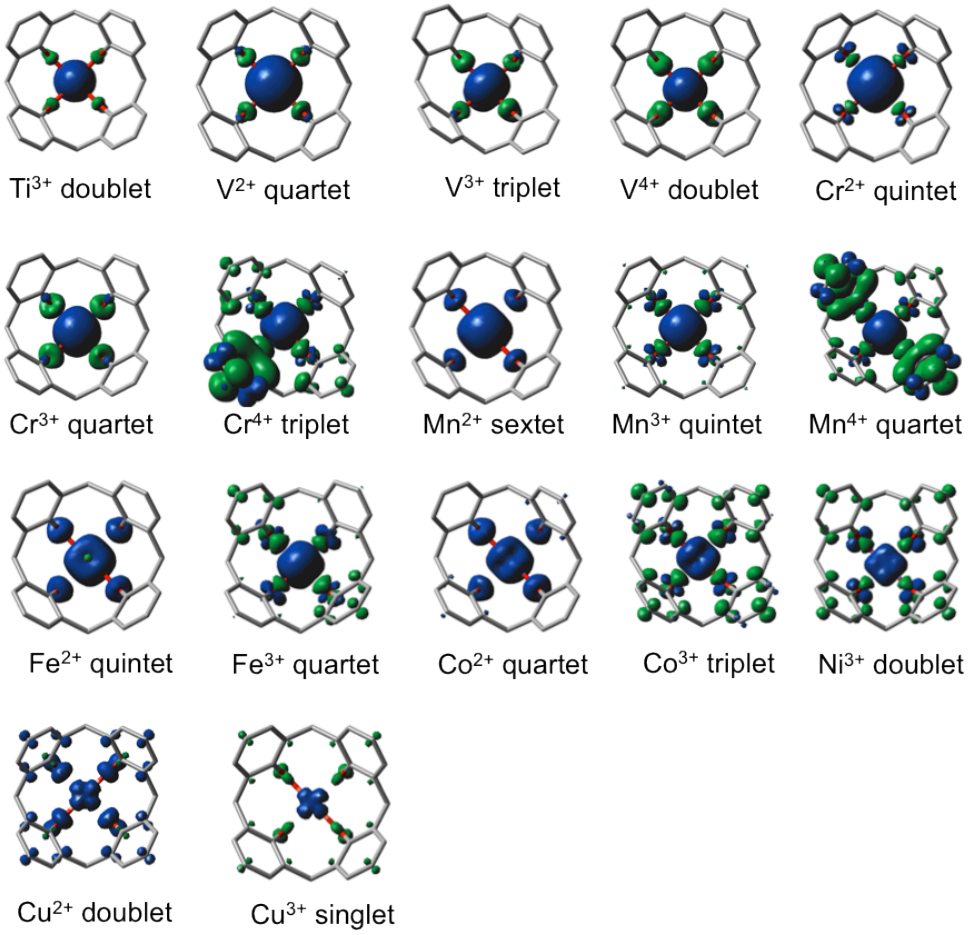

Figure 4.35: Spin densities of solvated metal-bound C4 complexes. Blue areas show an excess of α spin density. Green areas show an excess of β spin density.

Table 4.12: Spin density values and unpaired electron location within solvated complexes (Sc to Cr). Positive numbers refer to areas of excess α spin density. Negative numbers refer to areas of excess β spin density. Spin density values are reported as $2\langle \hat{S}_Z \rangle$

Metal	Spin	Spin Density
Sc^{3+}	singlet	No Spin Density - restricted singlet
Ti^{2+}	singlet	No Spin Density - restricted singlet
Ti^{3+}	doublet	+0.70 on Ti $3d_{z^2}$ orbital
Ti^{4+}	singlet	No Spin Density - restricted singlet
V^{2+}	quartet	+0.79 on V $3d_{yz}$ orbital
		+0.79 on V $3d_{xz}$ orbital
		+0.52 on V $3d_{z^2}$ orbital
V^{3+}	triplet	+0.82 on V $3d_{yz}$ orbital
		+0.69 on V $3d_{z^2}$ orbital
V^{4+}	doublet	+0.77 on V $3d_{z^2}$ orbital
Cr^{2+}	quintet	+0.80 on Cr $3d_{xy}$ orbital
		+0.78 on Cr $3d_{yz}$ orbital
		+0.78 on Cr $3d_{xz}$ orbital
		+0.65 on Cr $3d_{z^2}$ orbital
Cr^{3+}	quartet	+0.81 on Cr $3d_{xz}$ orbital
		+0.81 on Cr $3d_{yz}$ orbital
		+0.71 on Cr $3d_{z^2}$ orbital
		+0.12 on Cr $3d_{x^2-y^2}$ orbital
		-0.20 delocalised into O p orbitals
Cr^{4+}	triplet	+0.76 on Cr $3d_{z^2}$ orbital
		+0.75 on Cr $3d_{yz}$ orbital
		+0.64 on Cr $3d_{xy}$ orbital
		+0.34 on Cr $3d_{xz}$ orbital
		+0.12 on Cr $3d_{x^2-y^2}$ orbital
		-1.20 delocalised into O p orbitals and π system

Table 4.13: Spin density values and unpaired electron location within solvated metal-bound C4 Complexes (Mn to Fe). Positive numbers refer to areas of excess α spin density. Negative numbers refer to areas of excess β spin density. Spin density values are reported as 2 $\langle \hat{S}_Z \rangle$

Metal	Spin	Spin Density
Mn^{2+}	sextet	+0.82 on Mn $3d_{xy}$ orbital
		+0.82 on Mn $3d_{xz}$ orbital
		+0.82 on Mn $3d_{yz}$ orbital
		+0.81 on Mn $3d_{x^2-y^2}$ orbital
		+0.78 on Mn $3d_{z^2}$ orbital
Mn^{3+}	quintet	+0.83 on Mn $3d_{xz}$ orbital
		+0.83 on Mn $3d_{yz}$ orbital
		+0.81 on Mn $3d_{xy}$ orbital
		+0.77 on Mn $3d_{z^2}$ orbital
		+0.27 on Mn $3d_{x^2-y^2}$ orbital
Mn^{4+}	quartet	+0.82 on Mn $3d_{xy}$ orbital
		+0.81 on Mn $3d_{yz}$ orbital
		+0.81 on Mn $3d_{xz}$ orbital
		+0.80 on Mn $3d_{z^2}$ orbital
		+0.45 on Mn $3d_{x^2-y^2}$ orbital
		-1.36 delocalised into O p orbitals and π system
Fe^{2+}	quintet	+0.82 on Fe $3d_{xz}$ orbital
		+0.82 on Fe $3d_{yz}$ orbital
		+0.80 on Fe $3d_{xy}$ orbital
		+0.77 on Fe $3d_{x^2-y^2}$ orbital
Fe^{3+}	quartet	+0.81 on Fe $3d_{xz}$ orbital
		+0.79 on Fe $3d_{xy}$ orbital
		+0.77 on Fe $3d_{z^2}$ orbital
		+0.34 on Fe $3d_{x^2-y^2}$ orbital

Table 4.14: Spin Density Values and Unpaired Electron Location within Solvated metal-bound C4 Complexes (Co to Cu). Positive numbers refer to areas of excess α spin density. Negative numbers refer to areas of excess β spin density. Spin density values are reported as 2 $\langle \hat{S}_Z \rangle$

Metal	Spin	Spin Density
Co^{2+}	quartet	+0.79 on Co $3d_{xz}$ orbital
		+0.72 on Co $3d_{xy}$ orbital
		+0.57 on Co $3d_{x^2-y^2}$ orbital
		+0.28 on Co $3d_{z^2}$ orbital
Co^{3+}	triplet	+0.82 on Co $3d_{xz}$ orbital
		+0.77 on Co $3d_{xy}$ orbital
		+0.41 on Co $3d_{x^2-y^2}$ orbital
		+0.12 on Co $3d_{z^2}$ orbital
Ni^{2+}	singlet	No Spin Density - restricted singlet
Ni^{3+}	doublet	+0.76 on Ni $3d_{z^2}$ orbital
		+0.33 on Ni $3d_{x^2-y^2}$ orbital
		+0.19 on Ni $3d_{xy}$ orbital
		-0.50 delocalised into O p orbitals and π system
Cu^{2+}	doublet	+0.56 on Cu $3d_{xy}$ orbital
		-0.44 delocalised into O p orbitals and π system
Cu^{3+}	triplet	+0.20 on Cu $3d_{xy}$ orbital
		-0.20 delocalised into O p orbitals and π system

Kinetic studies are required in order to complete the picture and determine whether kinetic factors are able to counter the thermodynamic trends observed in this work. DFT was shown to work reasonably well for these types of molecule. The DFT functionals used were able to accurately predict geometries which matched known crystal structures to an acceptable degree. Finally, DFT was shown to accurately predict the energetic ordering of d-orbitals. For all of these reasons, it is reasonable to conclude that the use of DFT is justified for such systems.

4.5 Calix[4]arene Upper Rim Binding

The relevant published paper covering the work described in this section is provided in reference [90]. As described earlier, the emergence of polymetallic calixarene clusters using metals such as Fe and Cu [23][24], involves the binding of transition metals to the lower tetraphenolic pocket of the calixarene. In addition to affecting the geometry at the calixarene upper rim, the metal provides an extra binding site for guest molecules. This work seeks to clarify what effect, if any, the presence of a transition metal atoms in C4 has on the binding preferences at the upper rim towards small guest molecules. Some of the guest molecules are ambidentate and both linkage isomers are investigated. Comparison with metal-free C4 is considered.

4.5.1 Computational Details - Upper Rim Binding

All calculations in this subsection were performed using Gaussian 09 D01 [54]. Geometry optimisations were performed using 6-31G** basis set in conjunction with DFT functionals BLYP [62][71], B3LYP [55][56][71], CAM B3LYP [91], M06 [92], M06L [93], ωB97, ωB97X [94] and ωB97XD [95] for non metal atoms. SDD [73] was used for all metal atoms with 10 electrons included as core. GD3 [96] empirical dispersion was used for calculations involving M06 and M06L, GD3BJ [57] was used for BLYP and B3LYP and the ωB97 family used no added empirical dispersion. Energy values are corrected for zero point energy with no symmetry constraints applied.

All systems were checked for multi-reference behaviour using a modification of the Truhlar B_1 test detailed earlier for the lower rim binding preference work. Unlike with the lower rim binding work detailed earlier, it is necessary to include empirical

dispersion in the B_1 test. GD3BJ is not specified for B1LYP however and B3LYP has subsequently been used as a substitute. This doesn't create a problem as B3LYP contains 20% HF exchange and therefore contains a reasonably comparable amount with B1LYP. Equation 4.2, with references to B1LYP replaced by B3LYP, applies to the B_1 tests in this work. The value of $n = 1$ is assumed for all complexes as this is the worst case scenario. In the absence of certainty over exactly how many formal bonds are formed between the guest and the calixarene this is a reasonable position to take.

Analysis of analytical Hessian computations confirmed the nature of critical points as minima (all positive eigenvalues). After geometry optimisation was performed on each compound, wavefunction stability tests [75][76] were carried out. In the presence of instabilities, a new more stable wavefunction was found and used to re-optimise the structure until no further instabilities were uncovered. All calculations were checked for spin contamination [81][82][83][84][85].

Basis Set Superposition Error was corrected for using Counterpoise corrections as implemented within the Gaussian software [97][98] with subsequent basis set improvements to 6-311G**, 6-311+G** and 6-311++G** via single point calculations from the 6-31G* optimised geometry for each species. Binding energies are calculated as shown in equation 4.3 where $E_{complex}$ is the zero point corrected energy of the geometry optimised bound calixarene-gas complex, E_{gas} is the zero point corrected energy of the free gas molecule and E_{C4} is the zero point corrected energy of the geometry optimised C4 in the cone conformation. In the lower rim work earlier, all metals were modelled as 4 co-ordinate square planar complexes. Because of the dominance of dispersion effects in these calculations and the presence of the guest molecule in an axial position of the metal atom, it was necessary to use water molecules at the other axial position for metals which were normally 5 or 6 co-ordinate. Mn and Fe complexes are therefore modelled as 5 co-ordinate calixarenes, with the upper axial site free for binding to the guest. Cu, Ni and Co species were all modelled as square planar as before with the guest occupying a 5th co-ordination site to the metals. Example models are shown in figure 4.36.

Solvation was performed using the CPCM solvent model [66][67] with water solvent at the B3LYP/6-311++G** level with GD3BJ empirical dispersion. Spin density calculations were performed using an isovalue of 0.002 on all complexes.

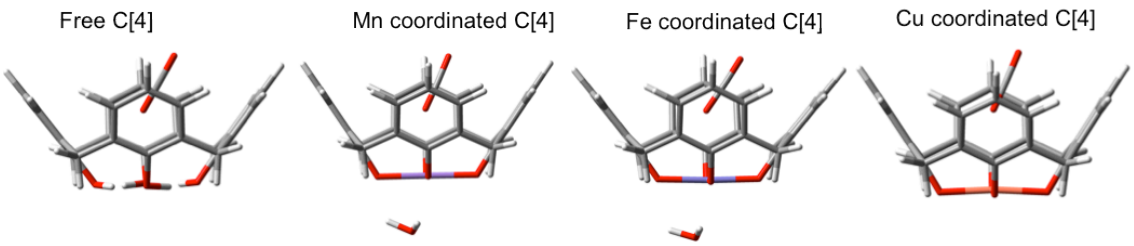

Figure 4.36: Model complexes for C4 upper rim binding calculations. The guest in this case is CO_2. The water molecule underneath the calixarene for Fe and Mn is bound to the metal and completes the 6-coordination sphere. In a crystal, this water molecule would be an alcohol solvent molecule. This is not required for square planar arrangements such as metal-free C4 or Cu-bound calixarene complexes.

Finally, NBO 3.0 calculations were performed at the B3LYP/6-311++G** level with GD3BJ empirical dispersion. Details of NBO 3.0 were given earlier for the lower rim binding preference work.

$$E_{bind} = E_{complex} - E_{gas} - E_{C4} \tag{4.3}$$

4.5.2 Results and Discussion - Upper Rim Binding

B_1 diagnostic tests were performed on a system consisting of a molecule of CO_2 bound in *endo* fashion within the upper rim of C4. A variety of transition metals in various oxidation and spin states were then placed within the tetraphenolic pocket before optimising. Results are shown in table 4.15.

All values are well under the 10 kcal mol^{-1} cutoff value of B1 which would indicate that all of these systems can reasonably be described as largely single reference. In this sense, hybrid functionals such as B3LYP are shown to be a reasonable choice of DFT functional. Before discussing the choice of DFT functional for this work, basis set choice was explored by examining the effect of a variety of basis sets on the binding energy of CO_2 to the upper rim of C4 with Fe^{3+} bound to the lower rim. Here the spin state of Fe^{3+} is taken to be the quartet as this was the most thermodynamically stable form found in the previous work on lower rim preferential bindings. Results are shown in table 4.16.

Table 4.15: Results of B_1 diagnostic tests on all C4 complexes within which a CO_2 molecule is bound in *endo* fashion within the upper rim. All energies are reported in kcal mol^{-1}.

Metal	Spin	B_1
No Metal	N/A	-1.21
Mn^{3+}	quintet	-0.70
Fe^{3+}	sextet	-0.77
	quartet	-2.17
	doublet	-1.93
Cu^{2+}	doublet	-0.37
Cu^{3+}	triplet	-0.23
	singlet	-0.31

Table 4.16: Effect of basis set on the binding energy of Fe^{3+} lower-rim-coordinated C4 (quartet spin) towards *endo* bound CO_2. All energies are reported in kcal mol^{-1}. All calculations use B3LYP with GD3BJ dispersion. Geometries are based on 6-31G** for Pople basis sets and cc-pVDZ for Dunning basis sets. All values are BSSE corrected.

Basis Set	Binding Energy
6-31G**	-6.31
6-311G**	-9.00
6-311+G**	-8.87
6-311++G**	-8.85
cc-pVDZ	-8.48
cc-pVTZ	-8.52

Starting with the Pople basis sets, it can be seen that the greatest difference in binding energies comes from the move from double-ζ to triple-ζ. Inclusion of diffuse functions appears to make relatively little difference in comparison. The inclusion of these diffuse functions however adds little in the way of extra basis functions and therefore 6-311++G** is the preferred Pople basis set. Good agreement between this basis set and both cc-pVDZ and cc-pVTZ is found indicating that triplet-ζ may be close to the basis set limit for binding energies. The difference between cc-pVTZ and 6-311++G** is just 0.33 kcal mol^{-1} but cc-pVTZ uses significantly more basis functions. It is therefore concluded that for this work, 6-311++G** represents a good compromise between computational cost and accuracy and this basis set is used for all further work.

The choice of DFT functional follows a similar principle. Using the same model system as that for the basis set selection, the likely non-covalent nature of the binding of guests to the calixarene warrants consideration to be given to functionals which are explicitly designed to correct capture long range effects such as dispersion and non-covalent bonding. To that end, the functionals CAM-B3LYP, M06, M06L, ωB97, ωB97X and ωB97XD are investigated along with the more common B3LYP. First the predicted binding energies on the model system above are compared. Results are shown in table 4.17 using the 6-311++G** basis set. Dispersion is added as needed for the functional: GD3BJ for B3LYP and CAM-B3LYP, with GD3 used for M06 and M06L. No empirical dispersion is added for the ωB97 family of functionals.

In the absence of experimental data, in order to make sense of which of these values can be relied upon, it is instructive to compare the capability of each of these functionals of predicting the geometry of the Fe^{3+} lower-rim-coordinated C4 (quartet spin) with no bound guest molecule. Crystal data for this complex [23] is used as a benchmark for the functionals. Key geometric parameters are described in figures 4.37 with results shown in tables 4.18, 4.19 and 4.20.

Table 4.21 shows the average errors for each DFT functional across the ten geometric properties detailed above. Here we see that the Truhlar Minnesota family of functionals appears to give the best performance with average errors slightly better than B3LYP. A problem is however seen at the upper rim. Although the surface area is predicted, by the Truhlar functionals, to be closer to the crystal data than B3LYP, a rectangular arrangement is predicted. This is at odds with the crystal

Table 4.17: Effect of DFT functional on the binding energy of Fe^{3+} lower-rim-coordinated C4 (quartet spin) towards *endo* bound CO_2. All energies are reported in kcal mol^{-1}. Appropriate dispersion corrections are included as described in the text. Geometries are based on 6-31G** with energies subsequently calculated as single point using 6-311++G** at these geometries. All values are BSSE corrected.

DFT Functional	Binding Energy
B3LYP	-8.85
CAM-B3LYP	-8.69
M06	-11.84
M06L	-10.82
ωB97	-7.87
ωB97X	-6.29
ωB97XD	-8.17

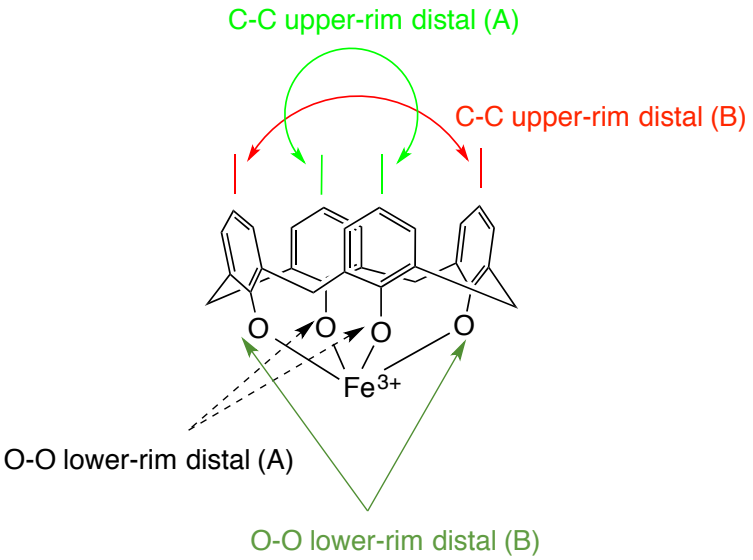

Figure 4.37: Geometric parameters for Fe^{3+}-coordinated C4 (quartet spin).

Table 4.18: Comparison of the geometric predictions of Fe^{3+}-bound C4 (quartet spin) with no guests bound for B3LYP and CAM-B3LYP. All distances in angstroms and all angles in degrees. Crystal results[23] are averaged over all similar bonds and angles. Values in parentheses represent percentage error compared to crystal structure.

Property	Crystal	B3LYP	CAM-B3LYP
C-C upper rim distal (A)	7.8212	8.3301 (6.5)	8.1309 (4.0)
C-C upper rim distal (B)	8.0462	8.3613 (3.9)	8.6475 (7.5)
average C-C upper rim distal	7.9337	8.3457 (5.2)	8.3892 (5.7)
upper rim surface area	62.930	69.650 (10.0)	70.312 (12.0)
Fe-O average distance	1.9763	1.9226 (2.7)	1.8850 (4.6)
Phenolic C-O average distance	1.3633	1.3327 (2.2)	1.3352 (2.1)
O-O lower rim distal (A)	3.9111	3.8459 (1.7)	3.8154 (2.4)
O-O lower rim distal (B)	3.9034	3.8437 (1.5)	3.7212 (4.7)
average O-O lower rim distal	3.9073	3.8448 (1.6)	3.7683 (3.6)
O-Fe-O angle	162.6	178.2 (9.6)	177.0 (8.9)

Table 4.19: Comparison of the geometric predictions of Fe^{3+}-bound C4 (quartet spin) with no guests bound for M06 and M06L. All distances in angstroms and all angles in degrees. Crystal results[23] are averaged over all similar bonds and angles. Values in parentheses represent percentage error compared to crystal structure.

Property	Crystal	M06	M06L
C-C upper rim distal (A)	7.8212	7.8929 (0.9)	8.1100 (3.7)
C-C upper rim distal (B)	8.0462	8.6125 (7.0)	8.5133 (5.8)
average C-C upper rim distal	7.9337	8.2527 (4.0)	8.3117 (4.8)
upper rim surface area	62.930	67.978 (8.0)	69.043 (9.7)
Fe-O average distance	1.9763	1.9522 (1.2)	1.9387 (1.9)
Phenolic C-O average distance	1.3633	1.3165 (3.4)	1.3243 (2.9)
O-O lower rim distal (A)	3.9111	3.9703 (0.0)	3.9354 (1.3)
O-O lower rim distal (B)	3.9034	3.8335 (1.8)	3.8144 (2.3)
average O-O lower rim distal	3.9073	3.9019 (0.1)	3.8749 (0.8)
O-Fe-O angle	162.6	178.3 (9.7)	177.8 (9.4)

Table 4.20: Comparison of the geometric predictions of Fe^{3+}-bound C4 (quartet spin) with no guests bound for ωB97, ωB97X and ωB97XD. All distances in angstroms and all angles in degrees. Crystal results[23] are averaged over all similar bonds and angles. Values in parentheses represent percentage error compared to crystal structure.

Property	Crystal	ωB97	ωB97X	ωB97XD
C-C upper rim distal (A)	7.8212	8.1331 (4.0)	8.6130 (4.4)	8.1121 (3.7)
C-C upper rim distal (B)	8.0462	8.6682 (7.7)	8.6547 (7.6)	8.5854 (6.7)
avg. C-C upper rim distal	7.9337	8.4007 (5.9)	8.4089 (6.0)	8.3488 (5.2)
upper rim surface area	62.930	70.499 (12)	70.648 (12)	69.646 (11)
Fe-O average distance	1.9763	1.8902 (4.4)	1.8952 (4.1)	1.9033 (3.7)
Phenolic C-O average dist.	1.3633	1.3409 (1.6)	1.3364 (2.0)	1.3311 (2.4)
O-O lower rim distal (A)	3.9111	3.8267 (2.2)	3.8358 (1.7)	3.8537 (1.5)
O-O lower rim distal (B)	3.9034	3.7304 (4.4)	3.7418 (4.1)	3.7586 (3.8)
avg. O-O lower rim distal	3.9073	3.7786 (3.3)	3.7888 (3.0)	3.8053 (2.6)
O-Fe-O angle	162.6	176.9 (8.8)	177.1 (9.0)	177.3 (9.1)

data which shows an almost square arrangement. Only B3LYP is able to predict this to any degree of accuracy. A similar story emerges from the results for the lower rim, with Truhlar functionals again predicting a rectangular arrangement at the tetraphenolic pocket as opposed to the square geometry of the crystal. Again B3LYP is the only functional which captures this well. Because the geometry of upper and lower rims of the structure is the most important for guest-host binding predictions, it was decided to use B3LYP as the desired DFT functional for all further work and the B3LYP energetic binding energy shown in table 4.17 is taken as the most reliable result. This validation of the use of B3LYP is consistent with our use of this functional in other calixarene work shown earlier.

A word of caution is necessary at this stage. B3LYP/6-31G* is known to have two systematic errors and it can be assumed that B3LYP/6-311++G** will also exhibit these flaws [99]. The two errors are as follows: firstly, the neglect of basis set superposition error (BSSE) results in over-binding of species and neglect of dispersion effects results in under-binding of species. When weak binding is present, as expected between the guest and the host in this work, both of these errors are

Table 4.21: Average errors of DFT functionals against the crystal structure for the ten geometric properties of Fe^{3+} lower-rim-coordinated C4 with no bound guest molecule. All values are in percent.

DFT Functional	Avg. Error
M06	3.5
M06L	4.3
B3LYP	4.5
ωB97XD	5.0
ωB97X	5.4
ωB97	5.4
CAM-B3LYP	5.6

very serious. Fortuitous cancelling can result in highly accurate calculations but this can neither be relied upon nor predicted in advance. Following advice in reference [99], to counter these problems within this work, dispersion effects are added as GD3BJ empirical dispersion and BSSE is accounted for using the counterpoise correction available within the Gaussian software package. The use of a triple-ζ basis set provides additional protection against these problems.

Following the choice of B3LYP/6-311++G**/GD3BJ and BSSE correction, attention now turns to the effect of the nature of the lower-rim-bound metal atom on the binding energy of guests at the upper rim. For this task, CO_2 is used as the guest molecule as a range of lower-rim-bound metals are investigated for their effect on CO_2 binding. For comparison, metal free calixarene results are also provided. The results are shown in table 4.22.

As can be seen, there is relatively little difference in binding energies when the nature of the metal is changed. The average binding energy of CO_2 when a metal is included is around -8.63 kcal mol^{-1}. It would appear that it is the presence of a metal of any kind which has the greatest impact on the binding energy rather than the nature of that metal. This may have implications for practical gas sensors using C4. As has been described earlier, the work of Ytreberg involves tethering the calixarene to a gold substrate with an increase in the magnitude of guest binding by 1.58 kcal mol^{-1}. The results shown here indicate an average increase of 1.97 kcal mol^{-1}, with a range of 1.07 kcal mol^{-1} to 2.98 kcal mol^{-1} which is in good

Table 4.22: Effect of variation of metal on binding energy of C4 towards *endo* bound CO_2. Values are in kcal mol^{-1}. All calculations use B3LYP/6-311++G** on non-metal atoms. SDD on metal atoms. GD3BJ empirical dispersion included. All values BSSE corrected.

Metal	Binding Energy
No Metal	-6.76
Fe^{3+} (quartet spin)	-8.85
Fe^{3+} (sextet spin)	-8.84
Cu^{2+} (doublet spin)	-8.83
Cu^{3+} (singlet spin)	-8.07
Cu^{3+} (triplet spin)	-8.18
Ni^{2+} (singlet spin)	-8.01
Ni^{2+} (triplet spin)	-8.41
Ni^{3+} (quartet spin)	-7.84
Co^{2+} (quartet spin)	-9.74
Co^{3+} (quintet spin)	-9.08
Mn^{3+} (quintet spin)	-9.05

Table 4.23: Results of Binding of Fe^{3+} (quartet) and Mn^{3+} (quintet) co-ordinated C4 towards *endo*-bound small guest molecules. Values are in kcal mol^{-1}. All calculations use B3LYP/6-311++G** on non-metal atoms. SDD on metal atoms. GD3BJ empirical dispersion included. All values BSSE corrected.

Guest	No Metal	Fe^{3+}	Mn^{3+}
H_2	-1.51	-1.83	-1.80
O_2	-3.69	-4.13	-4.32
N_2	-5.12	-7.01	-7.34
H_2O	-5.27	-10.71	-11.35
N_2O (O into cavity)	-6.30	-7.93	-8.10
N_2O (N into cavity)	-6.78	-9.19	-9.59
CO_2	-6.76	-8.85	-9.05
HCN (C into cavity)	-7.44	-9.86	-9.26
HCN (N into cavity)	-7.44	-9.48	-10.12
NH_3	-7.22	-16.92	-17.83
H_2S	-8.86	-12.42	-12.78
SO_2 (S into cavity)	-10.91	-14.47	-13.80
SO_2 (O into cavity)	-11.79	-17.08	-17.25

agreement. With calibration, therefore it may be possible to use transition metals instead of gold in these gas sensors. For the remainder of this work, advantage is taken of this relative invariance of the metal type and only two metal types are considered further, to ensure this invariance characteristic holds across the range of guests. The binding of a range of important small guest molecules at the upper rim of Fe^{3+} (quartet) lower-rim-bound C4 and Mn^{3+} (quintet) lower-rim-bound C4 systems are now investigated. Comparison is made with the metal-free case. Results are shown in table 4.23 and figures 4.38, 4.39 and 4.40.

The previous predictions that introduction of any metal would be the most important factor in changes to the binding energy of CO_2 is seen to be replicated across all of the guest molecules in this study. Most of the molecules experience in increase in magnitude of binding energy around 0.29 kcal mol^{-1} to 2.89 kcal mol^{-1} with the SO_2 and H_2S experiencing increases in binding of between 2.89 kcal mol^{-1} and 5.46 kcal mol^{-1} depending on the metal and the position of the guest. Overall, most guests

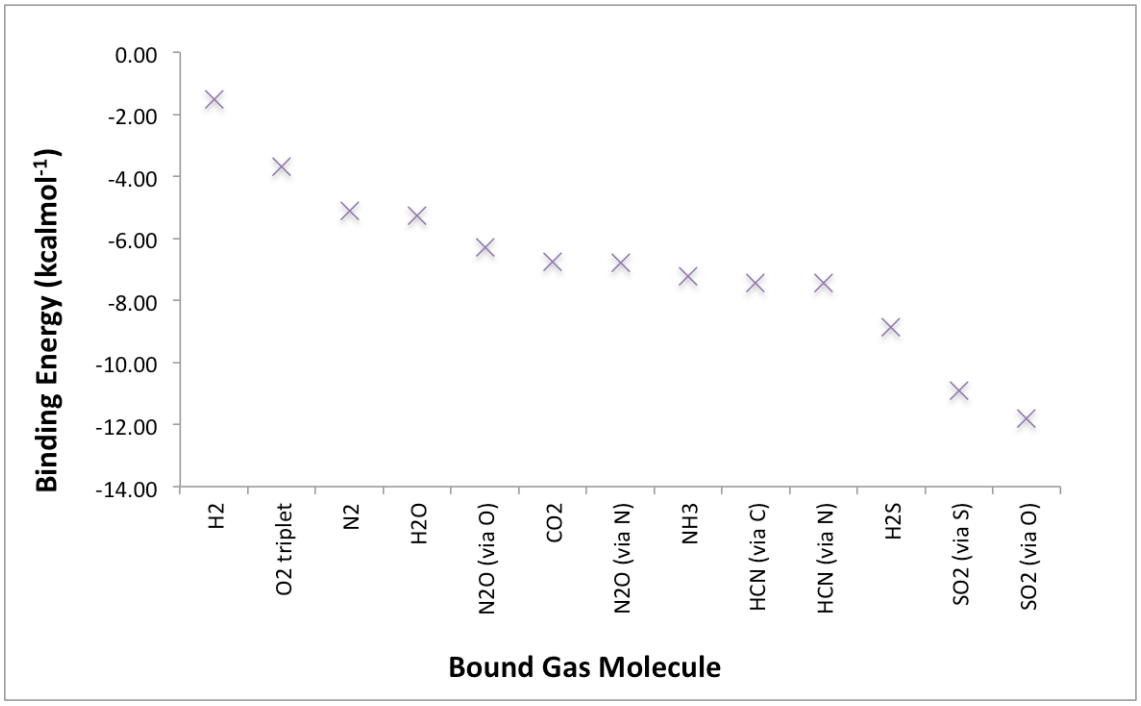

Figure 4.38: Binding energies of metal-free C4 with a variety of guest molecules. All calculations B3LYP/6-311++G** with GD3BJ empirical dispersion and BSSE corrections.

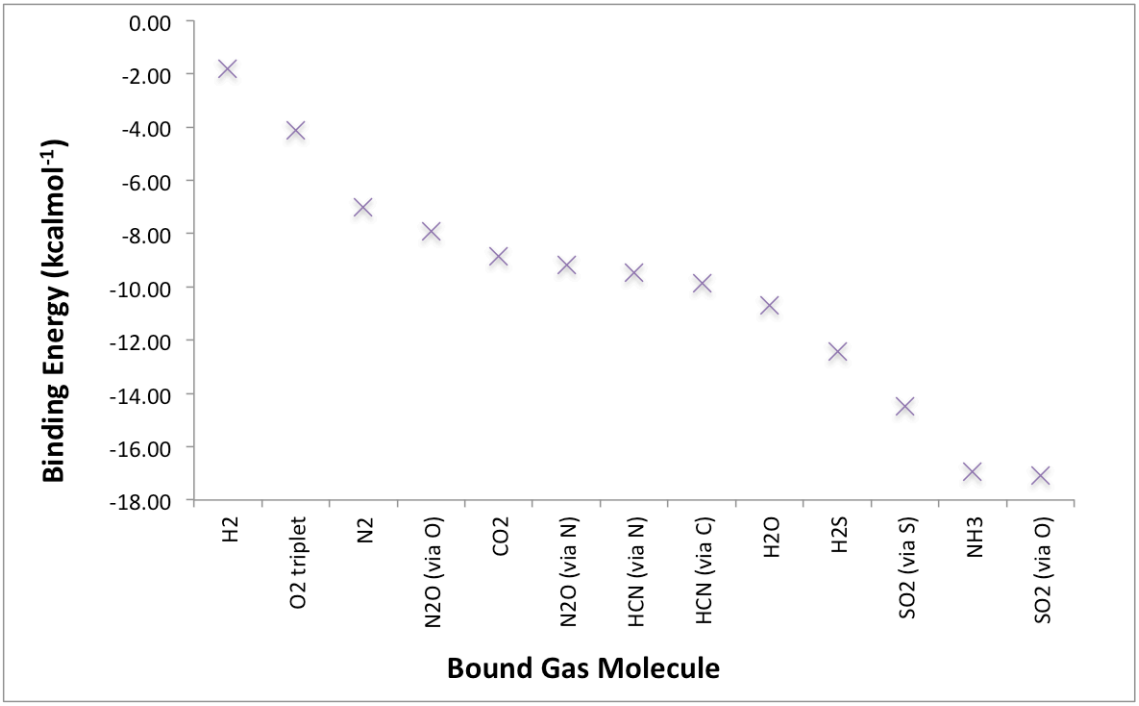

Figure 4.39: Binding energies of C4 with a variety of guest molecules. Fe^{3+} coordinated to C4. All calculations B3LYP/6-311++G** with GD3BJ empirical dispersion and BSSE corrections. SDD on metal atoms.

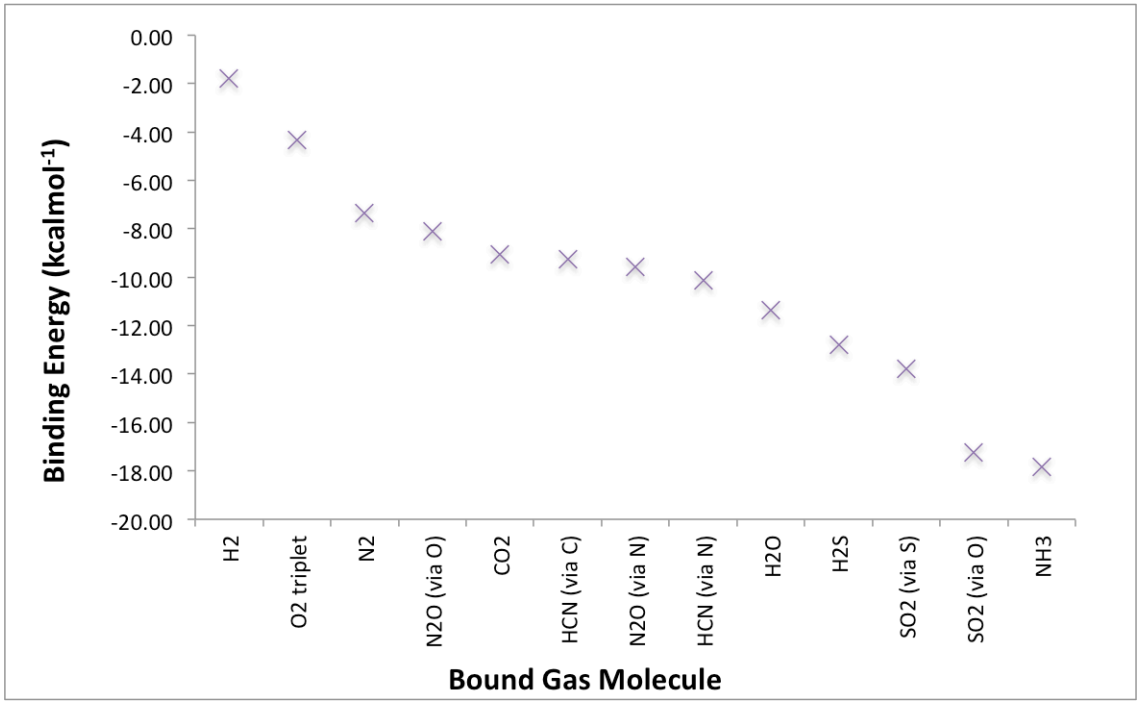

Figure 4.40: Binding energies of C4 with a variety of guest molecules. Mn^{3+} coordinated to C4. All calculations B3LYP/6-311++G** with GD3BJ empirical dispersion and BSSE corrections. SDD on metal atoms.

experience an increase in binding of 12% to 45% when a metal atom is included compared to just 1.0% to 6.8% when the metal is changed between Fe^{3+} and Mn^{3+}. Two guests, H_2O and NH_3, require special mention. Both these guests experience a substantial increase in binding of 103% and 134% respectively once a metal is added compared to 5.98% and 5.3% when the metal is changed. Clearly then, the nature of the metal is of less importance than the inclusion of a metal in the first place.

It should be noted that the metal-free binding energies of H_2O and NH_3 have been calculated both experimentally and using MP2. Results are shown in table 4.24. It can be seen that although MP2 outperforms DFT for H_2O (with DFT underbinding), the opposite is true for NH_3. For NH_3, DFT is in good agreement with experiment whilst MP2 shows overbinding. It is therefore evident that MP2 does not necessarily improve on the DFT results in this work and the method appears to be sensitive to the choice of basis set. It is also seen from these results that including solvation in the DFT results causes serious underbinding and is not considered further.

Inclusion of a metal at the lower rim of C4 not only increases the magnitude of the binding of each guest at the upper rim, it also alters the relative preferential

Table 4.24: Comparison of Binding of H_2O and NH_3 to metal-free C4 with experiment and MP2. Values are in kcal mol^{-1}. DFT calculations use B3LYP/6-311++G** on non-metal atoms. SDD on metal atoms. GD3BJ empirical dispersion included. All values BSSE corrected. Solvent calculations use CPCM and water. Values in parentheses after experimental results indicate the error in terms of +/- that value.

Guest	Method	Binding
H_2O	Experiment [43][44]	-8.977(0.002)
	DFT	-5.27
	DFT and Solvent	-3.61
	MP2 (CBS) [44]	-8.10
	MP2 (aug-cc-pVQZ) [43]	-8.94
NH_3	Experiment [43][44]	<-8.00
	DFT	-7.22
	DFT and Solvent	-4.07
	MP2 (CBS) [44]	-11.09

binding of those guest. Metal-free C4 preferentially binds to SO_2 compared to all other guests in the study, but metal co-ordinated C4 now shows an equal or greater preference for NH_3 compared to SO_2 as well as a preference for H_2O which is only slightly less favoured than H_2S. This is shown in figures 4.38, 4.39 and 4.40.

The effect on the geometry of adding a metal atom to the lower rim of C4 is illustrated in figures 4.41 and 4.42. Figure 4.41 shows instances of where there is significant movement of the position of the guest depending on what is bound at the C4 lower rim, whilst figure 4.42 shows guests which experience little difference. Figure 4.42 shows the binding geometry when Fe^{3+} is coordinated to the lower rim. Quantitatively, the key geometric parameters are the distance between the centroid of the tetraphenolic pocket and the lowest point of the bound guest within the cavity, see table 4.25, and the surface area of the upper rim once the guest is bound, see table 4.26.

As can be seen, the addition of a metal atom significantly changes the binding position of H_2O, both linkage isomers of HCN and NH_3. HCN is seen to prefer to

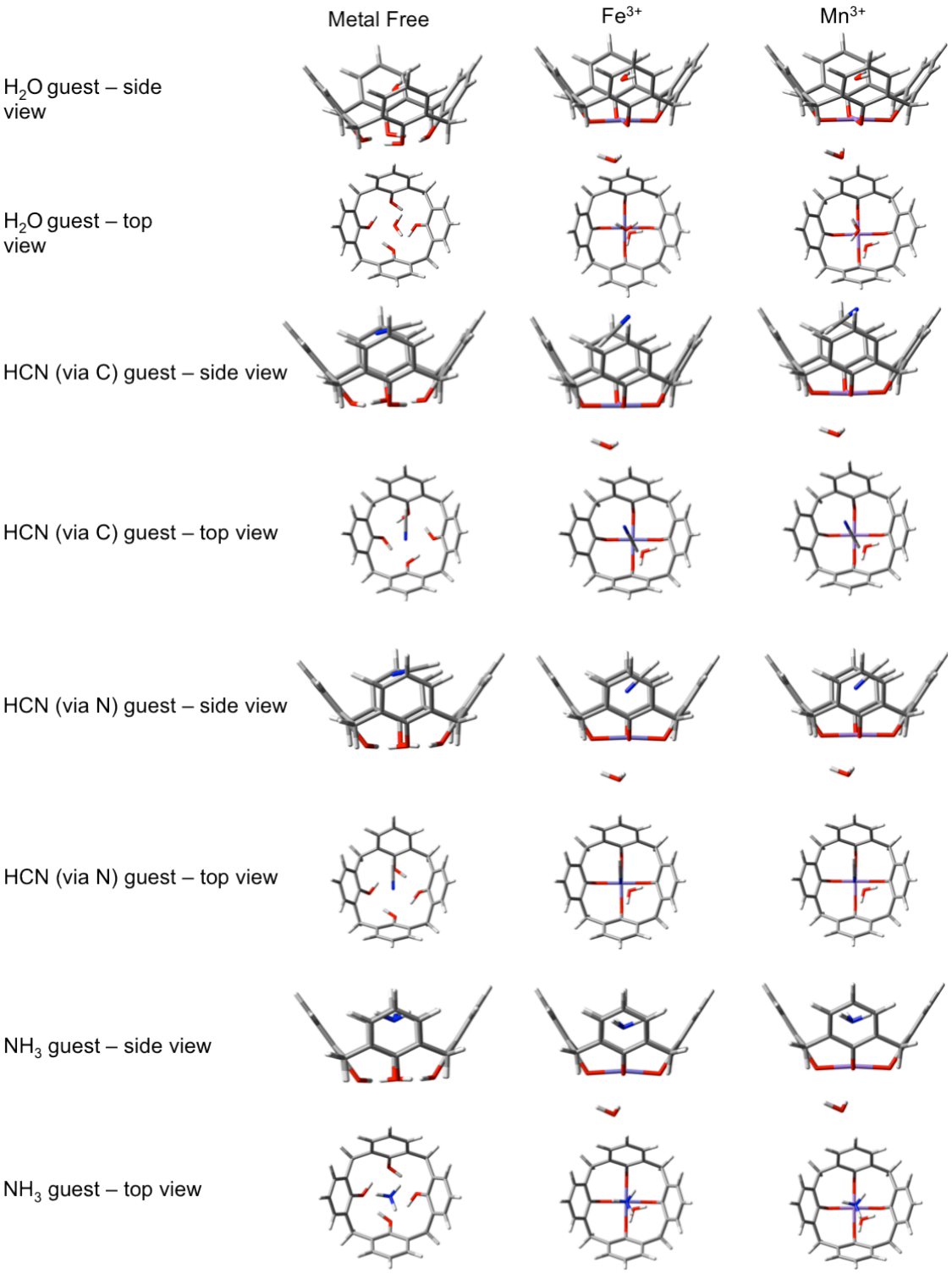

Figure 4.41: Geometry of C4-bound guests showing change of guest position within the upper rim as metal atoms are co-ordinated to the C4 lower rim. All calculations B3LYP/6-31G** with GD3BJ empirical dispersion. SDD on metal atoms.

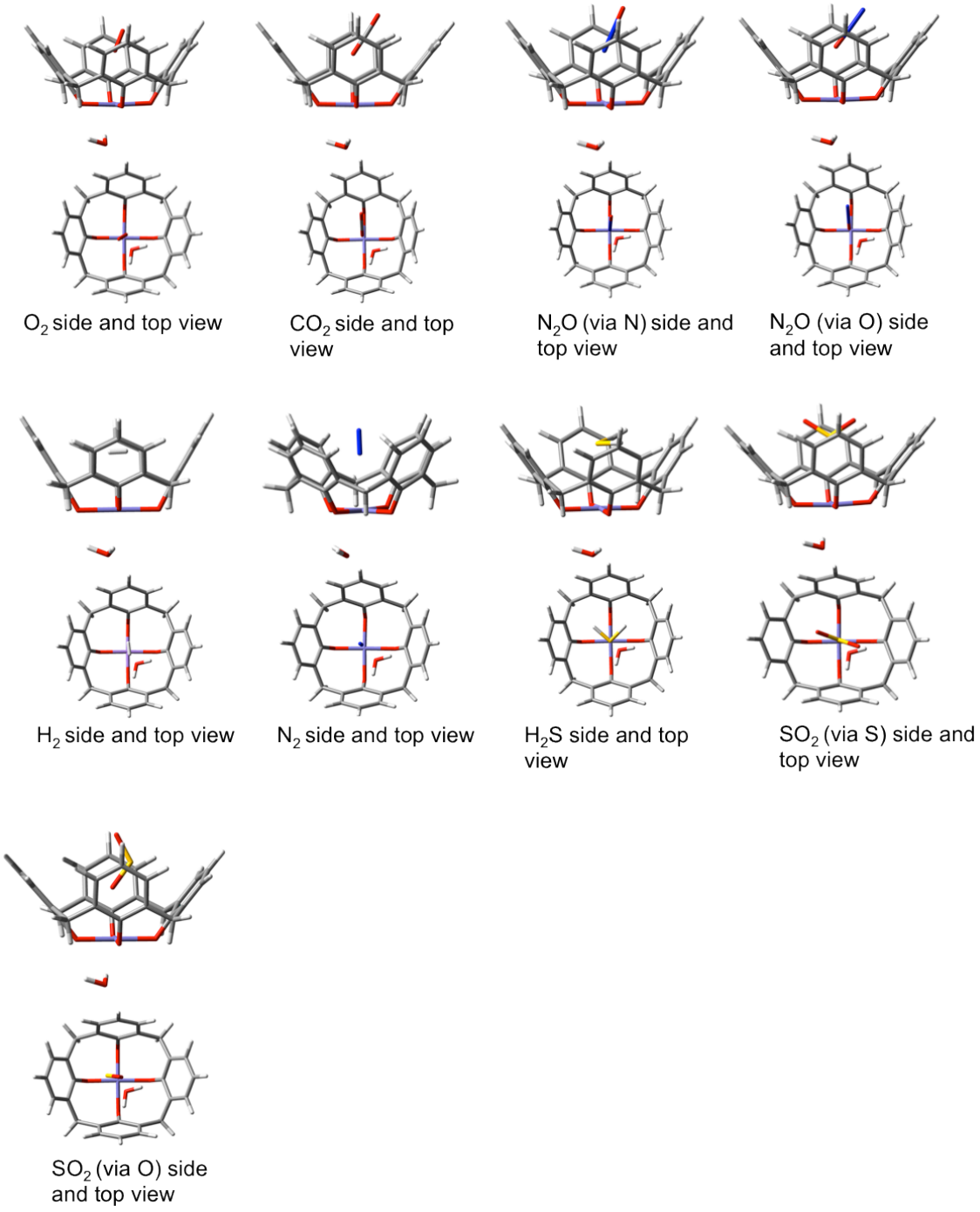

Figure 4.42: Geometry of C4-bound guests whose geometric binding position in the upper rim is not dependent on the C4 lower rim coordination. Shown here is the case for Fe^{3+} coordination to the lower rim. All calculations B3LYP/6-31G** with GD3BJ empirical dispersion. SDD on metal atoms.

Table 4.25: Effect of metal coordination on binding position of guest molecules within C4. Centroid of tetraphenolic pocket to lowest point of upper-rim-bound guest. All distances in angstroms. All calculations use B3LYP/6-31G** on non-metal atoms. SDD on metal atoms. GD3BJ empirical dispersion included.

Guest	No Metal	Fe^{3+}	Mn^{3+}
No Guest	N/A	N/A	N/A
H_2	3.0910	2.7986	2.8355
O_2	2.8533	2.9277	2.9769
N_2	2.8445	2.8079	2.8426
H_2O	2.6947	2.4008	2.4278
N_2O (O into cavity)	2.7214	2.7458	2.7000
N_2O (N into cavity)	2.8487	2.7186	2.7335
CO_2	2.3705	2.6652	2.6326
HCN (C into cavity)	3.4951	3.8029	3.7894
HCN (N into cavity)	3,4954	2.5468	2.5769
NH_3	2.9021	2.4563	2.4995
H_2S	3.5314	3.2753	3.2616
SO_2 (S into cavity)	3.4184	3.4045	3.4302
SO_2 (O into cavity)	2.6853	2.5327	2.5517

Table 4.26: Effect of metal coordination on binding position of guest molecules within C4. Surface area of upper-rim-bound guest. All distances in square angstroms. All calculations use B3LYP/6-31G** on non-metal atoms. SDD on metal atoms. GD3BJ empirical dispersion included.

Guest	No Metal	Fe^{3+}	Mn^{3+}
No Guest	71.1	69.6	69.7
H_2	70.6	69.2	68.4
O_2	70.1	68.4	70.0
N_2	69.7	67.9	68.3
H_2O	66.9	69.1	69.0
N_2O (O into cavity)	70.3	68.4	68.7
N_2O (N into cavity)	69.9	67.8	67.8
CO_2	64.8	67.9	68.6
HCN (C into cavity)	69.8	68.1	68.3
HCN (N into cavity)	69.8	68.8	68.5
NH_3	70.1	69.0	68.7
H_2S	69.7	68.6	68.5
SO_2 (S into cavity)	67.3	66.9	67.3
SO_2 (O into cavity)	66.4	64.3	67.3

bind with the N atom pointing into the cavity in the metal-free case. Addition of a metal allows for a stable binding position where the H atom points into the cavity. Without the metal, this binding arrangement would not be possible. Geometrically, all three of these guest molecules are drawn further into the cavity which explains visually why the binding is stronger. Much smaller geometric changes are observed with the other guest molecules. From table 4.25, it can be seen that changes to the distance between the centroid of the tetraphenolic pocket to the lowest binding point of the guest are between 1% and 8% for most guests as a metal is added. Earlier it was noted that H_2O and NH_3 were particularly affected by inclusion of a metal. Here, the geometric impact of that is clearly seen with reduction in the distance between the centroid and the guest of 14% and 20% respectively when a metal is added. Interestingly the change in this parameter when the metal is changed is only between 0.07% and 2.9%. The binding of each guest is now considered in more detail.

SO_2 Binding

SO_2 is an ambidentate ligand and can bind with either the O or the S atom pointing downwards into the cavity. Metal-free C4 is able to stabilise both binding arrangements via interactions between the S-O bonds and the phenyl rings in the upper rim. If the guest is bound with O pointing into the cavity a further stabilising interaction between the O atom and the tetraphenolic rim H atoms is observed hence the increased stability of this binding arrangement. When a metal is introduced, additional M-S or M-O bonds are formed, the latter being stronger. Thus the strongest binding occurs with O pointing into the cavity as evidenced by the shorter centroid to guest distance as described in table 4.25.

NH_3 and H_2O Binding

It is the inclusion of the metal which causes substantial increases in magnitude of binding for both these guests. This is as a result of very strong binding of the metal to the N or O atoms via lone pairs on these atoms. The more available lone pair on the N leads to NH_3 being favoured by both metals. Removing the metal sees both guests adopt a position higher up in the cavity although hydrogen bonds are made with the tetraphenolic pocket in both cases. Orientation of the guests is controlled by a combination of $\sigma - \pi$ binding between the X-H bonds and the aromatic rings and one or more methylene bridges of the calixarene.

CO_2 Binding

Without a metal atom, CO_2 largely binds via interaction between the π bonds of guest and those of the aromatic rings of the calixarene. Once a metal is included, the binding is dominated by the interaction between the metal and a lone pair on the O atom pointing into the cavity.

H_2S Binding

H_2S primarily binds via interaction between the S-H bond and the aromatic π-system. Introduction of a metal atom provides additional M-S bonding, further strengthening the binding with the M-S bond dominating the interactions.

N_2, H_2 and O_2 Binding

These three guests bind the weakest to the calixarene. N_2 sits vertically in the cavity interacting with the aromatic rings via $\pi - \pi$ bonding. O_2 on the other hand prefers to interact through the lone pairs on the O atom pointing into the cavity. H_2 is the weakest bonding guest, only interacting via weak van der Waal bonds to the aromatic ring. The inclusion of a metal atom provides extra binding between the metal and the lone pair on the N or O atoms. Fe^{3+} has a greater impact on N_2 than Mn^{3+}. In the case of O_2, the M-O bond dominates the interactions. H_2 binds to the metal via the H-H σ bond and this dominates the interaction.

N_2O Binding

N_2O can bind with either N or O atom pointing into the cavity with the main interaction being that between the N-N π bond and the aromatic ring. The case where N is pointing into the cavity is preferred however as this is when the N-N double bond is geometrically sited at its lowest point thereby strengthening this interaction. Inclusion of a metal provides an extra M-X bond and again the bond with N is favoured over O as a result of the more available lone pair.

HCN Binding

For the non-metal case, the guest only binds in one way: that of the N atom pointing into the cavity. The dominant interaction is that between the aromatic ring and the C-H σ bond and also to a lesser degree between the aromatic ring and the C and N atoms. With the inclusion of a metal atom the guest can now additionally bind with the H atom pointing into the cavity. When the N atom is pointing into the cavity, the metal atom provides an extra binding point for the C-N π system bringing the

guest further into the cavity. This brings an increase in binding between the C-N π system and the aromatic ring π system strengthening the binding of the guest. A strong interaction is seen between one of the methylene bridges on the calixarene and the C-N π system. It is noted that Mn^{3+} has a greater effect on the guest than Fe^{3+}. This appears to be because Mn^{3+} opens up the lower rim more than Fe^{3+}, causing a consequent closing of the upper rim, pushing the aromatic rings closer to the guest and strengthening the $\pi - \pi$ interaction. This explains the increase in binding energy when Mn^{3+} is used. When HCN binds with the H atom pointing into the cavity, the interactions are much weaker as the C-N bond is sited further out of the cavity away from the aromatic rings. The binding of the guest is therefore much weaker.

Spin density calculations were carried out to identify the location of the unpaired electrons in these systems. This was carried out for both Fe^{3+} (quartet) and Mn^{3+} (quintet) with results detailed in tables 4.27, 4.28, 4.29 and 4.30. For Fe^{3+} (quartet), the $3d_{yz}$ orbital is doubly occupied in most cases with the three unpaired electrons occupying the $3d_{z^2}$, $3d_{xz}$ and $3d_{xy}$ orbitals. When HCN binds with the N atom points downwards however, the $3d_{xz}$ orbital becomes doubly occupied with the $3d_{yz}$ becoming singly occupied. This suggests that the $3d_{xz}$ and $3d_{yz}$ orbitals are close in energy in the Fe system. For Mn^{3+} (quintet), three unpaired electrons appear in the $3d_{z^2}$, $3d_{xz}$ and $3d_{yz}$ orbitals with the fourth unpaired electron varyingly appearing in either the $3d_{x^2-y^2}$ or $3d_{xy}$ orbitals suggesting the latter two orbitals are close in energy in the Mn system. Although some spin polarisation is observed into the extended π system, this is a minor effect and as expected, spin contamination is not present to any degree in any of the systems. Finally, as expected, there is no spin density in any of the bound guest molecules with the exception of the triplet O_2 molecule. The presence of the guest molecule therefore doesn't affect spin density on the metal atom regardless of how strongly bound the guest is. This is true for both metals.

4.5.3 Summary and Conclusions - Upper Rim Binding

C4 complexes were investigated for their ability to bind a number of important small guest molecules. The inclusion of a first row transition metal atom at the lower rim

Table 4.27: Spin density values for Mn^{3+} and Fe^{3+}-coordinated C4. Positive values refer to areas of excess α spin.

Guest	Mn^{3+}	Fe^{3+}
No Guest	+0.77 on $3d_{z^2}$	+0.66 $3d_{z^2}$
	+0.82 $3d_{xz}$	+0.80 $3d_{xz}$
	+0.82 $3d_{yz}$	+0.15 $3d_{yz}$
	+0.71 $3d_{x^2-y^2}$	+0.36 $3d_{x^2-y^2}$
	+0.36 $3d_{xy}$	+0.77 $3d_{xy}$
H_2	+0.78 $3d_{z^2}$	+0.71 $3d_{z^2}$
	+0.82 $3d_{xz}$	+0.81 $3d_{xz}$
	+0.82 $3d_{yz}$	+0.11 $3d_{yz}$
	+0.33 $3d_{x^2-y^2}$	+0.36 $3d_{x^2-y^2}$
	+0.75 $3d_{xy}$	+0.79 $3d_{xy}$
O_2	+1.00 O(p_x), +0.97 O(p_y)	+0.99 O(p_x), +0.97 O(p_y)
	+0.77 $3d_{z^2}$	+0.66 $3d_{z^2}$
	+0.82 $3d_{xz}$	+0.81 $3d_{xz}$
	+0.82 $3d_{yz}$	+0.11 $3d_{yz}$
	+0.33 $3d_{x^2-y^2}$	+0.36 $3d_{x^2-y^2}$
	+0.75 $3d_{xy}$	+0.79 $3d_{xy}$
N_2	+0.79 $3d_{z^2}$	+0.73 $3d_{z^2}$
	+0.83 $3d_{xz}$	+0.81 $3d_{xz}$
	+0.83 $3d_{yz}$	+0.08 $3d_{yz}$
	+0.28 $3d_{x^2-y^2}$	+0.37 $3d_{x^2-y^2}$
	+0.80 $3d_{xy}$	+0.79 $3d_{xy}$

Table 4.28: Spin density values for Mn^{3+} and Fe^{3+}-coordinated C4. Positive values refer to areas of excess α spin.

Guest	Mn^{3+}	Fe^{3+}
H_2O	+0.80 $3d_{z^2}$	+0.78 $3d_{z^2}$
	+0.83 $3d_{xz}$	+0.82 $3d_{xz}$
	+0.83 $3d_{yz}$	+0.04 $3d_{yz}$
	+0.27 $3d_{x^2-y^2}$	+0.34 $3d_{x^2-y^2}$
	+0.80 $3d_{xy}$	+0.79 $3d_{xy}$
N_2O (O into cavity)	+0.78 $3d_{z^2}$	+0.72 $3d_{z^2}$
	+0.82 $3d_{xz}$	+0.81 $3d_{xz}$
	+0.83 $3d_{yz}$	+0.09 $3d_{yz}$
	+0.28 $3d_{x^2-y^2}$	+0.36 $3d_{x^2-y^2}$
	+0.80 $3d_{xy}$	+0.78 $3d_{xy}$
N_2O (N into cavity)	+0.79 $3d_{z^2}$	+0.74 $3d_{z^2}$
	+0.82 $3d_{xz}$	+0.81 $3d_{xz}$
	+0.83 $3d_{yz}$	+0.08 $3d_{yz}$
	+0.35 $3d_{x^2-y^2}$	+0.37 $3d_{x^2-y^2}$
	+0.74 $3d_{xy}$	+0.79 $3d_{xy}$
CO_2	+0.79 $3d_{z^2}$	+0.74 $3d_{z^2}$
	+0.82 $3d_{xz}$	+0.81 $3d_{xz}$
	+0.82 $3d_{yz}$	+0.08 $3d_{yz}$
	+0.53 $3d_{x^2-y^2}$	+0.36 $3d_{x^2-y^2}$
	+0.55 $3d_{xy}$	+0.79 $3d_{xy}$

Table 4.29: Spin density values for Mn^{3+} and Fe^{3+}-coordinated C4. Positive values refer to areas of excess α spin.

Guest	Mn^{3+}	Fe^{3+}
HCN (C into cavity)	+0.77 $3d_{z^2}$	+0.62 $3d_{z^2}$
	+0.82 $3d_{xz}$	+0.77 $3d_{xz}$
	+0.82 $3d_{yz}$	+0.22 $3d_{yz}$
	+0.61 $3d_{x^2-y^2}$	+0.45 $3d_{x^2-y^2}$
	+0.47 $3d_{xy}$	+0.72 $3d_{xy}$
HCN (N into cavity)	+0.79 $3d_{z^2}$	+0.78 $3d_{z^2}$
	+0.83 $3d_{xz}$	+0.08 $3d_{xz}$
	+0.83 $3d_{yz}$	+0.77 $3d_{yz}$
	+0.28 $3d_{x^2-y^2}$	+0.37 $3d_{x^2-y^2}$
	+0.80 $3d_{xy}$	+0.77 $3d_{xy}$
NH_3	+0.79 $3d_{z^2}$	+0.77 $3d_{z^2}$
	+0.83 $3d_{xz}$	+0.82 $3d_{xz}$
	+0.83 $3d_{yz}$	+0.04 $3d_{yz}$
	+0.52 $3d_{x^2-y^2}$	+0.37 $3d_{x^2-y^2}$
	+0.55 $3d_{xy}$	+0.75 $3d_{xy}$
H_2S	+0.78 $3d_{z^2}$	+0.74 $3d_{z^2}$
	+0.83 $3d_{xz}$	+0.81 $3d_{xz}$
	+0.83 $3d_{yz}$	+0.06 $3d_{yz}$
	+0.29 $3d_{x^2-y^2}$	+0.34 $3d_{x^2-y^2}$
	+0.78 $3d_{xy}$	+0.79 $3d_{xy}$

Table 4.30: Spin density values for Mn^{3+} and Fe^{3+}-coordinated C4. Positive values refer to areas of excess α spin.

Guest	Mn^{3+}	Fe^{3+}
SO_2 (S into cavity)	+0.77 $3d_{z^2}$	+0.68 $3d_{z^2}$
	+0.82 $3d_{xz}$	+0.79 $3d_{xz}$
	+0.83 $3d_{yz}$	+0.14 $3d_{yz}$
	+0.36 $3d_{x^2-y^2}$	+0.41 $3d_{x^2-y^2}$
	+0.72 $3d_{xy}$	+0.74 $3d_{xy}$
SO_2 (O into cavity)	+0.79 $3d_{z^2}$	+0.75 $3d_{z^2}$
	+0.82 $3d_{xz}$	+0.81 $3d_{xz}$
	+0.83 $3d_{yz}$	+0.07 $3d_{yz}$
	+0.29 $3d_{x^2-y^2}$	+0.37 $3d_{x^2-y^2}$
	+0.81 $3d_{xy}$	+0.79 $3d_{xy}$

of the calixarene was shown to increase binding of these guests with the nature of the guest being shown to be less important than the presence of a transition metal of some kind. In particular, the binding of the guest seemed relatively invariant to the oxidation or spin state of the metal. This offers the prospect of using cheaper transition metals as tethering surfaces in practical gas sensors as a replacement for more commonly used metals such as gold. It was found that SO_2 (with the O atom pointing into the cavity) bound most strongly than other gas molecules when no metal was present with NH_3 binding most strongly when a metal was introduced. The calculations also predict that with a spread of binding energies between approximately -2.00 kcal mol^{-1} and -18.00 kcal mol^{-1}, in a mixture of two or more gases, metal coordinated C4 could be useful in the preferential detection or separating out of the most strongly binding gas.

References

[1] J. W. Steed and J. L. Atwood, *Supramolecular Chemistry.* John Wiley & Sons Ltd: Hoboken NJ, 2009.

[2] C. D. Gutsche, *Monographs in Supramolecular Chemistry*. Royal Society of Chemistry: Cambridge, 1989.

[3] A. Ikeda and S. Shinkai, "Novel Cavity Design Using Calix[n]arene Skeltons: Toward Molecular Recognition and Metal Binding," *Chemical Reviews*, vol. 97, pp. 1713–1734, 1997.

[4] A. Zinke and E. Ziegler, "Zur Kenntnis des Hartungsprozesses von Phenol-Formaldehyd-Harzen, X. Mitteilung," *Chemische Berichte*, vol. 77, pp. 264–272, 1944.

[5] J. W. Cornforth, P. H. D'Arcy, G. A. Nicholls, R. J. W. Rees, and J. A. Stock, "Antituberculous Effects of Certain Surface Active Polyoxyethylene Ethers," *British Journal of Pharmacology*, vol. 10, pp. 73–86, 1955.

[6] J. W. Cornforth, E. D. Morgan, K. T. Potts, and R. J. W. Rees, "Preparation of Antituberculous Polyoxyethylene Ethers of Homogeneous Structure," *Tetrahedron*, vol. 29, pp. 1659–1667, 1973.

[7] B. T. Hayes and R. F. Hunter, "Rational Synthesis of Cyclic Tetranuclear Para-Cresol Novolak," *Chemistry and Industry (London)*, pp. 193–194, 1956.

[8] B. T. Hayes and R. F. Hunter, "Phenol Formaldehyde and Allied Resins VI: Rational Synthesis of a Cyclic Tetranuclear P-Cresol Novolak," *Journal of Applied Chemistry*, vol. 8, pp. 743–748, 1958.

[9] D. Gutsche, M. Iqbal, and D. Stewart, "Calixarenes. 18. Synthesis Procedures for *p*-tert-Butylcalix[4]arene," *Journal of Organic Chemistry*, vol. 51, pp. 742–745, 1986.

[10] J. L. Katz, M. B. Feldman, and R. R. Conry, "Synthesis of Functionalised Oxacalix[4]arenes," *Organic Letters*, vol. 7, pp. 91–94, 2005.

[11] W. Maes, W. V. Rossom, K. V. Hecke, and L. V. Meervelt, "Synthesis of Functionalised Thia- and Oxa-calix[2]arene[2]-pyrimidines," *Organic Letters*, vol. 8, pp. 4161–4164, 2006.

[12] L. T. Carroll, P. A. Hill, C. Q. Ngo, P. K. Klatt, and J. L. Fantini, "Synthesis and Reactions of a 2-Chlorocalix[4]arene and a 2,2'-Coupled Dicalixarene," *Tetrahedron*, vol. 69, pp. 5002–5007, 2013.

[13] I. Thorndorf, J. Brenn, W. Brandt, and V. Bohmer, "Ring Inversion Pathways of Exo- and Endo- Calix[4]arenes Studied by Means of the MM3 Force Field," *Tetrahedron Letters*, vol. 36, pp. 6665–6668, 1995.

[14] T. V. Tolpekina, *Free Energy Calculations of Conformational Transitions in Supramolecues and Amphiphilic Bilayers*. PhD thesis, University of Twente, 90-365-2092-4, 2004.

[15] K. Araki, S. Shinkai, and T. Matsuda, "Activation Parameters for Calixarene Ring Inversion as Determined by Computer Assisted Spectrum Simulation," *Chemistry Letters*, pp. 581–584, 1989.

[16] S. Fischer, P. D. J. Grootenhuis, L. C. Groenen, W. P. van Hoorn, F. C. J. M. van Heggel, D. N. Reinhoudt, and M. Karplus, "Pathways for Conformational Interconversion of Calix[4]arenes," *Journal of American Chemistry Society*, vol. 117, pp. 1611–1620, 1995.

[17] R. J. Bernardino and B. J. C. Cabral, "Structure, Conformational Equilibrium and Proton Affinity of Calix[4]arene by Density Functional Theory," *Journal of Physical Chemistry A*, vol. 103, pp. 9080–9085, 1999.

[18] K. Kim, S. J. Park, and J. I. Choe, "DFT Conformational Study of Calix[5]arene and Calix[4]arene: Hydrogen Bond," *Bulletin of Korean Chemistry*, vol. 29, pp. 1893–1897, 2008.

[19] B. Castellano, E. Scolari, C. Floriani, and R. Scopelliti, "Reactivity of a Vanadium(III) Center over an Oxo Surface Modelled by Calix[4]arene," *Inorganic Chemistry*, vol. 38, pp. 3406–3413, 1999.

[20] G. Karotsis, S. J. Teat, W. Wernsdorfer, S. Piligkos, S. J. Dalgarno, and E. K. Brechin, "Calix[4]arene Based Single Molecule Magnets," *Angewandte Chemie International Edition*, vol. 48, pp. 8285–8288, 2009.

[21] S. M. Taylor, R. D. McIntosh, S. Piligkos, S. J. Dalgarno, and E. K. Brechin, "Calixarene Supported Clusters: Employment of Complementary Cluster Ligands for the Construction of a Ferromagnetic $[Mn_5]Cage$," *Chemical Communications*, vol. 48, pp. 11190–11192, 2012.

[22] J. L. Atwood, E. K. Brechin, R. Inglis, L. F. Jones, A. Mossine, M. J. Paterson, and S. J. Teat, "Magnetism in Metal Organic Capsules," *Chemical Communications*, vol. 46, pp. 3484–3486, 2010.

[23] S. Sanz, K. Ferreira, R. D. McIntosh, S. J. Dalgarno, and E. K. Brechin, "Calix[4]arene-Supported $Fe_2^{III}Ln_2^{III}$ Clusters," *Chemical Communications*, vol. 47, pp. 9042–9044, 2011.

[24] G. Karotsis, S. Kennedy, S. J. Dalgarno, and E. K. Brechin, "Calixarene Supported Enneanuclear Cu(II) Clusters," *Chemical Communications*, vol. 46, pp. 3884–3886, 2010.

[25] P. M. Marcos, F. A. Teixeira, M. A. P. Segurado, J. R. Ascenso, R. J. Bernardino, P. J. Cragg, S. Michel, V. Hubscher-Bruder, and F. Arnaud-Neu, "Complexationb and DFT Studies of Lower Rim Hexahomotrioxacalix[3]arene Derivatives Bearing Pyridyl Groups with Transition and Heavy Metal Cations. Cone Versus Partial Cone Conformation," *Journal of Physical Organic Chemistry*, vol. 26, pp. 295–305, 2013.

[26] P. M. Marcos, B. Mellah, J. R. Ascenso, S. Michel, V. Hubscher-Bruder, and F. Arnaud-Neu, "Binding Properties of *p*-tert-butyldihomooxacalix[4]arene Tetra(2-Pyridylmethoxy) Derivative Towards Alkali, Alkaline Earth, Transition Metals and Heavy Metal Cations. ," *New Journal of Chemistry*, vol. 30, pp. 1655–1661, 2006.

[27] P. M. Marcos, F. A. Teixeira, M. A. P. Segurado, J. R. Ascenso, R. J. Bernardino, P. J. Cragg, S. Michel, V. Hubscher-Bruder, and F. Arnaud-Neu, "Complexation and DFT Studies of Lanthanide Ions by (2-pyridylmethoxy)homooxacalixarene Derivatives," *Supramolecular Chemistry*, vol. 25, no. 8, pp. 522–532, 2013.

[28] A. Arduini, M. Cantoni, E. Graviani, A. Pochini, A. Secchi, A. R. Sicuri, R. Ungaro, and M. Vincenti, "Gas Phase Complexation of Neutral Molecules by Upper Rim Bridged Calix[4]arenes," *Tetrahedron*, vol. 51, no. 2, pp. 599–606, 1995.

[29] J. L. Atwood, L. J. Barbour, A. Jerga, and B. L. Schottel, "Guest Transport in a Nonporous Organic Solid via van der Waals Cooperativity," *Science*, vol. 298, pp. 1000–1002, 2002.

[30] J. E. Adams, J. R. Cox, A. J. Christiano, and C. A. Deakyne, "Molecular Dynamics of Host-Guest Complexes of Small Gas Molecules with Calix[4]arenes," *Journal of Physical Chemistry A*, vol. 112, pp. 6829–6839, 2008.

[31] J. A. Ripmeester, G. D. Enright, C. I. Ratcliffe, K. A. Udachin, and I. L. Moudrakovski, "What We Have Learned From *p*-tert-Butylcalix[4]arene Compounds," *Chemical Communications*, pp. 4986–4996, 2006.

[32] D. H. Brouwer, I. L. Moudrakowski, K. A. Udachin, G. D. Enright, and J. A. Ripmeester, "Guest Loading and Multiple Phases in Single Crystals of the van der Waals Host *p*-tert-Butylcalix[4]arene," *Crystal Growth Design*, vol. 8, no. 6, pp. 1878–1885, 2008.

[33] K. A. Udachin, I. L. Moudrakovski, G. D. Enright, C. I. Ratcliffe, and J. A. Ripmeester, "Loading-Dependent Structures of CO_2 in the Flexible Molecular van der Waals Host *p*-tert-Butylcalix[4]arene with 1:1 and 2:1 Guest:Host Stoichiometries," *Physical Chemistry Chemical Physics*, vol. 10, pp. 4636–4643, 2008.

[34] G. D. Enright, K. A. Udachin, I. L. Moudrakovski, and J. A. Ripmeester, "Thermal Programmable Gas Storage and Release in Single Crystals of an Organic van der Waals Host," *Journal of American Chemical Society*, vol. 125, pp. 9896–9897, 2003.

[35] J. L. Atwood, L. J. Barbour, P. K. Thallapally, and T. B. Wirsig, "A Crystalline Organic Substrate Absorbs Methane under STP," *Chemical Communications*, pp. 51–53, 2005.

[36] P. K. Thallapally, T. B. Wirsig, L. J. Barbour, and J. L. Atwood, "Crystal Engineering of Nonporous Organic Solids for Methane Sorption," *Chemical Communications*, pp. 4420–4422, 2005.

[37] P. K. Thallapally, L. Dobrzanska, T. R. Gingrich, T. B. Wirsig, L. J. Barbour, and J. L. Atwood, "Acetylene Absorption and Binding in a Nonporous Crystal Lattice," *Angewandte Chemie International Edition*, vol. 45, pp. 6506–6509, 2006.

[38] G. V. Zyryanov, Y. Kang, and D. M. Rudkevich, "Sensing and Fixing of NO_2/N_2O_4 by Calix[4]arenes," *Journal of American Chemical Society*, vol. 125,

pp. 2997–3007, 2003.

[39] C. J. Liu, J. T. Lin, S. H. Wang, J. C. Jiang, and L. G. Lin, "Chromogenic Calixarene Sensors for Amine Detection," *Sensors and Actuators B*, vol. 108, pp. 521–527, 2005.

[40] S. Alavi, N. A. Afhag, J. A. Ripmeester, and D. L. Thompson, "Molecular Dynamics Simulations of *p*-tert-Butylcalix[4]arene with Small Guest Molecules," *Chemistry: A European Journal*, vol. 12, pp. 5231–5237, 2006.

[41] J. L. Daschbach, P. K. Thallapally, J. L. Atwood, B. P. McGrail, and L. X. Dang, "Free Energies of CO_2/H_2 Capture by *p*-tert-Butylcalix[4]arene: A Molecular Dynamics Study," *Journal of Chemical Physics*, vol. 127, p. 104703, 2007.

[42] F. M. Ytreberg, "Computational Study of Small Molecule Binding for Both Tethered and Free Conditions," *Journal of Physical Chemistry B*, vol. 114, pp. 5431–5434, 2010.

[43] N. Hontama, Y. Inokuchi, T. Ebata, C. Dedonder-Lardeux, C. Jouvet, and S. S. Xantheas, "Structure of the Cakix[4]arene-(H_2O) Cluster: The World's Smallest Cup of Water," *Journal of Physical Chemistry A*, vol. 114, pp. 2967–2972, 2010.

[44] S. Kaneko, Y. Inokuchi, T. Ebata, E. Apra, and S. S. Xantheas, "Laser Spectroscopic and Theoretical Studies of Encapsulation Complexes of Calix[4]arene," *Journal of Chemical Physics*, vol. 115, pp. 10846–10853, 2011.

[45] C. Ozbek, S. Okur, O. Mermer, M. Kurt, S. Sayin, and M. Yilmaz, "Effect of Fe Doping on the CO Gas Sensing of Functional Calixarene Molecules Measured with Quartz Crystal Microbalance Technique," *Sensors and Actuators B*, vol. 215, pp. 464–470, 2015.

[46] M. Coletta, R. McLellan, J. M. Cols, K. J. Gagnon, S. J. Teat, and S. J. Dalgarno, "Investigations into Cluster Formation with Alkyl-tethered Bis-calix[4]arenes," *Supramolecular Chemistry*, vol. 28, no. 5-6, pp. 557–566, 2016.

[47] M. Coletta, R. McLellan, A. Waddington, S. Sanz, K. J. Gagnon, S. J. Teat, E. K. Brechin, and S. J. Dalgarno, "Core Expansion of Bis-calix[4]arene-

supported Clusters," *Chemical Communications*, vol. 52, pp. 14246–14249, 2016.

[48] B. Lotfi, A. Tarlani, P. Akbari-Moghaddam, M. Mirza-Aghayan, A. A. Peyghan, J. Muzart, and R. Zadman, "Multivalent Calix[4]arene-based Fuorescent Sensor for Detecting Silver Ions in Aqueous Media and Physiological Environment," *Biosensors and Bioelectronics*, vol. 90, pp. 290–297, 2017.

[49] M. Nemati, R. Hosseinzadeh, R. Zadmard, and M. Mohadjerani, "Highly Selective Colormetric and Fluorescent Chemosensor for Fluoride Based on Fluorenone Armed Calix[4]arene," *Sensors and Actuators B - Chemical*, vol. 241, pp. 690–697, 2017.

[50] A. F. D. de Namor, N. A. Hakawati, W. A. Hamdan, R. Soualhi, S. Korfali, and L. Valiente, "Calix[4]pyrrole for the Removal of Arsenic(III) and Arsenic(V) from Water," *Journal of Hazardous Materials*, vol. 326, pp. 61–68, 2017.

[51] R. Zadmard, P. Akbari-Moghaddam, S. Darvishi, and M. Mirza-Aghayan, "A Highly Selective Fluoresent Chemosensor for NADH Based on Calix[4]arene Dimer," *Tetrahedron*, vol. 73, no. 5-6, pp. 604–607, 2017.

[52] F. Zou, B. Wu, A. Wang, Y. Chen, K. Koh, K. Wang, and H. Cheng, "Signal Amplification and Dual Recognition Strategy for Small Molecule Detection by Surface Plasmon Resonance Based on Calix[4]arene Crown Ether-modified Gold Nanoparticles," *Sensor and Actuators B - Chemical*, vol. 241, pp. 160–167, 2017.

[53] P. Murphy, S. J. Dalgarno, and M. J. Paterson, "Elucidating the Ring Inversion Mechanism(s) for Biscalixarenes," *The Journal of Physical Chemistry A*, vol. 118, pp. 7986–8001, 2014.

[54] M. J. Frisch, G. W. Trucks, H. B. Schlegel, G. E. Scuseria, M. A. Robb, J. R. Cheeseman, G. Scalmani, V. Barone, B. Mennucci, and G. A. Peterson, "Gaussian Inc. ," tech. rep., Wallingford, CT, 2013.

[55] A. D. Becke, "Density Functional Thermochemistry. III. The Role of Exact Exchange," *Journal of Chemical Physics*, vol. 98, pp. 5648–5652, 1993.

[56] P. J. Stephens, F. J. Devlin, C. F. Chabalowski, and M. J. Frisch, "Ab Initio Calculation of Vibrational Absorption and Circular Dichroism Spectra Using

Density Functional Force Fields," *Journal of Physical Chemistry*, vol. 98, no. 45, pp. 11623–11627, 1994.

[57] S. Grimme, S. Ehrlrich, and L. Goerigk, "Effect of the Damping Function in Dispersion Corrected Density Functional Theory," *Journal of Computational Chemistry*, vol. 32, pp. 1456–1465, 2011.

[58] M. J. S. Dewar, E. G. Zoebisch, and E. F. Healy, "A New General Purpose Quantum Mechanical Molecular Model," *Journal of American Chemical Society*, vol. 107, pp. 3902–3909, 1985.

[59] P. Hohenberg, "Inhomogeneous Electron Gas," *Physics Reviews*, vol. 136, pp. B864–B871, 1964.

[60] W. Kohn and L. J. Sham, "Self Consistent Equations Including Exchange and Correlation Effects," *Physics Reviews*, vol. 140, pp. A1133–A1138, 1965.

[61] S. H. Vosko, L. Wilk, and M. Nusair, "Accurate Spin Dependent Electron Liquid Correlation Energies for Local Spin Density Calculations: A Critical Analysis," *Canadian Journal of Physics*, vol. 58, pp. 1200–1211, 1980.

[62] A. D. Becke, "Density Functional Exchange Energy Approximation with Correct Asymptotic Behaviour," *Physical Review A*, vol. 38, no. 6, pp. 3098–3100, 1988.

[63] J. P. Perdew, "Density Functional Approximation for the Correlation Energy of the Inhomogeneous Gas," *Physics Reviews B*, vol. 33, pp. 8822–8824, 1986.

[64] G. Scalmani and M. Frisch, "Continuous Surface Charge Polarisable Continuum Models of Solvation. I. General Formalism," *Journal of Chemical Physics*, vol. 132, p. 114110, 2010.

[65] A. V. Marenich, C. J. Cramer, and D. G. Truhlar, "Universal Solvation Model Based on Solute Electron Density and on a Continuum Model of the Solvent Defined by the Bulk Dielectric Constant and Atomic Surface Tensions," *Journal of Physical Chemistry B*, vol. 113, pp. 6378–6396, 2009.

[66] V. Barone and M. Cossi, "Quantum Calculation of Molecular Energies and Energy Gradients in Solution by a Conductor Solvent Model," *Journal of Physical Chemistry A*, vol. 102, pp. 1995–2001, 1998.

[67] M. Cossi, N. Rega, G. Scalmani, and V. Barone, "Energies, Structures and Electronic Properties of Molecules in Solution with the CPCM Solvation Model," *Journal of Computational Chemistry*, vol. 24, pp. 669–681, 2003.

[68] J. Tomasi, B. Mennucci, and R. Cammi, "Quantum Mechanical Continuum Solvent Models," *Chemical Reviews*, vol. 105, pp. 2999–3093, 2005.

[69] G. D. Andreeti, R. Ungaro, and A. Pochini, "Crystal and Molecular Structure of Cycloquarter[(5-t-butyl-2-hydroxy-1,3-phenylene)-methylene] Toluene (1:1) Clathrate," *Chemical Communications*, pp. 1005–1007, 1979.

[70] P. Murphy, R. G. McKinlay, S. J. Dalgarno, and M. J. Paterson, "Toward Understanding of the Lower Rim Binding Preferences of Calix[4]arene," *The Journal of Physical Chemistry A*, vol. 119, pp. 5804–5815, 2015.

[71] C. Lee, W. Yang, and R. G. Parr, "Development of the Colle-Salvetti Correlation Energy Formula into a Functional of the Electron Density," *Physical Review B*, vol. 37, no. 20, pp. 785–789, 1988.

[72] A. D. Becke, "Density-functional thermochemistry. V. Systematic optimization of exchange- correlation functionals," *Journal of Chemical Physics*, vol. 107, pp. 8554–8560, 1997.

[73] M. Dolg, U. Wedig, H. Stoll, and H. Preuss, "Energy-Adjusted *ab initio* Pseudopotentials for the First Row Transition Elements," *Journal of Chemical Physics*, vol. 86, no. 2, pp. 866–872, 1987.

[74] J. W. Ochterski, "Thermochemistry in Gaussian," tech. rep., Gaussian Inc., 2000.

[75] R. Seeger and J. A. Pople, "Self-Consistent Molecular Orbital Methods. XVIII. Constraints and Stability in Hartree-Fock Theory," *Journal of Chemical Physics*, vol. 66, no. 7, pp. 3045–3050, 1977.

[76] R. Bauernschmitt and R. Ahlrichs, "Stability Analysis for Solutions of the Closed Shell Kohm-Sham Equations," *Journal of Chemical Physics*, vol. 104, no. 22, pp. 9047–9052, 1996.

[77] N. E. Schultz, Y. Zhao, and D. G. Truhlar, "Density Functionals for Inorganometallic and Organometallic Chemistry," *Journal of Physical Chemistry*

A, vol. 109, pp. 11127–11143, 2005.

[78] O. V. Gritsenko, P. R. T. Schipper, and E. J. Baerends, "Exchange and Correlation Energy in Density Functional Theory: Comparison of Accurate Density Functional Theory Quantities with Traditional Hartree-Fock Based Ones and Generalised Gradient Approximations for the Molecules Li_2, N_2, F_2," *Journal of Chemical Physics*, vol. 107, pp. 5007–5015, 1997.

[79] V. Tschinke and T. Zeigler, "On the Different Representations of the Hole Correlation Functions in the Hartree-Fock and the Hartree-Fock-Slater Methods and their Influence on Bond Energy Calculations," *Journal of Chemical Physics*, vol. 93, pp. 8051–8060, 1990.

[80] J. P. Coe and M. J. Paterson, "Investigating Multireference Character and Correlation in Quantum Chemistry," *Journal of Chemical Theory and Computation*, vol. 11, pp. 4189–4196, 2015.

[81] A. Szabo and N. S. Ostlund, *Modern Quantum Chemistry.* pp. 100–107, Dover Publications, 1996.

[82] J. C. Schug and D. H. Phillips, "Spin Contamination in Unrestricted Hartree-Fock Calculations," *Journal of Chemical Physics*, vol. 59, no. 4, pp. 1616–1624, 1973.

[83] F. Sasaki and K. Ohno, "Spin-Component Analysis of Single Determinant Wavefunctions," *Journal of Mathematical Physics*, vol. 4, no. 9, pp. 1140–1147, 1963.

[84] A. J. Cohen, D. J. Tozer, and N. C. Handy, "Evaluation of $\langle S^2 \rangle$ in Density Functional Theory," *Journal of Chemical Physics*, vol. 126, p. 214104, 2007.

[85] J. Baker, A. Scheiner, and J. Andzelm, "Spin Contamination in Density Functional Theory," *Chemical Physics Letters*, vol. 216, no. 3-6, pp. 380–388, 1993.

[86] A. J. Petrella, D. C. Craig, R. N. Lamb, C. L. Raston, and N. K. Roberts, "A Facile Route to Hetero-bimetallic Ti(IV)-Alkali Metal Calix[4]arene Complexes," *Dalton Transactions*, pp. 4590–4597, 2003.

[87] C. Aronica, G. Chastanet, E. Zueva, A. Borshch, J. M. Clemente-Juan, and D. Luneau, "A Mixed Valence Polyoxovanadate(III,IV) Cluster with a Cal-

ixarene Cap Exhibiting Ferromagnetic V(III)-V(IV) Interactions," *Journal of American Chemical Society*, vol. 130, pp. 2365–2371, 2008.

[88] R. D. Shannon, "Revised Effective Ionic Radii and Systematic Studies of Interatomic Distances in Halides and Chalcogenides," *Acta Crystallographica*, vol. A32, pp. 751–767, 1976.

[89] T. Bally and W. T. Borden, *Calculations on Open Shell Molecules: A Beginner's Guide, Reviews in Computational Chemistry*, vol. 13, ch. 1. John Wiley & Son, 1999.

[90] P. Murphy, S. J. Dalgarno, and M. J. Paterson, "Transition Metal Complexes of Calix[4]arene: Theoretical Investigations into Small Guest Binding with the Host Cavity," *The Journal of Physical Chemistry A*, vol. 120, pp. 824–839, 2016.

[91] T. Yanai, D. P. Tew, and N. C. Handy, "A New Hybrid Exchange-Correlation Functional Using the Coulomb-Attentuating Method (CAM-B3LYP)," *Chemical Physics Letters*, vol. 393, pp. 51–57, 2004.

[92] Y. Zhao and D. G. Truhlar, "The M06 Suite of Density Functionals for Main Group Thermochemistry, Thermochemical Kinetics, Noncovalent Interactions, Excited States and Transition Elements: Two New Functionals and Systematic Testing of Four M06-class Functionals and 12 Other Functionals," *Theoretical Chemistry Accounts*, vol. 120, pp. 215–241, 2008.

[93] Y. Zhao and D. G. Truhlar, "A New Local Density Functional for Main Group Thermochemistry, Transition Metal Bonding, Thermochemical Kinetics and Noncovalent Interactions," *Journal of Chemical Physics*, vol. 125, p. 194101, 2006.

[94] J.-D. Chai and M. Head-Gordon, "Systematic Optimisation of Long-Range Corrected Hybrid Density Functionals," *Journal of Chemical Physics*, vol. 128, p. 084106, 2008.

[95] J.-D. Chai and M. Head-Gordon, "Long-Range Corrected Hybrid Density Functionals with Damped Atom-Atom Dispersion Corrections," *Physical Chemistry Chemical Physics*, vol. 10, pp. 6615–6620, 2008.

[96] S. Grimme, J. Antony, S. Ehrlich, and H. Krieg, "A Consistent and accurate *ab initio* Parameterization of Density Functional Dispersion Correction (DFT-D) for the 94 Elements H-Pu," *Journal of Chemical Physics*, vol. 132, p. 154104, 2010.

[97] S. F. Boys and F. Bernardi, "Calculation of Small Molecular Interactions by Differences of Separate Total Energies - Some Procedures with Reduced Errors," *Molecular Physics*, vol. 19, pp. 553–566, 1970.

[98] S. Simon, M. Duran, and J. J. Dannanberg, "How Does Basis Set Superposition Error Change the Potential Energy Surfaces for Hydrogen Bonded Dimers," *Journal of Chemical Physics*, vol. 105, pp. 11024–11031, 1996.

[99] H. Kruse, L. Goerigk, and S. Grimme, "Why the Standard B3LYP/6-31g* Model Chemistry Should not be Used in DFT Calculations of Molecular Thermochemistry: Understanding and Correcting the Problem," *Journal of Organic Chemistry*, vol. 77, pp. 10824–10834, 2012.

Chapter 5

Conclusions and Future Work

The body of work covered in this thesis has examined the range of computational techniques required to deal with a range of systems from those which are geometrically simple but electronically complex through to those which are geometrically complex but electronically simple. It was discovered that for electronically complex systems, the multi-reference nature of these systems dictates that the recovery of electron correlation must be prioritised. The technique of Monte Carlo Configuration Interaction (MCCI) was shown to produce reasonably accurate predictions of the potential energy surfaces of traditionally challenging transition metal dimers, with highly compact wavefunctions compared to those required for Full Configuration Interaction (FCI). It was seen that no prior knowledge of the important molecular orbitals was required and the technique is essentially black box with the exception of a single parameter, c_{min}, which determines the minimum value of coefficient of each Slater determinant or CSF required for inclusion in the wavefunction. The potential energy landscapes of several transition metal dimers were elucidated, showing reasonably good agreement with both experiment and also with other computational methods but with significantly smaller wavefunctions compared to FCI. Having demonstrated the concept, it was then shown that ScNi represents the current limit of the MCCI method with results showing reasonable comparison to experiment where data is available.

Following on from this initial evaluation of MCCI, the technique was developed to determine Spin-Orbit Coupling (SOC) properties of a range of atoms and small dimers with results showing reasonable agreement with other techniques but again

with highly compact wavefunctions compared to FCI. One problem however represents a barrier to the further development of the MCCI method. This problem relates to the neglect of two electron effects in the Spin-Orbit Coupling implementation. Comparison of the results in this work with one electron only results from Spin-Extended Hartree Fock calculations show clearly that two electron effects must be included for quantitative results. It is possible that this could be achieved through an effective one electron operator and efforts continue to attempt to establish the best way forward. Success in this area could allow MCCI to be used to investigate singlet-triplet interactions, due to spin-orbit coupling, involving non-spin conserving processes.

Following on from the application and development of state of the art techniques to examine small atoms and molecules with simple geometry but complicated electronic structure, larger calixarene systems with more complicated geometries but simpler electronic structure were then investigated using DFT. Firstly, the mechanism of ring inversion of biscalix[4]arene was considered and resulted in elucidation of the key energy barriers, transition states and intermediates involved. It was discovered that the lowest energy pathway of 19.31 kcal mol^{-1} was only slightly above the experimentally observed 13-15 kcal mol^{-1} expected for a single C4 entity. Although with energy barriers such as this, the interconversion between the anti-conformation and the desired syn-conformations (rate constant around 0.05 s^{-1} when estimated using the Eyring equation) is relatively slow compared to experimental observations on C4 (around 150 s^{-1}), the barriers between the intermediates are considerably smaller indicating much faster interconversion rate constants and synthetic attempts to crystallise these structures should (and indeed do) prove challenging as a result. Mitigation procedures are recommended.

In order to better understand the formation of polymetallic clusters involving C4, a study was undertaken of the binding preferences of the C4 lower rim tetraphenolic pocket towards the first row transition metals in various oxidation and spin states. It was found that the bonding between C4 and the metals was electrostatic in nature with preference towards higher oxidation states and late transition metals. Maximal spin states were generally but not universally favoured, indicative of a delicate balance between electron pairing energies and d orbital splitting energies as illustrated by the Mn^{3+}(quintet spin)-bound calixarene presented in this work.

Finally, the preference for C4 to bind a range of important small molecules was investigated and the change in binding for these guest species as the metal at the lower rim was changed was considered. It was found that increased binding of a few kcal mol^{-1} was introduced depending on the type of metal introduced. A range of binding energies for certain gases such as CO_2 and SO_2 suggests that polymetallic clusters could potentially find practical use as gas storage or gas separation devices.

Future work regarding these calixarenes is currently focussed on investigating the effect on binding of guests when the tetraphenolic pocket design is changed from OH groups to groups where the hydrogen bonding at the lower rim is disturbed (which causes subsequent geometric changes at the upper rim). Such calculations are expected to reveal whether calixarenes can be fine-tuned in this way to preferentially store specific guests over others and to provide further details of the potential of these devices for reversible storage of guests. This work is ongoing and is expected to be published later this summer. Other future work seeks to investigate the nature of multiple substitution at the biscalixarene methylene bridge hydrogens via a process of deprotonation and is designed to help answer a range of questions observed synthetically by experimentalists. Again this work is expected to be completed and published in the summer. A more long term piece of future work is to consider changes at the methylene bridge carbon atoms: replacing them with other atoms such as O, N and S and to investigate the effect of this on small guest binding.